DOCTORAL DISSERTATION

Micromechanical Study of Cold Dwell Fatigue in Titanium Alloys

チタン合金の室温 Dwell 疲労に関する微視力学的研究

Graduate School of Engineering Science
Yokohama National University

Liangwei Yin

殷 良偉

March 2022

Preface

This dissertation is submitted for the degree of Doctor of Philosophy in Engineering at the Graduate School of Engineering Science, Yokohama National University. The research was conducted under the supervision of Professor Osamu Umezawa from the Faculty of Engineering, Yokohama National University from April 2019 to March 2022.

The work in this thesis is my own, except where acknowledgements and references are made to previous work.

Acknowledgements

During the COVID-19 pandemic, studying at Yokohama National University has been an unforgettable memory full of happiness and sorrows for me and I was very excited to be at the Laboratory of Metal Physics to do the presented research in this thesis.

Firstly, I wish to acknowledge my gratitude to my supervisor Prof. Osamu Umezawa for the continuous support of my Ph.D. research in terms of the insightful advice and free space provided by him. I also thank Professors: Shoichi Hirosawa, Wataru Nakao, Makoto Hasegawa, and Naoko Ohno for their advice.

I would like to thank Dr. Yang Liu from Imperial College London, Daijun Hu from National University of Singapore for sharing the fundamental knowledge of continuum mechanics and crystal plasticity modeling, Dr. Shinichi Takagi from Kanagawa Institute of Industrial Science and Technology for the support in performing nanoindentation tests, and Assoc. Prof. Haibin Tang from Nanjing University of Science and Technology for reading and editing papers.

In addition, much gratitude to my former colleagues Yan Xu, Baiyang Li from AECC Commercial Aircraft Engine Co. Ltd., and friends Xu Liu from AECC Shenyang Engine Design and Research Institute, Mingxuan Cai from AECC China Gas Turbine Establishment, Sihui Yang from AECC China Aero Power Machine Research Institute for providing crucial knowledge related to the fan and compressor stages in aero-engine, Xiaojin Chen from Bosch (China) Co. Ltd. for the preceding work concerning the Voronoi tessellation, Wentian Zhang from Nanjing University of Aeronautics and Astronautics for generously offering the code calculating geometrical compatibility, and Dr. Bo Peng from Zhejiang University, Lingfeng Wang from Air Force Engineering University, Sicheng Dai from Nanjing University of Aeronautics and Astronautics for the fruitful discussions.

Finally, and most importantly, I gratefully acknowledge the invaluable encouragement and love of my parents, without whom I would never finish my Ph.D. study.

Liangwei Yin

February 2022

Abstract

Titanium alloys are lightweight structural materials for aerospace applications such as jet engine components, where the titanium alloy discs and blades suffer a significant lifetime reduction due to the cold dwell effect. This thesis is committed to deepening the basic understanding of the phenomenon called cold dwell sensitive fatigue. A thorough study is performed using multiscale experiments, from nanoindentation test to digital image correlation (DIC) technique and macroscopic mechanical tests, and numerical modeling methods from the grain scale to component level, to elucidate the effect of plastic deformation modes, microstructural morphology, and external loading conditions on dwell fatigue sensitivity of titanium alloys. Firstly, the formulation of a dislocation mechanism-based strain gradient crystal plasticity model incorporating thermally activated dislocation escape and deformation twinning is presented. Next, the crystal plasticity model is adopted in conjunction with DIC strain mapping to evaluate the plastic deformation mechanisms operating under dwell fatigue loading and resulting strain localization in commercially pure titanium. It is shown that dwell strain accumulation is dominated by dislocation slip and the nucleation of deformation twinning has a limited impact on stress redistribution procedure, i.e., dwell facet formation. Then, the attention is shifted to dual-phase titanium alloys. The elastoplastic properties of the β phase in Ti-Fe-O alloy are determined by nanoindentation tests. On this basis, an intergranular β lath with low α/β geometrical compatibility and large thickness is suggested to significantly inhibit the redistribution of stress from the soft to hard α grain. Meanwhile, the stress concentration in the β lath at high stress levels is assumed to cause two competing dwell fatigue crack initiation modes, shear-induced cavity and basal faceting. Finally, the effect of temperature on stress redistribution in Ti-6Al-4V alloy is assessed in terms of temperature-dependent strain rate sensitivity and creep mechanisms to understand the dwell fatigue sensitivity of an aero-engine fan disc during operation. A relation between rate-dependent crystal plasticity parameters and strain rate sensitivity is established for a soft α grain. The variation in strain rate sensitivity of the soft grain with temperature affects the magnitude of stress shed onto the adjacent hard grain, and in turn, changes the dwell fatigue sensitivity. The influences of temperature, loading state, and size of macrozones on local stress redistribution and dwell facet nucleation at the bore of the fan disc are comprehensively addressed using crystal plasticity finite element submodeling approach.

Publication List

The material covered in this thesis has been published (or under review) in various journals and has been presented at an international conference.

Journal Articles

(1) Liangwei Yin, Osamu Umezawa, Heterogeneous deformation in a commercially pure titanium sheet under dwell fatigue loading: Crystal plasticity modeling and experiment, ISIJ International, Vol. 61, No. 6, pp. 1990-2001, (2021.6.15), DOI:10.2355/isijinternational.ISIJINT-2020-702.

(2) Liangwei Yin, Osamu Umezawa, Influence of dispersed β phase on local deformation pattern in mill-annealed Ti-Fe-O alloy under dwell fatigue loading, International Journal of Fatigue, Vol. 152, (2021.11), 106447, DOI:10.1016/j.ijfatigue.2021.106447.

(3) Liangwei Yin, Osamu Umezawa, Crystal plasticity analysis of temperature-sensitive dwell fatigue in Ti-6Al-4V titanium alloy for an aero-engine fan disc, International Journal of Fatigue, Vol. 156, (2022.3), 106688, DOI:10.1016/j.ijfatigue.2021.106688.

(4) Liangwei Yin, Osamu Umezawa, Crystal plasticity investigation on the evolution of stress redistribution and local plastic deformation in a grade 1 commercially pure titanium under dwell fatigue loading condition, Rare Metal Materials and Engineering, to be submitted.

Conference Presentations

(1) Liangwei Yin, Osamu Umezawa, Crystal plasticity analysis of temperature-sensitive dwell fatigue in Ti-6Al-4V alloy for an aero-engine fan disk. Annual Meeting & Exhibition of the Minerals, Metals, and Materials Society, Late News Poster Session, Anaheim, California, USA, (2022.2).

Table of Contents

List of Figures

List of Tables

List of Abbreviations and Nomenclature

Abbreviations

CSM	Constant stiffness measurement
CRSS	Critical resolved shear stress
DIC	Digital image correlation
EBSD	Electron backscattered diffraction
GND	Geometrically necessary dislocation
RVE	Representative volume element
SEM	Scanning electron microscopy
SF	Schmid factor
SRS	Strain rate sensitivity
SSD	Statistically stored dislocation
TEM	Transmission electron microscopy
TF	Stress triaxiality factor
$WASF$	Weighted averaged Schmid factor

Nomenclature (symbols and corresponding units)

A	Zener anisotropy ratio
A_c	Contact area (nm^2)
b	Burgers vector (μm)
C	Empirical parameter obtained from the power-law equation
d	Thermal activation event (μm)
$\boldsymbol{D}$	Symmetric rate of stretching
$\boldsymbol{D}_e, \boldsymbol{D}_p$	Elastic, plastic components of the symmetric rate of stretching
E	Young's modulus (GPa)
E_r	Reduced elastic modulus (GPa)
e	Geometry-dependent parameter
$\boldsymbol{E}$	Elastic stiffness tensor
$\boldsymbol{F}$	Deformation gradient
$\boldsymbol{F}_e, \boldsymbol{F}_p, \boldsymbol{F}_T$	Elastic, plastic, and thermal components of the deformation gradient
ΔF	Helmholtz free energy (J)

ΔG	Gibbs free energy (J)
G	Shear modulus (GPa)
g_0	Reference slip resistance (GPa)
h	Nanoindentation displacement (nm)
h_c	Contact depth (nm)
h_{max}	Maximum depth (nm)
h_{ii}, h_{ij}	Self-hardening and latent-hardening moduli
h_0	Initial hardening modulus (MPa)
H	Indentation hardness (GPa)
$\boldsymbol{I}$	Identity tensor
$\boldsymbol{J}$	Jacobin matrix
k	Boltzmann constant (J/K)
l	Pinning distance (μm)
l_{int}	Intrinsic length scale of the material
$\boldsymbol{L}$	Velocity gradient
$\boldsymbol{L}_p$	Plastic component of the velocity gradient
m	Strain rate sensitivity exponent
m'	Geometrical compatibility factor
$\boldsymbol{m}$	Slip/twinning plane normal
$\boldsymbol{N}$	Shape function
P	Indentation load (mN)
$\boldsymbol{p}$	Symmetric slip system tensor
q	Latent hardening constant
r	Rate sensitivity index
R	Stress ratio
$\boldsymbol{R}$	Rotation matrix computed by Bunge Euler angles
$\boldsymbol{R_{rot}}$	Rotation matrix transforming local elastic matrix to global elastic matrix
$\boldsymbol{R}^{tw}$	Rotation tensor
S	Stiffness
$\boldsymbol{s}$	Slip/twinning direction
T	Temperature (K)
ΔV	Activation volume (μm^3)

V	Twinning Volume fraction
V_{th}	Threshold volume fraction
$\boldsymbol{W}$	Antisymmetric spin tensor
$\boldsymbol{W}_e, \boldsymbol{W}_p$	Elastic, plastic components of the antisymmetric spin tensor
$\boldsymbol{\alpha}$	Tensor containing thermal expansion coefficient
α_T	Empirical coefficient
γ	Cumulative shear strain on all slip/twinning systems
$\dot{\gamma}$	Shearing rate of slip/twinning system
γ_0	Shear strain that is work conjugate to the resolved shear stress
$\dot{\gamma_0}$	Reference slipping rate
γ_{twin}	Cumulative shear strain on a twinning system
γ_{ref}	Reference twinning shear
$\dot{\varepsilon}$	Strain rate (s^{-1})
κ	Angle between incoming and outgoing slip directions (°)
λ	Geometry-related parameter
ν_D	Debye frequency (Hz)
υ	Poisson's ratio
ρ_m	Mobile dislocation density (μm^{-2})
ρ_{GND}	Effective density of geometrically necessary dislocations (μm^{-1})
$\sigma_{0.2}$	0.2% proof stress (MPa)
σ_t	Ultimate tensile strength (MPa)
σ_0	Permissible stress (MPa)
τ_e	Effective resolved shear stress (MPa)
τ	Resolved shear stress (MPa)
τ_c	Effective critical resolved shear stress (MPa)
τ_{SSD}	Slip strength induced by statistically stored dislocations (MPa)
τ_0	Initial critical resolved shear stress (MPa)
τ_∞	Saturated critical resolved shear stress (MPa)
τ_{GND}	Slip strength induced by geometrically necessary dislocations (MPa)
υ_g	Average glide velocity of dislocations
φ	Angle between the normal of incoming and outgoing slip plane (°)
$\boldsymbol{\psi}$	Isoparametric coordinates of the Gauss point

$\boldsymbol{\omega}$	Spin tensor

1 Introduction

1.1 Development of titanium and its application in the aerospace industry

Titanium is a transition metal with a 0.6 percent abundance in the earth's crust, making it the fourth most plentiful structural metal after aluminum, iron, and magnesium. After the Second World War, in the late 1940s and early 1950s, there was a surge of interest in commercial titanium manufacturing and alloy research [1]. As a result, a variety of titanium alloys have been developed. Owing to their prominent properties of high specific strength (strength-to-weight ratio), excellent fatigue performance and creep resistance up to a temperature of 873 K, and good producibility, there is an increasing usage of titanium alloys in aerospace and marine applications. For instance, particular titanium alloys have been used throughout aircraft production such as landing gear, tail core, flap track beam, and aero-engine. Fig. 1.1 gives the cross-section of the General Electric GEnx-1B dual-spool high-bypass civil turbofan engine equipped by the wide-body jet airliner Boeing 787. The major components of this engine include a 1-stage fan, 4-stage booster, 10-stage high-pressure compressor (HPC), annular combustor, 2-stage high-pressure turbine (HPT), and 7-stage low-pressure turbine (LPT). Nickel-based superalloys (e.g., directional solidified, powder metallurgy, and single crystal Ni-based alloys) are generally used in the hot section, i.e., HPT, LPT, and HPC stages because of superior strength and corrosion resistance at high temperatures. Titanium alloys are candidate materials for the cold section of aero-engines. The material selections for the fan, booster, and HPC stages of the GEnx-1B engine are listed in Table 1.1 [2]. It can be found that titanium alloys are widely used to manufacture rotor components in the cold section of the GEnx-1B engine such as discs and blades of the fan and compressor stages. In particular, Ti-6Al-4V alloy is taken as the mainstay for the aero-engine industry dominated by leading manufacturers such as General Electric, Rolls-Royce, Pratt & Whitney, and Safran Aircraft Engines. Although new composites like carbon fiber and ceramics are regarded as lightweight alternatives, the role of titanium remains vital in the foreseeable future considering the balance of the aforementioned qualities [3],[4]. Therefore, an in-depth understanding of material behavior in titanium and its alloys enables producers to process titanium for optimum performance, which in turn allows engineers to accomplish structural optimization of aero-engine components. The following section will systematically introduce titanium in terms of crystallography, processing,

microstructure, and resulting mechanical properties.

Table 1.1 Material selections for the fan, booster, and HPC stages in the GEnx-1B engine [2].

Stage	Component	Material
Fan	Fan blade	Composite
	Fan disc	Titanium alloy Ti-6Al-4V
	Fan case	Composite
	Fan shaft	C250 steel
Booster	Booster rotator blade	Titanium alloy Ti-6Al-4V
	Drum shaft	Titanium alloy Ti-6Al-4V
	Booster stator blade	Composite
	Booster stage case	Composite
High-pressure compressor (HPC)	1^{st}, 2^{nd} blisc	Titanium alloy Ti-6Al-4V
	3^{rd}, 4^{th} blisc	Titanium alloy Ti6242
	5^{th} blisc	Nickel alloy Inconel 718
	6^{th}, 7^{th} disc	Nickel alloy Inconel 718
	8^{th} disc	Nickel alloy Inconel 718
	9^{th} disc, seal disc	Nickel alloy René 88DT
	10^{th} disc	Nickel alloy René 88DT
	6^{th} ~8^{th} rotor blade	Nickel alloy Inconel 718
	9^{th} ~10^{th} rotor blade	Nickel alloy UDIMET 720
	Front case	M152 steel
	Inner case	Nickel alloy Inconel 718

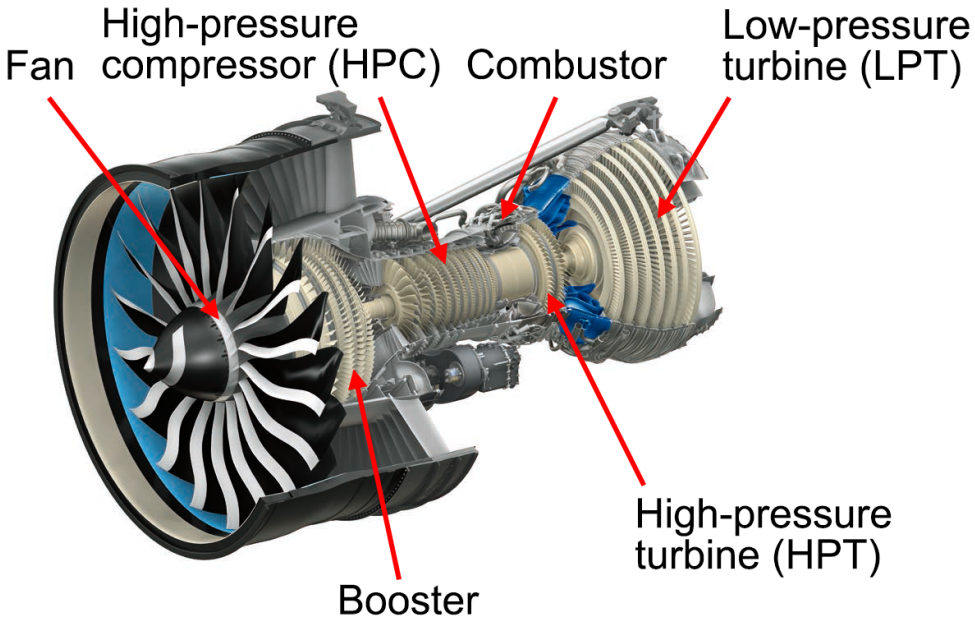

Fig. 1.1 GEnx-1B turbofan engine cross-section.

1.2 Basic knowledge of titanium

1.2.1 Metallurgy of titanium

Pure titanium demonstrates an allotropic phase transformation at 1155 K, which changes from β phase with a body-centered cubic (BCC) crystal structure at higher temperature to α phase with a hexagonal close-packed (HCP) crystal structure at lower temperatures, as shown in Fig. 1.2.

The β-transus temperature is markedly influenced by alloying elements. The substitutional element aluminum and interstitial element oxygen, nitrogen, carbon are α-stabilizing elements that can extend the α phase field to temperatures higher than 1155 K. In contrast, the β-isomorphous elements molybdenum, vanadium, niobium, thallium, and β-eutectic chromium, iron, manganese, nickel, copper, cobalt are β-stabilizing elements that lower the transus temperature. Neutral elements such as tin and zirconium insignificantly affect the phase transformation. Depending on the addition of different alloying elements, titanium alloys are conventionally classified in five categories as α, near-α, $\alpha+\beta$, metastable β, and stable β alloys. The pseudobinary β-isomorphous phase diagram is shown in Fig. 1.3.

Some of the commercial titanium alloys, belonging to one of four groups (commercial alloys are excluded from stable β alloys) are tabulated in Table 1.2.

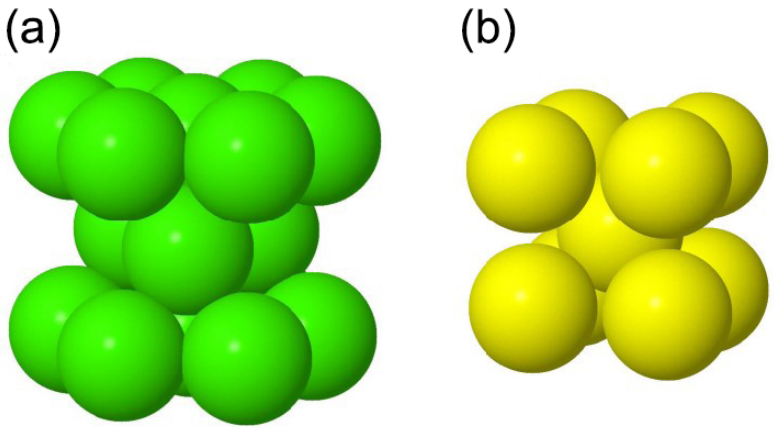

Fig. 1.2 (a) α-titanium with HCP structure, (b) β-titanium with BCC structure.

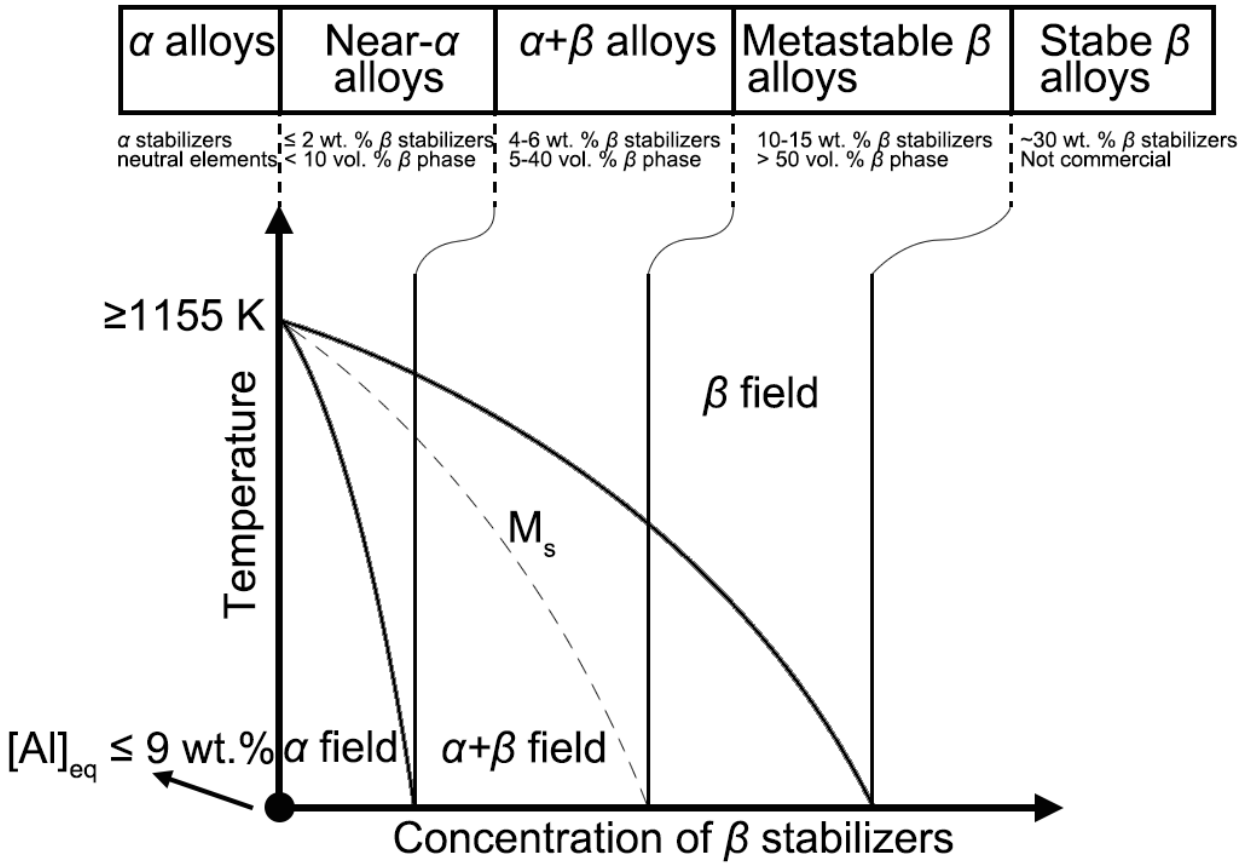

Fig. 1.3 Pseudobinary β isomorphous equilibrium phase diagram.

Table 1.2 Commercial titanium alloys.

Classification	Alloy	T_β (K)
α alloys	Commercially pure titanium (CP-Ti)	890-950
	Ti-5Al-2.5Sn	1040
Near-α alloys	Ti-6Al-5Zr-0.5Mo-0.25Si (IMI685)	1020
	Ti-5.5Al-3.5Sn-3Zr-1Nb-0.25Mo-0.3Si (IMI829)	1015
	Ti-5.8Al-4Sn-3.5Zr-0.5Mo-0.7Nb-0.35Si-0.06C (IMI834)	1045
	Ti-6Al-2Sn-4Zr-2Mo-0.1Si (Ti-6242)	995
$\alpha + \beta$ alloys	Ti-6Al-4V (Ti-64)	995
	Ti-6Al-2Sn-4Zr-6Mo (Ti-6246)	940
	Ti-5Al-2Sn-2Zr-4Mo-4Cr (Ti-17)	890
Metastable β alloys	Ti-10V-2Fe-3Al (Ti-1023)	800
	Ti-15V-3Cr-3Al-3Sn (Ti-15-3-3-3)	760

1.2.2 Thermomechanical processing and resulting microstructure

The microstructure of titanium alloys can be altered by thermomechanical processing. The effect of thermomechanical processing on microstructural morphology depends on the type of titanium alloys.

For commercially pure titanium, the thermomechanical processing is usually performed completely in the α phase field and the main purpose is to adjust the α grain size to the required level. For instance, small α grain sizes ($10\ \mu m$) can be achieved by recrystallization at around $973\ K - 1023\ K$, whereas larger α grain sizes can be obtained by recrystallization at about $1173\ K$ [1]. Commercially pure titanium is used annually in heat exchangers, liners for tanks, and other applications in chemical and petrol-chemical industries.

In the dual-phase titanium alloys (near-α alloys, $\alpha + \beta$ alloys, and metastable β alloys), three different types of microstructures can be produced by changing the thermomechanical processing route: bimodal or duplex structure containing primary α grains in the $\alpha + \beta$ colonies, globular structure, and fully lamellar structure. The typical microstructures in commercially pure titanium and dual-phase titanium alloys are illustrated in Fig. 1.4 [5],[6].

A typical processing route to obtain bimodal microstructure (Fig. 1.4b) can be divided into four steps: homogenization in the β phase field, deformation in the $\alpha + \beta$ phase field, recrystallization in

the $\alpha + \beta$ phase field, and aging at lower temperatures. Near-α alloys with bimodal microstructure have advantages in high-temperature use (service temperature ≥ 600 K) [7]. In this regime, forged near-α alloys possess moderate strength and excellent creep resistance, which meet the requirement of highly stressed rotors at the first several stages of the high-pressure compressor within aero-engines (Table 1.1). A balance between creep resistance and fatigue performance can be achieved by producing a volume fraction of the primary α phase between approximately 10 % and 18 % [8]. The addition of carbon to near-α alloy IMI834 makes this microstructure more reproducibly attainable during solution heat treatment [1].

The processing to generate a globular microstructure (Fig. 1.4c) with transformed β phase located at the grain boundaries or "triple points" of the α grains is the same as that of bimodal microstructure except for a slower cooling rate from the recrystallization temperature or a sufficiently low recrystallization temperature. Mill-annealed $\alpha + \beta$ alloys (notably Ti-6Al-4V and Ti-6Al-4V ELI) with globular microstructure contribute to the structural efficiency due to higher strength levels at temperatures lower than 573 K, the primary use of this kind of alloys in wrought form is therefore for fan and booster rotors in aero-engines (Table 1.1) and deep-sea submersibles [5],[9],[10].

The processing route for a fully lamellar microstructure (Fig. 1.4c) consists of a homogenization treatment in the β phase field and an aging (stress relieving) treatment. Since the method of damage tolerance design used for aerospace engineering allows the rotor components in aero-engine to service only if the fatigue crack length is under a critical value, near-α alloys with fully lamellar microstructure are also acceptable candidates for compressor discs due to high fatigue crack propagation resistance and fracture toughness [1].

The three microstructures mentioned above can also be exhibited by metastable β alloys through heat treatment. Although the commercial applications of metastable β alloys are not as extensive as those of near-α alloys and $\alpha + \beta$ alloys, these alloys are still attractive for highly loaded structures because of the highest strength and fracture toughness among conventional titanium alloys. For example, forgings made by Ti-1023 alloy are applied to manufacture the landing gear components of the airliner Boeing 777 [3].

Apart from the phase morphology, regions with distinct textures are naturally present in alloys during the thermomechanical process. A cluster of grains with a preferred crystallographic orientation, the so-called macrozone or microtextured region, is a special area where slip is considered to be

continuous between primary α grains because of low-angle grain boundaries, as the central zone with red color in Fig. 1.5 [11]. Thus, the macrozone may act as a large grain. To describe the large colony of aligned α grains, Rugg et al. [12] have come up with a rough conception of "Effective structural unit". Nevertheless, more detailed studies with respect to the definition of macrozone and its influence are required [13].

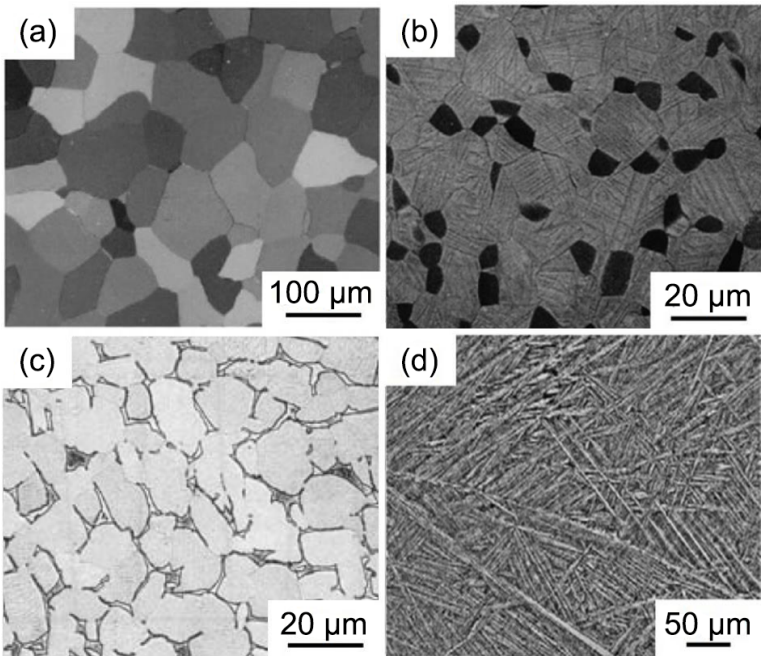

Fig. 1.4 (a) Single-phase polycrystalline α, (b) bimodal microstructure with equiaxed α grains and $\alpha + \beta$ colonies, (c) globular microstructure with equiaxed α grains and transformed β phase at α grain boundaries [6], (d) fully lamellar microstructure.

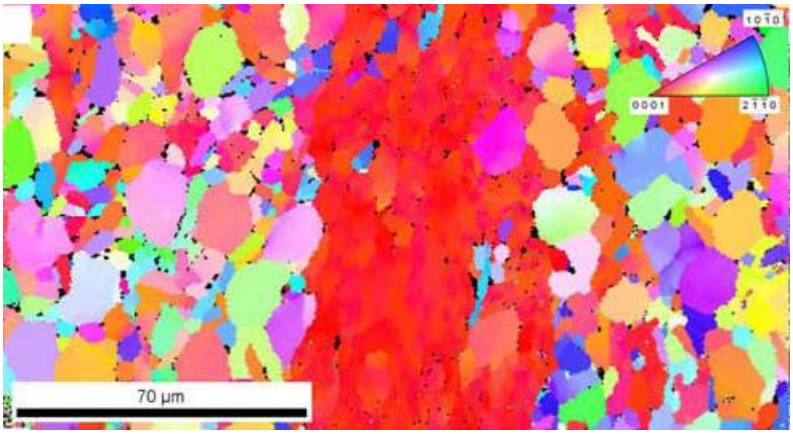

Fig. 1.5 Typical morphology of the macrozone in Ti-6Al-4V alloy [11].

1.2.3 Elastoplastic properties

Both α-titanium and β-titanium exhibit a high elastic anisotropy. As shown in Fig. 1.6, although the alloying elements have an impact on the value of Young's modulus, there exists a common trend that the directional Young's modulus decreases when the c-axis of the HCP lattice rotates from the direction parallel to the principal stress to direction perpendicular to it [14],[15],[16]. Also, the Zener anisotropy ratio (A) of BCC β-titanium displays a substantial scatter from 0.2 to 8.3, which demonstrates a strong dependence on β-stabilizers [17],[18],[19]. In general, the Young's modulus of metastable β alloys are lower than that of α and $\alpha + \beta$ alloys.

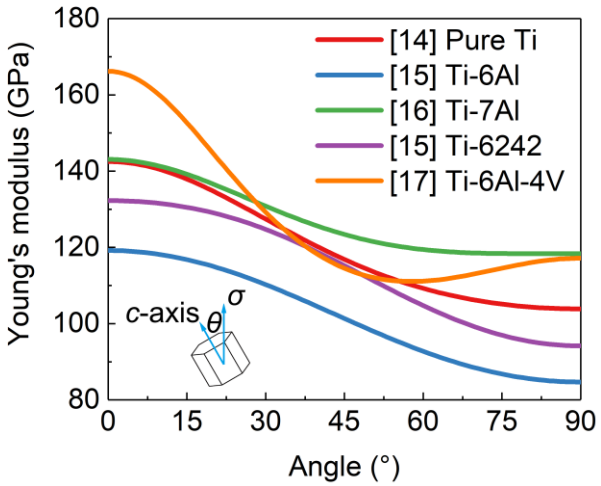

Fig. 1.6 Directional Young's modulus of α-titanium with different alloying elements.

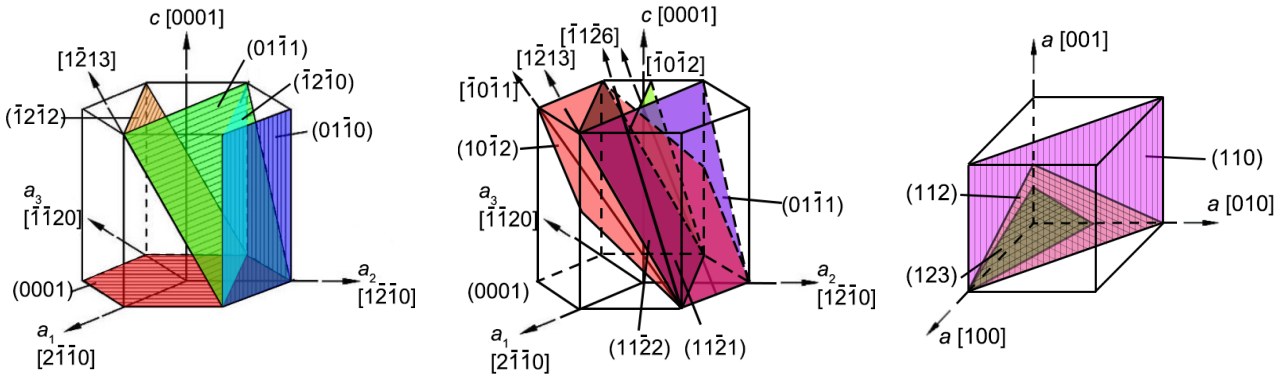

(a) (b) (c)

Fig. 1.7 HCP lattice with (a) related slip planes and directions and (b) twinning planes and directions, (c) BCC lattice with related slip planes and directions.

Plastic anisotropy is conspicuous in α-titanium with HCP lattice. As indicated in Fig. 1.7(a), five active slip system families in α phase include $3\,(0001)<11\bar{2}0>$ basal, $3\,\{10\bar{1}0\}<11\bar{2}0>$ prismatic, $6\,\{10\bar{1}1\}<11\bar{2}0>$ pyramidal, $12\,\{10\bar{1}1\}<11\bar{2}3>$ 1st pyramidal, and $6\,\{11\bar{2}2\}<11\bar{2}3>$ 2nd pyramidal slip systems. The close-packed plane changes from (0001) plane to $\{10\bar{1}0\}$ plane as the c/a ratio of α phase is 1.587 (the lattice parameters are $a = 0.295$ nm and $c = 0.468$ nm), which is smaller than the ideal ratio of 1.633 for the HCP crystal structure. Consequently, the critical resolved shear stress (CRSS) required to activate prismatic slip is the lowest, while the value of CRSS for pyramidal <c+a> slip is $2-6$ times higher across a wide range of temperatures [20], as shown in Fig. 1.8. To achieve a homogeneous deformation along the *c*-axis, many deformation twinning modes are observed in α -titanium, which are $6\,\{10\bar{1}2\}<10\bar{1}1>$ tension twins, $6\,\{11\bar{2}1\}<11\bar{2}6>$ tension twins, $6\,\{11\bar{2}2\}<11\bar{2}3>$ compression twins, and $12\,\{10\bar{1}2\}<10\bar{1}1>$ compression twins, as shown in Fig. 1.7(b). Among them, $\{10\bar{1}2\}<10\bar{1}1>$ tension twinning and $\{11\bar{2}2\}<11\bar{2}3>$ compression twinning are two most active twinning systems in titanium, which will be particularly considered in this thesis. The plastic deformation of β-titanium is more compliant than α-titanium since numerous slip systems can be activated, which are $12\,\{110\}<111>$, $12\,\{112\}<111>$, and $24\,\{123\}<111>$ slips, as shown in Fig. 1.7(c). The CRSS for $<111>$ slips is slightly higher than that for the prismatic slip in α phase. The slip and twinning mechanism will be discussed in detail in Chapter 3.

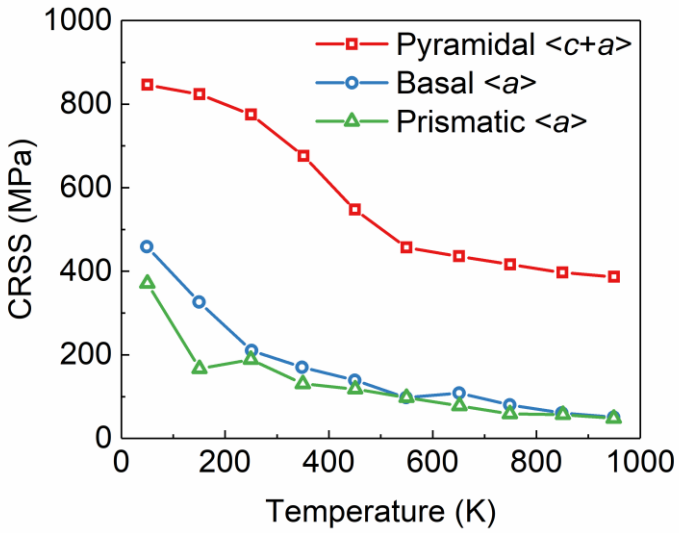

Fig. 1.8 CRSS vs deformation temperature for prismatic, basal, and pyramidal <*c*+*a*> slips in Ti-6.6Al single crystal [20].

1.3 Lifetime reduction in titanium alloy aero-engine components

The loading history of aero-engine components during a commercial flight operation cycle is illustrated in Fig. 1.9 [21]. When a passenger airliner is taxing from a terminal to the runway, the engines remain idling. When takeoff begins, the rotational speed of rotor components and working temperature in engines is close to the redline to provide the maximum thrust. Shortly after takeoff, a lower climbing thrust will be used until the cruising altitude is reached. During cruising, a constant high mean load hold (dwell) occurs. To approach for landing, the thrust of engines is reduced for descending. After touchdown, the engines immediately change to the maximum power to ensure sufficient reverse thrust for deceleration. When the airliner leaves the runway and heads to the apron, the engines will return to the idle state.

The load-dwell at the cruise phase leads to substantial fatigue life reduction compared with the prediction obtained from the traditional life assessment method, e.g., fatigue design principle that permissible stress level falls below the S-N curve [22],[23]. The overestimation of the lifetime was first acknowledged from the premature failures of two near-α alloy IMI685 fan discs of the Rolls-Royce RB211 engine, which was equipped by Lockheed L-1011 TriStar aircraft in the 1970s [24]. Since the accidents of the TriStar, at least five other incidents with respect to civil airliners have been attributed to the cold dwell fatigue effect on high-pressure compressor discs made of Ti-6242 on General Electric CF6 engines: at Dakar in 1985, at Seoul in 1991, at Los Angeles in 1993, at Bangkok in 1995, and at Beijing in 1996 [25],[26]. From an industrial perspective, IMI685 was replaced by $\alpha + \beta$ Ti-6Al-4V alloy in wrought form, which was initially considered to be dwell insensitive [23]. In addition, the volume fraction of the primary α phase in the rotor grade Ti-6242 alloy with bimodal microstructure was optimized to a low degree below 20 % through heat treatment to achieve a balance among fatigue, creep, and dwell resistance, as mentioned in Section 1.2.2. Nevertheless, the high-energy uncontained failure of a Ti-6Al-4V fan hub within the Engine Alliance GP7270 engine in 2017 first demonstrated that the Ti-6Al-4V fan disc is susceptible to lifetime reduction during operation [27]. Thereafter, the failures of Ti-6Al-4V fan blades in the GP7270 engine and Pratt & Whitney PW4077 engine in the next two years repeatedly proved that fan blades are also involved in the cold dwell fatigue phenomenon [28]. Hence, the dwell effect continues to be a serious problem for the manufacturers and operators of aircraft because the periodic inspections of the compressor discs and

blades and replacement of rotor components in which cracks are detected are necessary during service. It also leads to the over-design of discs and blades, with a consequent increase in the rate of fuel consumption, adding up to a considerable amount of fuel over the lifetime of a commercial aircraft. Considering the underlying mechanism of the aforementioned scenario is still elusive, the direction of the thesis is enlightened to thoroughly understand the mechanism of cold dwell sensitive fatigue in titanium alloys, thereby meeting the challenge of structural integrity evaluation for the aero-engine design process [29].

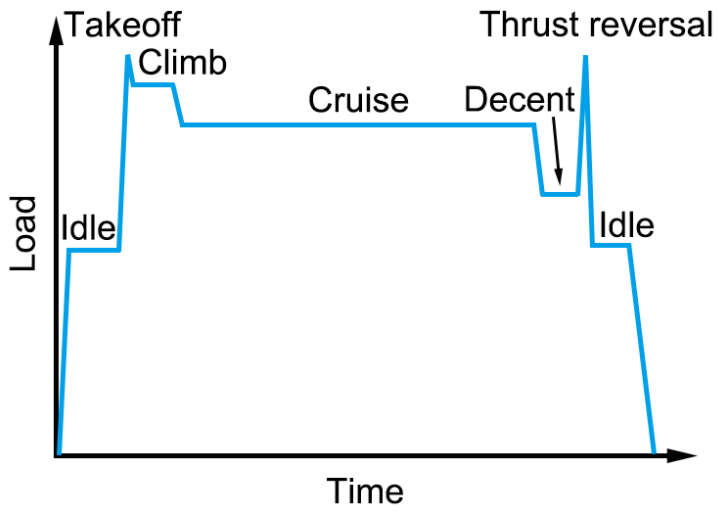

Fig. 1.9 Loading history of aero-engine components during a whole flight process.

1.4 Objective and thesis outline

This thesis aims to deepen the mechanistic understanding of the mechanism of cold dwell sensitive fatigue in titanium alloys and bridge the gap between alloy development and aero-engine component design, with special emphasis on stress redistribution and resulting dwell facet nucleation at both specimen and component levels. The outline of the thesis is concisely listed below.

Chapter 2 surveys the pertinent literature about the cold dwell fatigue in titanium alloys, which begins with some common views of this phenomenon, followed by a broad review of some key factors that influence the dwell fatigue sensitivity, and subsequently points out some outstanding questions requiring additional investigations.

Chapter 3 develops a new crystal plasticity constitutive model that will be used in the following

chapters for thermomechanical analysis.

Chapters 4 and 5 respectively select CP-Ti and Ti-Fe-O alloy to analyze the roles of deformation twinning and intergranular β phase in cold dwell fatigue by using experimental and numerical approaches.

Chapter 6 is an engineering-based study discussing the effect of temperature on grain-scale strain rate sensitivity and creep mechanisms in Ti-6Al-4V alloy to understand the dwell fatigue sensitivity of an aero-engine fan disc.

Finally, Chapter 7 gives a conclusive summary of this thesis and a prospect for future work.

2. Literature review

2.1 Introduction

This chapter gives a systematic overview of the experimental and numerical studies on cold dwell sensitive fatigue in polycrystal titanium. This review aims to discuss some metallurgical and external factors affecting cold dwell fatigue sensitivity, such as the alloy composition, microstructure, deformation mode, temperature, and loading condition, which in turn highlight the meaningful position of the work presented in this thesis.

2.2 Dwell fatigue in titanium and its alloys

The reduction in fatigue life under dwell fatigue loading condition has been observed in near-α, $\alpha + \beta$ titanium alloys, and CP-Ti [30]. The degree of fatigue life reduction is usually evaluated by the ratio of lives compared to an equivalent normal cyclic fatigue test, which is denoted as "dwell fatigue life debit" [31].

$$\text{Dwell debit} = \frac{N_{normal}}{N_{dwell}} \tag{2.1}$$

Both normal cyclic fatigue and dwell fatigue failures can be divided into three stages: crack initiation, crack propagation, and ultimate rupture. Since the fatigue crack initiation stage occupies the majority of the total life for titanium alloys, especially within the low cycle fatigue (LCF) regime, the dwell fatigue life debit is presumably related to the early crack initiation. To verify this hypothesis, pilot investigations into the fracture morphology at the grain scale have been propelled in the past few decades [32],[33],[34],[35]. Fractographic examinations of dwell fatigue loaded near-α and α/β titanium alloys reveal that crack initiation sites are predominantly subsurface [32]. These sites demonstrate discontinuous planar facets with sizes close to grain size, as shown in Fig. 2.1 [33]. Electron backscattered diffraction (EBSD) measurement confirms that these facets have near-basal orientations with normal $10^{\circ} - 25^{\circ}$ perpendicular to the loading direction [34],[35]. The early facet formation is thought to be closely associated with the dwell fatigue life debit.

Evans and Bache [36] adopted Stroh's dislocation pile-up model to illuminate the early dwell facet nucleation and subsequently developed an alternative stress redistribution model considering the

elastoplastic anisotropy of hexagonal close-packed (HCP) α-titanium [23],[37]. Fig. 2.2 gives a schematic diagram of modified Stroh's model. Provided a line of dislocations in a well-orientated (soft) grain glide under the imposition of shear stress and impinging on a grain boundary, the pile-up stress ahead of the dislocation pile-ups is considered to be redistributed to the adjacent poorly-orientated (hard) grain and induce the grain boundary stress concentration. The stress redistribution, or load shedding, was first captured by Hasija et al. [38] via rate-dependent crystal plasticity modeling. According to their study, due to the creep deformation of the soft grain during the stress-dwell period, the redistributed stress from the soft (*c*-axis perpendicular to the loading direction) to the adjacent hard (*c*-axis parallel to the loading direction) grain is presumed to generate the required stress field (a critical combination of high resolved normal stress on the basal plane and shear stress) for faceting in the hard grain, as shown in Fig. 2.3.

Based on the modified Stroh model and crystal plasticity modeling of stress redistribution, the following factors are reported to influence the dwell fatigue mechanisms in titanium and titanium alloys.

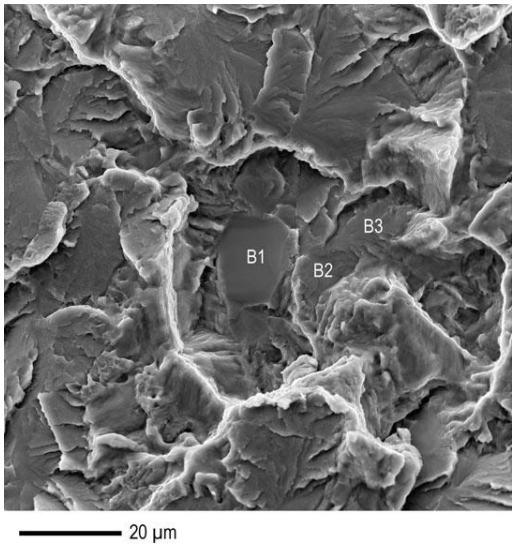

Fig. 2.1 Typical dwell facets within a crack initiation site [33].

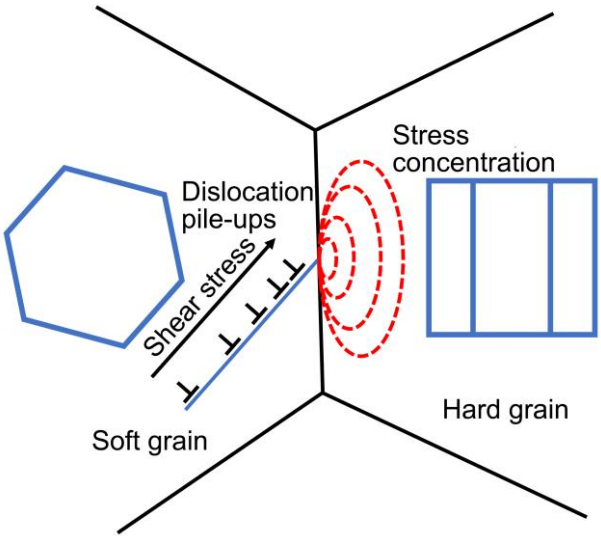

Fig. 2.2 Modified Stroh model for dwell facet nucleation.

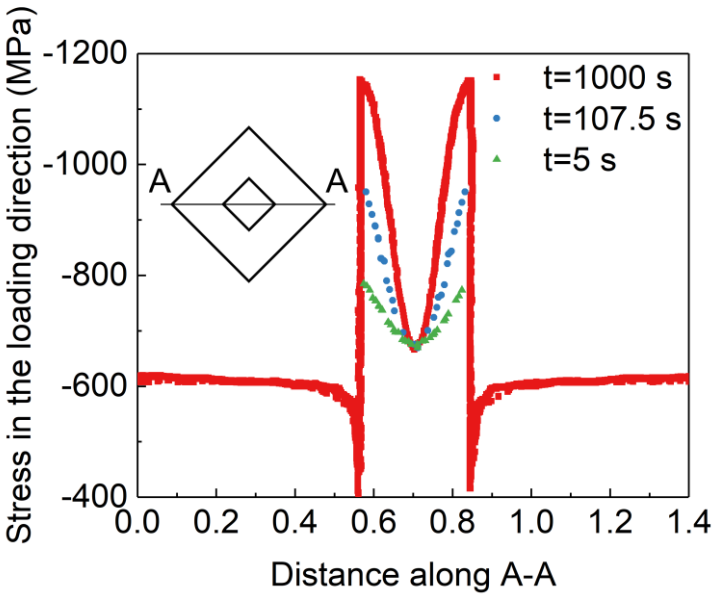

Fig. 2.3 Stress along A-A within a hard-soft grain combination in the work of Hasija [38].

2.3 Metallurgical factors affecting dwell fatigue sensitivity

2.3.1 Alloy composition

Hydrogen is a special alloying element that influences the deformation behavior in titanium alloys. The dwell fatigue sensitivity of near-α titanium alloys is also reported to change with hydrogen content. Mills et al. [39] investigated the effect of internal hydrogen on low cycle fatigue and dwell fatigue

properties of Ti-6242 alloy with bimodal microstructure, as illustrated in Fig. 2.4(a). It can be found that the low cycle fatigue life decreases as the hydrogen content increases. On the contrary, dwell fatigue life shows a crosscurrent and the dwell fatigue life debit decreases, especially when the concentration of hydrogen is higher than 150 ppm. Similarly, Evans et al. [40] studied the influence of hydrogen content on dwell fatigue sensitivity of IMI685 alloy with aligned microstructure. They found that the dwell fatigue life decreases with rising hydrogen content, as shown in Fig. 2.4(b). Mills et al. [39] attribute the reverse trend in two near-α titanium alloys to the different diffusion rates of hydrogen in α and β phases. The higher diffusion rate of hydrogen in β phases results in hydrogen concentration in β phase, which is prone to aggravate the dwell fatigue sensitivity of IMI685 alloy with continuous β matrix [40]. Sinha et al. [41] linked hydrogen content to stress redistribution to explicate the variation of dwell fatigue life in Ti-6242 alloy with bimodal microstructure, whilst additional evidence is needed. Gerland et al. [42] pointed out that the effect of hydrogen on dwell fatigue sensitivity is load-dependent. At low stress level below $\sigma_{0.2}$, the softening effect of hydrogen increase the creep capability, whereas the hardening effect of hydrogen at high stress levels inhibits the creep deformation.

Oxygen is another interstitial element that can influence the dwell fatigue behavior of titanium alloys, especially CP-Ti. Xiong et al. [43] found that the increase of oxygen content in CP-Ti leads to more strain accumulation during creep, which may promote stress redistribution within a hard-soft grain combination. However, the relevant mechanism is not clear.

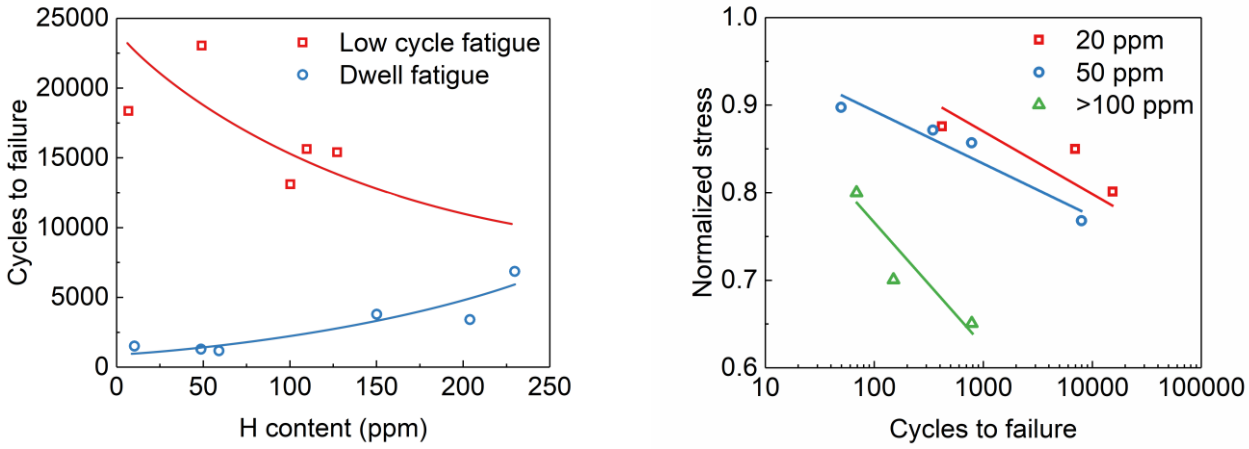

(a) (b)

Fig. 2.4 Influence of hydrogen contents on fatigue properties of (a) Ti-6242 alloy with bimodal microstructure ($\sigma_{max} = 0.95\sigma_{0.2}$) [39], (b) IMI685 alloy with aligned microstructure [40].

2.3.2 Microstructure

For dual-phase titanium alloys, the microstructural morphology affects the dislocation slip [44],[45]. The slip activities influence the cold creep ($T < 0.4T_m$, T_m is the melting temperature of the material) in dwell fatigue, which causes stress redistribution and concentration at hard-soft grain boundaries. Ashton et al. [46] noted that soft $\alpha + \beta$ colonies in the bimodal microstructure could release the stress concentration in adjacent hard primary α grains since the presence of β laths shortened the slip length and reduced the dislocation pile-ups at hard-soft grain boundaries after stress dwell, as shown in Fig. 2.5(a). A low volume fraction of the primary α phase in the bimodal microstructure, associated with higher solution temperatures, further reduces the dwell fatigue susceptibility as the dispersed primary α grains hamper the continuous slip transmission [47],[48]. Soft basketweave structure has also been reported to inhibit slip accumulation during dwell time because of the distinct soft α laths formed inside the β matrix [49],[50], as shown in Fig. 2.5(b). These assumptions are consistent with the experimental results that titanium alloys with lamellar or basketweave structures are less susceptible to dwell fatigue life reduction [51].

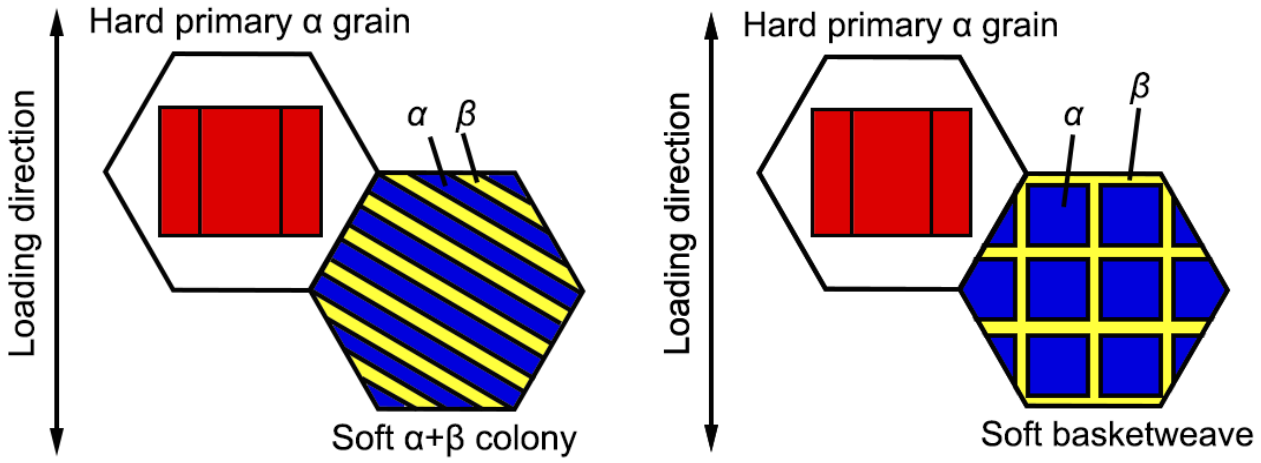

(a) (b)

Fig. 2.5 Combination of a hard primary α grain and (a) soft $\alpha + \beta$ colony, (b) soft basketweave structure.

In addition to the aforementioned microstructures, α laths in lamellar colonies can be spheroidized through dynamic recrystallization to achieve a globular structure with β at α grain boundaries. The resulting morphologies of the α phase within the globular structure are equiaxed α grains or elongated α platelets depending on the hot deformation and heat treatment processing parameters. Dwell fatigue tests have also been conducted for $\alpha + \beta$ titanium alloys with this practical microstructure. A comparison of the dwell fatigue life debit of Ti-6Al-2Sn-4Zr-xMo (Ti-624x, $x = 2 - 6$) alloys with equiaxed α grains suggested that the dwell sensitivity of Ti-624x faded out as the addition of Mo could refine the size of primary α grains and reduce slip band spacing [52], as shown in Fig. 2.6. This study highlighted the role of the α phase, the concurrent growth of the intergranular β phase volume fraction was not taken into account. The deviation from the Burgers orientation relationship (BOR) between the α and β phase after the dynamic recrystallization process could block the slip transfer at the α/β interface, as well as dislocation interactions [53]. On the other hand, β laths decorating two geometrically incompatible equiaxed α grains were capable of coordinating local deformation by continuous slip transmission under certain crystallographic orientation relationships [54]. However, most of the previous studies on the intergranular β phase have focused on deformation mechanisms under monotonic loading, the effect of intergranular β phase on the creep resistance and dwell fatigue sensitivity remains elusive in near-α and $\alpha + \beta$ titanium alloys with globular structure.

The size and intensity of the macrozones, which depend on the size of the billet during the recrystallization stage and subsequent thermomechanical processing, were also reported to significantly affect the dwell fatigue sensitivity as the rate of the faceted crack growth within a macrozone can be two orders of magnitude quicker than that under cyclic fatigue loading [13]. As shown in Fig. 2.7, the dwell fatigue lives exhibit a stronger dependence on the size of macrozones than cyclic fatigue at low stress levels, whilst the relative importance decreases as the stress increases.

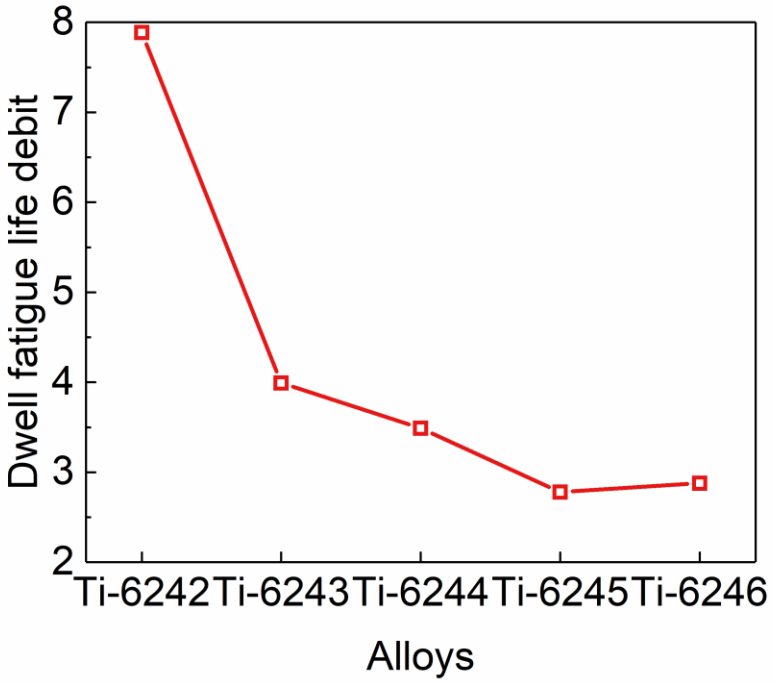

Fig. 2.6 Variation of dwell fatigue life debit in Ti-624x alloys [52].

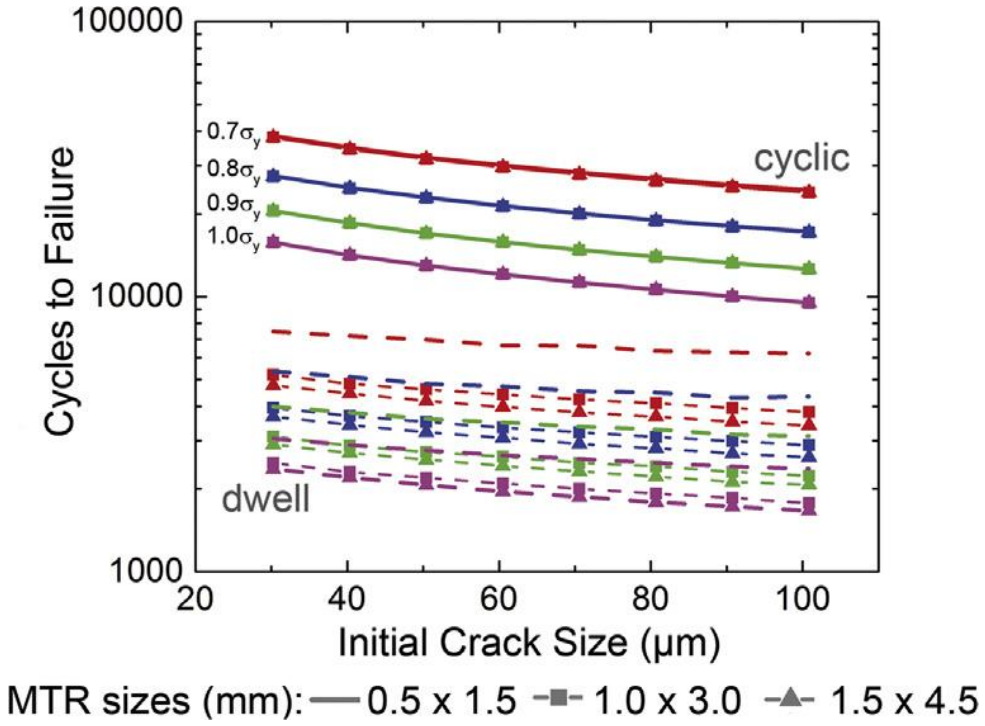

Fig. 2.7 Effect of macrozone size on cyclic and dwell fatigue lives [13].

2.3.3 Plastic deformation mode

In near-α and $\alpha + \beta$ titanium alloys, the plastic deformation is principally carried by slip activities. However, slip and deformation twinning are competitive plastic deformation mechanisms in CP-Ti with a low oxygen content (mass% $O < 0.11$) [55]. Since the activation of high-CRSS pyramidal <*c*+*a*> slips are difficult, $\{10\bar{1}2\}$ tension twinning and $\{11\bar{2}2\}$ compression twinning act as primary substitutes to achieve homogeneous deformation along the *c*-axis for hard grains [56], as shown in Fig. 2.7 [57]. Deformation twinning can also be observed during creep deformation, which is closely related to the strain accumulation during dwell fatigue [58]. Oberson et al. [59] conducted creep tests on Ti-1.6V alloy and found that slip was dominant at low strain but few twins were observed, whereas deformation twinning was relatively more common although slip continued as the accumulated strain became higher. Furthermore, Luan et al. [60] presumed that twinning nucleation and propagation in soft grains could interrupt continuous slip, thereby reducing the dislocation pile-ups at grain boundaries and the possibility of dwell facet generation in CP-Ti. Nevertheless, the influence of deformation twinning on dwell fatigue susceptibility of CP-Ti is still not properly understood, supplemental exploration (including crystal plasticity modeling [61]) is necessary.

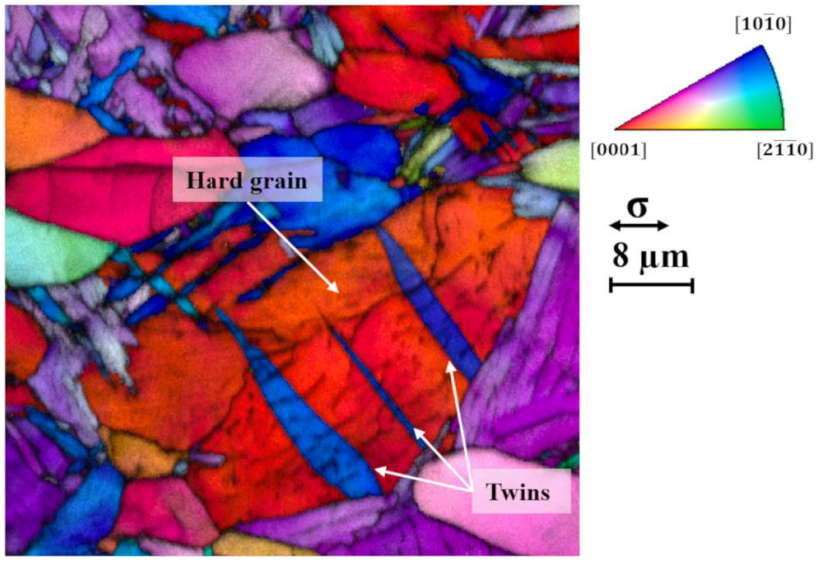

Fig. 2.8 Onset of the deformation twinning in a hard grain [57].

2.4 Effect of loading condition on dwell fatigue sensitivity

2.4.1 Temperature

The temperature sensitivity of dwell fatigue was first recognized in the near-α Ti-624x alloy system. Unlike Ti-6242 alloy, the disappearances of subsurface facets and dwell fatigue life debit in Ti-6246 alloy from 293 K to 423 K have confirmed the temperature sensitivity of dwell fatigue in different titanium alloys [61]. It has been reported that the dwell fatigue life debit in Ti-6Al and Ti-6242 alloys is the largest at around 393 K and almost fades out at temperatures higher than 503 K, but Ti-6246 alloy suffers the severest life reduction between 723 K and 823 K [63],[64]. These experimental findings are consistent with the discrete dislocation plasticity (DDP) predictions that stress redistribution in Ti-6Al and Ti-6242 is most notable at 393 K and drops to a low level at temperatures higher than 503 K, whereas the redistributed stress in Ti-6246 alloy is the greatest at a much higher temperature of 573 K, as shown in Fig. 2.8 [65]. Therefore, the discrepancy of dwell fatigue sensitivity between Ti-6242 and Ti-6246 is presumably attributed to the temperature-dependent stress redistribution phenomenon rather than the difference in composition, that is, the addition of Mo [66].

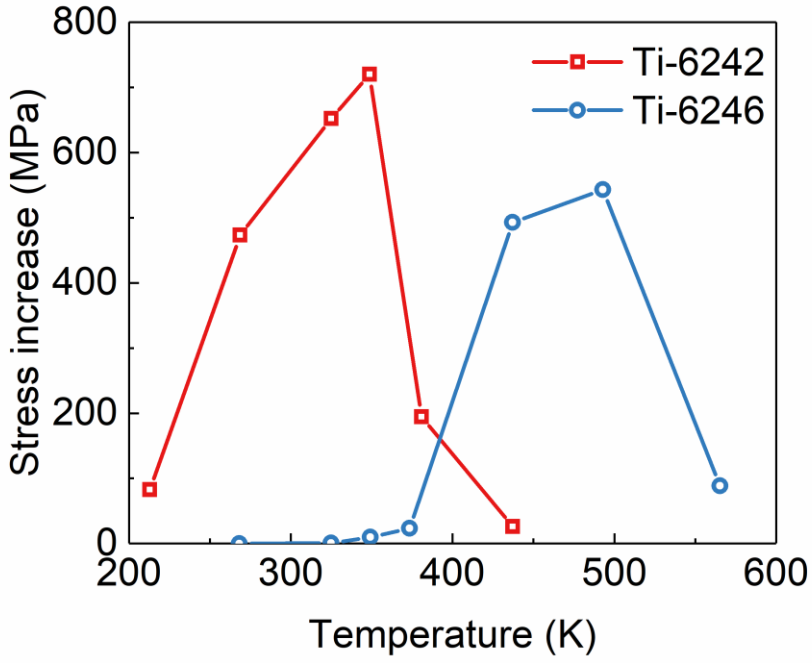

Fig. 2.9 Variation of stress redistribution at different temperatures in Ti-6242 and Ti-6246 alloys [65].

As the cold creep in titanium alloys is an important factor affecting the stress redistribution and concentration, Yazar et al. [67] paid attention to the influence of temperature on creep deformation and carried out dwell fatigue tests on a near-α IMI834 alloy at temperatures ranging from room temperature (RT) to 633 K. They found that the strain accumulation was highest at 393 K, followed by RT, 513 K, and 633 K under the same normalized stress level. Similarly, Peng et al. [68] conducted constant load creep tests for CP-Ti at low and intermediate temperatures. The creep strain was pointed out to increase with temperature from 273 K to 388 K, then decreased gradually and diminished at 498 K. Given that the macroscopic creep is dominated by microscopic dislocation slip, Harr et al. [69] further used high-resolution digital image correlation (HR-DIC) technique to quantitatively analyze the onset of slip traces in Ti-6242 alloy under dwell fatigue. Their observations suggested that the slip trace accumulation at 393 K was greater than those at RT and 473 K. To fill the gap between the crystal slip and macroscale creep, the stress-related strain rate sensitivity (SRS) of individual slip was linked with the temperature-dependent creep response in Ti-6Al alloy [70]. In addition to cold creep, the plastic anisotropy of the HCP lattice plays a vital role in the temperature sensitivity of the stress redistribution [71]. At low temperatures, plastic deformation along the *c*-axis is difficult for hard grains because the CRSS required to activate pyramidal <*c*+*a*> slips is $2-6$ times higher than that for prismatic <*a*> slip [6]. Hence, the soft grain sheds stress onto the abutting hard grain during the dwell period to ensure the deformation compatibility near the hard-soft grain boundary. With elevating temperature, the noticeable decrease in CRSS for pyramidal <*c*+*a*> slips results in a competitive strength between prismatic <*a*> and pyramidal <*c*+*a*> slips. The continuous slip transmission at hard-soft grain boundaries can coordinate local deformation, resulting in vanishment of the stress redistribution [54]. The above studies regarding the effect of temperature on dwell fatigue have focused on near-α titanium alloys, while very limited work has been committed to $\alpha+\beta$ titanium alloy. Further investigations into the temperature-sensitive dwell fatigue in $\alpha+\beta$ titanium alloy (notably Ti-6Al-4V alloy) are crucial because Ti-6Al-4V aero-engine components also undergo complex temperature history during takeoff, climbing, cruise, descent, and landing (e.g., the Ti-6Al-4V fan disc in the GP7270 engine is reported to be exposed to temperatures from 294 K to 343 K [27]).

2.4.2 Dwell time

Although the duration of the cruise phase in a long haul varies from dozens of minutes to more than ten hours for an airliner, the dwell time in each dwell fatigue cycle is generally below 20 min considering the cost and efficiency of tests in the laboratory environment. Fig. 2.9 summarizes the variation of dwell fatigue lives with increasing dwell time in CP-Ti, near-α IMI834 alloy, and $\alpha + \beta$ Ti-6Al-4V ELI alloy [10],[30],[72].

It can be seen that the cycles to failure decrease with increasing dwell time, especially when the dwell time is shorter than 120 s. It may partly be related to that the introduction of the dwell period results in an increase in the dislocation pile-ups at hard-soft grain boundaries and dwell fatigue crack propagation rate [73],[74]. However, the dwell fatigue lives are close to a constant when the dwell time is longer than this threshold value (denoted as "saturated dwell time" [10]). This phenomenon reflects the intrinsic property of dwell fatigue that cyclic fatigue interacts with cold creep [75], and a 2-minute dwell time is generally applied to carry out material-level tests and fatigue life assessment of real components.

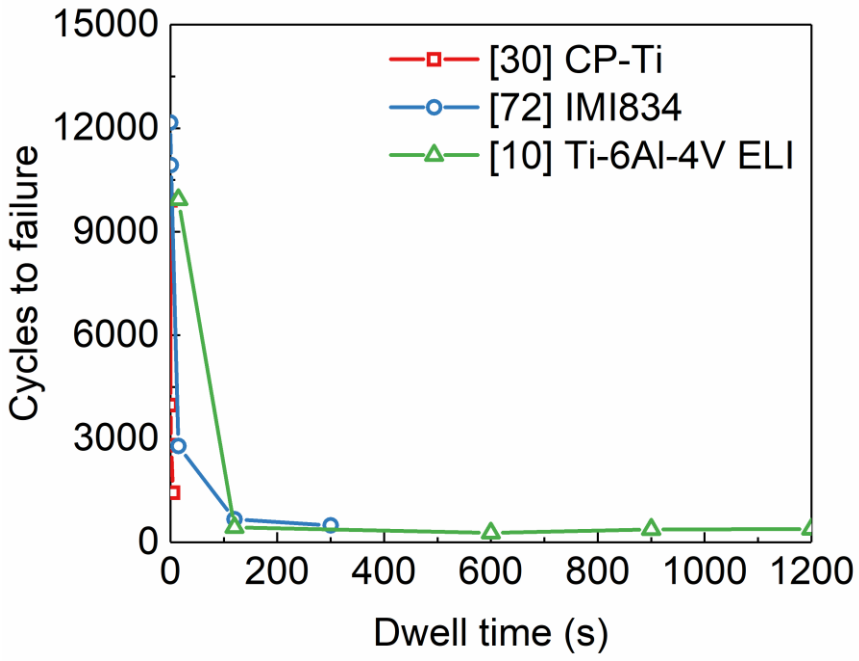

Fig. 2.10 Effect of dwell time on the dwell fatigue lives in CP-Ti, IMI834 alloy, and Ti-6Al-4V ELI alloy [10],[30],[72].

2.4.3 Stress state

Rotor components in aero-engines are subjected to multiaxial loading (e.g., centrifugal load, aerodynamic force, pressure, and sometimes maneuver load) [76],[77], which is distinct from the typical uniaxial dwell fatigue tests under laboratory environment. To consider the stress multiaxiality, Bache et al. [36] performed biaxial dwell fatigue tests for IMI685 alloy under tension and torsion loadings. It was found that dwell life debit under biaxial stress was less than that under the pure tension-tension loading. Doquet et al. [78] replaced the torsion load with internal pressure to reflect the in-service loading on compressor discs and concluded that biaxial loading could delay the facet nucleation and resist fatigue crack propagation in Ti-6Al-4V alloy. Additionally, the permissible stress for titanium alloy rotors is well below the yield strength to ensure a profitable service hour, whereas the specimens are mainly tested at maximum dwell stress of over $0.9\sigma_y$ to initiate dwell facet nucleation in dwell fatigue tests [79].

Besides, the traditional cyclic fatigue life is associated with stress amplitude, showing the law that fatigue life decreases with the increase of stress amplitude. A large amount of experimental data indicate that the dwell fatigue life increases as the peak stress decreases. Bache et al. studied the effect of stress ratio (R) on dwell fatigue in IMI834 alloy, as shown in Fig. 2.10(a) [72]. Compared to the condition when $R = 0.1$, the dwell fatigue life is reduced when $R = 0.5$. They assumed that high stress ratio and mean stress accelerate the strain accumulation and dislocation pile-ups at grain boundaries, which promoted stress redistribution and quasi-cleavage facet formation. In contrast, a negative stress ratio makes the dislocations slip in the opposite direction, which can alleviate the pile-up stress and retard the facet nucleation. Hommer [80] also investigated the effect of stress ratio on dwell fatigue mechanism in Ti-7Al alloy under biaxial tension-tension loading and found both negative and positive stress ratios could reduce the dwell fatigue sensitivity. The discrepancy between the two results is still not clear. Moreover, the fact that the dwell fatigue crack growth rates under different stress ratios vary faintly indicated that the dwell fatigue sensitivity of Ti-6246 alloy is independent of the stress ratio [62].

Owing to the aspects mentioned above, the effect of stress state continues to be a concern when the laboratory results obtained from specimens are applied to actual parts.

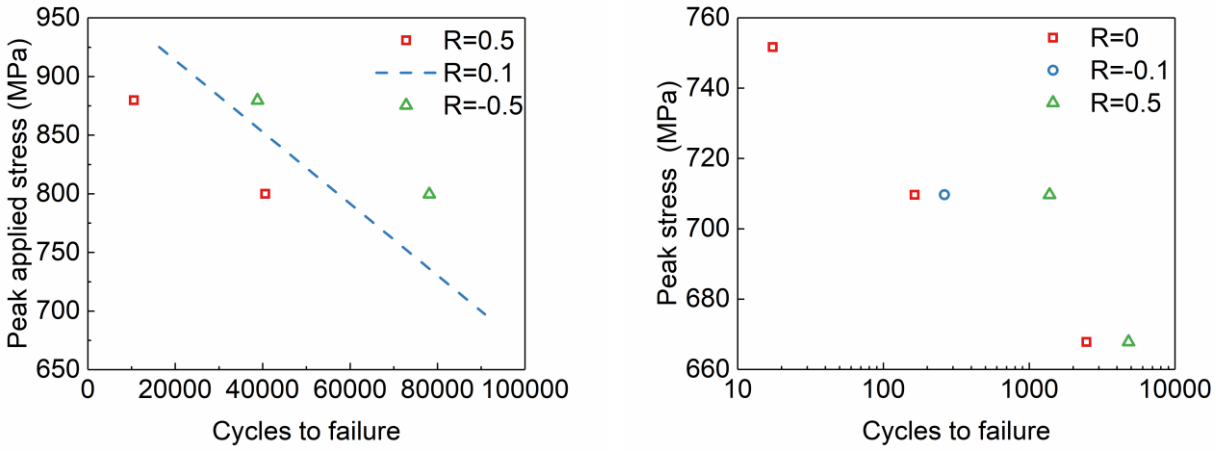

(a) (b)

Fig. 2.11 Effect of stress ratio on dwell fatigue of (a) IMI834 alloy, (b) Ti-7Al alloy [72],[80].

2.5 Summary

This chapter has comprehensively reviewed the preceding research concerning the cold dwell sensitive fatigue in titanium alloys. Some experimental investigations are summarized in Appendix A in terms of the effect of metallurgical characteristics and test conditions on dwell fatigue sensitivity of titanium alloys.

Although some phenomenological factors affecting cold dwell fatigue have been recognized, there are still some crucial fields where methodical understanding is insufficient. One deformation mode-related question is the role of deformation twinning in dwell fatigue, especially the relationship between stress redistribution within a hard-soft grain combination and twinning nucleation. Another tough task is to address the effect of the intergranular β phase on dwell fatigue sensitivity, which may enable us to elucidate the classical Ti-624x problem. The ultimate target is to go a step further to accomplish the multiscale modeling for cold dwell fatigue characterization, which links the local deformation at the grain scale and working conditions at the component level.

The aforementioned aspects will be experimentally and numerically tackled in Chapters 4-6, as detailed in Fig. 2.12, which are preceded by an all-inclusive description of the dislocation mechanism-based strain gradient crystal plasticity modeling method incorporating deformation twinning.

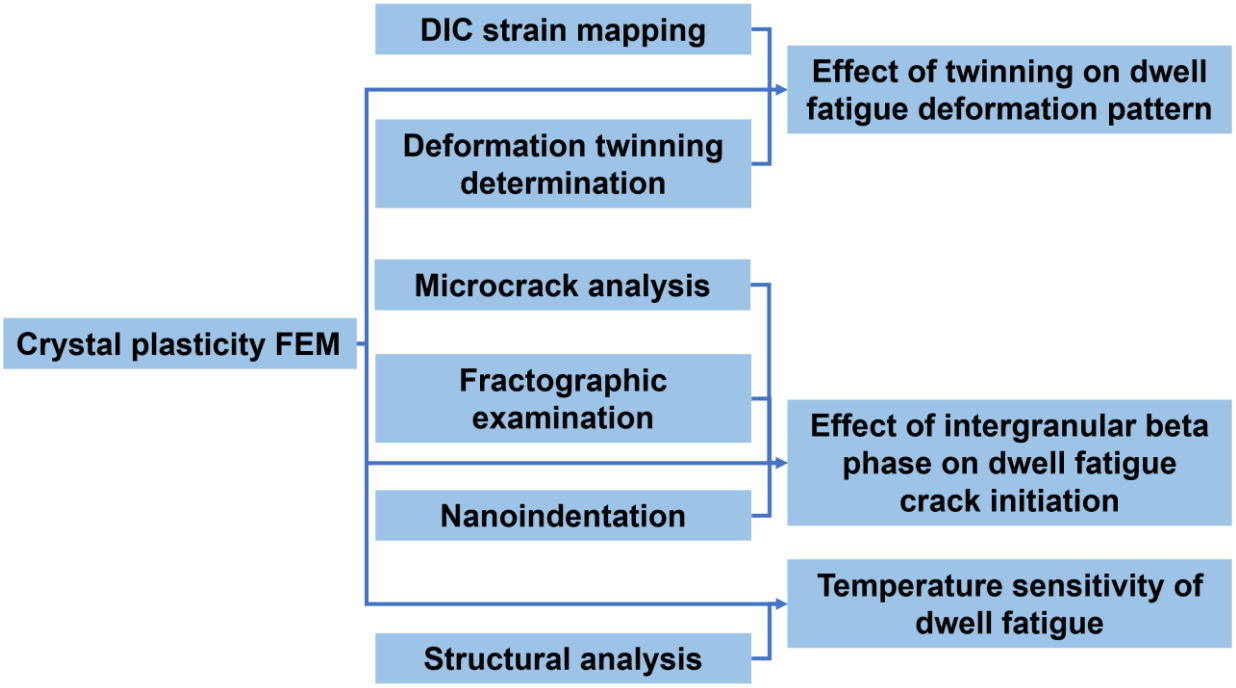

Fig. 2.12 Outline of this thesis.

3. Rate-dependent strain gradient crystal plasticity framework

3.1 Introduction

The commercial finite element and computer-aided engineering (CAE) software ABAQUS has been widely used in the modeling and analyses of mechanical components and assemblies, computational fluid dynamic (CFD) simulations, and electromagnetic applications. Especially, the software provides a powerful interface where users can write their constitutive models in a subroutine denoted UMAT for the deformation and stress analysis of solids. The primary objective of this chapter is to develop the finite element code, a new ABAQUS user-material subroutine, for the constitutive relationship of single crystals in a continuum framework, which can be used to perform stress, strain, and fracture analyses of single crystals or polycrystalline materials [81],[82].

3.2 Crystal plasticity constitutive model

The rate-dependent crystal plasticity constitutive law used in this study was originally formulated by Huang based on the work of Peirce, Asaro, and Rice [83],[84],[85]. A crystalline material is embedded in its lattice that undergoes elastic deformation and rotation. The plastic deformation of a single crystal is assumed here to arise solely from crystalline slip and twinning, whereas the deformation by diffusion and grain boundary sliding that prevail at high temperatures are not considered here. As illustrated in Fig. 3.1, the multiplicative decomposition of the current deformation gradient $\boldsymbol{F}$ is given by

$$\boldsymbol{F} = \boldsymbol{F}_e \cdot \boldsymbol{F}_p \cdot \boldsymbol{F}_T \tag{3.1}$$

where $\boldsymbol{F}_e$ refers to lattice stretching and rigid body rotation, $\boldsymbol{F}_p$ accounts for the deformation caused by plastic shear of the material, and $\boldsymbol{F}_T$ denotes the deformation of crystal lattice because of thermal expansion and evolves as [86]

$$\dot{\boldsymbol{F}}_T = \dot{T}\boldsymbol{\alpha}\boldsymbol{F}_T \tag{3.2}$$

where T is the temperature and $\boldsymbol{\alpha}$ is a diagonal tensor with respect to the principal crystallographic coordinate system containing thermal expansion coefficients along the principal crystallographic directions and rotated appropriately to the global configuration using the measured orientation of the

crystal. If the environment is isothermal, the thermal deformation can be neglected and the $\boldsymbol{F}_T$ reduces to an identity tensor during deformation.

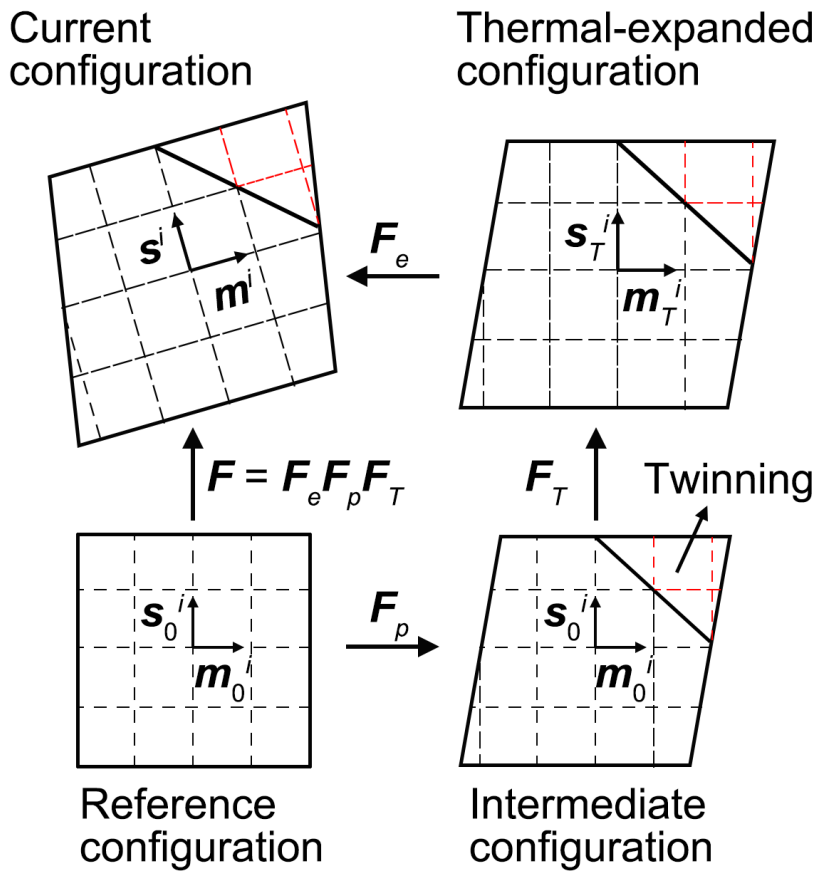

Fig. 3.1 Schematic illustration of the multiplication of total deformation gradient.

The change of $\boldsymbol{F}_p$ in rate form is written as

$$\dot{\boldsymbol{F}}_p = \boldsymbol{L}_p \cdot \boldsymbol{F}_p \tag{3.3}$$

Assuming that the plastic deformation results from all active slip and twinning systems, which obey Schmid's law,

$$\boldsymbol{L}_p = \sum_{i=1}^{n} \dot{\gamma}^i \left(\boldsymbol{m}^i \otimes \boldsymbol{s}^i\right) \tag{3.4}$$

where n is the total number of slip and twinning systems, $\dot{\gamma}^i$ is the shearing rate of the ith slip/twinning system, $\boldsymbol{m}^i$and $\boldsymbol{s}^i$ are slip/twinning plane normal and slip/twinning direction, respectively. The slip and twinning systems for HCP crystals are summarized in Appendix B. The velocity gradient $\boldsymbol{L}$ in the current state is

$$\begin{aligned}\boldsymbol{L} &= \boldsymbol{L}_e + \boldsymbol{L}_p + \boldsymbol{L}_T = \boldsymbol{D} + \boldsymbol{W}\\ \boldsymbol{L}_e &= \boldsymbol{D}_e + \boldsymbol{W}_e\\ \boldsymbol{L}_p &= \boldsymbol{D}_p + \boldsymbol{W}_p\\ \boldsymbol{L}_T &= \boldsymbol{D}_T + \boldsymbol{W}_T\\ \boldsymbol{D} &= \boldsymbol{D}_e + \boldsymbol{D}_p + \boldsymbol{D}_T\\ \boldsymbol{W} &= \boldsymbol{W}_e + \boldsymbol{W}_p + \boldsymbol{W}_T\end{aligned} \tag{3.5}$$

where the symmetric rate of stretching $\boldsymbol{D}$ and the antisymmetric spin tensor $\boldsymbol{W}$ can be decomposed into elastic ($\boldsymbol{D}_e$, $\boldsymbol{W}_e$), plastic ($\boldsymbol{D}_p$, $\boldsymbol{W}_p$), and thermal ($\boldsymbol{D}_T$, $\boldsymbol{W}_T$) parts, respectively. The thermal strain and spin rates are defined as $\boldsymbol{D}_T = \dot{T}\boldsymbol{\alpha}$ and $\boldsymbol{W}_T = 0$. The plastic strain rate tensor $\boldsymbol{D}_p$ and plastic spin tensor $\boldsymbol{W}_p$ represent the symmetric and skew-symmetric parts of the plastic velocity gradient:

$$\begin{aligned}\boldsymbol{D}_p &= \frac{\left[\boldsymbol{L}_p + \boldsymbol{L}_p{}^T\right]}{2} = \sum\nolimits_{\alpha=1}^{n} \boldsymbol{p}^i\,\dot{\gamma}^i, \boldsymbol{p}^i = \frac{\boldsymbol{m}^i\boldsymbol{s}^i + \boldsymbol{s}^i\boldsymbol{m}^i}{2}\\ \boldsymbol{W}_p &= \frac{\left[\boldsymbol{L}_p - \boldsymbol{L}_p{}^T\right]}{2} = \sum\nolimits_{\alpha=1}^{n} \boldsymbol{\omega}^i\,\dot{\gamma}^i, \boldsymbol{\omega}^i = \frac{\boldsymbol{m}^i\boldsymbol{s}^i - \boldsymbol{s}^i\boldsymbol{m}^i}{2}\end{aligned} \tag{3.6}$$

where $\boldsymbol{p}^i$ and $\boldsymbol{\omega}^i$ are "Schmid factor" and spin tensor, respectively. The relation between the symmetric rate of lattice stretching, $\boldsymbol{D}_e$, and the corotational stress rate with respect to lattice rotation, $\hat{\boldsymbol{\sigma}}_e$, is given by

$$\hat{\boldsymbol{\sigma}}_e = \hat{\boldsymbol{\sigma}} + \boldsymbol{W}_p \cdot \boldsymbol{\sigma} - \boldsymbol{\sigma} \cdot \boldsymbol{W}_p = \boldsymbol{E}(T) : \boldsymbol{D}_e \tag{3.7}$$

where $\boldsymbol{E}(T)$ represents the temperature-dependent symmetrical elastic modulus tensor that can be written as

$$\boldsymbol{E}(T)_{ij} = \begin{pmatrix} E(T)_{11} & E(T)_{12} & E(T)_{13} & 0 & 0 & 0 \\ E(T)_{21} & E(T)_{22} & E(T)_{23} & 0 & 0 & 0 \\ E(T)_{31} & E(T)_{32} & E(T)_{33} & 0 & 0 & 0 \\ 0 & 0 & 0 & E(T)_{44} & 0 & 0 \\ 0 & 0 & 0 & 0 & E(T)_{55} & 0 \\ 0 & 0 & 0 & 0 & 0 & E(T)_{66} \end{pmatrix} \tag{3.8}$$

where $E(T)_{44} = (E(T)_{11} - E(T)_{12})/2$ for HCP crystal, and $E(T)_{11} = E(T)_{22} = E(T)_{33}$, $E(T)_{12} = E(T)_{13} = E(T)_{23}$, $E(T)_{44} = E(T)_{55} = E(T)_{66}$ for BCC crystal. The elastic modulus tensor is transformed from crystal coordinate to global coordinate using the rotation matrix in Appendix C. The constitutive equation of a single crystal can therefore be deduced by combining Eqs. (3.5-3.7):

$$\hat{\boldsymbol{\sigma}} = \boldsymbol{E}(T) : \boldsymbol{D} - \boldsymbol{E}(T) : \boldsymbol{D}_T - \sum\nolimits_{\alpha=1}^{n} \left[\boldsymbol{E}(T) : \boldsymbol{p}^i + \boldsymbol{\omega}^i \cdot \boldsymbol{\sigma} - \boldsymbol{\sigma} \cdot \boldsymbol{\omega}^i\right]\dot{\gamma}^i \tag{3.9}$$

The slipping rate $\dot{\gamma}^i$ of an un-trapped dislocation on slip system i, as shown in Fig. 3.2, follows the Orowan equation

$$\dot{\gamma}^i = \rho_m v_g b^i \tag{3.10}$$

where ρ_m is the mobile dislocation density, b^i is the Burgers vector, v_g is the average glide velocity of dislocations having the following form [87]:

$$v_g = \frac{d\nu_D b^i}{2l} \exp\left(-\frac{\Delta G}{kT}\right) \tag{3.11}$$

where ν_D is the Debye frequency, k is the Boltzmann constant, and ΔG is the Gibbs free energy.

As shown in Fig. 3.3, The applied stress field dose work as the dislocation moves, hence, the Gibbs free energy ΔG for an activation event is

$$\Delta G = \Delta F - \tau_e^i \gamma_0 l b^i d = \Delta F - \tau_e^i \Delta V \tag{3.12}$$

where ΔF is the Helmholtz free energy, τ_e^i is the effective resolved shear stress, γ_0 is the shear strain that is work conjugate to the resolved shear stress, and ΔV is the activation volume.

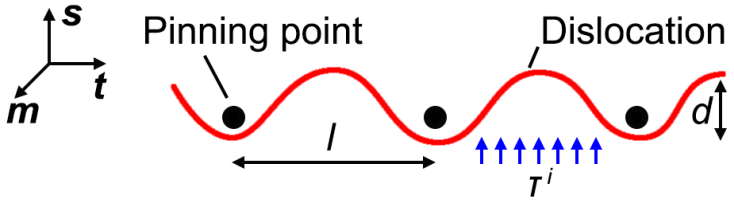

Fig. 3.2 Schematic diagram of a pinned dislocation on a slip plane with normal $\boldsymbol{m}$, and slip direction $\boldsymbol{s}$. The pinning distance is l and length of thermal activation event d.

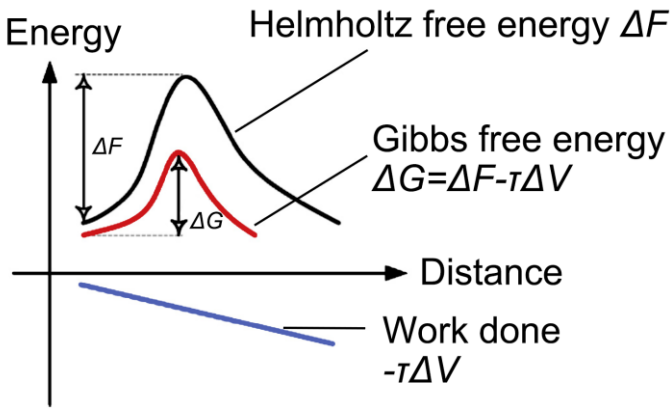

Fig. 3.3 Energy barrier curves for a thermal activation event.

Combining Eq. (3.11) and Eq. (3.12), the average glide velocity of the dislocation considering the forward and backward dislocation activation events is

$$\begin{aligned} v_g &= \frac{d}{l}\left(\Gamma_{front} - \Gamma_{back}\right) \\ &= \frac{d}{l}\left[\frac{\nu_D b^i}{2l}\exp\left(-\frac{\Delta F}{kT} + \frac{\tau_e^i \Delta V}{kT}\right) - \frac{\nu_D b^i}{2l}\exp\left(-\frac{\Delta F}{kT} - \frac{\tau_e^i \Delta V}{kT}\right)\right] \\ &= \frac{d\nu_D b^i}{2l^2}\exp\left(-\frac{\Delta F}{kT}\right)\left[\exp\left(\frac{\tau_e^i \Delta V}{kT}\right) - \exp\left(-\frac{\tau_e^i \Delta V}{kT}\right)\right] \end{aligned} \tag{3.13}$$

The slipping rate is usually given as below [88]:

$$\begin{cases} \dot{\gamma}^i = 0 & \text{if } \left|\tau^i\right| \le \tau_c^i \\ \dot{\gamma}^i = \rho_m \left(b^i\right)^2 \nu_D \exp\left(-\frac{\Delta F}{kT}\right)\sinh\left[\frac{\left(\left|\tau^i\right| - \tau_c^i\right)\Delta V}{kT}\right] sign\left(\tau^i\right) & \text{if } \left|\tau^i\right| > \tau_c^i \end{cases} \tag{3.14}$$

where $\tau^i = \boldsymbol{\sigma}:\left(\boldsymbol{s}^i \otimes \boldsymbol{m}^i\right)$ is the resolved shear stress and τ_c^i is the effective CRSS.

The twinning systems are modeled as pseudo slips and allowed to be activated when resolved shear stresses are positive and negative, respectively. The shearing rate on the twinning system obeys the following viscoplastic formula:

$$\dot{\gamma}^i = \dot{\gamma}_0 \left(\frac{\tau^i}{\tau_{SSD}^i}\right)^{\frac{1}{r}} sgn\left(\tau^i\right) \tag{3.15}$$

where $\dot{\gamma}_0$ is the reference slipping rate, r is the rate sensitivity index, and τ_{SSD}^i is the slip strength induced by statistically stored dislocations (SSDs). The Voce-type hardening model is applied to describe the evolution of τ_{SSD}^i:

$$\tau_{SSD}^i = \sum_{j=1}^{n} h_{ij}\left|\dot{\gamma}^j\right| \tag{3.16}$$

where h_{ij} is the hardening moduli representing the interaction among slip/twinning systems. The self-hardening moduli h_{ii} and latent-hardening moduli h_{ij} are expressed as follows [89]:

$$h_{ii} = h(\gamma) = h_0\left(1 - \frac{\tau_0}{\tau_\infty}\right)\exp\left(-\frac{h_0\gamma}{\tau_\infty}\right), \gamma = \sum_{i=1}^{n}\int_0^t \left|\dot{\gamma}^i\right| dt\,, h_{ij} = qh(\gamma) \tag{3.17}$$

where h_0, τ_∞, and τ_0 are the initial hardening modulus, saturated CRSS, and initial CRSS, respectively. γ is the cumulative shear strain on all slip/twinning systems, and q is the latent hardening constant.

Based on the strain gradient crystal plasticity model developed by Han et al. [90],[91], the effective CRSS τ_c^i of slip system i takes the contributions of SSDs and geometrically necessary dislocations

(GNDs) into account [92]:

$$\tau_c^i = \sqrt{\left(\tau_{SSD}^i\right)^2 + \left(\tau_{GND}^i\right)^2} \tag{3.18}$$

The intrinsic length scale of the material, l_{int}, is introduced to describe the GND-induced hardening:

$$l_{int} = \frac{\alpha_T^2 G^2 b}{(g_0)^2} \tag{3.19}$$

where α_T is an empirical coefficient that ranges from 0.3 to 0.5, G is the shear modulus, and g_0 is the reference slip resistance, which is expressed as $g_0 = G/100$. The slip strength due to the accumulation of GNDs is then computed based on the Taylor dislocation model [93],

$$\tau_{GND}^i = g_0\sqrt{l_{int}\rho_{GND}^i} = \alpha_T G\sqrt{b^i \rho_{GND}^i} \tag{3.20}$$

where ρ_{GND} is the effective density of GNDs in the following form at small deformations:

$$\rho_{GND}^i = \left|\frac{\partial \gamma^i}{\partial \boldsymbol{x}}\right| = \left|\boldsymbol{m}^i \times \sum\nolimits_{j=1}^{n}\left[\left(\boldsymbol{s}^i \cdot \boldsymbol{s}^j\right)\nabla\gamma^j \times \boldsymbol{m}^j\right]\right| \tag{3.21}$$

The calculation of the effective density of GNDs requires the evaluation of the shear strain gradient at each element integration point, which will be discussed later in the next section based on the method of Busso et al. [94]. Combining Eqs. (3.18) and (2.20), the effective CRSS of the slip system can be rewritten as:

$$\tau_c^i = \sqrt{\left(\tau_{SSD}^i\right)^2 + (\alpha_T G)^2 b^i \rho_{GND}^i} \tag{3.22}$$

The twinning model in the current model is based on the conventional predominant twin reorientation (PTR) scheme proposed by Tomé et al. [95], which has computational advantages over another approach named volume fraction transfer (VFT) model. In this scheme, the volume fraction of the twinning is assigned for a crystal. When the volume fraction is smaller than a threshold value, the crystal orientation and volume fraction of the matrix remain unchanged at the end of each increment. The volume fraction V of a twinning system is defined as:

$$V = \frac{\gamma_{twin}}{\gamma_{ref}} \tag{3.23}$$

where γ_{twin} is the cumulative shear strain on a twinning system, γ_{ref} is the reference twinning shear.

When the volume fraction V is greater than the threshold volume fraction V_{th}, lattice reorientation occurs. The orientations of the twin and matrix are symmetric about the twin boundary. Consequently, the orientations of all slip and twinning systems at each integration point are rotated from matrix to

twinned region by the following rotation tensor $\boldsymbol{R}^{tw}$:

$$\boldsymbol{R}^{tw} = 2\boldsymbol{m}^{tw} \otimes \boldsymbol{m}^{tw} - \boldsymbol{I} \tag{3.24}$$

where $\boldsymbol{m}^{tw}$ is the normal vector of the twinning plane, $\boldsymbol{I}$ is the identity tensor. The corresponding elastic modulus tensor is also transformed as:

$$\boldsymbol{E}^{tw}_{ijkl} = \boldsymbol{E}_{pqrs}\boldsymbol{R}^{tw}_{ip}\boldsymbol{R}^{tw}_{jq}\boldsymbol{R}^{tw}_{kr}\boldsymbol{R}^{tw}_{ls} \tag{3.25}$$

It should be mentioned that the deformation gradient is assumed to be the same within a matrix before twinning occurs. To prevent a rapid increase in the non-equilibrated state of the global stiffness matrix that is prone to cause iterative fluctuation and divergence, the variable PNEWDT is used to reduce the time increment when twinning occurs, i.e., the UMAT subroutine interrupts the current time increment in favor of a new time increment given by PNEWDT*DTIME. In the present model, PNEWDT is selected as 0.1. Except for the calculation of shear strain gradient for each slip system, the code of the crystal plasticity model is scripted in the UMAT subroutine incorporated within ABAQUS 6.13/Implicit [96].

3.3 Numerical procedure in the calculation of GND density

Since the strain gradient at integration points cannot be calculated directly as an independent variable, the URDFIL subroutine is utilized to achieve this process and the Fortran code is detailed in Appendix D. For an eight-node hexahedral C3D8 fully integrated solid element (as shown in Fig. 3.4), the numerical procedures are as follows:

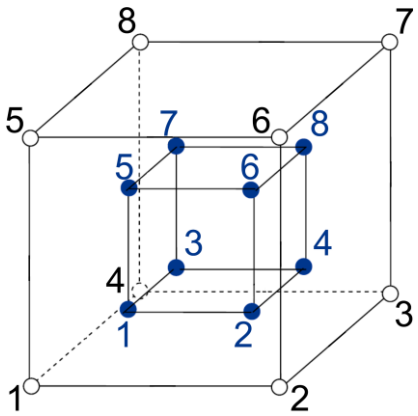

Fig. 3.4 Schematic diagram of the 3D linear 8-noded element and the 8 internal Gauss points (blue), together with the corresponding number.

1. At the end of each integration, the shear strain on slip system i at each Gauss integration point, $\gamma_{G,j}^{i}$ (j is the number of the integration point), are saved as state variables, which can be extracted and stored in a MODULE block (designated storage in memory) using the URDFIL subroutine.
2. The shear strains at eight nodes, $\gamma_{N,j}^{i}$, can be determined using the shape functions $\boldsymbol{N}^{j}(\boldsymbol{\psi})$ of C3D8 element, as listed in Table 3.1.

$$\gamma_{G,j}^{i} = \sum_{j=1}^{8} \boldsymbol{N}^{j}(\boldsymbol{\psi})\, \gamma_{N,j}^{i} \tag{3.26}$$

where $\boldsymbol{\psi}$ represents the isoparametric coordinates of the Gauss point, as detailed in Table 3.2. To ensure the current method can give the same results as the finite element simulation, the sequence of nodes and Gauss points with respect to their coordinates should be addressed appropriately in Eq. (3.26)

Table 3.1 Shape functions of the C3D8 element.

$\boldsymbol{N}^1$	$\frac{1}{8}(1+\xi)(1-\eta)(1+\zeta)$	$\boldsymbol{N}^2$	$\frac{1}{8}(1+\xi)(1+\eta)(1+\zeta)$
$\boldsymbol{N}^3$	$\frac{1}{8}(1+\xi)(1+\eta)(1-\zeta)$	$\boldsymbol{N}^4$	$\frac{1}{8}(1+\xi)(1-\eta)(1-\zeta)$
$\boldsymbol{N}^5$	$\frac{1}{8}(1-\xi)(1-\eta)(1+\zeta)$	$\boldsymbol{N}^6$	$\frac{1}{8}(1-\xi)(1+\eta)(1+\zeta)$
$\boldsymbol{N}^7$	$\frac{1}{8}(1-\xi)(1+\eta)(1-\zeta)$	$\boldsymbol{N}^8$	$\frac{1}{8}(1-\xi)(1-\eta)(1-\zeta)$

Table 3.2 Isoparametric coordinates of each Gauss point.

Gauss point (j)	ξ	η	ζ
1	0.5774	−0.5774	0.5774
2	0.5774	0.5774	0.5774
3	0.5774	−0.5774	−0.5774
4	0.5774	0.5774	−0.5774
5	−0.5774	−0.5774	0.5774
6	−0.5774	0.5774	0.5774
7	−0.5774	−0.5774	−0.5774
8	−0.5774	0.5774	−0.5774

Table 3.3 Spatial derivatives of shape functions.

Shape function (j)	$\frac{\boldsymbol{N}^j(\boldsymbol{\psi})}{\partial\xi}$	$\frac{\boldsymbol{N}^j(\boldsymbol{\psi})}{\partial\eta}$	$\frac{\boldsymbol{N}^j(\boldsymbol{\psi})}{\partial\zeta}$
1	$\frac{1}{8}(1-\eta)(1+\zeta)$	$-\frac{1}{8}(1+\xi)(1+\zeta)$	$\frac{1}{8}(1+\xi)(1-\eta)$
2	$\frac{1}{8}(1+\eta)(1+\zeta)$	$\frac{1}{8}(1+\xi)(1+\zeta)$	$\frac{1}{8}(1+\xi)(1+\eta)$
3	$\frac{1}{8}(1+\eta)(1-\zeta)$	$\frac{1}{8}(1+\xi)(1-\zeta)$	$-\frac{1}{8}(1+\xi)(1+\eta)$
4	$\frac{1}{8}(1-\eta)(1-\zeta)$	$-\frac{1}{8}(1+\xi)(1-\zeta)$	$-\frac{1}{8}(1+\xi)(1-\eta)$
5	$-\frac{1}{8}(1-\eta)(1+\zeta)$	$-\frac{1}{8}(1-\xi)(1+\zeta)$	$\frac{1}{8}(1-\xi)(1-\eta)$
6	$-\frac{1}{8}(1+\eta)(1+\zeta)$	$\frac{1}{8}(1-\xi)(1+\zeta)$	$\frac{1}{8}(1-\xi)(1+\eta)$
7	$-\frac{1}{8}(1+\eta)(1-\zeta)$	$\frac{1}{8}(1-\xi)(1-\zeta)$	$-\frac{1}{8}(1-\xi)(1+\eta)$
8	$-\frac{1}{8}(1-\eta)(1-\zeta)$	$-\frac{1}{8}(1-\xi)(1-\zeta)$	$-\frac{1}{8}(1-\xi)(1-\eta)$

3. Based on the obtained shear strains at eight nodes, the shear strain gradients at eight Gauss points are calculated using the spatial derivatives of linear shape functions, that is, the spatial derivative of Eq. (3.26), as summarized in Table 3.3.

$$\nabla\gamma^i_{G,j} = \frac{\partial\gamma^i_{G,j}}{\partial\boldsymbol{x}} = \frac{\partial\gamma^i_{G,j}}{\partial(\boldsymbol{\psi})}\frac{\partial(\boldsymbol{\psi})}{\partial\boldsymbol{x}} = \sum\nolimits_{j=1}^{8}\left[\boldsymbol{N}^j(\boldsymbol{\psi})\nabla_{\boldsymbol{\psi}}\right]\gamma^i_{N,j}\boldsymbol{J}^{-1} \tag{3.27}$$

where $\boldsymbol{J}$ is the Jacobin matrix obtained as [97]

$$\boldsymbol{J} = \frac{\partial\boldsymbol{x}}{\partial(\boldsymbol{\psi})} = \begin{pmatrix} \frac{\partial x}{\partial\xi} & \frac{\partial x}{\partial\eta} & \frac{\partial x}{\partial\zeta} \\ \frac{\partial y}{\partial\xi} & \frac{\partial y}{\partial\eta} & \frac{\partial y}{\partial\zeta} \\ \frac{\partial z}{\partial\xi} & \frac{\partial z}{\partial\eta} & \frac{\partial z}{\partial\zeta} \end{pmatrix} = \sum\nolimits_{j=1}^{8}\begin{pmatrix} x_j \\ y_j \\ z_j \end{pmatrix}\otimes\begin{pmatrix} \frac{\boldsymbol{N}^j(\boldsymbol{\psi})}{\partial\xi} \\ \frac{\boldsymbol{N}^j(\boldsymbol{\psi})}{\partial\eta} \\ \frac{\boldsymbol{N}^j(\boldsymbol{\psi})}{\partial\zeta} \end{pmatrix} \tag{3.28}$$

Here, $\nabla_{\boldsymbol{\psi}}$ is the nabla operator related to the isoparametric coordinate system.

4. The calculated shear strain gradients at each Gauss point for slip systems can be stored in the predefined MODULE block and passed into the UMAT subroutine in the next time increment.

The effective density of GNDs at Gauss points can be calculated by Eq. (3.21).

3.4 Forward gradient time integration scheme and incremental formulation

The increment of the shear strain γ^i in slip/twinning system i within the time increment Δt by

$$\Delta\gamma^i = \gamma^i(t+\Delta t) - \gamma^i(t) \tag{3.29}$$

and employ a linear interpolation within Δt:

$$\Delta\gamma^i = \Delta t\left[(1-\theta)\dot{\gamma}_t^i + \theta\dot{\gamma}_{t+\Delta t}^i\right] \tag{3.30}$$

where t is the time at which the slipping rate $\dot{\gamma}^i$ is evaluated. The parameter θ ranges from 0 to 1, with $\theta = 0$ corresponding to the simple Euler time integration scheme. A choice of θ between 0.5 and 1 is recommended. In this thesis, $\theta = 0.5$.

The slipping rate $\dot{\gamma}^i$ is a function of the resolved shear stress τ^i, the SSDs-induced strength τ_{SSD}^i, and temperature T. Thus, the Taylor expansion of slipping rate is

$$\dot{\gamma}_{t+\Delta t}^i = \dot{\gamma}_t^i + \frac{\partial\dot{\gamma}^i}{\partial\tau^i}\Delta\tau^i + \frac{\partial\dot{\gamma}^i}{\partial\tau_{SSD}^i}\Delta\tau_{SSD}^i + \frac{\partial\dot{\gamma}^i}{\partial T}\Delta T \tag{3.31}$$

where $\Delta\tau^i$ and $\Delta\tau_c^i$ are the increments of resolved shear stress, effective resolved shear stress in slip/twinning system i and temperature within the time increment Δt, respectively. Eqs (3.30) and (3.31) can be rearranged to the following incremental relation:

$$\Delta\gamma^i = \Delta t\left(\dot{\gamma}_t^i + \theta\frac{\partial\dot{\gamma}^i}{\partial\tau^i}\Delta\tau^i + \theta\frac{\partial\dot{\gamma}^i}{\partial\tau_{SSD}^i}\Delta\tau_{SSD}^i + \theta\frac{\partial\dot{\gamma}^i}{\partial T}\Delta T\right) \tag{3.32}$$

From the Voce-type hardening equation, the increment of strain hardening function $\Delta\tau_{SSD}^i$ is given by

$$\Delta\tau_{SSD}^i = \sum_{j=1}^{n} h_{ij}\Delta\gamma^j \tag{3.33}$$

The increment of resolved shear stress $\Delta\tau^i$ is related to the strain increment $\Delta\boldsymbol{\varepsilon}$ through the constitutive law and the decomposition of strain increment to lattice part, plastic part, and thermal part

$$\Delta\tau^i = \left(\boldsymbol{E}(T):\boldsymbol{p}^i + \boldsymbol{\omega}^i\cdot\boldsymbol{\sigma} - \boldsymbol{\sigma}\cdot\boldsymbol{\omega}^i\right)\left(\Delta\boldsymbol{\varepsilon} - \boldsymbol{\alpha}\Delta T - \sum_{i=1}^{n}\boldsymbol{p}^i\Delta\gamma^i\right) \tag{3.34}$$

For a given strain increment $\Delta\boldsymbol{\varepsilon}$, the increment of shear strain $\Delta\gamma^i$ is uniquely determined by the following linear algebraic equation, which is obtained by inserting the above incremental relations Eq. (3.33) and Eq. (3.34) into Eq. (3.32)

$$\sum_{j=1}^{n}\left[\delta_{ij}+\theta\Delta t\frac{\partial\dot{\gamma}^{i}}{\partial\tau^{i}}\left(\boldsymbol{E}(T):\boldsymbol{p}^{i}+\boldsymbol{\omega}^{i}\cdot\boldsymbol{\sigma}-\boldsymbol{\sigma}\cdot\boldsymbol{\omega}^{i}\right)\boldsymbol{p}^{i}-\theta\Delta t\frac{\partial\dot{\gamma}^{i}}{\partial\tau_{SSD}^{i}}h_{ij}sign\left(\dot{\gamma}_{t}^{j}\right)\right]\Delta\gamma^{j}$$

$$=\dot{\gamma}_{t}^{i}\Delta t+\theta\Delta t\left[\frac{\partial\dot{\gamma}^{i}}{\partial\tau^{i}}\left(\boldsymbol{E}(T):\boldsymbol{p}^{i}+\boldsymbol{\omega}^{i}\cdot\boldsymbol{\sigma}-\boldsymbol{\sigma}\cdot\boldsymbol{\omega}^{i}\right)(\Delta\boldsymbol{\varepsilon}-\boldsymbol{\alpha}\Delta T)+\frac{\partial\dot{\gamma}^{i}}{\partial T}\Delta T\right] \tag{3.35}$$

where δ_{ij} is the Kronecker delta.

The increment of the corotational stress $\Delta\boldsymbol{\sigma}$ (see Eq. (3.9)) can be written as

$$\Delta\boldsymbol{\sigma}=\boldsymbol{E}(T):\Delta\boldsymbol{\varepsilon}-\boldsymbol{\sigma}\cdot tr(\Delta\boldsymbol{\varepsilon})-\boldsymbol{E}(T):\boldsymbol{\alpha}\Delta T-\sum_{j=1}^{n}\left(\boldsymbol{E}(T):\boldsymbol{p}^{i}+\boldsymbol{\omega}^{i}\cdot\boldsymbol{\sigma}-\boldsymbol{\sigma}\cdot\boldsymbol{\omega}^{i}\right)\Delta\gamma^{j} \tag{3.36}$$

Once the $\Delta\gamma^{i}$ is known in terms of the strain increment $\Delta\boldsymbol{\varepsilon}$ and temperature increment ΔT, all other increments, i.e., the increments of shear strain $\Delta\gamma^{i}$, slip strength $\Delta\tau_{SSD}^{i}$, and corotational stress $\Delta\boldsymbol{\sigma}$, can be calculated according to Eq. (3.33), Eq. (3.34), and Eq. (3.36). It should be mentioned that $\frac{\partial\dot{\gamma}^{i}}{\partial T}$ and ΔT will degenerate to zero for an isothermal analysis.

The Eq. (3.35) in linear form for the increment of shear strain $\Delta\gamma^{i}$ of slip/twinning system i is replaced by the following nonlinear equation, which can be solved by the Newton-Rhapson method until the iterative convergence is satisfied

$$\Delta\gamma^{i}-(1-\theta)\Delta t\dot{\gamma}_{t}^{i}-\theta\Delta t\dot{\gamma}_{t+\Delta t}^{i}\leq r \tag{3.37}$$

where r corresponding to a residual of shear strain in slip/twinning systems is set to $r=10^{-5}$ in this study. It should be mentioned that the linear solution of Eq. (3.35) is taken as an initial guess before the iteration begins.

The crystal lattice undergoes distortion and rotation as the crystal deforms. If the iteration is converged, the corresponding increments of slip/twinning plane normal $\boldsymbol{m}^{i}$ and slip/twinning direction $\boldsymbol{s}^{i}$ in terms of the increment of strain $\Delta\boldsymbol{\varepsilon}$ and shear strain $\Delta\gamma^{i}$ are given by

$$\Delta\boldsymbol{s}^{i}=\left\{\Delta\boldsymbol{\varepsilon}+\boldsymbol{W}\Delta t+\boldsymbol{\alpha}\Delta T-\sum_{j=1}^{n}\left[\left(\boldsymbol{p}^{j}+\boldsymbol{\omega}^{j}\right)\Delta\gamma^{j}\right]\right\}\cdot\boldsymbol{s}^{i}$$

$$\Delta\boldsymbol{m}^{i}=-\boldsymbol{m}^{i}\cdot\left\{\Delta\boldsymbol{\varepsilon}+\boldsymbol{W}\Delta t+\boldsymbol{\alpha}\Delta T-\sum_{j=1}^{n}\left[\left(\boldsymbol{p}^{j}+\boldsymbol{\omega}^{j}\right)\Delta\gamma^{j}\right]\right\} \tag{3.38}$$

3.5 Summary

This chapter has incorporated thermal expansion, dislocation mechanism, and deformation twinning into the phenomenological crystal plasticity model developed in previous work. This constitutive law

will be used later in this thesis. Even though it is still challenging to explicitly calculate or measure the density of SSDs, a non-local scheme for calculating shear strain gradient is introduced in detail to consider the hardening effect of GNDs, which can extend the simulation scale of the crystal plasticity modeling from slip (mesoscale) to dislocation (microscale).

4. Effect of deformation twinning on local deformation pattern in commercially pure titanium under dwell fatigue loading

4.1 Introduction

This chapter investigates the heterogeneous deformation of a hot-rolled CP-Ti grade 1 sheet under dwell fatigue loading. Firstly, a series of mechanical tests and parallel simulations are conducted to calibrate the crystal plasticity parameters of CP-Ti. The residual strain fields within two regions of interest are measured by digital image correlation (DIC) after an interrupted dwell fatigue test and compared to predictions of crystal plasticity finite element (CPFE) simulations. Then, the mechanisms driving axial strain localization are discussed in terms of active plastic deformation modes and Schmid factors. Furthermore, the influence of deformation twinning on facet nucleation is studied based on the analysis of cyclic stress redistribution within a soft-hard-soft grain combination.

4.2 Experimental procedure

4.2.1 Material

The chemical compositions of tested JIS grade 1 CP-Ti are tabulated in Table 1. The material was hot-rolled into a 30-mm-thick sheet and annealed at 973 K for 1 h. The average grain size after heat treatment is 17 μm in diameter. The flat dog-bone specimens with a thickness of 2 mm were machined parallel to the rolling direction (RD), transverse direction (TD), and 45° from RD to TD for tensile, stress relaxation, and dwell fatigue tests. The configuration of specimens is shown in Fig. 1(a).

Prior to mechanical tests, the specimens were first polished using SiC papers to #2400, electropolished at -40 ℃ for 30 s in a solution of 440 ml methanol, 264 ml butanol, and 44 ml $HClO_4$, and then etched by Kroll reagent for 60 s for microstructure characterization.

Table 4.1 Chemical compositions of the grade 1 CP-Ti under investigation (mass%).

O	C	N	H	Fe	Ti
0.092	0.002	0.005	0.001	0.041	Bal.

4.2.2 Mechanical tests and strain measurement

Mechanical tests were performed using a motor-driven tester (SHIMAZU AG-IS 20kNT). Tensile tests were conducted under three different strain rates ($2.3 \times 10^{-4}\ s^{-1}, 2.3 \times 10^{-3}\ s^{-1}, 2.3 \times 10^{-2}\ s^{-1}$) to obtain stress-strain curves for calibrating rate-sensitive parameters. Since the tensile anisotropy of the high-textured CP-Ti sheet was pointed out to be a reflection of CRSS differences, RD, TD, and 45° specimens were used to determine CRSS relationships [98]. In addition, stress relaxation tests, which interrupted the tensile tests at 260 MPa by a 300 s stress relaxation period followed by unloading, were also carried out for three kinds of specimens to furtherly identify strain-hardening parameters.

DIC was applied to examine the heterogeneous deformation in the RD specimen under dwell fatigue loading. A large area was assigned at the center of the gauge section in advance, as shown in Fig. 4.1(a). To combine the local strain field with the initial microstructure, EBSD measurement was conducted in this area using a JEOL JSM-6400F scanning electron microscope (SEM) equipped with a TSL™ EBSD detector. EBSD scan was performed at an accelerating voltage of 15 kV with a step size of 1.0 μm. The data was analyzed by TSL OIM analysis 7 software and MTEX-5.7.0 toolbox in MATLAB [99]. The SEM image (resolution: 0.12 μm/pixel) of the area and corresponding inverse pole figure (IPF) map of RD are shown in Figs. 4.1(b) and (c). Ex-situ DIC analyses were performed in two regions of interest (ROIs) surrounded by blue dashed lines (see Fig. 4.1(c)). The fabrication of the speckle pattern for DIC strain mapping was referred to Bandyopadhyay et al. [100]. First, 30 mg Mo powder (2.56 μm in diameter) and 200 ml methanol were mixed and the mixture was then placed into an ultrasonic cleaner for 30 min to make a homogeneous suspension. Then ten thousand Pb balls with a diameter of 1 mm were added to shrink the Mo agglomerates. The suspension was rested for 24 h and applied to the surface of the specimen using a dropper. Finally, the specimen was left for 6 h to achieve a rigid attachment of pattern. The patterns of two ROIs before and after the dwell fatigue test were analyzed by an open source 2D DIC MATLAB program Ncorr [101] to provide residual strain fields with a subset radius of 26 and a subset spacing of 2. Dwell fatigue load was applied in a trapezoidal waveform with a loading/unloading time of 1 s. The stress ratio R was set to 0.01. In each cycle, the load was held at 293.55 MPa ($0.95\sigma_y$ at strain rate $2.3 \times 10^{-4}\ s^{-1}$) for 5 s [30]. It was

reported that strain field was established at the early stage of the dwell fatigue test [102], and strain accumulation was most pronounced at the beginning of the loading history [63]. Thus, the dwell fatigue test was interrupted after 20 cycles. Meanwhile, the computation time of the accompanying CPFE simulation could be reduced.

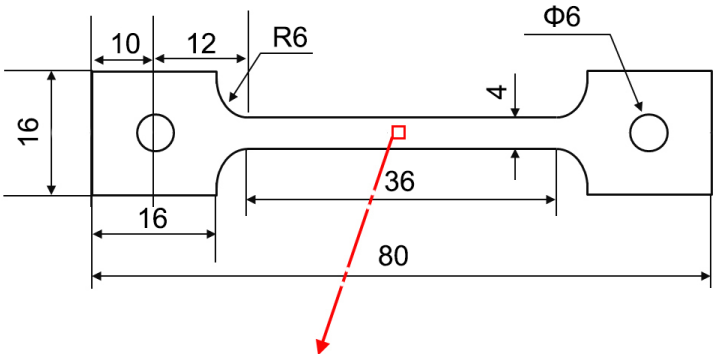

(a)

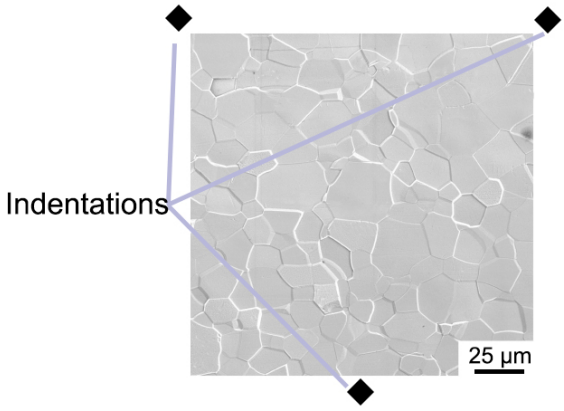

(b)

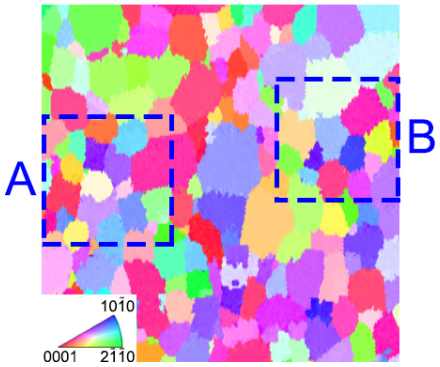

(c)

Fig. 4.1 (a) Geometry of specimens, (b) microstructure of the selected area on dwell fatigue test specimen, and (c) corresponding IPF map of RD. DIC measurements are performed in regions A and B.

4.3 Polycrystalline aggregate modeling

A cuboidal representative volume element (RVE) comprising 512 grains is applied to calibrate the crystal plasticity parameters of grade 1 CP-Ti, as shown in Fig. 4.2(a). The dimension of the RVE is 100 × 100 × 100 μm. Each grain is meshed with 1, 8, and 27 8-node C3D8 brick elements to investigate the sensitivity of RVE response to element size, as detailed in Fig. 4.2(b)-(d). The x, y, and

z directions represent TD, RD, and normal direction (ND), respectively. The initial crystallographic orientations have been selected from the EBSD measurements. The comparison between the pole figures of EBSD data and the RVE model is illustrated in Fig. 4.3. The basal pole tilts approximately $\pm 40°$ from ND to TD, a typical basal texture for rolled CP-Ti sheet [103],[104]. The boundary conditions are assigned as $u_{X'} = 0$, $u_{Y'} = 0$, and $u_{Z'} = 0$. The uniform displacements are imposed along RD, 45°, and ND, respectively. The constant-strain-rate displacement boundaries are imposed on the top (tension along RD) and right (tension along TD) surface.

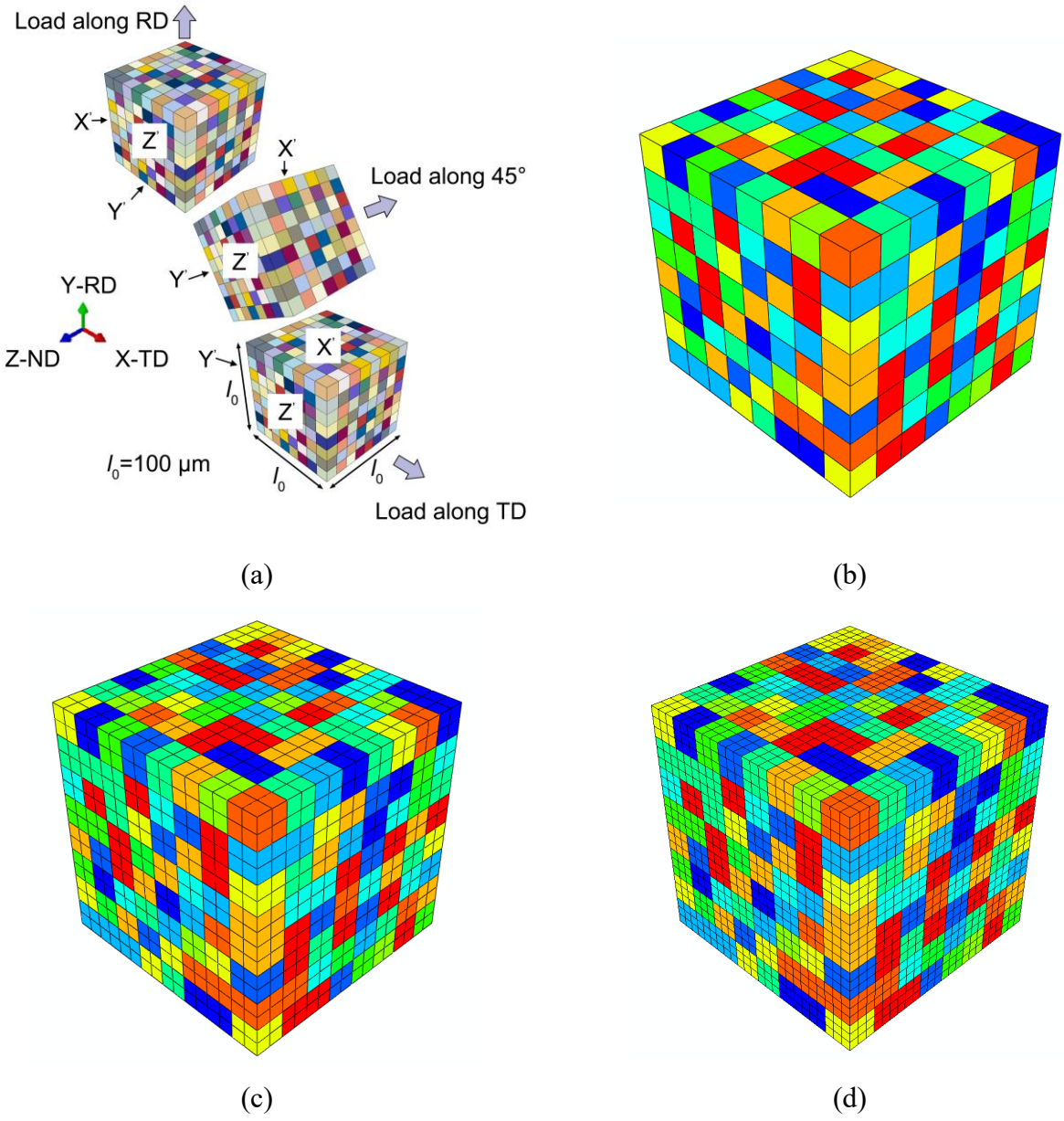

Fig. 4.2 (a) RVE model containing 512 grains and boundary conditions, each grain is made up of (b) 1 element, (c) 8 elements, and (d) 27 elements.

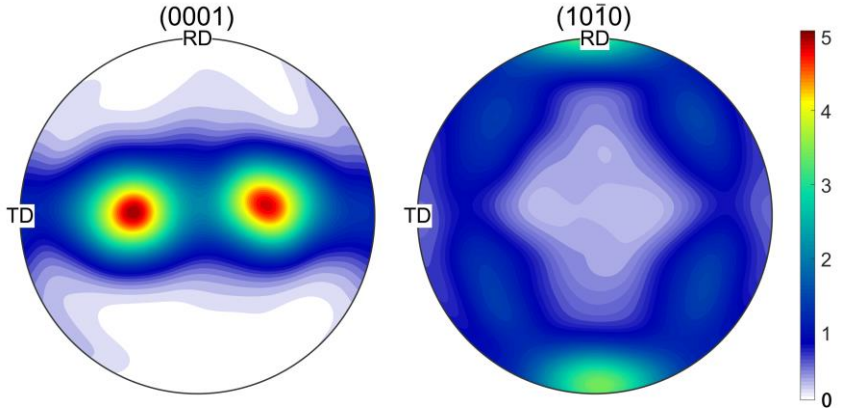

(a)

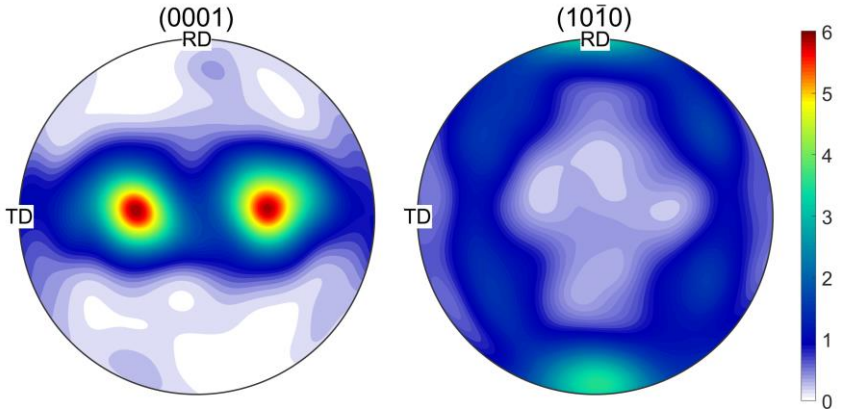

(b)

Fig. 4.3 Initial pole figures of RD: (a) results measured by EBSD scanning, (b) crystallographic orientations adopted for RVE.

For purpose of comparison with DIC strain measurements, two quasi-3D polycrystalline aggregate models are reconstructed within the abovementioned ROIs (see Fig. 3.1(c)) via an image-based approach, as shown in Fig. 4.4. The sketches of 2D microstructures are depicted in AutoCAD to obtain smooth grain boundaries (as illustrated in Fig. 4.4(a), including the number of particular grains for later discussion), extruded along the *z*-axis and meshed by 8-node C3D8 brick elements (19872 elements in region A and 16542 elements in region B) in HyperMesh, as illustrated in Fig. 4(b). Two models have the same dimension of $80 \times 80 \times 8$ μm. Given the influence of subsurface microstructure on the free-surface deformation, each model contains a surface layer and a subsurface layer with the same thickness, mesh size, and grain morphology (green area in Fig. 4.4(b)) [105],[106]. Therefore, the influence of subsurface microstructure is focused on crystallography. The crystal orientations of grains on the surface layer are specified by corresponding Bunge Euler angles, whilst

the orientations of grains on the subsurface layer are randomly selected from the EBSD data. The dwell fatigue load is applied on the right surface along RD and the waveform is identical to the experiment. The freedoms of left, bottom, and back surfaces are fixed to eliminate rigid body movement.

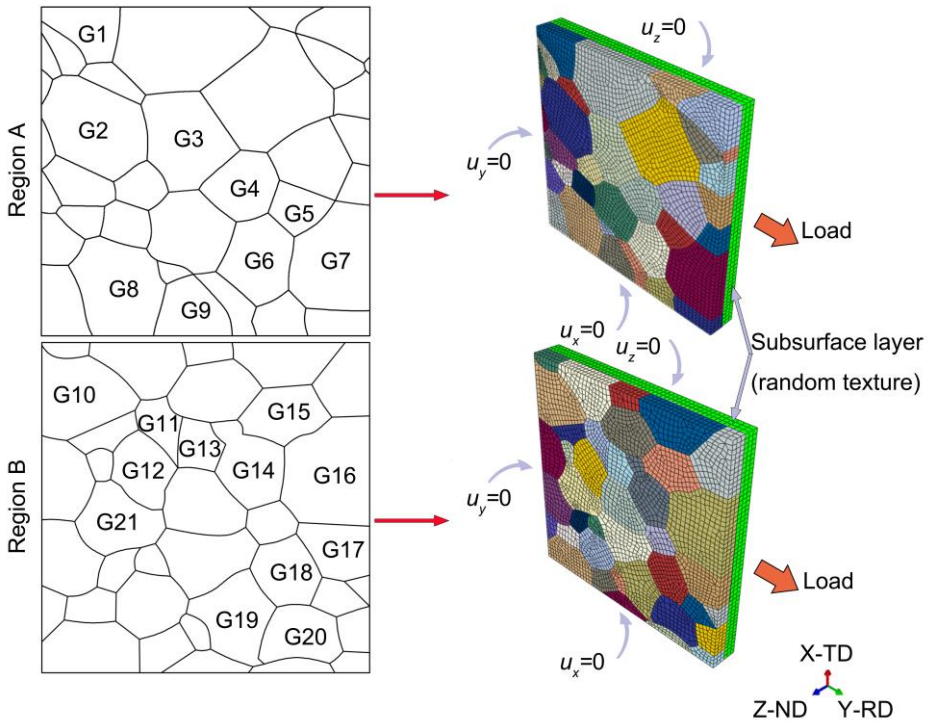

(a) (b)

Fig. 4.4 Image-based modeling: (a) microstructure sketches of two ROIs with a dimension of 80 μm × 80 μm, (b) quasi-3D models meshed by 8-node C3D8 elements and imposed boundary conditions.

4.4 CPFE constitutive parameter calibration

The CPFE constitutive characteristics of the tested CP-Ti should be found in order to quantitatively duplicate the experimental results.

With respect to the data related to SRS, the mobile dislocation density ρ_m, Burgers vector b^i, and Debye frequency υ_D in Eq. (3.14) are referred to Cuddihy et al. [79], whereas the activation energy ΔF, activation volume ΔV and the rate-sensitive parameters of deformation twinning in Eq. (3.16) are determined via calibration. Recently, Xiong et al. [107] have found that the SRS of prismatic slip is higher than that of basal slip in a grade 4 CP-Ti, and the activation energy ΔF of basal slip is also greater than that of prismatic slip, similarly to Ti-6242 alloy [108]. Although slip-dependent SRS

variations are considered to have an influence on creep deformation in cold dwell fatigue, the concrete mechanisms are still unknown. Besides, the diversity in chemical compositions should not be ignored. Thus, the activation energy and activation volume of each slip system is assumed to be the same in this study.

Determination of the CRSS relationships is conducted simultaneously. The CRSSs of 1st and 2nd pyramidal <*c*+*a*> slips are taken to be the same, three times the CRSS of prismatic slip [109]. The calibration procedure for the CRSS ratio between basal and prismatic slips is based on previous works. Since the increased concentration of oxygen can improve the strength of CP-Ti for the solid-solution strengthening effect, and the strengthening effect of oxygen is reported to be more remarkable on prismatic slip than basal slip, the CRSS ratio between basal and prismatic slips, therefore, decreases with increased amounts of oxygen [110],[111]. Moreover, the macroscopic strength of tested grade 1 CP-Ti in the present study is between the counterparts reported by Hama et al. [98] and Xiong et al. [107]. In terms of these relationships, the initial $CRSS_{basal}/CRSS_{prismatic}$ in this study is optimized between 1.63 and 2.14, values reported by the abovementioned two works. The $CRSS_{\{10\bar{1}2\}}/CRSS_{prismatic}$ is set to 2.1 as Wang et al. [109] and CRSS values of pyramidal <*a*> slip, $\{11\bar{2}2\}$ compression twinning are calibrated using the curve-fitting method due to a lack of systematic researches into these two systems.

The anisotropic elastic stiffness matrix [14], rate-sensitive, and strain gradient parameters of CP-Ti are summarized in Tables 4.2-4.3. The activation energy ΔF for each slip system is 0.5447 eV, which is slightly smaller than the value of prismatic slip reported by Xiong and co-workers [107]. The activation volume ΔV is $26b^3$, the same as the value calibrated by Gong et al. [112] between $8b^3 \sim 80b^3$, a general range for titanium and its alloys.

The reference shearing rate $\dot{\gamma}_0$ for twinning systems is taken to be $\dot{\gamma}_0 = 0.001$. The rate sensitivity parameter r for deformation twinning basically ranges from 0.01 to 0.1, and the most widely used value is $r = 0.02$ [113],[114],[115]. However, previous studies which adopted this value barely focused on rate-dependent deformation. Besides, $r = 0.02$ was selected for both titanium and aluminum alloys in preceding works although aluminum alloys were proved to be less rate sensitive than titanium alloys [116],[117],[118]. Therefore, a relatively small rate sensitive parameter is considered to be improper to describe the rate sensitivity of deformation twinning in CP-Ti, and rate

sensitive index r for twinning systems is therefore set to $r = 0.05$.

The rank of CRSSs in ascending order is prismatic, pyramidal <*a*>, basal, $\{10\bar{1}2\}$ tension twinning, $\{11\bar{2}2\}$ compression twinning and pyramidal <*c*+*a*> slip, which resembles the work of Hama et al. [98]. Among these values, $CRSS_{basal}/CRSS_{prismatic} = 1.71$ is a reasonable ratio in consideration of the biased strengthening effect caused by interstitial oxygen. $CRSS_{pyramidal<a>}/CRSS_{prismatic} = 1.64$, $CRSS_{\{11\bar{2}2\}}/CRSS_{prismatic} = 2.37$, are also acceptable with consideration of the previous literature [109].

Table 4.2 Anisotropic elastic constants of grade 1 CP-Ti.

C_{11} (GPa)	C_{22} (GPa)	C_{12} (GPa)	C_{13} (GPa)	C_{44} (GPa)
162.4	180.7	92.0	69.0	46.7

Table 4.3 Rate-sensitive and strain gradient parameters for grade 1 CP-Ti.

Slip		Twinning		Strain gradient	
Parameters	Value	Parameters	Value	Parameters	Value
$\rho_m\ (\mu m^{-2})$	5	$\dot{\gamma}_0\ (s^{-1})$	0.001	α_T	0.4
$\nu_D\ (Hz)$	1×10^{11}	r	0.05	$G\ (MPa)$	44230
$b_{<a>}\ (\mu m)$	0.32				
$b_{<c+a>}\ (\mu m)$	0.51				
$\Delta F\ (eV)$	0.5447				
$k\ (J/K)$	1.38×10^{-23}				
ΔV	$26b^3$				

According to the conclusion of Mikami et al. [119], the strain-hardening effect becomes higher with increasing initial hardening modulus h_0 (at small strains) and saturated CRSS τ_∞ (at large strains). The different stress-strain behaviors in three directions, which result from distinctive evolutions of

relative activities, could be used to calibrate these hardening parameters. Furthermore, the rate dependent deformation during stress relaxation is influenced by hardening parameters as well. The amplitude of stress relaxation increases as h_0 and τ_∞ become larger. Therefore, hardening parameters were optimized to reproduce macroscopic responses of uniaxial tensile and stress relaxation tests based on the abovementioned method.

The strain-hardening parameters are listed in Table 4.4. Besides, the latent hardening constant in Eq. (3.17) is assumed to be $q = 1$ for all slip and twinning systems. The reference twinning shear γ_{ref} in Eq. (3.23) is calculated by [120]

$$\gamma_{ref,\{10\bar{1}2\}} = \frac{\sqrt{3}a}{c} - \frac{c}{\sqrt{3}a}, \gamma_{ref,\{11\bar{2}2\}} = \frac{2\left(\left(\frac{c}{a}\right)^2 - 2\right)}{\frac{3c}{a}} \tag{4.1}$$

For CP-Ti, $c/a \approx 1.587$. Thus, $\gamma_{ref,\{10\bar{1}2\}} = 0.175$, $\gamma_{ref,\{11\bar{2}2\}} = 0.218$. The threshold value of V_{th} is randomly generated from 0.1 to 1.0 for each twinning system [98].

It should be noted that the parameter determination in this study still lacks a mechanistic understanding to some extent, further investigation on some unsure parameters (e.g., the activation energy and activation volume, CRSSs of pyramidal <*a*> slip and twinning) should be carried out.

Table 4.4 CRSS and strain-hardening parameters for slip and twinning systems, in MPa.

	Basal <*a*>	Prismatic <*a*>	Pyramidal <*a*>	1st Pyramidal <*c*+*a*>	2nd Pyramidal <*c*+*a*>	$\{10\bar{1}2\}$ Twinning	$\{11\bar{2}2\}$ Twinning
h_0	850	1750	750	2050	2050	1050	1050
τ_∞	183	155	173	362	362	249	267
τ_0	130	76	125	228	228	159	180

4.5 Macroscopic response

The experimental 0.2% proof strength $\sigma_{0.2}$ and ultimate tensile strength σ_t at different strain rates are listed in Table 4.5.

Stress-strain curves at the strain rate of $2.3 \times 10^{-4}\ s^{-1}$ in RD are obtained from the RVE model with different element sizes, as shown in Fig. 4.5. These curves exhibit small deviations regardless of the element size. Thus, the insensitivity of the stress-strain curves to element size is demonstrated. To reduce the computational cost, the following results in this section are all based on the coarse mesh model (Fig. 4.2(b)) because the coarse-mesh strategy has sufficient precision. The data of monotonic tensile, stress relaxation tests, and relevant simulation results are plotted in Fig. 4.6(a) and (b). The macroscopic SRS, strong tensile anisotropy, and stress relaxation are faithfully reproduced by the response of the RVE model. Therefore, the rationality of CPFE constitutive parameters is verified.

Table 4.5 Tensile properties of CP-Ti at different strain rates.

Strain rate (s^{-1})	RD		TD	
	$\sigma_{0.2}$ (MPa)	σ_t (MPa)	$\sigma_{0.2}$ (MPa)	σ_t (MPa)
2.3×10^{-4}	309	420	265	422
2.3×10^{-3}	320	465	285	460
2.3×10^{-2}	340	488	301	497

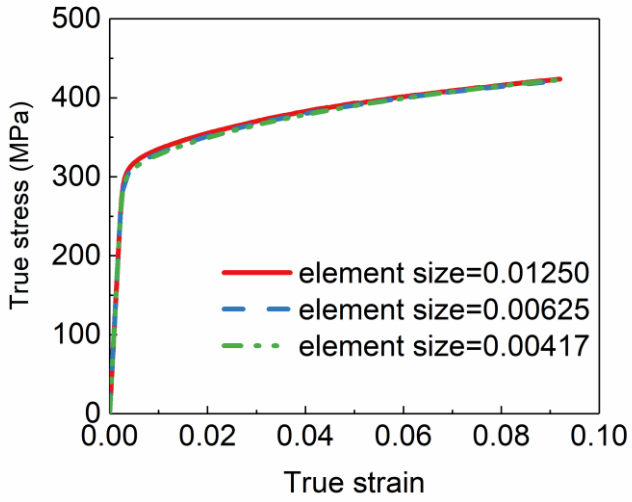

Fig. 4.5 Stress-strain curves obtained with different element sizes at a constant strain rate of 2.3×10^{-4} s^{-1} in RD.

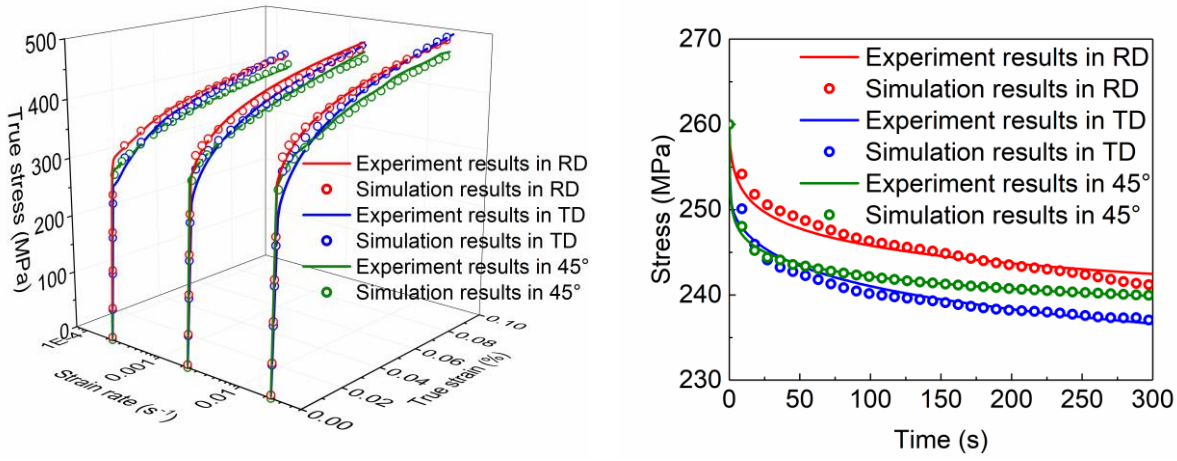

(a) (b)

Fig. 4.6 Macroscopic responses obtained from (a) tensile, (b) stress relaxation tests.

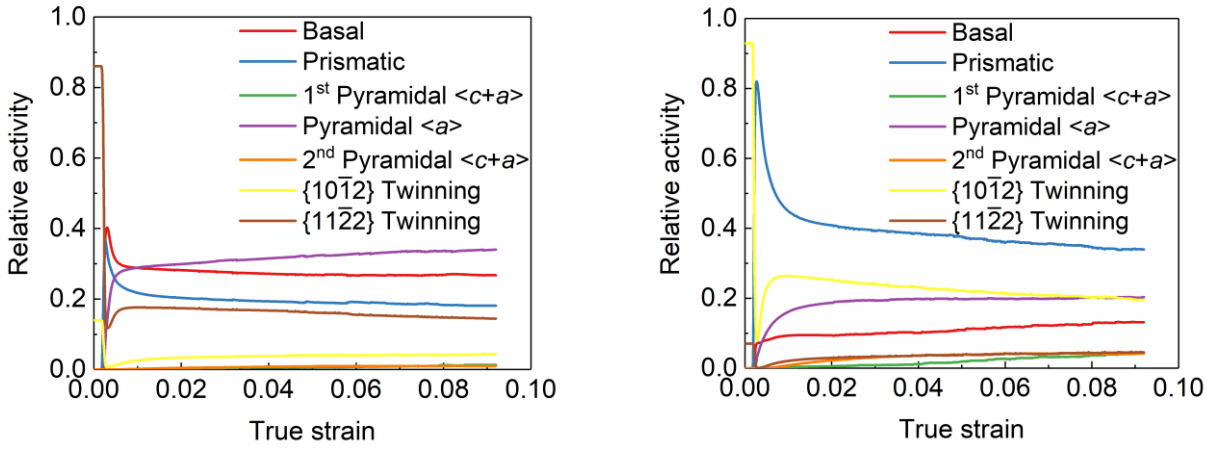

(a) (b)

Fig. 4.7 Evolutions of relative activities under 2.3×10^{-4} s^{-1} strain rate during tension in (a) RD, (b) TD.

To study the relation between tensile anisotropy and deformation mechanisms, relative activities of different deformation modes at the strain rate of 2.3×10^{-4} s^{-1} are depicted in Fig. 4.7 [98]. The lower yield strength in TD can be attributed to the high relative activity of prismatic slip at macroscopic yield since the CRSS of prismatic slip is the smallest. In contrast, the basal-dominant pattern at the beginning of plastic deformation leads to higher yield strength in RD. Additionally, a large initial hardening modulus (see Table 4.4) and continuous activity of the prismatic slip also lead to greater

strain-hardening in TD. Although the activity of pyramidal <*a*> slip remains at a high level after the yield in RD, the strain-hardening effect is not as conspicuous as that of TD because of the low initial hardening modulus [119].

Tensile anisotropy also manifests in twinning activities. The simulation results reveal that $\{11\bar{2}2\}$ compression twinning and $\{10\bar{1}2\}$ tension twinning are respectively dominant twinning systems in RD and TD, which keeps consistent with the experimental twin boundary maps after the tension, as given in Fig. 4.8(a) and (b). Furthermore, relative activities of twinning at $\varepsilon = 0.05$ increase as the strain rate becomes higher in both RD and TD, as shown in Fig. 4.8(c). This observation captures the phenomenon that twinning is more active at high strain rates.

Although the cyclic strain history was not monitored by extensometer or strain gauges considering the speckle pattern on the surface of the specimen, based on the calibrated parameters, the simulated cyclic responses of two ROIs are plotted in Fig. 4.9. The strain accumulates at a reducing rate per dwell cycle and macroscopic stress-strain behaviors are similar to the experimental trend in Peng et al. [30], as well as the simulated response in Cuddihy [121].

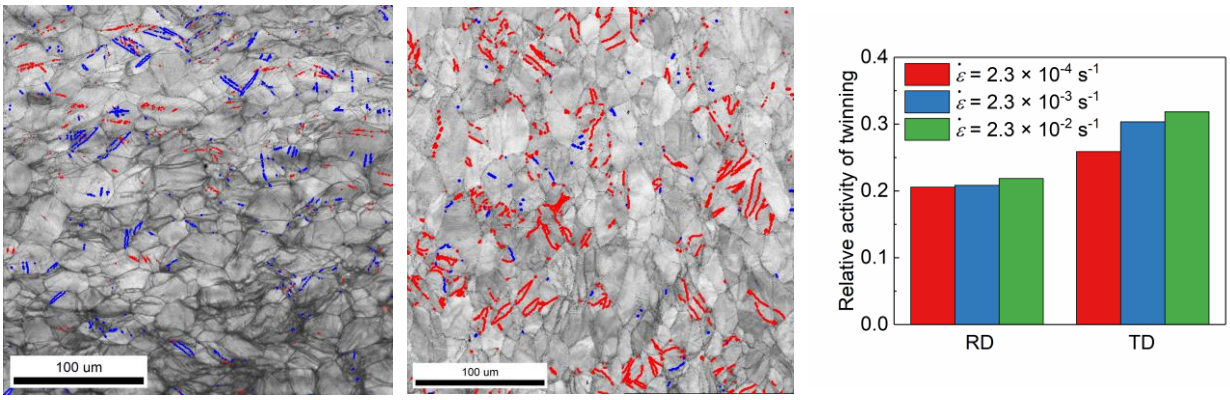

(a) (b) (c)

Fig. 4.8 Twin boundary maps on (a) RD, (b) TD samples after tension. The tension and compression twin boundaries were respectively marked by red and blue lines. (c) relative activities of twinning at different strain rates when $\varepsilon = 0.05$.

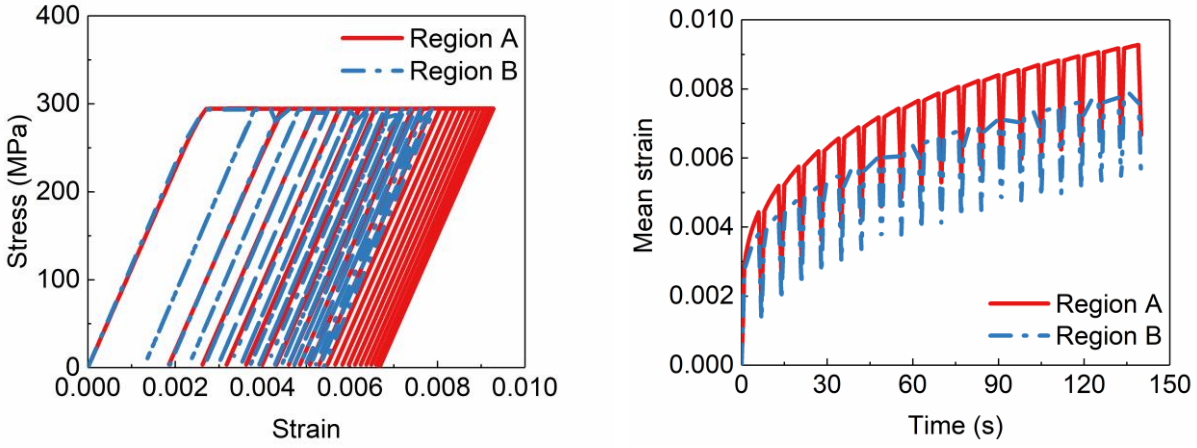

(a) (b)

Fig. 4.9 Simulated cyclic responses of two ROIs. (a) Stress-strain curves, (b) Strain-time curves.

4.6 Strain fields and deformation mechanisms

To analyze the evolution of strain field under dwell fatigue loading, Schmid factor (SF) is employed to link the deformation mechanism with strain localization. The SF maps of basal, prismatic, pyramidal <*a*> slips, and $\{11\bar{2}2\}$ compression twinning system within two ROIs are plotted in Fig. 4.10. Two ROIs are revealed to be soft-grains-dominant. Pyramidal <*c*+*a*> slip and $\{10\bar{1}2\}$ tension twinning systems are not taken into account because the activations are difficult in RD, as plotted in Fig. 4.7(a).

The evolutions of axial strain ε_{yy} fields within two ROIs in the first dwell fatigue cycle are predicted by CPFE modeling, as shown in Fig. 4.11. Due mainly to the elastic anisotropy of HCP lattice, strain heterogeneity at the beginning of dwell time (point D1) is observed even the maximum stress is under macroscopic yield strength. Due to cold creep during the load-holding period, the strain accumulation at the end of dwell time (point D2) is conspicuous, which in turn aggravates the strain incompatibility between soft and hard grains at the unload state (point D3).

An overall comparison between the experimental and numerical results with respect to residual strain distributions after 20 cycles are illustrated in Fig. 4.12. The numerical contours of residual axial strain ε_{yy} and transverse strain ε_{xx} are not in strict agreement with DIC measurements and manifest more heterogeneous deformation (i.e., strain incompatibility among grains), whereas most of the strain localizations are identified by CPFE modeling with fair accuracy. Additionally, despite the plastic strain accumulation, no significant discrepancy is discovered between the predicted axial strain

distributions at the end of the 1st and 20th cycle, as illustrated in Figs. 3.11 and 3.12(a). Thus, it can be concluded that the local deformation pattern forms at the early stage of the dwell fatigue. This result is consistent with the DIC interpretation given by Littlewood et al. [102].

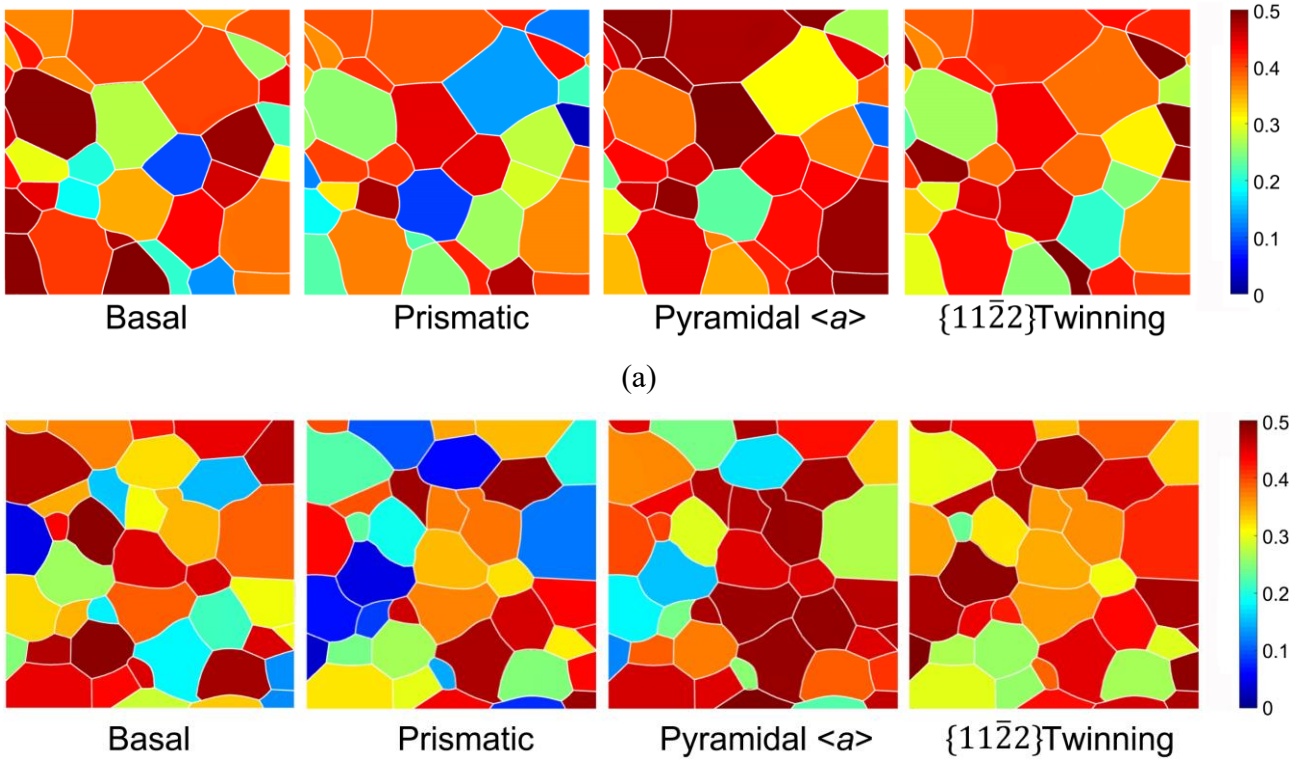

Fig. 4.10 Schmid factor maps in (a) region A (b) region B.

Regarding the residual axial strain ε_{yy} field within two ROIs after 20 cycles, the experimental and numerical results exhibit similar strain localization paths, as highlighted in Fig. 4.12(a) by white dashed lines. In region A, the strain localizations are located at grain G1 (see Fig. 4.4(a)) and its neighborhood with high SFs for basal, prismatic, and pyramidal <*a*> slip systems, as well as the center and bottom right corner including grains G3, G4, G5, and G7. In region B, grains G10-G14 and G17-G20 along the aforementioned paths demonstrate larger axial strain accumulation. In contrast, axial strain accumulation is less obvious in hard grains with low SFs for basal, prismatic, and pyramidal <*a*> slip systems, such as grain G21. It should be noted that some deviations between DIC analysis and CPFE computation are observed at the center bottom of region A (grains G8 and G9) and the lower right corner of region B (grains G18, G19, and G20), especially the area containing grains G8 and G9. Since the spatial distribution of strain field on the free surface is likely to be affected by the subsurface

layer, the local strain deviation between DIC strain mapping and CPFE simulation is possibly attributed to the mischaracterization of subsurface microstructure.

The experimental and numerical mappings of residual transverse strain ε_{xx} in two ROIs after 20 cycles achieve a better agreement than in the axial direction, as illustrated in Fig. 4.12(b). The localization band of compressive strain in region A is approximately along the top left corner to the bottom right corner, whilst numerical prediction also misses the transverse strain concentration in grains G8 and G9 measured by DIC. As for the transverse strain field in region B, except for some small zones such as the top left corner, the overall compressive strain accumulation of region B is less pronounced than of region A.

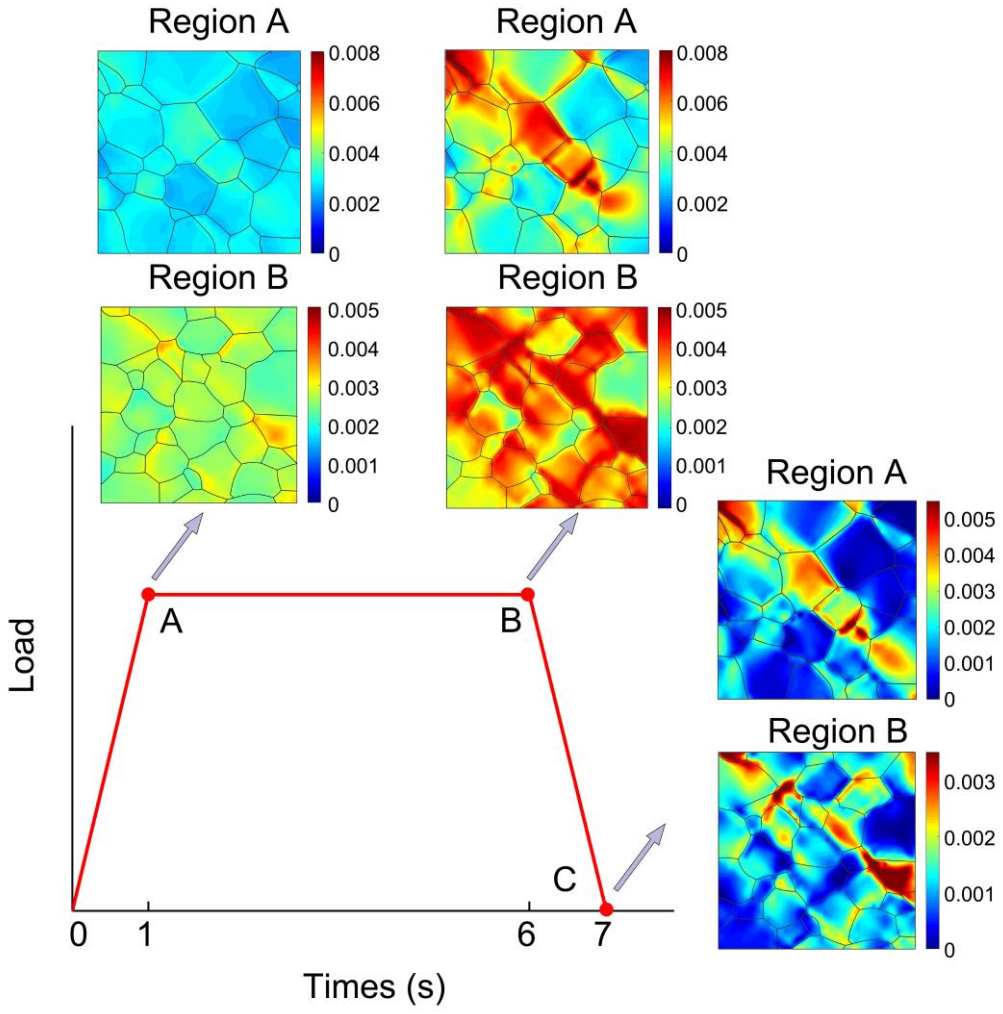

Fig. 4.11 Evolutions of predicted axial strain fields within two ROIs in the first dwell fatigue cycle.

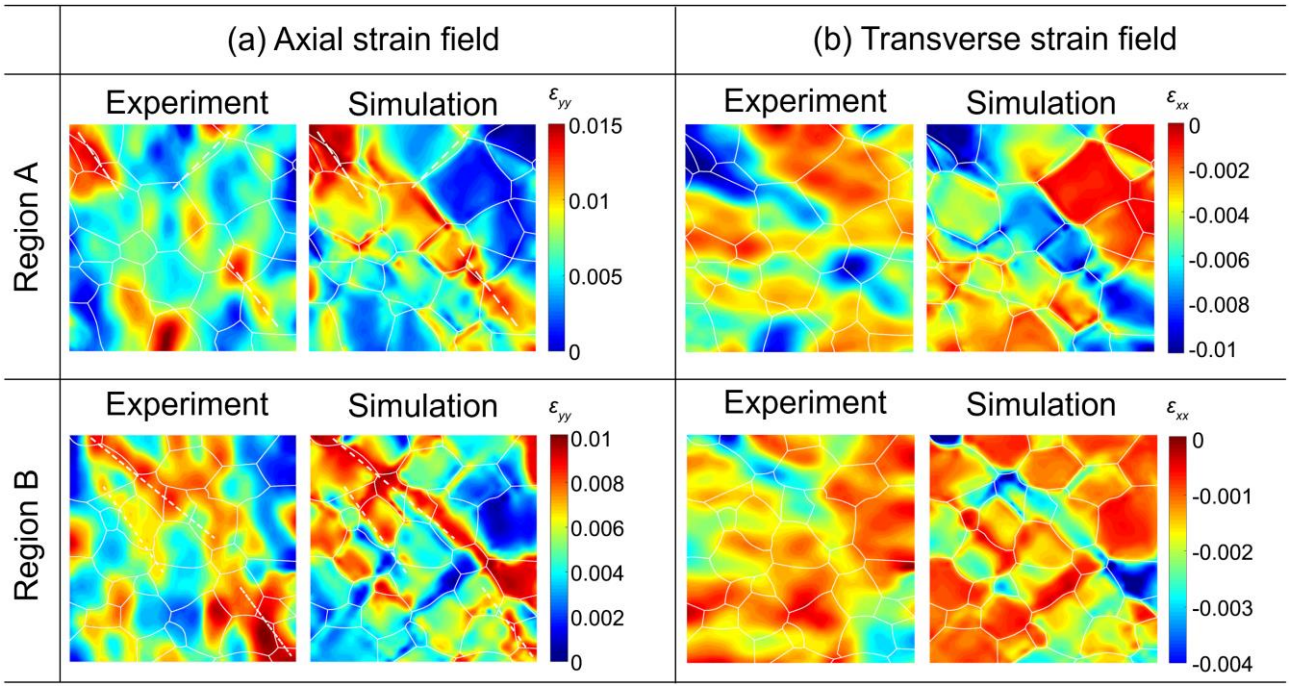

Fig. 4.12 Experimental and numerical results in ROIs after 20 cycles: (a) axial strain field, (b) transverse strain field.

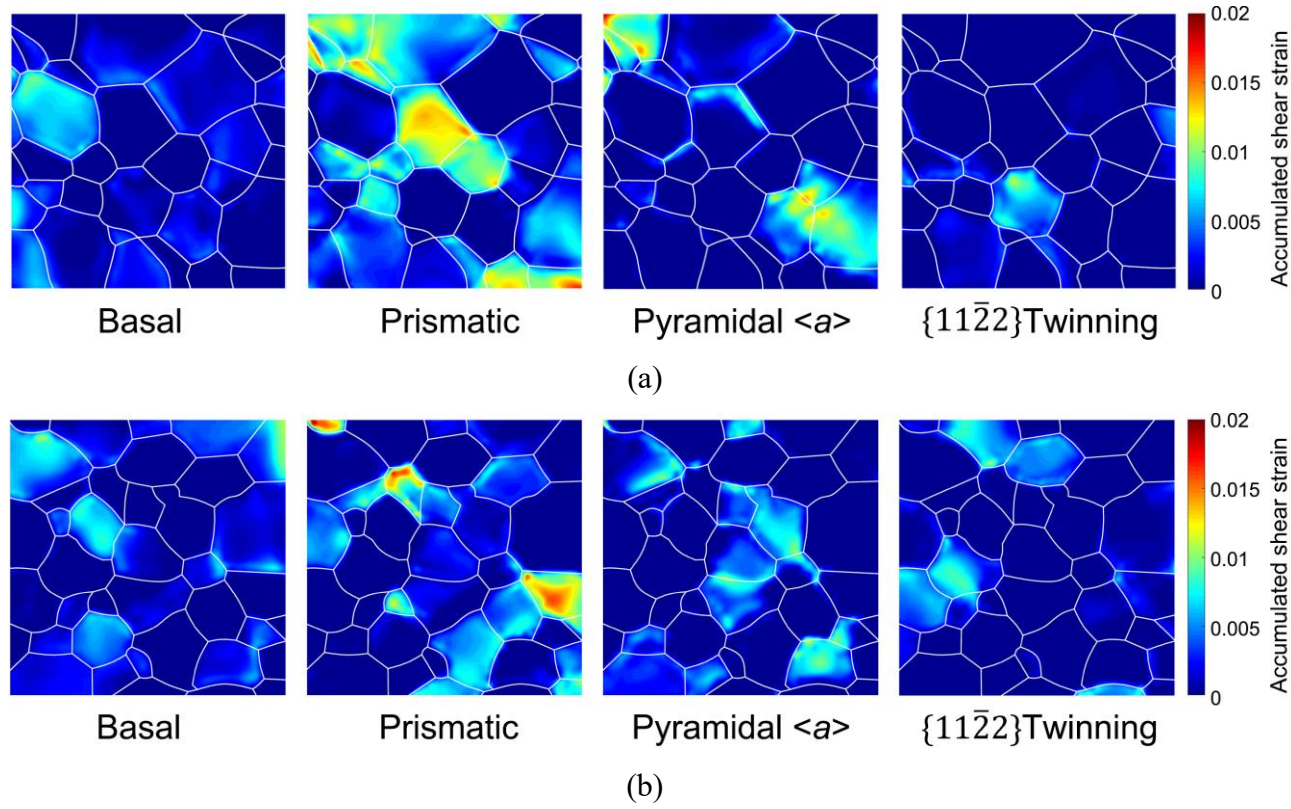

Fig. 4.13 Contours of maximum accumulated shear strains on active slip and twinning systems in (a) region A, (b) region B.

The strain localization directly results from slip and twinning activities. Although the operating slip and twinning systems are not incorporated explicitly as traces in the crystal plasticity model, the activities can be captured by corresponding shear strain accumulation implicitly. To determine the contribution of individual plastic deformation modes to axial strain localization, the maximum shear strain accumulation on four active slip and twinning systems (basal, prismatic, pyramidal <*a*> slips, and $\{11\bar{2}2\}$ compression twinning systems) are calculated by CPFE simulations, as given in Fig. 4.13. In region A, the axial strain accumulation within grains G1, G3, G4, and G7 is basically dominated by prismatic and pyramidal <*a*> slip activities because of high corresponding SFs. However, the contribution of basal slip activity is inconspicuous in region A. Concerning region B, the axial strain localizations in grains G11, G13, G15, G17, G18, and G19 are derived from the prismatic slip activity. Pyramidal <*a*> slip activity dominates the axial strain concentrations in grains G14 and G20, while basal slip activity leads to high axial strain accumulation in grains G10 and G12. This comparative analysis reveals that the activity of prismatic slip plays a primary role in axial strain localization, followed by pyramidal <*a*> and basal slips. In contrast, the activity of $\{11\bar{2}2\}$ compression twinning demonstrates a low level in two ROIs considering the relatively high CRSS. As previously reported, the slip and twinning activations in CP-Ti under tension are observed to be prismatic slip-dominant, followed by pyramidal <*a*> slip, twinning, and basal <*a*> slip [103],[110],[122]. Besides this, previous studies have reported that the deformation mechanisms under different loading conditions (i.e., tension, fatigue and dwell fatigue loading) exhibit similar patterns with respect to the frequency of different slip systems [106],[123]. The predicted slip activations, which are related to axial strain localization, closely match the quantitative results from previous slip trace analyses. However, the twinning activity is likely to be underestimated by the CPFE modeling considering only two twinning systems are modeled.

Since the strain localization in an individual grain results from multiple active deformation modes, a weighted averaged Schmid factor (WASF) is developed to evaluate the axial strain accumulation comprehensively. Following the study of Zhao et al. [124], the WASF in the present work is defined as

$$WASF = \frac{\sum_{p=1}^{4} \frac{CRSS_{prismatic}}{CRSS_p} \cdot SF_p}{4} \tag{4.2}$$

where p represents the four active slip and twinning systems. The SFs and relevant WASFs of numbered grains (Fig. 4.4(a)) are listed in Table 4.6.

Table 4.6 Schmid factors of numbered grains in Fig. 4.4(a).

Grain	Schmid factor				
	Basal	Prismatic	Pyramidal <*a*>	$\{11\bar{2}2\}$ twinning	WASF
G1	0.368	0.396	0.494	0.330	0.268
G2	0.493	0.254	0.376	0.241	0.222
G3	0.274	0.448	0.499	0.414	0.278
G4	0.091	0.447	0.434	0.496	0.251
G5	0.458	0.291	0.438	0.178	0.228
G6	0.436	0.263	0.431	0.165	0.215
G7	0.380	0.369	0.486	0.308	0.259
G8	0.408	0.374	0.443	0.253	0.251
G9	0.498	0.250	0.352	0.230	0.217
G10	0.477	0.223	0.368	0.271	0.214
G11	0.155	0.483	0.474	0.435	0.268
G12	0.493	0.190	0.294	0.291	0.200
G13	0.306	0.374	0.474	0.385	0.257
G14	0.346	0.380	0.486	0.349	0.262
G15	0.148	0.487	0.481	0.460	0.272
G16	0.388	0.115	0.273	0.357	0.170
G17	0.303	0.434	0.471	0.355	0.268
G18	0.213	0.458	0.488	0.454	0.275
G19	0.181	0.477	0.487	0.459	0.276
G20	0.481	0.248	0.390	0.244	0.221
G21	0.262	0.043	0.153	0.457	0.128

The relationship between the grain-averaged axial strain accumulations and the WASFs of grains GXs ($X = 1 - 21$, as given in Fig. 4.4(a)) is illustrated in Fig. 4.14. The grain-averaged axial strains

measured by DIC agree with the CPFE predicted results in sound accuracy, although some deviations exist. In addition, grains with high WASF values generally exhibit high axial strain accumulation. Therefore, WASF is an effective parameter to predict the degree of strain localization.

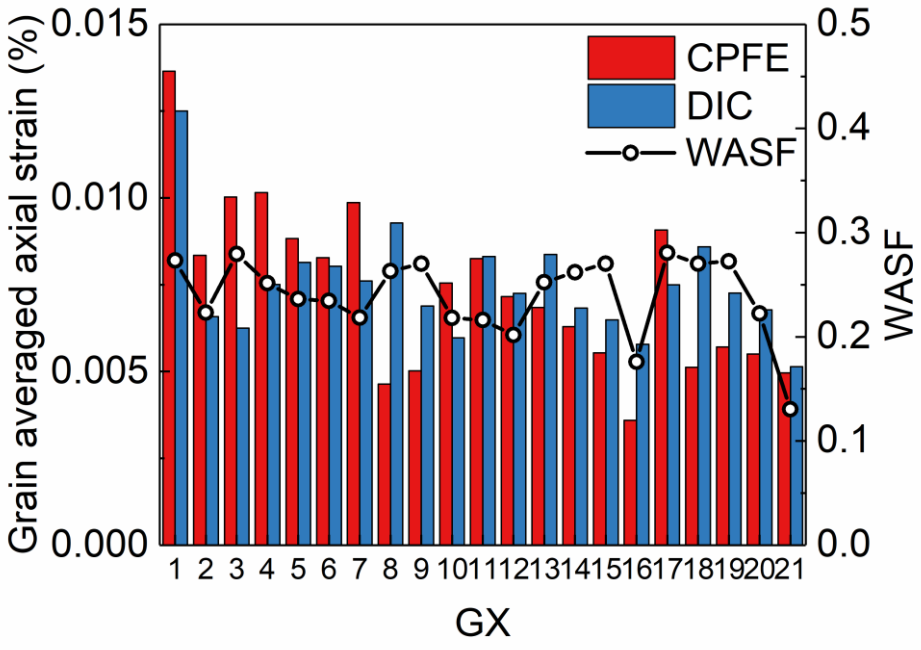

Fig. 4.14 Relationship between grain-averaged axial strain and WASF.

4.7 Stress redistribution

The strain incompatibility within a hard-soft grain pair can result in stress redistribution from the soft grain to adjacent hard grain during dwell fatigue, which is termed as "load shedding" [125]. This scenario is thought to generate high basal plane normal stress in hard grains and trigger the dwell facet nucleation [79]. Compared to the synthetic microstructure-based works, an authentic soft-hard-soft grain combination is identified in region B, as shown in Fig. 4.15. The angle between the *c*-axis of hard grain G21 and loading direction is 17°. Experimental results have shown that the basal facets in hard grains are mainly oriented at 10°~25° perpendicular to the direction of macro principal stress and therefore grain G21 is a potential site for facet formation [33],[123]. The two soft grains are G12 with a basal SF of 0.493 and G22 with a prismatic SF of 0.459. Thus, the dislocation pile-ups at two hard-soft grain boundaries are induced by different slip systems based on an adaption of the dislocation pile-up model.

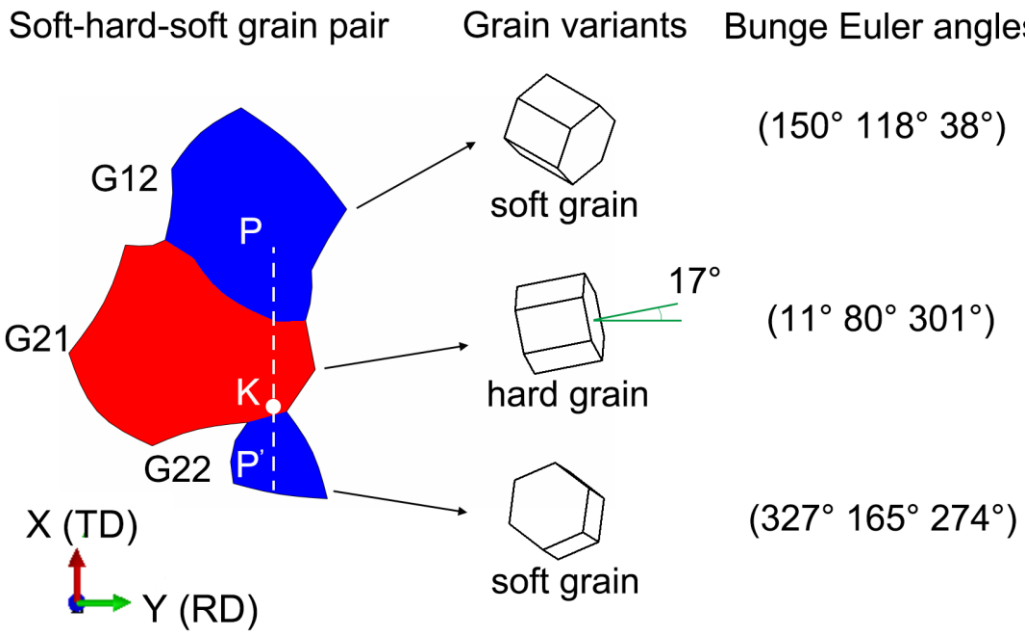

Fig. 4.15 Schematic diagram of the soft-hard-soft grain combination.

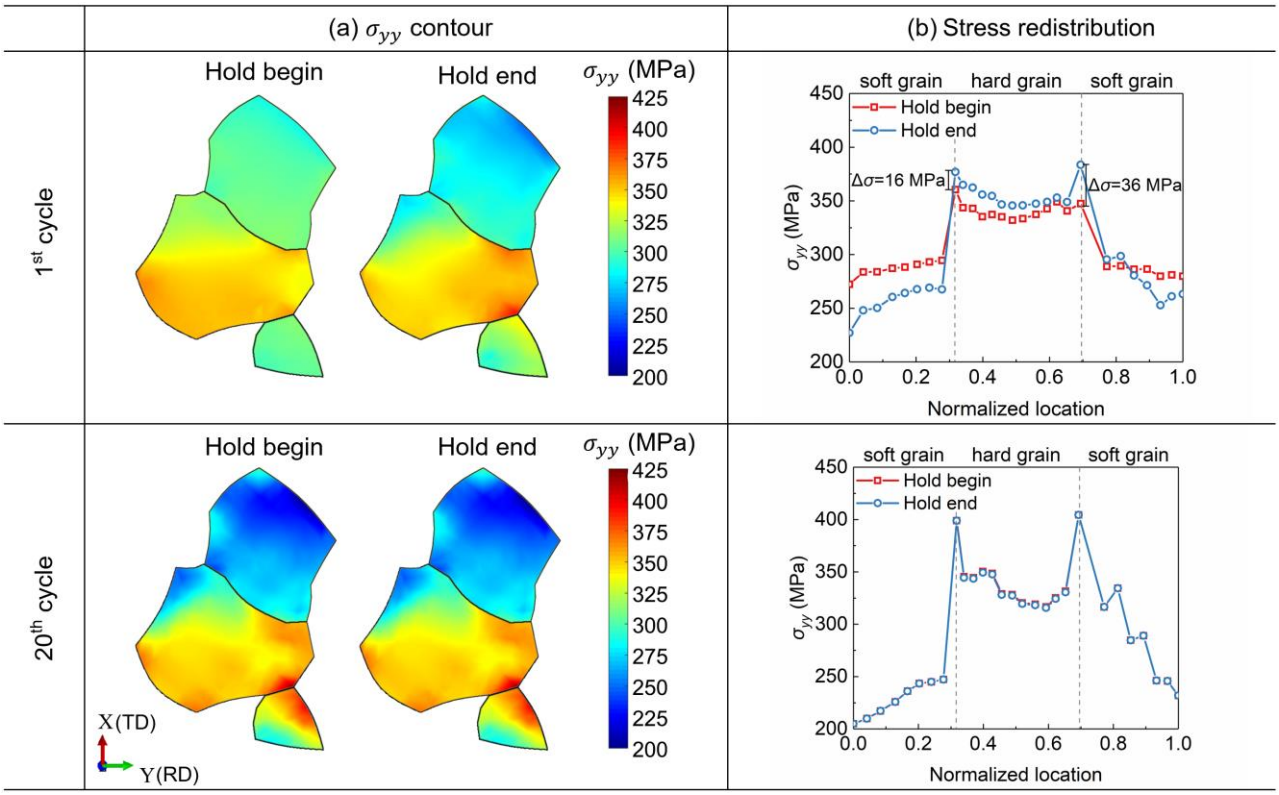

Fig. 4.16 (a) Contours of σ_{yy} within the soft-hard-soft grain pair, (b) Stress redistribution along path $P - P'$.

The contours of stress σ_{yy} (parallel to loading direction) at the beginning/ending of dwell time in the 1st cycle and 20th cycle are shown in Fig. 4.16(a). The σ_{yy} stress near the hard-soft grain boundaries increases dramatically when the stress-hold ends in the 1st cycle. Compared to the 1st cycle, the area of stress concentration in hard grain expands in the 20th cycle, whilst little stress contour variation can be found at the beginning and end of dwell time. Besides, the local grain boundaries near stress concentration sites are nearly parallel to the loading direction because the stress redistribution necessitates a near Taylor condition, in which soft and hard grains are subject to the same amount of uniaxial strain [126].

The σ_{yy} stress along path $P - P'$ are plotted in Fig. 4.16(b). The magnitude of stress redistribution in the 1st cycle induced by basal slip is 16 MPa, while 36 MPa is caused by prismatic slip. Due to the shapes of two hard-soft grain boundaries near stress concentration sites are similar, the influence of grain boundary morphology on stress redistribution is negligible. Thus, prismatic slip can enhance more dislocation pile-ups at the grain boundary and lead to greater σ_{yy} stress increase during the dwell period even though the smaller size of grain G22 than that of G12 may reduce the average slip distance. This result is opposite to the assumption of Zhang et al. [49] because the CRSS of prismatic slip is lower than basal slip and the rate-sensitivity of two slip systems is the same in present work. However, the peak σ_{yy} stress at start and end of dwell time in the 20th cycle manifests little variation, which implies that the cyclic stress redistribution diminishes gradually.

The resolved normal stress on the basal plane of hard grain plays an important role in facet initiation. Here the resolved normal stress is

$$\sigma_{basal} = \boldsymbol{m}_{basal} \cdot \boldsymbol{\sigma} \cdot \boldsymbol{m}_{basal} \tag{4.3}$$

where $\boldsymbol{m}_{basal}$ is the normal vector of the basal plane. The evolutions of resolved normal stress on the basal plane at point K during dwell periods of the 1st and 20th cycles are illustrated in Fig. 4.17. The resolved normal stress increases rapidly in the 1st cycle, as a result of significant σ_{yy} stress redistribution. However, this trend is smoother in the 20th cycle.

The cyclic stress redistribution phenomenon predicted by CPFE modeling is combined with experimental results to understand the influence of deformation twinning on dwell fatigue. No deformation twinning is observed on the surface of two ROIs after the interrupted dwell fatigue test. The accumulated shear strain on $\{11\bar{2}2\}$ twin plane is also not sufficient to activate the twinning nucleation in the CPFE model, as shown in Fig. 4.13. According to the results of the present study,

stress redistribution and stress redistribution are most pronounced at the beginning of dwell fatigue loading history, while twinning nucleation and propagation are relatively difficult at this time. Therefore, the resolved normal stress on the basal plane of hard grains increases drastically because the continuous dislocation pile-ups at hard-soft grain boundaries can hardly be hindered by twins in adjacent soft grains. In light of the above discussion, the typical hard-soft grain pair is still a detrimental site for facet nucleation and leads to a great dwell life debit for CP-Ti [30]. It has to be emphasized that the deformation twinning is treated as pseudo slip in the current CPFE model. For the twinning nucleation mechanisms which cannot be explained by global Schmid factors, more integrated research is needed [127],[128].

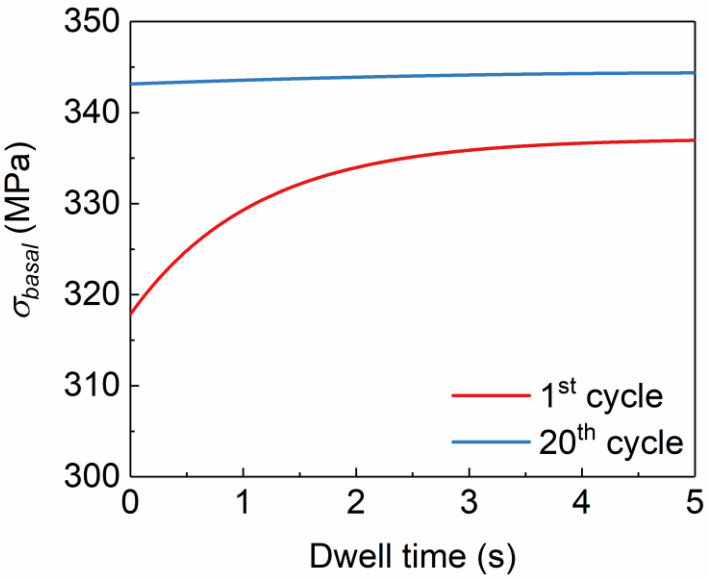

Fig. 4.17 Evolution of the resolved normal stress on the basal plane at point K during dwell period of the 1st and 20th cycles.

4.8 Effect of deformation twinning on stress redistribution: Explicit modeling

According to the results of the DIC experiment and crystal plasticity modeling, deformation twins in soft grains have limited influence on stress redistribution and facet nucleation in CP-Ti. Nevertheless, as shown in Fig. 2.7, the deformation twins form in the hard grain. Therefore, this section investigates the effect of deformation twin in hard gain on stress redistribution based on explicit crystal plasticity modeling.

A quasi-3D polycrystalline aggregate model with dimensions of 80 μm × 80 μm × 6 μm is constructed and meshed by 12684 C3D8 hexahedral elements, as shown in Fig. 4.18. A hard grain is embedded at the center area of a cluster of 37 soft grains. The *c*-axis of the hard grain is parallel to the loading direction along the y axis, while the *c*-axis of the adjacent soft grain is perpendicular to the loading direction. In particular, a yellow band is a predefined region along the $\{10\bar{1}2\}$ twin plane for depicting explicit twinning nucleation because the CRSS for $\{10\bar{1}2\}$ tensile twinning is smaller than that of $\{11\bar{2}2\}$ compressive twinning. The thickness of this band is assumed to be 1 μm for simplicity, whilst the twin growth is ignored. The procedure with respect to the activation of this twin variant is as follows:

1. At the beginning of the analysis, the crystal orientation of this band is the same as that of the parent hard grain. The numbers of all integration points in this region are exported and saved to an external file.
2. At the beginning of each time increment, the numbers of these integration points are transferred from the external file into UMAT using the UEXTERNALDB subroutine. The volume fractions of twinning at numbered integration points are compared with the threshold value.
3. Due to the plastic deformation, the shear strain on the twin plane accumulates. When the volume fraction of twinning at any integration point is greater than the threshold value, crystal orientations at all integration points in this band are rotated by the rotation tensor in Eq. (3.24).

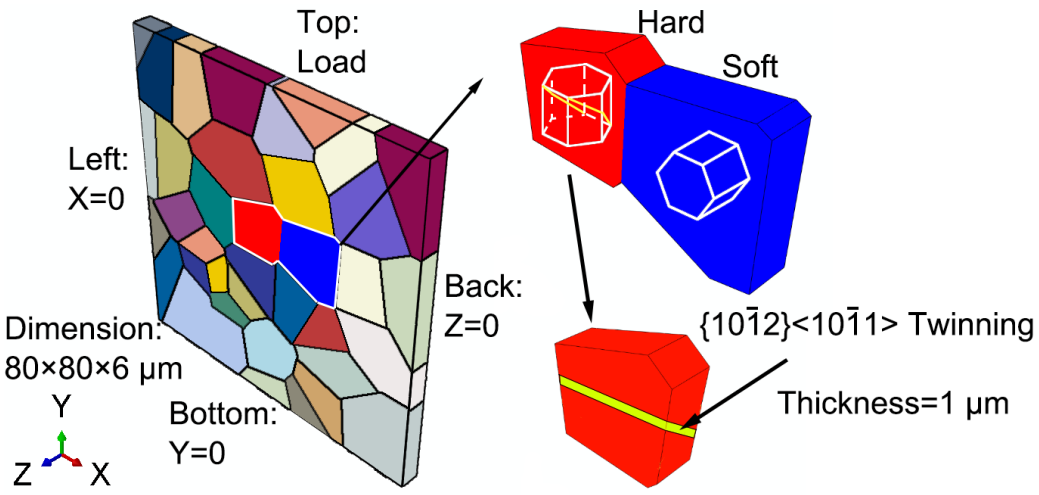

Fig. 4.18 Polycrystal model with a hard grain embedded in a colony of soft grains. A band with a thickness of 1 μm is defined in the hard grain along the $\{10\bar{1}2\}$ twin plane for explicit investigation of twinning nucleation.

It should be mentioned that the twinning volume fraction of the hard grain is set to a relatively smaller value of 0.05 on purpose to ensure the deformation twinning can be activated in one dwell fatigue cycle that has the same waveform as the dwell fatigue test in Section 4.2.2 as the stress redistribution is most significant in the first cycle.

The state of deformation twinning and stress distributions within the hard-soft grain combination at the beginning of the stress dwell, the time when twinning nucleation occurs, and the end of the dwell period, are plotted in Fig. 4.19. At the beginning of the dwell time ($t = 0$ s), no twin is observed within the hard-soft grain combination and the stress concentration occurs in the hard grain. Since the high SF of the $\{10\bar{1}2\}$ twinning system, the shear strain accumulates during the cold creep. At the dwell time of 2.55 s, twin nucleates in the hard grain. The plastic deformation of the twinned region becomes easier, and the pile-up stress starts to be alleviated (as the sites where the arrow points in stress contours). From the time when twinning formation to the end of the dwell ($t = 5$ s), although the stress concentration in the parent hard grain continues rising, it can be found that the stress in the vicinity of the twinned region is less marked than the parent hard grain.

The stress distribution along paths 1 (through the twinned region and soft grain) and 2 (through the parent hard grain and soft grain) in Fig. 4.19 are plotted in Fig. 4.20 (a) and (b), respectively. The overall distributions along the two paths are almost the same at $\mathrm{t} = 0$ s and $\mathrm{t} = 2.55$ s. After the nucleation of the twin,i.e., at the end of the dwell period, the stress at the hard-soft grain boundary decreases slightly on path 1. On the contrary, the grain boundary stress on path 2 keeps increasing. Therefore, it is clear that the onset of twin in the hard grain can inhibit the local stress enhancement at the hard-soft grain boundary during the stress dwell period, which may, in turn, reduce the possibility of basal facet nucleation at this position. Concerning that the grain boundary stress increases within the parent hard grain, the trend of stress redistribution remains continuous. However, the twin propagation in length and thickness, as well as nucleation of multiple deformation twins (see Fig. 2.7) in the hard grain is likely to expand the local influence.

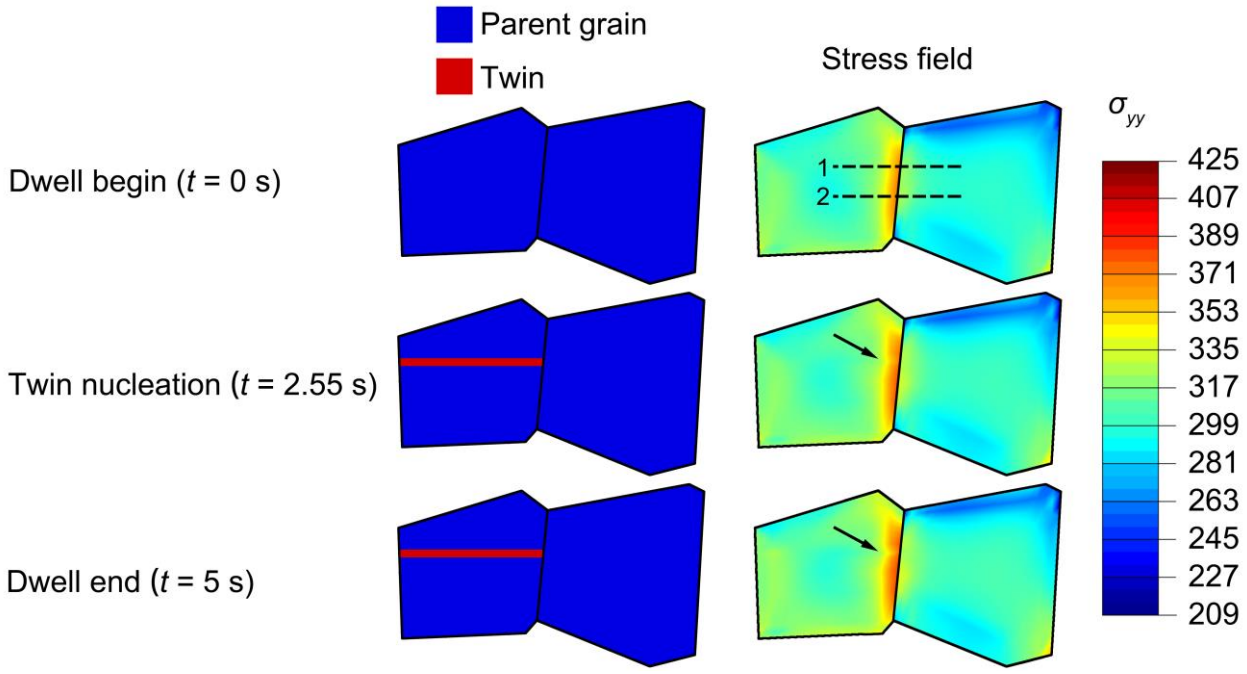

Fig. 4.19 State of deformation twinning and stress contours within the hard-soft grain combination at different times of the dwell period.

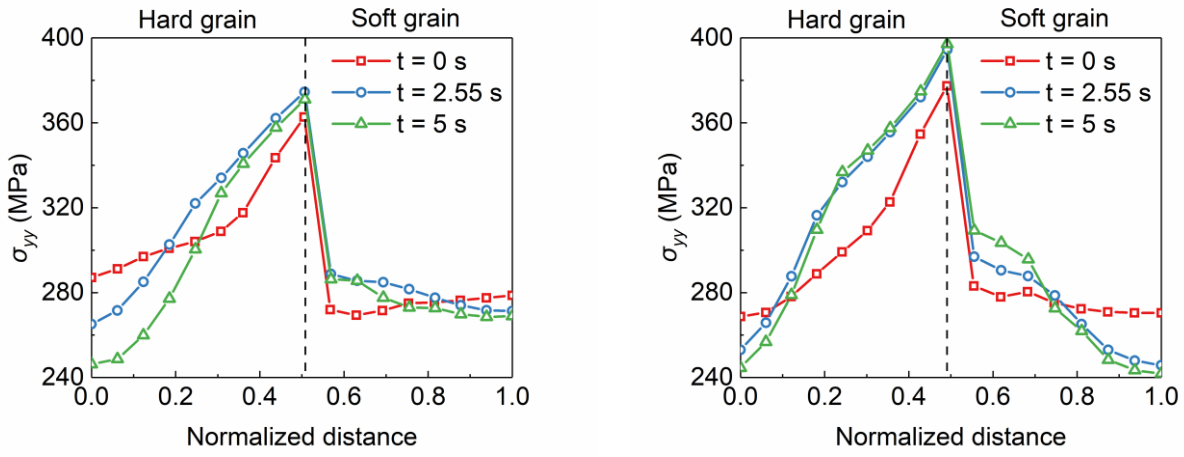

(a) (b)

Fig. 4.20 Stress distribution along (a) path 1 and (b) path 2 at the corresponding times in Fig. 4.19.

4.9 Summary

The heterogeneous deformation of a hot-rolled commercially pure titanium grade 1 sheet under dwell fatigue stress was explored experimentally and numerically in this chapter. The crystal plasticity predictions and the DIC strain values were compared quantitatively. To define the strain localization

processes, the active plastic deformation modes, crystallographic orientations, and effect of subsurface microstructure are numerically investigated. Furthermore, the influence of deformation twinning on titanium dwell fatigue behaviors is explored by looking at stress redistribution within a soft-hard-soft grain combination. The results are listed below:

1. Reasonable agreements are achieved between the residual strain fields mapped by DIC and CPFE simulations within two ROIs. The axial strain localizations are dominated by the activity of prismatic slip, followed by pyramidal <*a*> and basal slip, whereas the activity of $\{11\bar{2}2\}$ compression twinning is insignificant.
2. A weighted averaged Schmid factor, which takes the contribution of each active deformation mode into account, is proven to be effective to link the amount of axial strain accumulation and crystallographic orientation of individual grains.
3. The CPFE simulation results show that stress redistribution within a soft-hard-soft grain pair leads to a notable increase in basal plane normal stress within the hard grain at the beginning of dwell fatigue loading history. The twinning nucleation in the soft grain is difficult during this period because of insufficient accumulated shear strain on the twin plane. The explicit modeling of deformation twin in the hard grain indicates that the stress enhancement in the twinned region is inhibited, whereas the stress keeps increasing in the parent grain. Therefore, the influence of deformation twinning on basal facet formation is considered to be limited.

5. Role of intergranular β phase in dwell fatigue crack initiation in Ti-Fe-O alloy

5.1 Introduction

This chapter aims to evaluate the effect of the β phase on the local deformation behaviors in mill-annealed Ti-Fe-O alloy under dwell fatigue loading. First, constant stiffness measurement (CSM) nanoindentation tests and dislocation mechanism-based crystal plasticity finite element simulations are performed to identify the elastoplastic parameters of the β phase. The data of the α phase are also calibrated via a series of macroscopic mechanical tests. Then, based on the examination of the dwell fatigue failure modes, a polycrystalline aggregate model is established using Voronoi tessellation to investigate the stress redistribution procedure in the hard-soft grain combination containing the intergranular β lath. A geometrical compatibility factor is employed to link the dislocation pile-ups at the α/β interfaces and stress redistribution in terms of the resistance against slip transfer. On the basis of the proposed relationship and analysis of crystallographic orientation in Ti-Fe-O alloy, the influence of β lath thickness on the dwell fatigue sensitivity and two load-dependent competing crack initiation modes are discussed.

5.2 Nanoindentation technique

Illustration of nanoindentation test and typical load-displacement curves are shown in Fig. 5.1. The diamond probe with a sharp tip (e.g., Berkovich indenter, Conical indenter) is used to indent the surface of a sample. The load applied to the tip and the displacement of penetration are subsequently measured during the load and unload processes. To calculate the indentation hardness and Young's modulus of materials, Oliver and Pharr [129],[130] used a power-law formula to fit the obtained load-displacement curves,

$$P = Ch^2 \tag{5.1}$$

where C is an empirical parameter obtained from the power-law equation, h is the indentation depth corresponding to load P.

The contact depth h_c can be calculated from the maximum depth h_{max} and maximum load P_{max} by using the following equation

$$h_c = h_{max} - e\frac{P_{max}}{S} \tag{5.2}$$

where e is a geometry-dependent parameter. For a Berkovich indenter, $e = 0.75$. For a Conical indenter, $e = 0.72$. Stiffness, S, is given by

$$S = \left.\frac{dP}{dh}\right|_{h=h_{max}} \tag{5.3}$$

The indentation hardness H is calculated as

$$H = \frac{P_{max}}{A_c} \tag{5.4}$$

where A_c is the contact area that can be estimated as below for an ideal Berkovich indenter

$$A_c = 3\sqrt{3}h_c^2 tan^2(65.3°) \approx 24.56h_c^2 \tag{5.5}$$

The reduced elastic modulus E_r is calculated from stiffness S and contact area A_c as

$$E_r = \frac{\sqrt{\pi}}{2\lambda}\frac{S}{\sqrt{A_c}} \tag{5.6}$$

where λ is also a geometry-related parameter. For Berkovich indenter, $\chi = 1.034$. For Conical indenter, $\chi = 1$. The Young's modulus of the material is derived from the relation

$$\frac{1}{E_r} = \left(\frac{1-v^2}{E} - \frac{1-v_i^2}{E_i}\right) \tag{5.7}$$

where v and E are Poisson's ratio and Young's modulus of the sample, respectively. v_i and E_i denote the counterparts of the indenter, respectively. For diamond indenter, the elastic modulus and Poisson's ratio are 1141 GPa and 0.07.

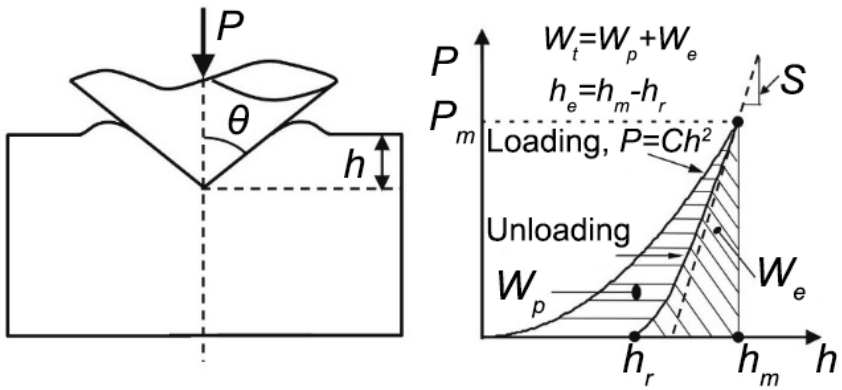

Fig. 5.1 Schematic diagram of nanoindentation test.

5.3 Experimental procedure

5.3.1 Material

The main chemical compositions of the tested near- α Ti-Fe-O alloy (Nippon Steel Corporation) are as follows: 0.994 Fe, 0.386 O, 0.003 N, 0.003C, 0.0005 H, and balance of Ti in mass% [131]. In this alloy, O and Fe are respectively used as α and β stabilizers for strength improvement, cost reduction, and grain size control. The Ti-Fe-O alloy was double-melted in vacuum arc remelting, forged (1273 K heating), and hot-rolled (1123 K heating) along the rolling direction (RD) to an 80-mm-thick plate. The 80-mm-thick plate was cross-rolled (1123 K heating) along the transverse direction (TD) to a 33-mm-thick plate. Thereafter, the plate was annealed at 1023 K for 1 h, and subsequently air-cooled. This thermomechanical processing route resulted in a typical mill-annealed microstructure containing primary α grains (light region) with a certain elongation along RD and transformed β phase (dark region) at the α grain boundaries, as shown in Fig. 5.1(a) and (b). The average size of the primary α grain shrinks to 35 μm in diameter as the addition of Fe accelerates heterogeneous grain nucleation. According to Fig. 5.1(b), the thickness of β lath approximately ranges from 0.5 μm to 2 μm.

A sample with dimensions of 10 mm × 5 mm × 1 mm was prepared for nanoindentation tests. In addition, flat dog-bone specimens with gauge sections of 30 mm long, 5 mm wide, and 2 mm thick were machined parallel to RD for quasi-static tensile, stress relaxation, and dwell fatigue tests at the specimen level.

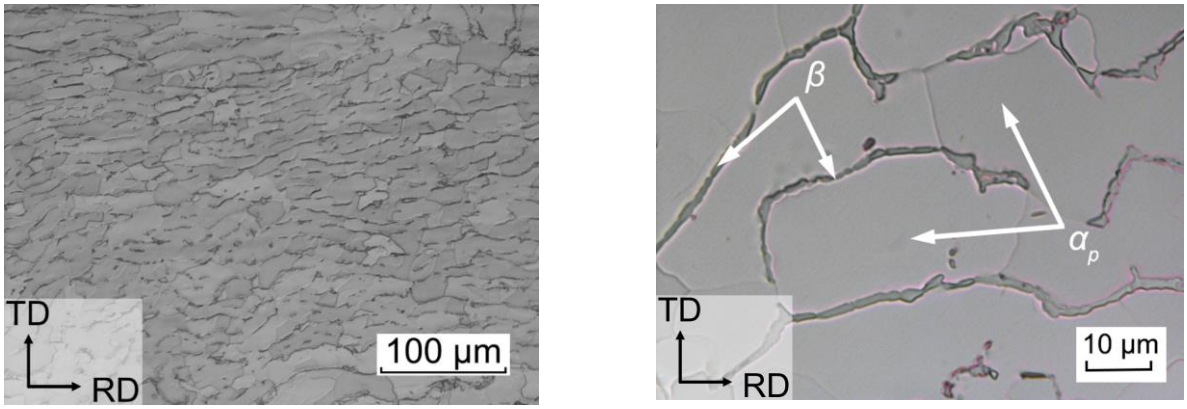

(a) (b)

Fig. 5.2 (a) Optical microstructure of Ti-Fe-O alloy on the ND plane, (b) intergranular β phase at primary α (α_p) grain boundaries.

Before mechanical tests, the specimens were mechanically and electrolytically polished. The procedure is the same as that in Section 4.2.2. EBSD measurements were then conducted using a JEOL JSM-7100F SEM with a step size of 0.5 μm, and raw data were also analyzed using the TSL OIM analysis 7 software and MTEX-5.7.0 toolbox in MATLAB.

5.3.2 Mechanical tests

Elucidating the effect of the β phase necessitates the calibration of its elastoplastic properties such as elastic stiffness constants and CRSS. The small volume fraction of the β phase in near-α and $\alpha + \beta$ titanium alloys makes it difficult to extract these datasets from bulk materials. Consequently, micro-scale mechanical tests such as nanoindentation and micro-pillar test were developed for accurate measurements in individual phases [132],[133],[134]. In this thesis, nanoindentation tests were applied and conducted using Hysitron Ti-750 TriboIndenter equipped with a Berkovich diamond indenter. The loading/unloading procedures comprised three stages: displacement-controlled loading to a maximum depth of 250 nm using the CSM method, 10 s holding, and 20 s unloading. The indentation strain rate $\dot{\varepsilon}$ in the CSM method is expressed as follows [135]

$$\dot{\varepsilon} = \frac{\dot{h}}{h} \approx \frac{1}{2}\frac{\dot{P}}{P} \tag{5.8}$$

where h and $\dot{h}$ are the displacement and corresponding rate, P and $\dot{P}$ are the indentation load and loading rate, respectively. To achieve a constant indentation strain rate, the following equation should be satisfied [136]

$$h = h_0 \exp(\dot{\varepsilon} t) \tag{5.9}$$

where h_0 is the initial displacement. The experimental indentation strain rates were set to $0.05\ \mathrm{s}^{-1}$ and $0.1\ \mathrm{s}^{-1}$ to investigate the SRS of the β phase, which is linked to the creep deformation during dwell fatigue.

The macroscopic responses of near-α and $\alpha + \beta$ titanium alloys are barely influenced by the minor β phase during deformation, therefore, macroscopic mechanical tests were performed to calibrate the crystal plasticity parameters of the α phase [6]. Quasi-static uniaxial tensile tests were performed on the same motor-driven tester under three strain rates ($8.3 \times 10^{-4}\ \mathrm{s}^{-1}, 8.3 \times 10^{-3}\ \mathrm{s}^{-1}, 8.3 \times 10^{-2}\ \mathrm{s}^{-1}$) to obtain stress-strain curves at 298 K, as the experiments in Chapter 4. Slip trace analysis was

implemented on one specimen tested at the strain rate of 8.3×10^{-4} s^{-1} to identify the operating slip and twinning systems in the α phase and determine the CRSS relationships. In this procedure, the active slip trace was designated as the slip system with the highest global SF. In addition, the stress relaxation test, which interrupted the tensile tests at 540 MPa by a 300 s stress relaxation period followed by unloading, was also carried out to further calibrate the SRS parameters of the α phase.

Load-controlled dwell fatigue tests were carried out at room temperature (298 K). The dwell fatigue load was applied in a trapezoidal waveform with a loading/unloading time of 1 s and dwell times of 120 s and 600 s at the peak stress of 602 MPa ($0.95\sigma_y$ at the strain rate of $8.3 \times 10^{-4}s^{-1}$). Besides, dwell fatigue test at a low stress of 538 MPa ($0.85\sigma_y$ at the strain rate of $8.3 \times 10^{-4}s^{-1}$) with a dwell time of 120 s was also implemented to investigate the effect of stress level on the fatigue crack initiation behavior. The stress ratio R of all tests was set to 0.01.

5.4 Finite element simulation

The grain size distribution, grain boundary misorientation angle distribution, and crystallographic orientations for the α phase of Ti-Fe-O alloy, as given in Fig. 5.3(a)-(c), are obtained from EBSD measurement and imported into an open-source software Dream.3D [137] to generate a cuboidal RVE comprising 147 globular α grains, as shown in Fig. 4.3(d).

Considering the effect of the β phase on the macroscopic responses can be neglected due to the limited volume fraction (~8%), the pure α phase RVE model is used to produce numerical stress-strain and stress relaxation curves [124]. The RVE is meshed by 32768 C3D8 fully integrated solid elements. The *x*, *y,* and *z* directions represent the TD, RD, and ND, respectively. Uniform displacement is imposed along the RD.

A three-dimensional model, which consisted of a single crystal with dimensions of 5 μm × 5 μm × 3 μm and a rigid Berkovich indenter with a sharp tip, is constructed for nanoindentation simulation, as shown in Fig. 5.4. The single crystal and indenter are meshed by 26944 C3D8 elements and 180 R3D4 discrete rigid elements, respectively. All freedoms of the bottom surface are fixed, and the contact surface is assumed to be frictionless [138]. It has to be mentioned that the crystal orientation is assigned as the average value of original orientations in a grain.

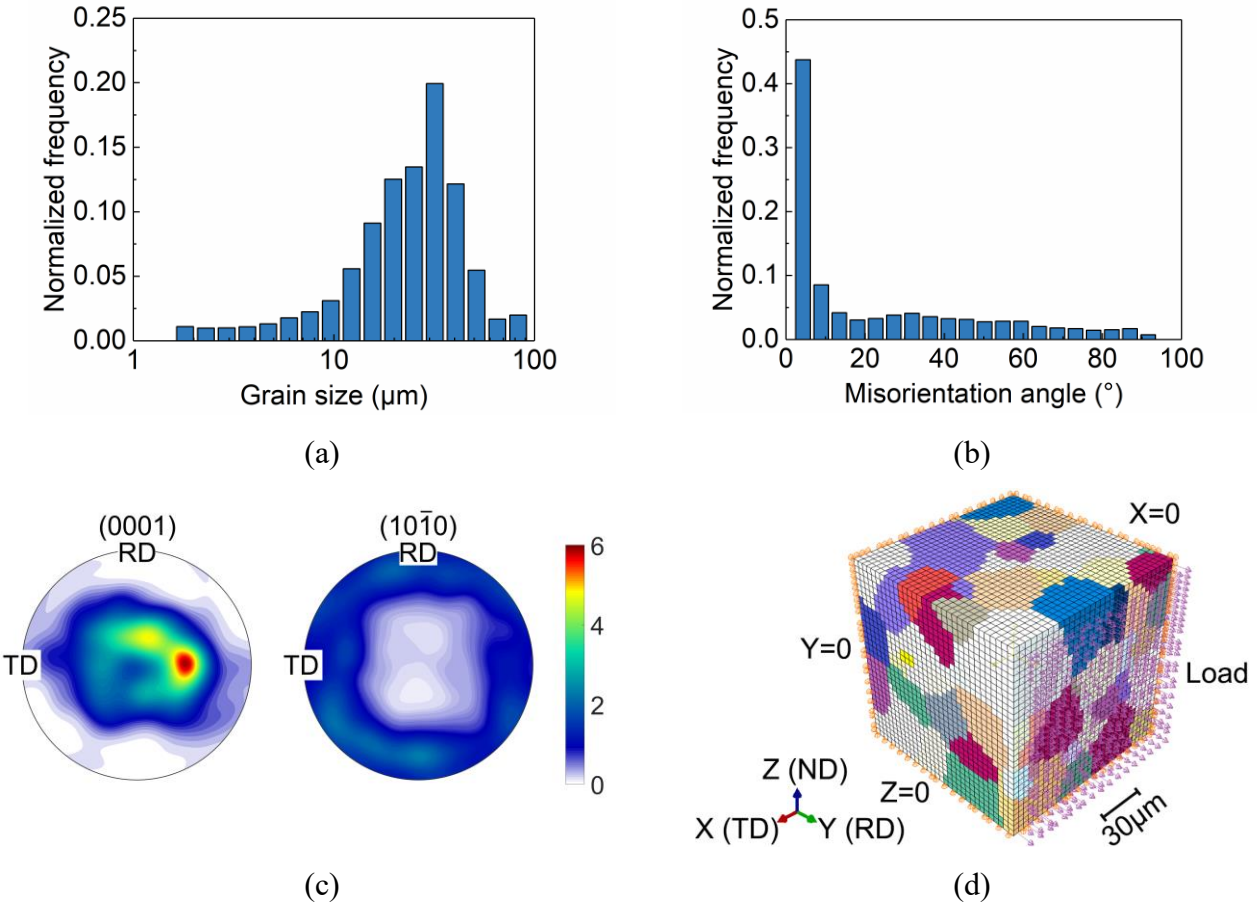

Fig. 5.3 (a) Grain size distribution, (b) grain boundary misorientation distribution, (c) pole figure of the α phase in Ti-Fe-O alloy and (d) resulting representative volume element.

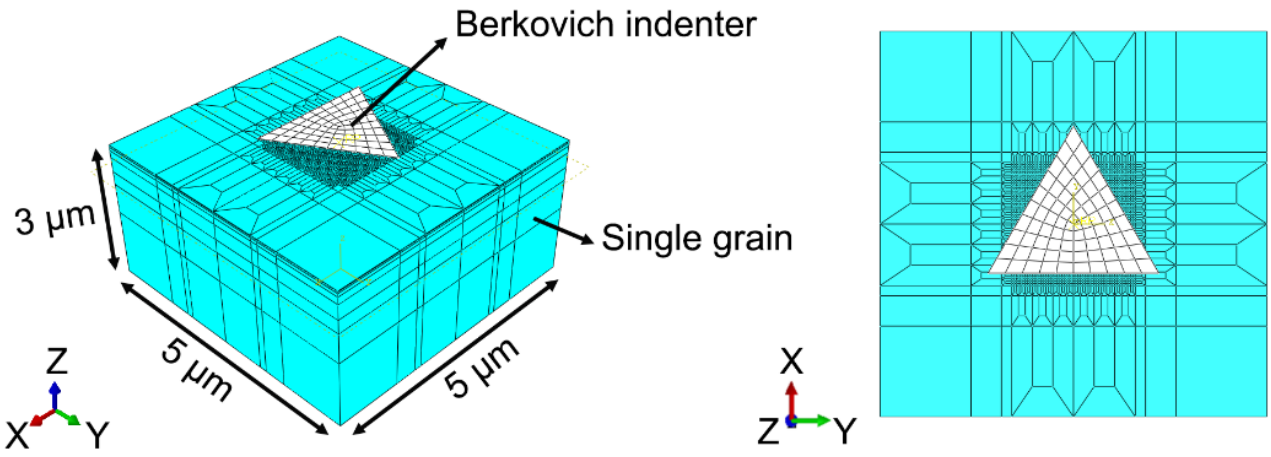

Fig. 5.4 Nanoindentation finite element model.

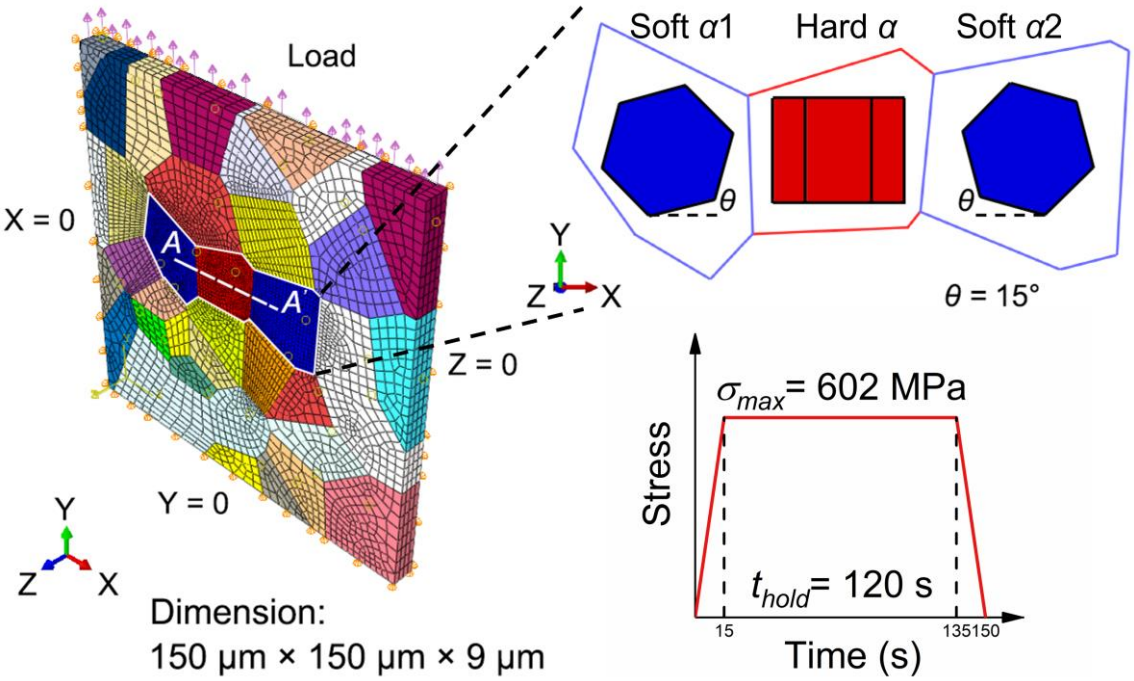

Fig. 5.5 Polycrystalline aggregate model with a hard-soft grain combination at the center region, and corresponding loading condition.

A quasi-3D polycrystalline aggregate model (the grain morphology is the same as Fig. 4. 18) is extruded from 2D Voronoi tessellation to study the stress redistribution between hard and soft grains during dwell fatigue, as shown in Fig. 5.5. The basic model is meshed by 15740 C3D8 elements, and the element size is refined within a hard-soft grain combination in the central area. Soft grains with prismatic SF of 0.5 ($\theta = 15°$) can result in the most severe condition for facet nucleation [139]. The crystalline orientations of the surrounding grains are randomly generated. The normal displacements of the left, bottom, and back surfaces are fixed to eliminate rigid body movements. A dwell fatigue cycle is applied on the top surface with a maximum stress of 602 MPa and a hold time of 120 s. Based on this pure α polycrystalline model, β laths with two thicknesses are explicitly inserted into the hard-soft grain boundary to investigate the effect of the β phase on the stress redistribution during the stress-dwell period, as shown in Fig. 5.6. The thickness of the β lath in Fig. 5.6(a) is 1.8 μm, which is near the upper limit of the thickness range in Fig. 5.1(b), while the thin β lath with thickness of 0.75 μm in Fig. 5.6(b) is close to the lower limit.

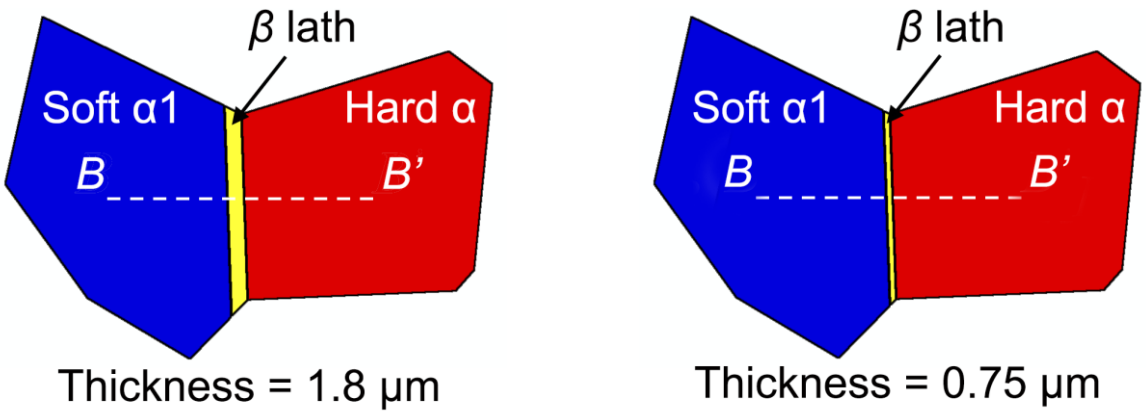

(a) (b)

Fig. 5.6 Intergranular β lath between soft and hard α grains with thicknesses of (a) 1.8 μm, and (b) 0.75 μm.

5.5 Parameter identification

To numerically reproduce the experimental results, the crystal plasticity parameters of the α and β phases should be calibrated. The anisotropic elastic stiffness matrix of the α phase is referred to Kim et al. [14], the same as the CP-Ti in Chapter 3. Since the elastic anisotropy of β phase varies dramatically due to different compositions, the isotropic elastic β phase is assumed in this study. The Young's modulus of β phase is measured by nanoindentation tests using the method in Section 5.2, Poisson's ratio is set to be 0.34.

Concerning the parameters related to the SRS property, the mobile dislocation density ρ_m, Burgers vector b^i, and Debye frequency ν_D are also referred to Cuddihy et al. [79], whereas the activation energy ΔF and activation volume ΔV are determined via calibration. For the α phase in Ti-Fe-O alloy, the CRSS relationships in the Ti-O system are applied since no Fe is observed within the α phase according to our previous energy-dispersive X-ray spectroscopy (EDS) chemical microanalysis [140]. For the Ti-O system, prismatic slip is generally recognized as the most active slip system. By contrast, the CRSS value of basal slip is the highest [122]. $CRSS_{pyramidal<a>}/CRSS_{prismatic}$ decreases with increasing oxygen content in light of the slip trace analysis conducted by Morita et al. [110]. Thus, $CRSS_{pyramidal<a>}/CRSS_{prismatic}$ in Ti-Fe-O alloy can be extrapolated from this relationship. Similarly, pyramidal <*c*+*a*> slip can also be promoted with the addition of oxygen to achieve homogeneous deformation along the *c*-axis as substitutions of deformation twinning [56]. Based on previous studies, the CRSS rank of the α phase in ascending order is prismatic, pyramidal <*a*>,

pyramidal <*c*+*a*> and basal slip. In addition, given the fact that atomic size difference between Fe and Ti enables substantial solution strengthening, the slip strength of β phase in Ti-Fe-O alloy is assumed to be higher than that of prismatic slip in the α phase [141],[142]. The slip-dependent strain-hardening parameters are calibrated using the curve-fitting method.

The crystal plasticity parameters for the α and β phases are summarized in Tables 5.1 and 5.2. The activation energy ΔF and activation volume ΔV are smaller for the β phase than those of the α phase. This trend is similar to the results of Zhang et al. [134] and implies that the β phase is more rate sensitive than the α phase. The CRSS ratio of the α phase is 1: 1.67: 2.5: 2.5: 3 for the prismatic: pyramidal <*a*>: 1st pyramidal <*c*+*a*>: 2nd pyramidal <*c*+*a*>: basal slip systems. The CRSS ratio of $< 111 >$ slip to prismatic slip is 1.4. Besides, the latent hardening constant in Eq. (3.17) is assumed to be $q = 1$ for all slip systems, and the empirical coefficient α_T in Eq. (3.19) is set to 0.7 [143].

Table 5.1 Rate-sensitive and strain gradient parameters for the Ti-Fe-O alloy.

Parameters		α phase	β phase
Rate sensitivity	ρ_m (μm^{-2})	5	
	υ_D (Hz)	1×10^{11}	
	k (J/K)	1.38×10^{-23}	
	b (μm)	0.295 (<*a*> slip) 0.468 (<*c*+*a*> slip)	0.332
	ΔF (eV)	0.5194	0.4758
	ΔV	$14.97b^3$	$3.56b^3$
Strain gradient	α_T	0.7	
	G (MPa)	44230	

Table 5.2 CRSS and strain-hardening parameters for slip systems, in MPa.

	α phase					β phase
	Basal <*a*>	Prism <*a*>	Pyramidal <*a*>	1st Pyramidal <*c*+*a*>	2nd Pyramidal <*c*+*a*>	⟨111⟩
h_0	500	150	150	450	450	300
τ_∞	850	328	570	718	718	455
τ_0	636	212	354	530	530	297

5.6 Macroscopic and microscopic responses

The results of quasi-static tensile, stress relaxation tests, and accompanying crystal plasticity simulations are plotted in Fig. 5.7(a) and (b). The responses of the RVE model closely match the experimental results. The macroscopic yield strength and ultimate tensile strength of the tested Ti-Fe-O alloy is lower than those of Ti-6Al-4V and Ti-6242 at room temperature. Thus, the prismatic CRSS value of the α phase in Ti-Fe-O alloy is relatively small.

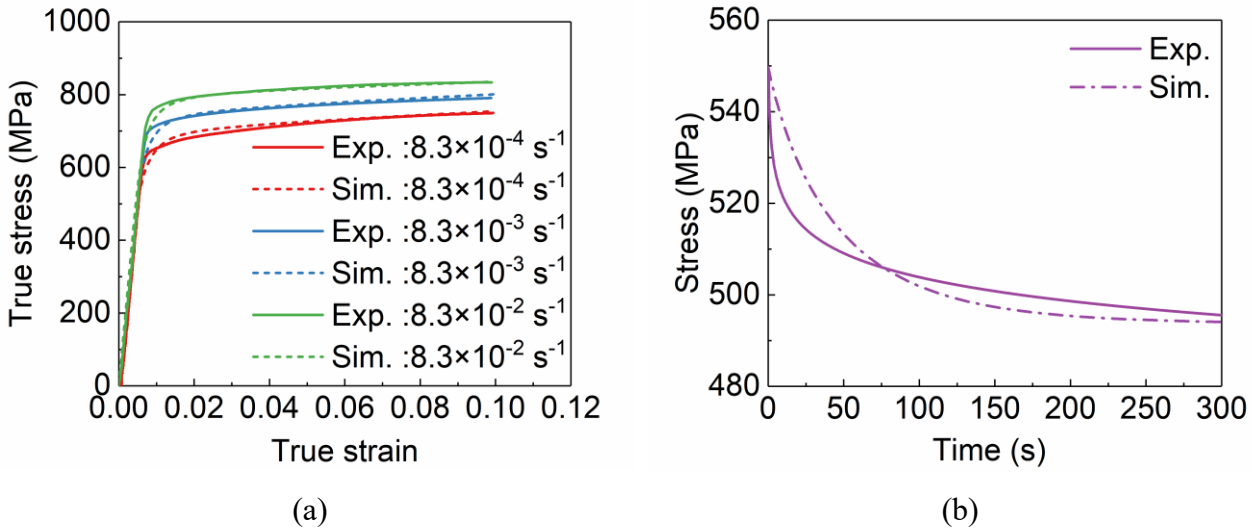

(a) (b)

Fig. 5.7 Macroscopic responses obtained from (a) tensile, (b) stress relaxation tests.

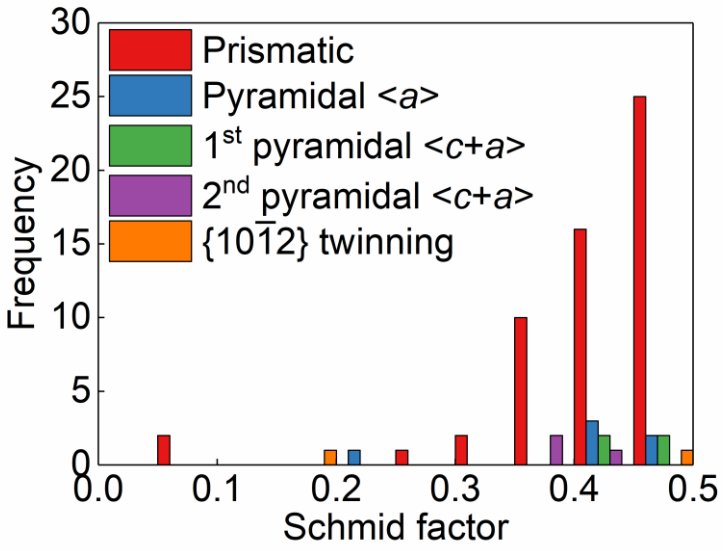

Fig. 5.8 Histogram of the Schmid factor distribution of different deformation modes in α phase at 3% strain.

Furthermore, the quantitative analysis of slip trace in α phase is given in Fig. 4.8. The results indicate that plastic deformation is dominated by prismatic slip, followed by pyramidal <*a*> slip, pyramidal <*c*+*a*> slips, and negligible {$10\bar{1}2$} tension twinning, whereas basal slip is not observed. Hence, the identification of the CRSS relationship is validated to be reasonable. In addition, although the <*a*>-basal dislocation pile-ups in soft grains is reported to generate more stress redistribution than <*a*>-prismatic dislocation in Ti-6242, the current work only focuses on the latter since the nucleation of <*a*>-basal dislocation in Ti-Fe-O alloy is difficult, as shown in Fig. 5.8 [144].

The SEM images and relevant inverse pole figure (IPF) maps for two β ($\beta1$ and $\beta2$) and neighboring α grains after nanoindentation tests, together with corresponding experimental and numerical load-displacement curves, are plotted in Fig. 5.9. Two β grains with relatively coarse sizes are selected to ensure the experimental results can precisely reflect the intrinsic properties of the β phase without the influence of surrounding α/β grain boundaries. Grain $\beta1$ is used to calibrate the parameters of the β phase and validation is carried out on grain $\beta2$. Six indentations are numbered from 1 to 6. Among those, indentations 1 (3) and 2 (4) are tested on the two β grains at indentation strain rates of 0.05 s^{-1} and 0.1 s^{-1}, respectively. Indentations 5 and 6 are tested on the soft α grain. The load-displacement curves of the β phase obtained from the nanoindentation tests are faithfully reproduced by numerical computations, as shown in Fig. 8(a) and (b). Although the single crystal finite

element model cannot precisely reflect the local grain morphology, the distances from indentations to grain boundary are sufficiently large such that the influence of grain boundary on load-displacement curves is trivial [145]. The mean Young's modulus of the β phase is measured to be 98 GPa since the interaction of Fe with interstitial O, referred to Snoek effect, can pronouncedly increase the elastic stiffness [141]. According to the micro-pillar compression tests and crystal plasticity modeling conducted by Zhang et al. [134], a thickness difference had little effect on the slip properties of the β phase within $\alpha + \beta$ colonies. Kapoor et al. [146] also carried out high energy X-ray diffraction (HEXD) experiment and CPFE simulation to obtain a set of CPFE parameters independent of β phase volume for Ti-6Al-4V alloy with bi-modal and globular microstructures. Therefore, the effect of size on intrinsic properties of the β phase is insignificant within a few microns and the calibrated parameters are considered to be adequate for thin intergranular β phase, as the β laths modeled in the polycrystalline aggregate model (Fig. 5.6).

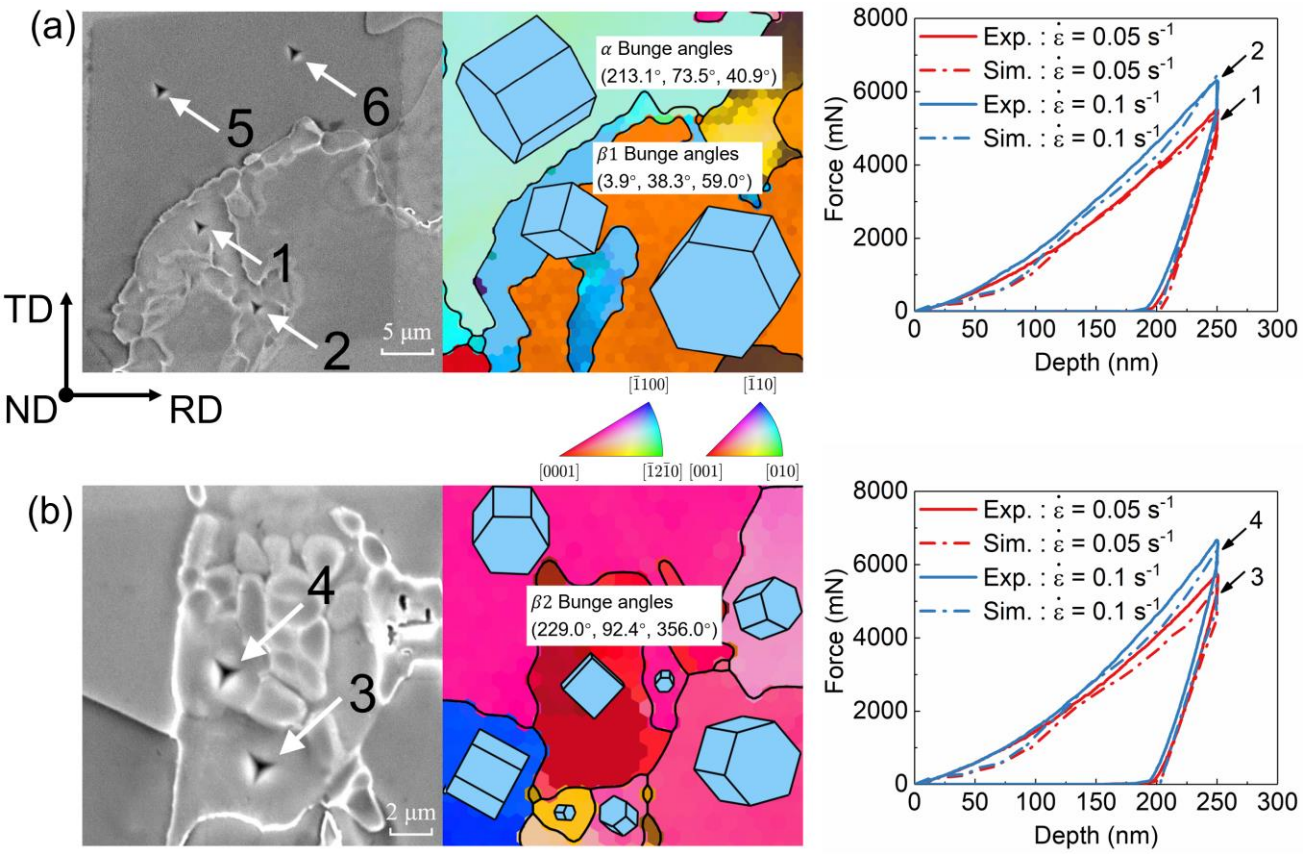

Fig. 5.9 SEM micrographs with indentations, related IPF maps of ND, and load-displacement curves for nanoindentations of (a) grain $\beta 1$, (b) grain $\beta 2$.

Moreover, the load-displacement curves obtained by nanoindentation tests on the soft α grain (Fig. 5.8(a)) are also predicted by simulations with a sound accuracy, as shown in Fig. 5.10, which demonstrates that the material parameters of the α phase calibrated by macroscopic responses are reasonable.

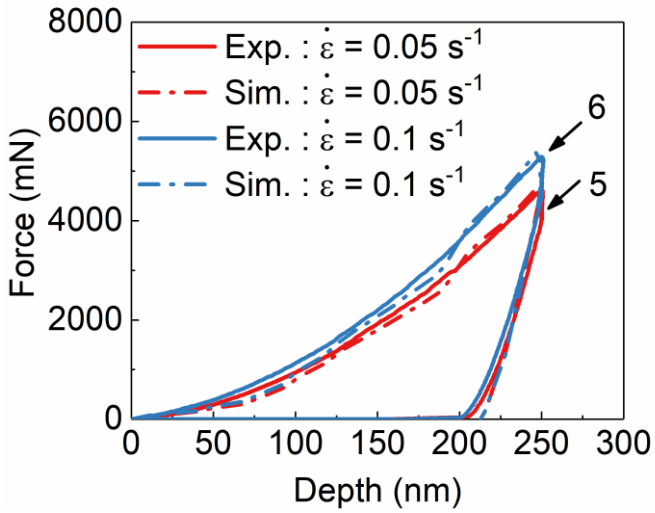

Fig. 5.10 Load-displacement curves for nanoindentation of the soft α grain shown in Fig. 5.9(a).

5.7 Fatigue life and crack initiation mode

The comparison of the results between dwell fatigue tests with a dwell time of 120 s and normal cyclic fatigue tests are summarized in Fig. 5.11(a) [147]. Conspicuous reduced lives can be seen under dwell fatigue loading. The dwell fatigue life debit increases from 13.8 at $\sigma_{max} = 538$ MPa to around 30 at $\sigma_{max} = 602$ MPa. This trend is identical to previous experimental results that dwell fatigue life debit increases with increasing stress levels [23]. Besides, as the dwell time increases from 120 s to 600 s at $\sigma_{max} = 602$ MPa, the dwell fatigue life debit smoothly increases from 30 to 41, as shown in Fig. 5.11(b). Therefore, the saturated dwell time of Ti-Fe-O alloy is assumed to be equal to or less than 120 s at the stress level of $0.95\sigma_{0.2}$ [10].

The fracture surface of the failed sample under $\sigma_{max} = 538$ MPa is illustrated in Fig. 5.12(a) and (b). The subsurface crack initiation site is about 40 μm from the surface and demonstrates a planar facet. Moreover, a large number of subsurface cavities are observed to form in the intergranular β laths of the failed sample under $\sigma_{max} = 602$ MPa, as shown in Fig. 5.13(a)-(d). It should be mentioned that

although the two hard α grains are respectively tilted 53° (Fig. 5.13(b)) and 24° (Fig. 5.13(d)) from loading direction and result in high basal SF, the onset of plastic slip is still difficult concerning the high CRSS of basal slip and low prismatic SF. According to Fig. 5.13(a) and (c), both quasi-crack cavities (C1 and C5) are within the hard-soft grain combination and nearly perpendicular to the loading direction. In particular, only the cavities (C1, C5) initiated in the intergranular β laths of hard-soft grain combination can propagate into neighboring α grains and form a quasi-microcrack, while the nucleated cavities (C3, C4, C6, and C7) in intergranular β laths sandwiched between two soft α grains cannot break the α/β interface and grow along the direction normal to the external load. Therefore, the intergranular β phase is likely to play an important role in dwell fatigue behavior at high stress state and the influence will be discussed in the following sections.

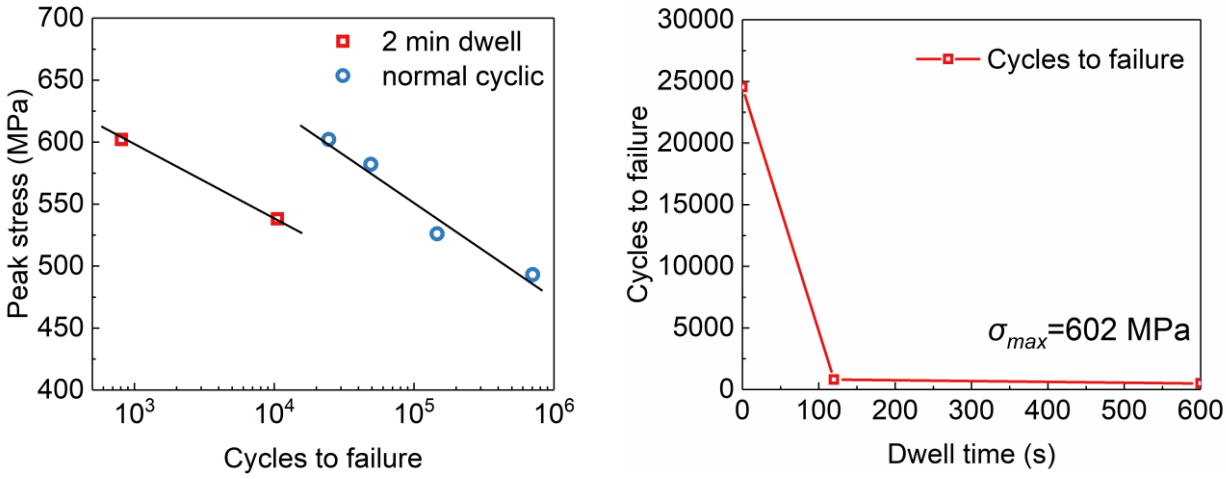

Fig. 5.11 (a) Fatigue experimental results of dwell fatigue tests and normal cyclic fatigue tests. The normal cyclic fatigue life data can be found in [147], (b) relationship between cycles to failure and dwell time.

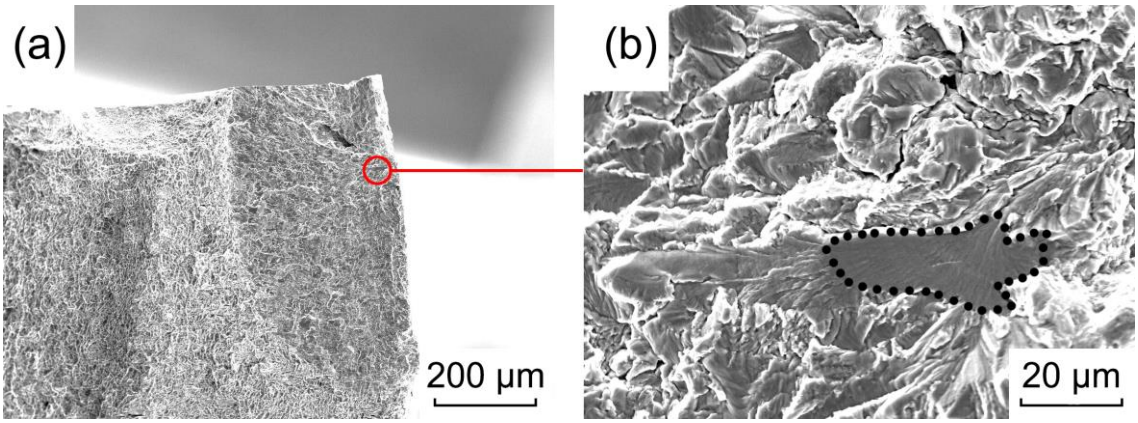

Fig. 5.12 Fracture surface of the failed sample at $\sigma_{max} = 538$ MPa: (a) low magnification (encircled region indicates the fatigue crack initiation site) (b) high magnification of crack initiation site with facet.

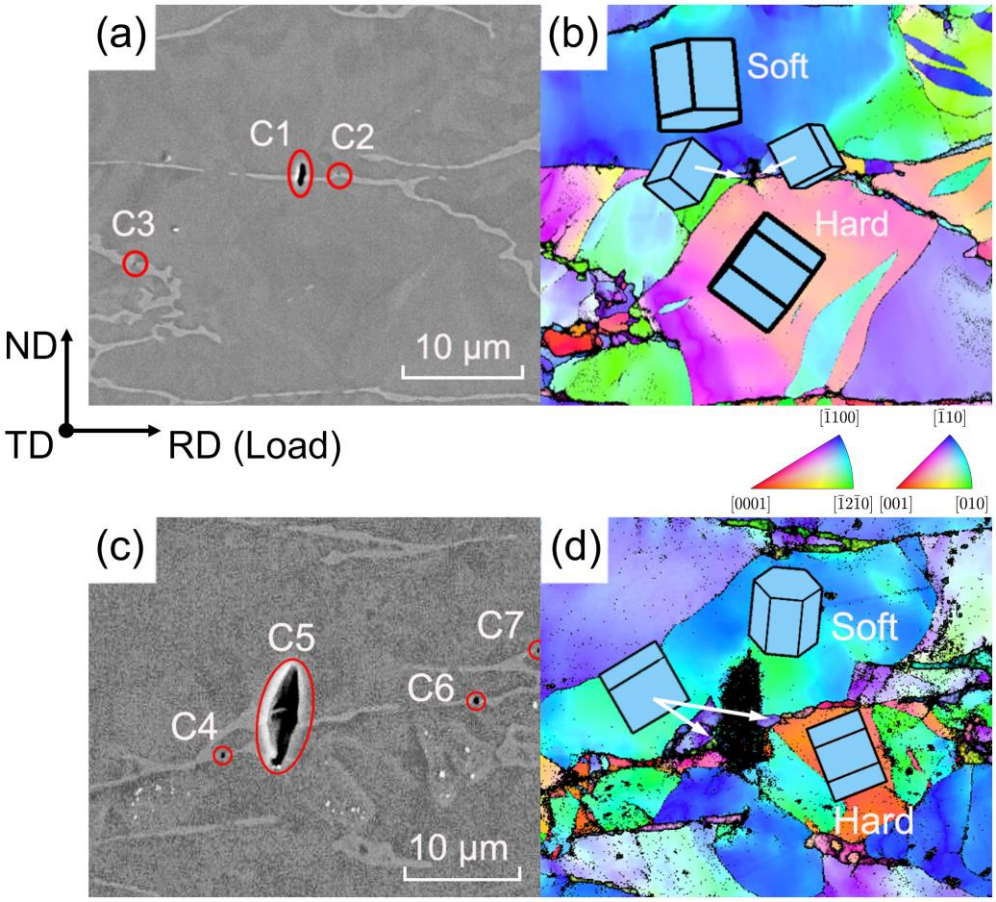

Fig. 5.13 Subsurface cavity nucleation in the intergranular β phase (light region) near two hard-soft grain combinations (dark region): (a) and (c) SEM images, encircled regions indicate the cavities, (b) and (d) corresponding IPF maps of RD.

5.8 Influence of intergranular β phase on dwell fatigue

Experimental studies in the literature generally adopt a dislocation pile-up model proposed by Stroh to explicate the basal facet nucleation under dwell fatigue loading [37]. This analytical model has been verified by crystal plasticity modeling of Hasija et al. [38], in which the cold creep of soft grains induces stress concentration at the hard-soft grain boundaries during the dwell time, as shown in the simulated stress σ_{yy} and strain ε_{yy} contours in Fig. 5.14(a) and (b). The increased grain boundary stress σ_{yy} at the dwell end in turn causes early quasi-cleavage fracture on the basal plane of the hard grain with normal parallel to the loading direction, as shown in Fig. 5.14(c). However, the intergranular β phase tends to alter the time-dependent dislocation pile-ups at soft-hard grain boundaries in consideration of the slip transfer at the α/β interface (Fig. 5.15(a)), especially for the globular α microstructure that demonstrates no exact orientation relationship between the α and β phases, as illustrated in Fig. 5.15(b). Thus, the effect of the intergranular β phase on the dwell fatigue behaviors of Ti-Fe-O alloy is numerically characterized in the following sections.

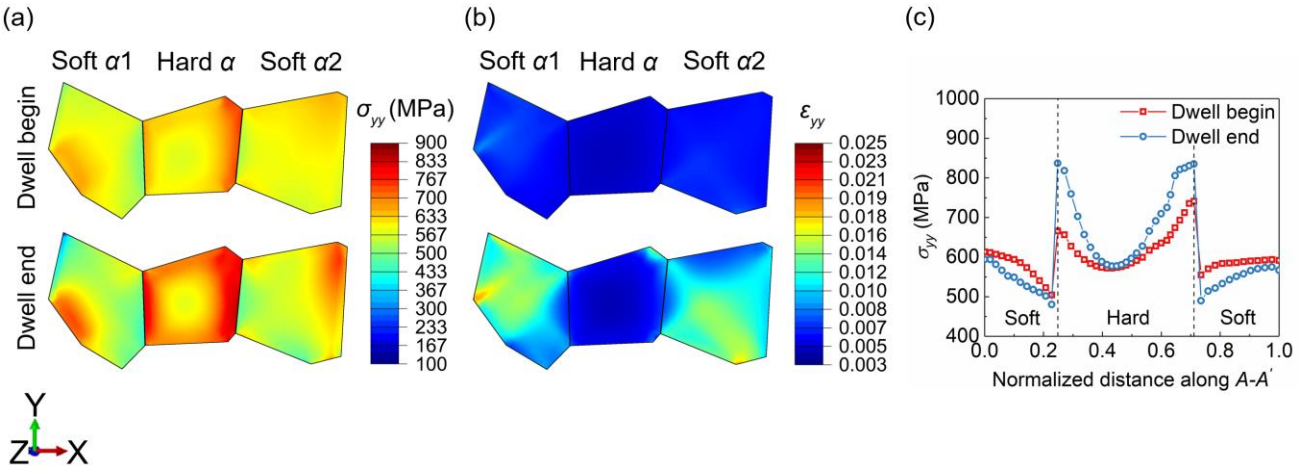

Fig. 5.14 Simulated (a) stress and (b) strain contours within the hard-soft grain combination at the beginning and end of the dwell time for the pure α model in Fig. 4, and (c) stress redistribution along the path $A - A'$.

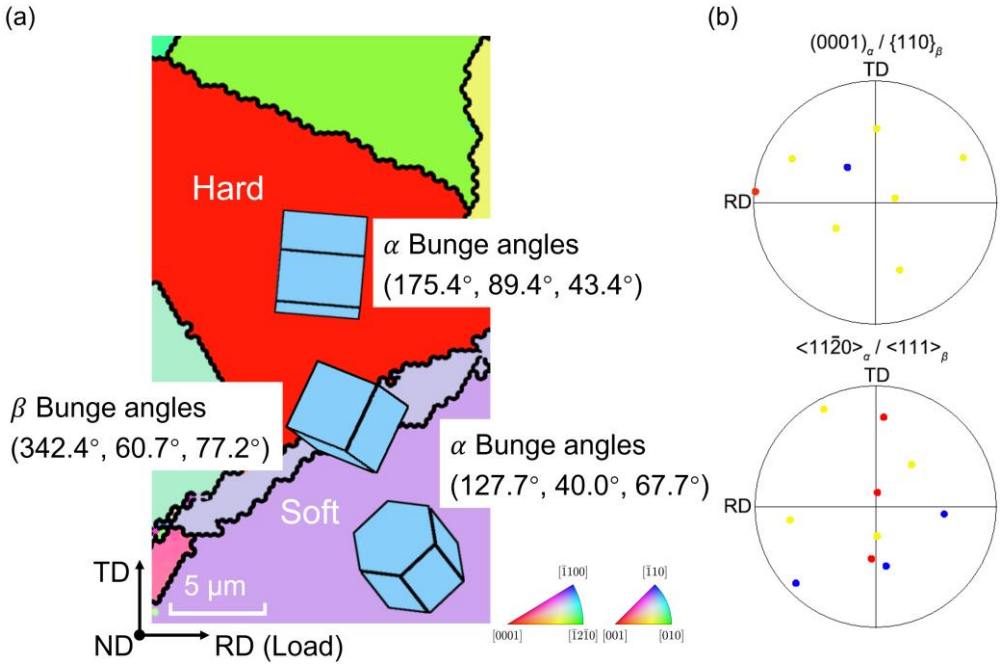

Fig. 5.15 (a) IPF map of the RD related to a hard-soft grain combination with the intergranular β lath in Ti-Fe-O alloy, (b) $(0001)_\alpha/\{110\}_\beta$ and $\langle 11\bar{2}0\rangle_\alpha/\langle 111\rangle_\beta$ pole figures of the hard-soft grain combination. Red, blue, and yellow dots represent the orientations for the hard α, soft α and intergranular β lath, respectively.

5.8.1 Slip transfer at the α/β interface

In previous research, various parameters have been proposed to assess the ease of slip transfer at grain boundaries. A geometrical compatibility factor m', developed by Luster and Morris [148], is repeatedly employed:

$$m' = cos\varphi \cdot cos\kappa \tag{5.10}$$

where φ is the angle between the normal factors of the incoming slip plane and the outgoing slip plane, κ is the angle between incoming and outgoing Burgers vectors, as shown in Fig. 5.16. The m' factor ranges from 0 to 1, and the larger the value of m' is, the easier slip can traverse grain boundaries. Besides, the slip transfer also requires a high resolved shear stress on the outgoing slip system.

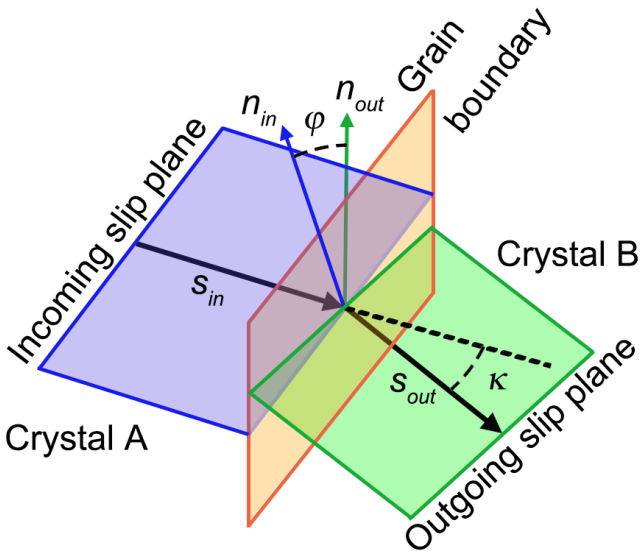

Fig. 5.16 Geometrical relationship of the slip transfer.

On the basis of the aforementioned discussions, five cases are embedded in the soft α-β-hard α grain combination with a thick β lath (Fig. 5.6(a)), as presented in Fig. 5.17. For all cases, the orientations of the soft and hard α grains remain constant, whereas different Bunge Euler angles are given to the sandwiched β lath. As a result, the m' factor, which represents the geometrical compatibility between the prismatic slip (SF=0.5) in soft α grain and the $< 111 >$ slip with the highest value of SF in the β lath, lies from 0.11 to 1. The maximum SF of the $< 111 >$ slip is set to 0.5 to ensure the occurrence of plastic shear in the β lath and the dominant position of the given slip system on creep deformation in the β lath. The influence of lattice rotation on the SF during creep deformation is ignored because the strain level is low. Concerning the narrow slip length in the β lath and high CRSS for the $< 111 >$ slip, the dislocations transmitted from soft α grain presumably dominate the dislocation pile-ups at hard α-β boundary rather than those nucleate in the β lath. Therefore, this study mainly focuses on the impact of slip transfer at the α/β interface (i.e., m' factor) on stress redistribution mechanisms, while the dislocation nucleated in β lath is ignored.

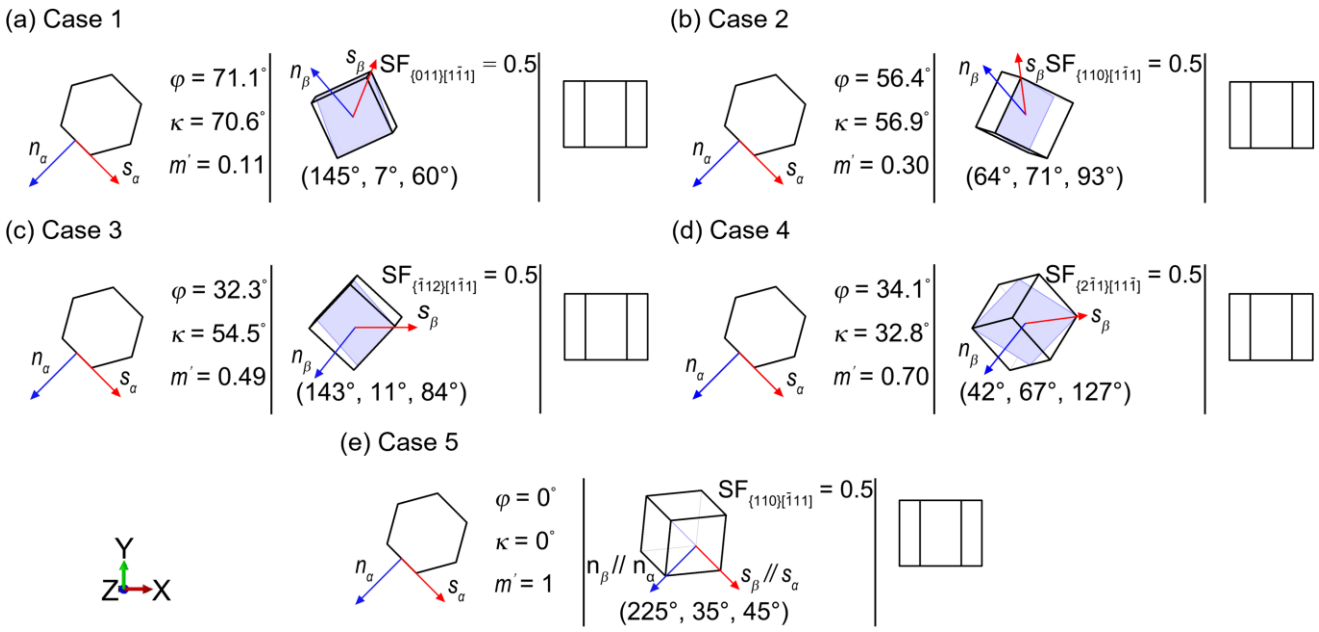

Fig. 5.17 (a-e) α-β-α grain pair with different orientation relationships. The m' factor represents geometrical compatibility between the prismatic slip (SF = 0.5) and $\langle 111 \rangle$ slip with the highest SF.

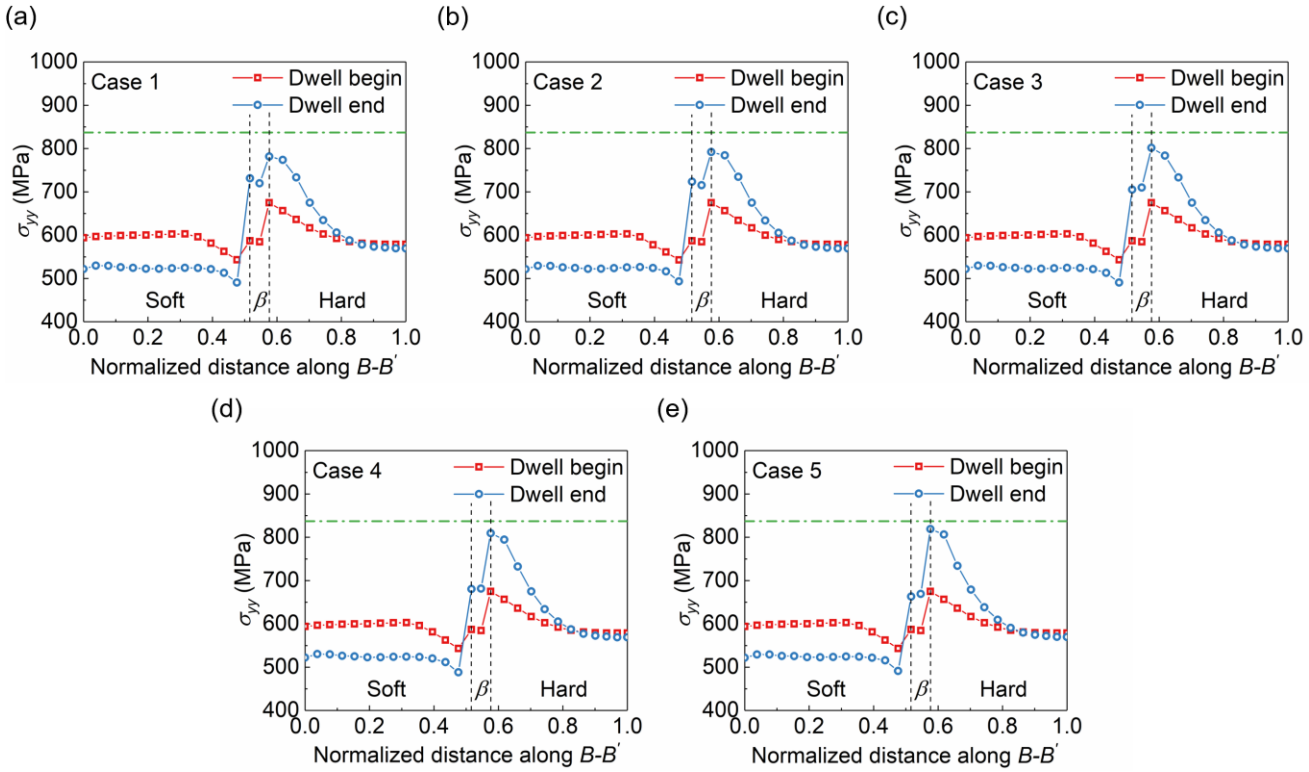

Fig. 5.18 (a-e) Stress redistribution along the path $B - B'$ for five cases with m' factor ranging from 0.11 to 1. The green dash-dotted line indicates the value of the peak stress after the stress dwell for the pure α structure.

The simulated results of stress redistribution along the path $B - B'$ are plotted in Fig. 5.18. The green dash-dotted line depicts the value of the peak stress after the stress dwell for the pure α structure. Compared to the results of the pure α structure, the stress distributions at the dwell beginning exhibit subtle differences for the five cases, however, the peak stress σ_{yy} in the hard α grain decreases at the dwell end since the insertion of the β lath can interrupt continuous slip, thereby reducing the dislocation pile-ups at the hard α-β boundary. By contrast, the rise of stress at the soft α-β boundary is notably greater at the dwell end than that at the dwell beginning. Zhang et al. [134] have reported similar stress differences in stress relaxation tests for Ti-6242 since the β phase is more rate sensitive than the α phase. However, the effect of the CRSS difference between the $< a >$ slip and $< 111 >$ slip on stress redistribution is ignored. Considering the CRSS of the $< 111 >$ slip in the β phase is higher than that of the prismatic slip in Ti-Fe-O alloy, the stress concentration in the β lath may also be attributed to dislocation pile-ups at grain boundaries when the slip transfers from low-CRSS slip systems to high-CRSS slip systems [149],[150]. Given that this CRSS relationship also exists in commercial titanium alloys such as Ti-6242, Ti-6Al-4V, and IM834, the stress redistribution between soft α grains and β laths is likely to emerge in a wide range of $\alpha + \beta$ titanium alloys with equiaxed microstructure [6].

In addition, the σ_{yy} at the soft α-β boundary reduces by 9.4% (from 731 MPa to 662 MPa) with greater m' factor, whereas the peak stress at the hard α-β boundary increases by 4.7% (from 782 MPa to 819 MPa), as shown in Fig. 5.19. As the m' factor increases, the resistance of slip transfer at the soft α-β boundary diminishes and the stress concentration in the β lath is inhibited due to lower dislocation pile-ups in adjacent soft α grain. Meanwhile, smoother slip transmission accelerates the dislocation pile-ups at the hard α-β boundary and promotes the stress change during the stress-hold period. It is also interesting to note that the change in peak stress σ_{yy} at the soft α-β boundary is more sensitive to the m' factor than that at the hard α-β boundary.

The abovementioned numerical results keep consistent with previous CPFE predictions reported by Hamid et al. [151] that slip transmission across grain boundaries is easier when the misorientation angle between adjacent grains is small. Additionally, the geometrical compatibility between the β lath and abutting soft α grain is confirmed to significantly affect the stress redistribution process during the dwell time. Therefore, the orientation relationship between the β lath and the two α neighbors in Ti-Fe-O alloy should be characterized. To this end, the angles between the slip plane normal (φ) and

slip direction (κ) of most active slip systems within 28 contiguous α/β grain pairs (i.e., 56 α/β grain boundaries) are counted in Fig. 5.20(a)-(c) via EBSD angular calculation. These statistics suggest that over 50% of the $\{10\bar{1}0\}_\alpha/\{110\}_\beta$ and $\{10\bar{1}0\}_\alpha/\{112\}_\beta$ planar misorientation angles exceed 60°. Likewise, 53% of the $\langle 11\bar{2}0\rangle_\alpha/\langle 111\rangle_\beta$ direction misorientation angles are greater than 60°. Due to that the prismatic and $\langle 111\rangle$ slips are respectively primary deformation modes in the α and β phase, these misorientation distributions are prone to result in α/β grain boundaries with low geometrical compatibility (low m' factor). These conditions resemble the description in case 1 (Fig. 5.17(a)), which promotes dislocation pile-ups at the α/β interfaces under dwell fatigue loading.

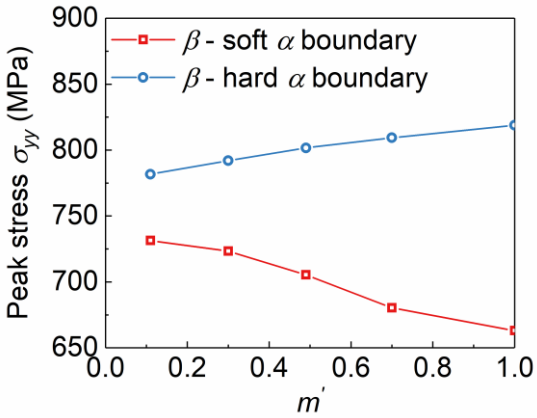

Fig. 5.19 Relationship between the peak stress and m' factor at dwell end.

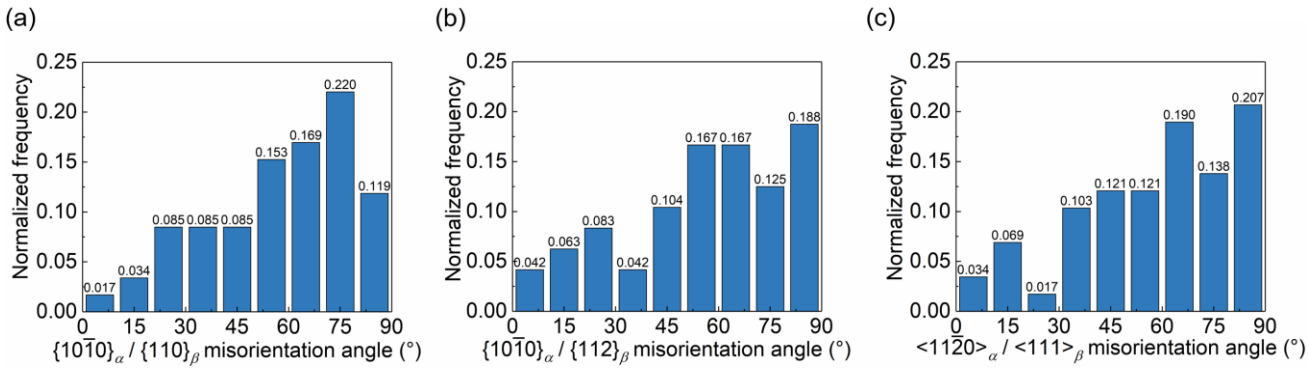

Fig. 5.20 Misorientation angle distribution between (a) $\{10\bar{1}0\}_\alpha$ and $\{110\}_\beta$ planes, (b) $\{10\bar{1}0\}_\alpha$ and $\{112\}_\beta$ planes, (c) $\langle 11\bar{2}0\rangle_\alpha$ and $\langle 111\rangle_\beta$ directions at α/β interfaces.

5.8.2 β lath thickness

The stress redistribution between hard primary α grains and soft basketweaves with different β lath thicknesses has been evaluated by Zhang et al. [49] and their results reveal that the β lath thickness plays a less important role in inhibiting mobile dislocations than multiple α variants. Motivated by the investigation concerning the morphological features, the influence of the intergranular β lath thickness on the stress redistribution is examined in this section utilizing models illustrated in Fig. 5.6.

In line with the EBSD measurement, the orientation relationship in case 1 (Fig. 5.17(a)) is adopted for the following simulations because it represents the most universal condition in Ti-Fe-O alloy. The stress redistribution process along the path $B - B'$ is plotted in Fig. 5.21(a) for the thin β lath. The magnitude of the stress change, $\Delta\sigma_{yy}$, is compared with counterparts of the thick β lath and pure α cases, as depicted in Fig. 5.21(b). The comparison reveals that the redistribution of stress from soft to hard α grain is more inhibited by the thick β lath since sliding dislocations can be halted by more pinning points and the dislocation pile-ups at the hard α-β boundary are reduced.

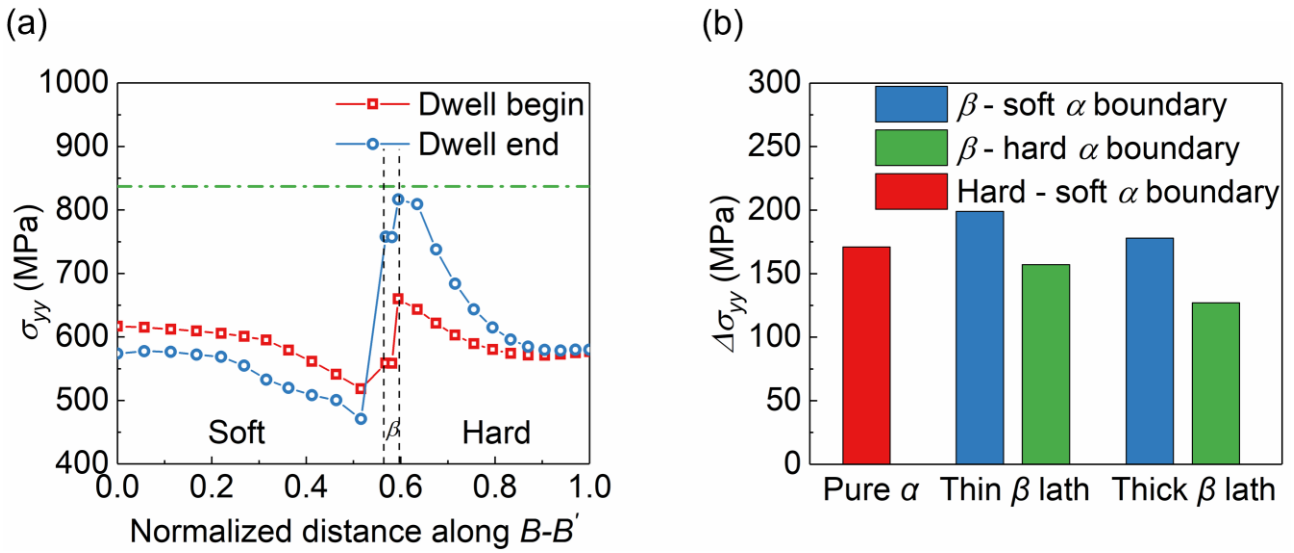

Fig. 5.21 (a) Stress redistribution along the path $B - B'$ for the thin lath, (b) histogram of the stress change at the grain boundaries for three microstructural morphologies. The green dash-dotted line indicates the value of the peak stress after the stress dwell for the pure α structure.

The peak stress at the soft α-β boundary is higher in the thin β lath than in the thick one, which may be attributed to the strong restriction of hard α grain upon the overall creep deformation of the thin β

lath, as shown in Fig. 5.22. The accumulated strain in the thick β lath is markedly larger than that in the thin one at the dwell end. The strain incompatibility between the soft α grain and β lath consequently generates higher grain boundary stress [152]. Additionally, the size-dependent effect with respect to GND accumulation is also involved in local hardening behaviors at a small scale (< 10μm) [88]. Thus, the effective density of GNDs along the path $B - B'$ after the dwell period is plotted in Fig. 5.23. The simulated results demonstrate the concentration of GNDs in the β lath, which is consistent with the predictions of Ashton et al. [46]. The decrease in the β lath thickness results in steeper strain gradient and higher effective density of GNDs. Since GNDs can act as obstacles that impede the motion of SSDs and cause work hardening at the grain boundaries, the stresses in the thin β lath and adjacent hard α grain increase from 731 MPa (781 MPa) to 758 MPa (816 MPa) compared to those in the thick one. It should be mentioned that lengthscale-dependent slip transfer mechanisms at the α/β interface have been reported in recent experimental study [150]. According to related observations, the slip from the α phase is inclined to transmit to the slip plane of the β phase that is almost parallel to the incoming plane when the β lath is relatively thin, whereas the slip tends to transfer to the slip system of the β phase with the highest SF when the β lath thickens. To describe the effect of this slip system selection mechanism on the dwell fatigue in $\alpha + \beta$ titanium alloys, a more integrated crystal plasticity modeling is required.

In summary, thick intergranular β laths can reduce the dwell fatigue sensitivity of $\alpha + \beta$ titanium alloys with globular microstructure. Therefore, the reduction of dwell fatigue life debit from Ti-6242 to Ti-6246 with equiaxed structure is not just connected with the disappearance of macrozones and smaller α grain size, the larger volume fraction of the β phase also plays a crucial role although a high Mo content in the α phase is insufficient to prevent vacancy diffusion induced by the cold creep of soft α grains [66].

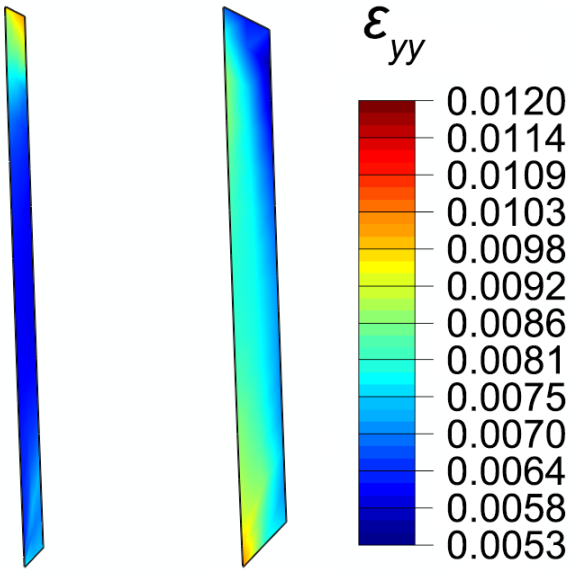

Fig. 5.22 Strain contours within two intergranular β laths at the dwell end.

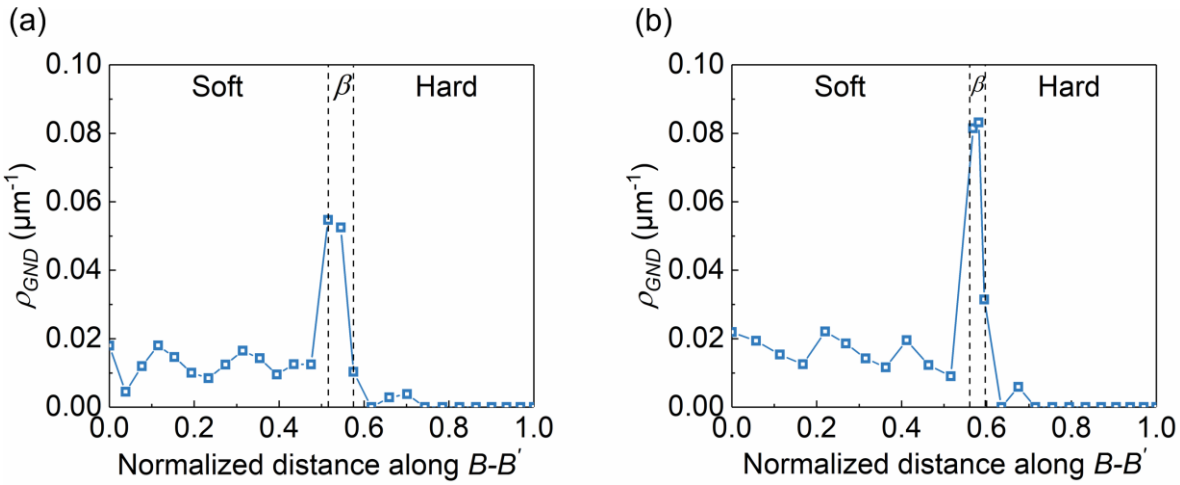

Fig. 5.23 Distribution of the effective density of GNDs along the path $B - B'$ at the dwell end for the (a) thick β lath, (b) thin β lath.

5.8.3 Maximum stress

In general, early nucleation of basal facets is widely accepted to cause a visible reduction in the time to fracture of titanium alloys under dwell fatigue loading. However, the dwell fatigue fracture mechanism has been reported to convert from facet nucleation to cavity nucleation and coalescence within $\alpha + \beta$ colonies in Ti-6242 when the maximum stress is comparatively high ($\sigma_{max} > 0.92\sigma_{0.2}$)

[153]. Cavity nucleation is induced by dislocation pile-ups at α/β interfaces even though the BOR relationship is satisfied in the $\alpha+\beta$ colonies. Similarly, the quasi-crack cavities within the β laths aligned in the loading direction have been identified in Ti-Fe-O alloy (Fig. 5.13) because of the low geometrical compatibility at the α/β interface, and more dislocation pile-ups induced by high $CRSS_{<111>}/CRSS_{prismatic}$ ratio . Inspired by prior works, the influence of the maximum stress on the micromechanical response of the intergranular β phase within a hard-soft grain combination is further studied.

Like the previous section, case 1 with a thick β lath is applied for the crystal plasticity simulation, whilst the maximum stress declines to 538 MPa ($0.85\sigma_{0.2}$ at the strain rate of 8.3×10^{-4} s^{-1}). Fig. 5.24 shows the stress redistribution along the path $B-B'$. Compared to the high stress condition, the stress change at the soft α-β boundary decreases from 178 MPa to 89 MPa. The stress increase at the hard α-β boundary drops from 127 MPa to 72 MPa. The peak stress at the soft α-β boundary is 89% of that in the hard α grain, which is smaller than the value (95%) at high stress level. The simulated result indicates that higher stress levels can induce more dislocation pile-ups and stress increase at the soft α-β boundary. The increased stress σ_{yy} contributes to the opening stress, which is required for the cavity nucleation in the intergranular β lath parallel to the principal load.

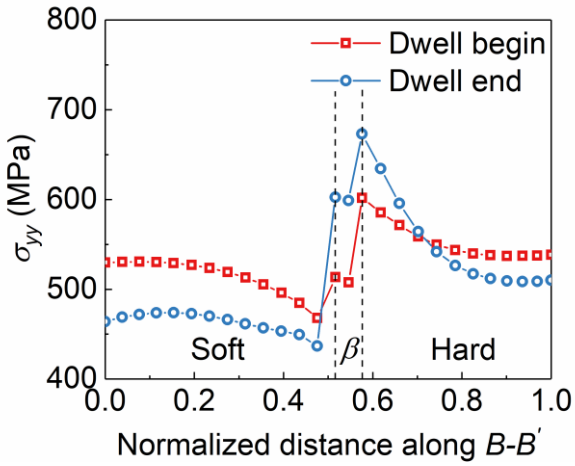

Fig. 5.24 Stress redistribution along the path $B-B'$ at a maximum stress level of 538 MPa.

Based on the aforementioned numerical predictions at high stress level, the competing mode for crack initiation from basal planes and cavities in the β lath should be considered to comprehensively

predict the dwell fatigue life of not only near- α Ti-Fe-O alloy but α/β titanium alloy with globular structure. For crack initiation from basal facets, the relationship between a proposed effective traction on the basal plane and dislocation density evolution at the soft-hard grain boundary has been constructed to predict the facet nucleation life in an equiaxed structure Ti-6242 alloy [155]. As for the initiation of cracks from cavities in the β lath, the number of dislocations has been adopted as a fatigue indicator parameter (FIP) to predict the cavity nucleation in Ti-6242 alloy with lamellar structure using discrete dislocation dynamics, but the opening stress is not taken into consideration [153]. Following our predicted stress distribution at the dwell end, the opening stress for cavity nucleation in β lath is closer to the peak stress in hard α grain at high stress level. To precisely predict the dwell fatigue crack initiation life for Ti-Fe-O alloy, deduction of a unified FIP available for predicting facet/cavity nucleation and further experimental validation should be carried out to characterize the competing failure modes in the future.

5.9 Summary

The influence of phase on local deformation in the globular grain structure of Ti-Fe-O alloy during dwell fatigue loading is comprehensively studied in this chapter.. The results are summarized as follows:

1. The crystal plasticity parameters of β phase in Ti-Fe-O alloy are determined using nanoindentation tests and crystal plasticity modeling. The slip strength of the β phase is higher than that of the prismatic slip in α phase due to the significant solid solution strengthening of Fe. Reasonable agreements are achieved in predicting the experimental load-displacement, stress-strain, and stress relaxation curves.
2. The presence of intergranular β lath within the hard-soft grain combination inhibits the stress redistribution from the soft to hard α grain. A soft α-β boundary with low geometrical compatibility promotes increased stress in the β lath and further releases the stress concentration in the hard grain during the dwell period.
3. The increase of intergranular β lath thickness is beneficial for reducing the dwell fatigue sensitivity of the $\alpha + \beta$ titanium alloys with globular microstructure. Thus, the diminishment of dwell fatigue life debit in Ti-6246 is partly attributed to the high volume fraction of the β phase.

4. Relatively high opening stress for cavity nucleation is developed in the intergranular β lath within the hard-soft grain combination at high stress state, which may result in two competing premature fracture modes, i.e., basal facet nucleation in the hard α grain and cavity nucleation in the β lath.

The current crystal plasticity predictions concerning stress redistribution can be extended to a diversity of $\alpha + \beta$ titanium alloys having globular microstructure.

6. Investigation of temperature-sensitive dwell fatigue in Ti-6Al-4V titanium alloy for an aero-engine fan disc

6.1 Introduction

In this chapter, the effect of temperature on the dwell fatigue behavior of Ti-6Al-4V alloy is numerically investigated to address the dwell fatigue sensitivity of an aero-engine fan disc in operation. Firstly, temperature-dependent crystal plasticity parameters of the α phase are calibrated from a series of tensile and creep tests at ambient and intermediate temperatures ranging from 293 K to 664 K. Then, the relationship between the strain rate sensitivity of a single α crystal in Ti-6Al-4V alloy and temperature is analytically established. Based on this relationship, a polycrystalline aggregate model is generated to predict the stress redistribution within the hard-soft grain combination and assess the effect of temperature on dwell fatigue sensitivity. Furthermore, structural analysis of a Ti-6Al-4V three-web fan disc is performed under two operating conditions, i.e., takeoff and cruise phases. The results are applied to determine the roles of temperature, loading state, and macrozone morphology in local stress redistribution and dwell facet nucleation under the service environment.

6.2 Elastoplastic parameter identification for Ti-6Al-4V alloy

The material of this chapter is a mill-annealed Ti-6Al-4V rolled plate with elongated primary α grains and transformed β phase at the α grain boundaries, which satisfies the AMS 4911 specification [156],[157]. The cylindrical samples were machined parallel to the rolling direction (RD) of the plate [156]. Quasi-static tensile tests were carried out under two strain rates ($6 \times 10^{-7}\ s^{-1}$ and $1 \times 10^{-3}\ s^{-1}$) at 293 K, 473 K and 664 K. The constant load creep tests were performed at 293 K with creep stresses of 690 MPa and 621 MPa, at 589 K with a creep stress of 587 MPa, and at 664 K with a creep stress of 345 MPa, respectively [157].

As the effect of β phase on macroscopic responses can be neglected owing to the minor volume fraction for the tested Ti-6Al-4V alloy [158], a RVE comprising 200 elongated α grains is generated using Neper [159] to produce numerical stress-strain and strain-time curves, as shown in Fig. 6.1(a). The 50 μm × 50 μm × 50 μm RVE model is meshed by 39304 C3D8 fully integrated solid elements.

Although the hexahedron element cannot sketch smooth grain boundaries, its influence on macroscopic responses has been proved to be negligible [160]. The x, y, and z directions represent transverse direction (TD), RD, and normal direction (ND), respectively. The normal displacements of the left, bottom, and back surfaces are fixed to eliminate the rigid body movements. Uniform displacement is imposed on the top surface along the RD for tensile simulation, while a surface load is held to initiate creep after reaching the experimental stress level. The pole figures of the initial crystallographic orientations for the RVE, which exhibit a typical transverse texture with basal poles perpendicular to the RD, are visualized by the MTEX-5.7.0 toolbox in MATLAB, as illustrated in Fig. 6.1(b). Concerning that former studies usually applied random-textured RVE to calibrate the crystal plasticity parameters [63],[158], a random orientation distribution is also generated in this study to evaluate the effect of texture on parameter identification, as shown in Fig. 6.1(c).

The temperature-dependent anisotropic stiffness constants of α phase [71],[161], together with Young's modulus E and shear modulus G [157] of the bulk material, are plotted in Fig. 6.2. The linear relations are as follows:

$$\begin{aligned} C_{11} &= 183.860 - 0.075T \\ C_{22} &= 194.971 - 0.051T \\ C_{12} &= 103.432 - 0.040T \\ C_{13} &= 69.777 - 0.003T \\ C_{44} &= 52.056 - 0.019T \\ E &= 129.099 - 0.051T \\ G &= 48.171 - 0.019T \end{aligned} \tag{6.1}$$

Note that the unit of temperature is Kelvin, and that of the modulus is GPa.

For the slip properties in Eq. (3.14) that are assumed to be athermal, the mobile dislocation density is $\rho_m = 5\ \mu\text{m}^{-2}$ [162], Burgers vectors are $b^{<a>} = 2.95 \times 10^{-4}$ μm for <*a*> type slips and $b^{<c+a>} = 4.68 \times 10^{-4}$ μm for <*c*+*a*> type slips, Debye frequency is $\nu_D = 1 \times 10^{11}$ Hz [158], whereas the thermal activation energy ΔF and activation volume ΔV affecting the rate-dependence of slip are determined via calibration. As for the CRSS relationships in the α phase, the prismatic slip is the easiest to be activated [6]. The CRSS ratios of basal, pyramidal <*a*> slip to prismatic slip are taken as 1.125 and 1.3, respectively [158],[163]. In accordance with the single crystal compression tests conducted by Williams et al. [20], the CRSS value of pyramidal <*c*+*a*> slip is the highest, and the

CRSS ratio between pyramidal <*c*+*a*> and prismatic slip decreases dramatically with rising temperature. Based on the aforementioned literature, the CRSS rank of the α phase in ascending order is prismatic, basal, pyramidal <*a*> and pyramidal <*c*+*a*> slip. The strain-hardening parameters in Eq. (3.17) are calibrated using curve fitting.

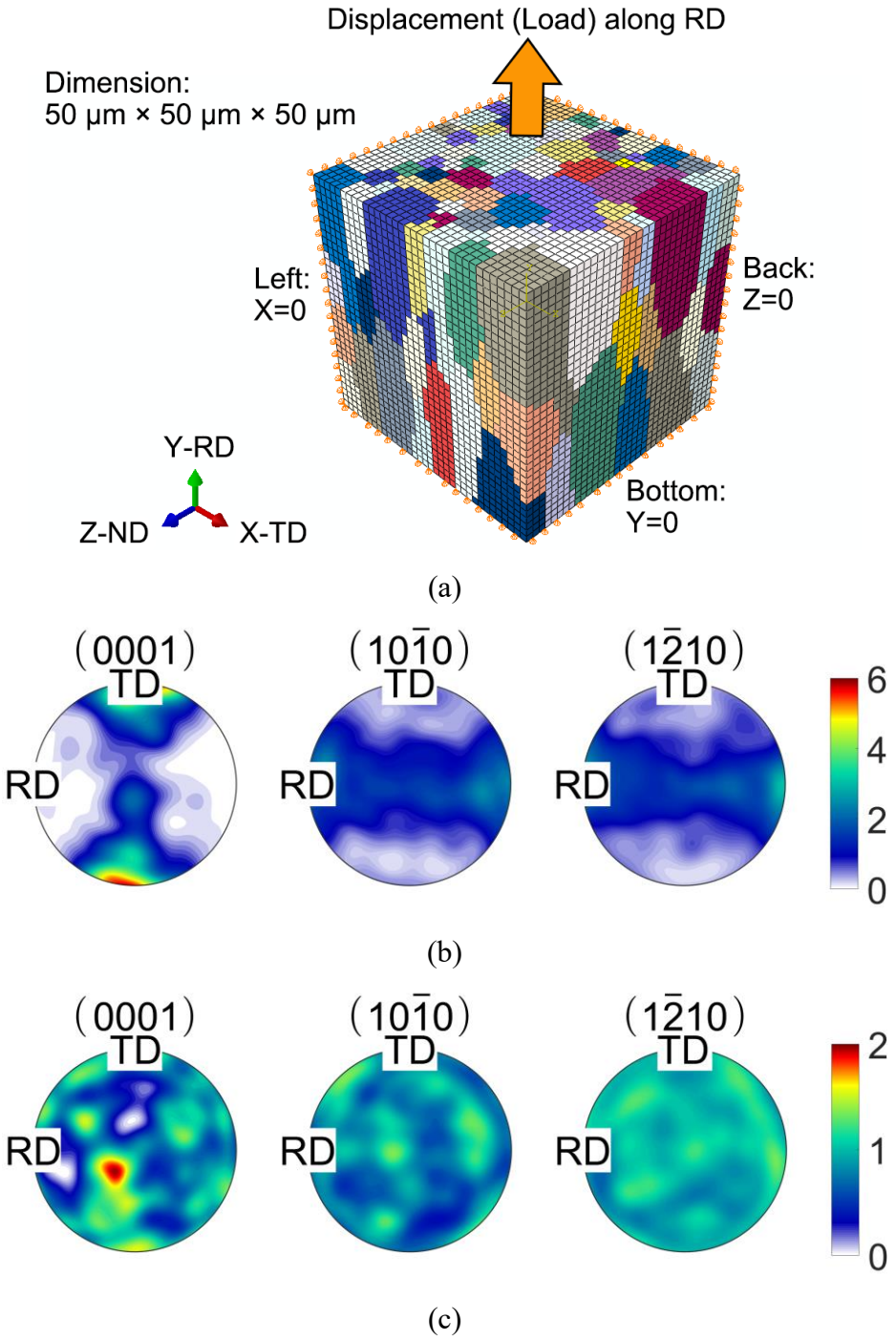

Fig. 6.1 (a) RVE model containing 200 elongated α grains and boundary conditions, initial crystallographic orientations for the RVE with (b) transverse texture, and (c) random texture.

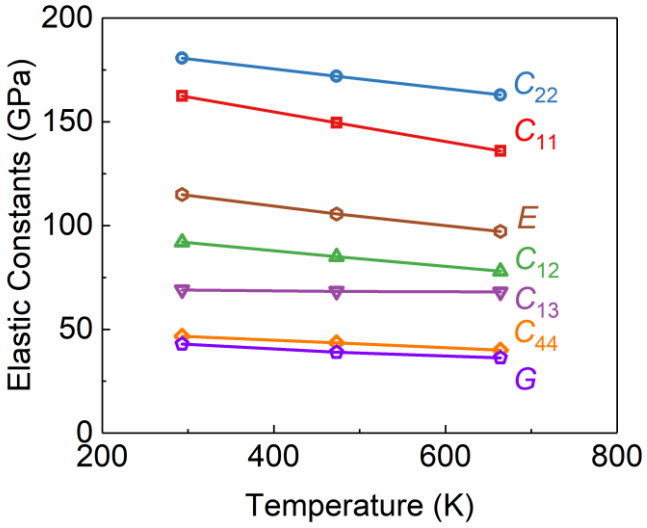

Fig. 6.2 Temperature-dependent elastic stiffness constants for α phase, and Young's modulus, shear modulus for polycrystalline Ti-6Al-4V alloy.

A comparison between the experimental results obtained from the report of NASA [157] and the parallel crystal plasticity predictions in this study are plotted in Fig. 6.3(a-b). The responses of the RVE model basically match the experimental results. It should be noted that RVE with random texture provides higher yield strength and lower strain hardening than that with transverse texture under a strain rate of $1 \times 10^{-3}\ s^{-1}$ at 293 K, as shown in Fig. 6.3(c). Thus, a RVE with representative texture is of great importance to extract the reliable crystal plasticity parameters. The resulting temperature-dependent CRSS values for prismatic <*a*>, pyramidal <*c*+*a*> slip systems, and 0.2% proof stress at a strain rate of $1 \times 10^{-3}\ s^{-1}$, are illustrated in Fig. 6.4(a). The relationships are fitted using second-order polynomials as follows:

$$\tau_0^{prismatic} = 602.763 - 1.073T + 7.406 \times 10^{-4}T^2$$

$$\tau_0^{pyr\,<c+a>} = 2010.163 - 3.943T + 0.239 \times 10^{-2}T^2$$

$$\sigma_{0.2} = 1655.750 - 3.206T + 0.239 \times 10^{-2}T^2 \quad (6.2)$$

The initial CRSS ratio of pyramidal <*c*+*a*> to prismatic slip is 3.01 at 293 K and decreases to 2.09 at 664 K. The temperature-dependent ΔF and ΔV are given in Fig. 6.4(b) and calculated by

$$\Delta F = 0.009 + 1.410 \times 10^{-3}T$$

$$\Delta V = 24.093 - 0.015T + 8.479 \times 10^{-5}T^2 \quad (6.3)$$

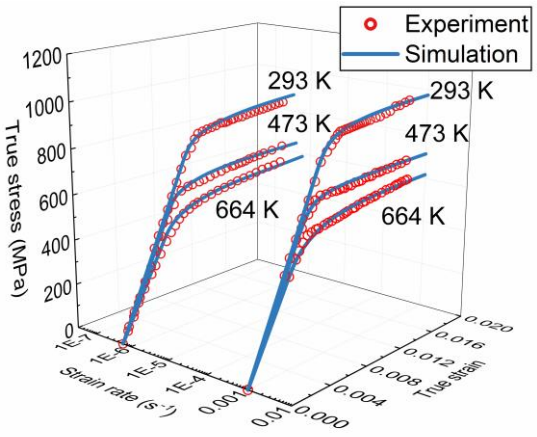

(a)

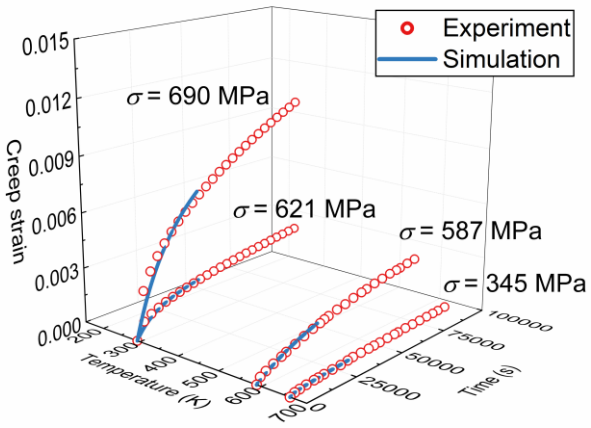

(b)

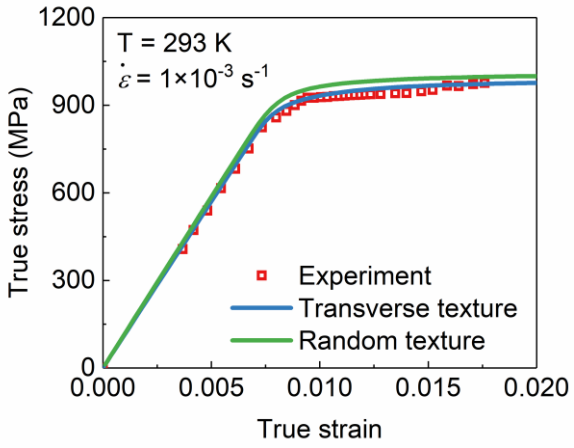

(c)

Fig. 6.3 Macroscopic responses obtained from (a) quasi-static tensile, (b) constant load creep tests [157] and accompanying simulations, and (c) comparison between stress-strain curves of RVE with different textures under a strain rate of $1 \times 10^{-3}\ s^{-1}$ at 293 K.

where ΔF takes the unit of eV and the unit of ΔV is b^3. The fitted relations align with the results of Xiong et al. [43] and Conrad [164] that the ΔF for α-titanium is proportional to temperature when $T < 0.4T_m$ and ΔV is an increasing function of ΔF ranging from $8b^3$ to $80b^3$ due to the kink-pair mechanism. Moreover, the calibrated activation volume of slip systems in Ti-6Al-4V is greater than that of near-α Ti6242 alloy at RT [65]. Given the inverse relationship between the activation volume and SRS, Ti-6Al-4V alloy is less rate-sensitive than Ti-6242 alloy at RT, which results in alleviated cold creep and stress redistribution in Ti-6Al-4V alloy during dwell fatigue. This agrees with the

experimental results at RT that the dwell life debit in Ti-6Al-4V alloy is only 2-3 while the Ti-6242 alloy endures a dwell life debit of more than 10 under the same stress of $0.9\sigma_y$ [69]. Hence, the determined parameters are validated to be reasonable. Besides, the strain hardening parameters in Eq. (3.17) are listed in Table 6.1. A single set of initial hardening modulus is employed because the work hardening in Ti-6Al-4V alloy exhibits trivial differences below 773 K [165]. The latent hardening constant is assumed to be $q = 1$ and the empirical coefficient in Eq. (3.22) is $\alpha_T = 0.4$ [92].

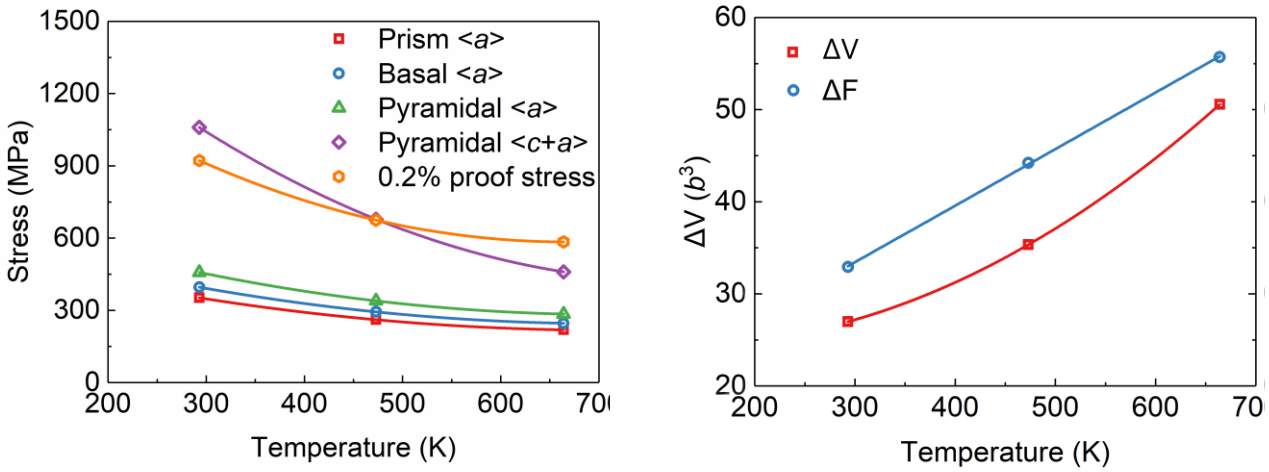

(a) (b)

Fig. 6.4 (a) Temperature-dependent initial CRSS of active slip systems in α phase and 0.2% proof stress at the strain rate of $1 \times 10^{-3}\ s^{-1}$, and (b) temperature-dependent activation energy and activation volume.

Table 6.1 Strain hardening parameters for slip systems of α phase, in MPa.

	Basal <a>	Prismatic <a>	Pyr. <a>	1st Pyr. <c+a>	2nd Pyr. <c+a>
h_0	100	100	150	200	200
τ_∞	$\tau_0^{basal} + 210$	$\tau_0^{prism} + 225$	$\tau_0^{pyr<a>} + 260$	$\tau_0^{pyr\ <c+a>} + 288$	$\tau_0^{pyr\ <c+a>} + 288$

6.3 Temperature-dependent strain rate sensitivity

Dwell fatigue tests from previous work suggest that a combination of high SRS and low strain hardening leads to large macroscopic strain accumulation in IMI834 alloy in the temperature range of

293 K to 513 K [67]. To further understand the creep behavior and temperature sensitivity of dwell fatigue at the grain scale, the relationship between the rate-dependent characteristic of individual slip systems and the SRS should be established. To this end, the conventional SRS exponent m ($m = \frac{dln\sigma}{dln\dot{\varepsilon}}|_{\dot{\varepsilon},T}$, where σ is the flow stress at a constant strain rate and temperature, $\dot{\varepsilon}$ is the strain rate) for a single crystalline α-titanium is rederived following a prior study [166],

$$m = \frac{dln\sigma}{dln\dot{\varepsilon}} = \frac{\psi}{\sqrt{1+\psi^2}\left[\sinh^{-1}\psi + \chi\tau_c^i\right]} = \frac{\sinh\left[\frac{(\tau^i - \tau_c^i)\Delta V}{kT}\right]}{\sqrt{1+\sinh^2\left[\frac{(\tau^i - \tau_c^i)\Delta V}{kT}\right]}}\frac{kT}{\tau^i \Delta V} \tag{6.4}$$

where $\psi = \frac{\dot{\varepsilon}}{\xi} = \sinh\left(\frac{(\tau^i - \tau_c^i)\Delta V}{kT}\right)$, $\xi = \rho_m \nu_D (b^i)^2 \exp\left(-\frac{\Delta F}{kT}\right) SF^i$, SF^i is the Schmid factor of a slip system describing the influences of crystal orientation and loading direction on the SRS exponent value, and $\chi = \frac{\Delta V}{kT}$.

Using the identified crystal plasticity parameters for α phase of Ti-6Al-4V alloy and Eq. (6.4), the effect of temperature and rate-dependent slip properties on the SRS exponent, m, can be estimated for an α single crystal (grain) in Ti-6Al-4V alloy. Since the highly accumulated strain in soft grains induced by creep dwell enhances the magnitude of the redistributed stress on neighboring hard grains and causes earlier quasi-cleavage fracture on the basal planes, this study focuses on soft grains rather than hard grains. Although both the activations of prismatic and basal slips in soft grains are likely to trigger stress redistribution [49], a soft grain orientated for prismatic slip is modeled here because the transmission electron microscopy (TEM) observations conducted by Joseph et al. [167] indicates that only <*a*>-prismatic dislocation pile-ups in the soft grain can promote the nucleation of <*a*>-basal dislocations in the adjacent hard grain, which is necessary for dwell facet formation. Provided a single soft grain with prismatic Schmid factor of 0.5 in Ti-6Al-4V alloy is subjected to the uniaxial tensile load under a strain rate of $1 \times 10^{-3}\ s^{-1}$, similar to the tension-tension dwell fatigue loading condition, and experiences temperatures ranging from 293 K to 664 K (293 K, 393 K, 473 K, and 664 K), the relationship between the slip-based rate sensitive parameters (i.e., activation energy ΔF and activation volume ΔV) and SRS exponent in Eq. (6.4), is depicted at different temperatures, as detailed in Fig. 6.5(a-d). The ranges of activation energy ΔF and activation volume ΔV are respectively taken from 0.1 eV to 1 eV and $1b^3$ to $50b^3$ in order to cover the regime in Fig. 6.4(b). It should be noted that plastic

shear of the soft grain is assumed to be solely dominated by the given prismatic slip, and the dislocation-based work hardening is ignored (i.e., τ_c^i in Eq. (6.4) is the initial CRSS) because of the low initial hardening modulus, as listed in Table 6.1.

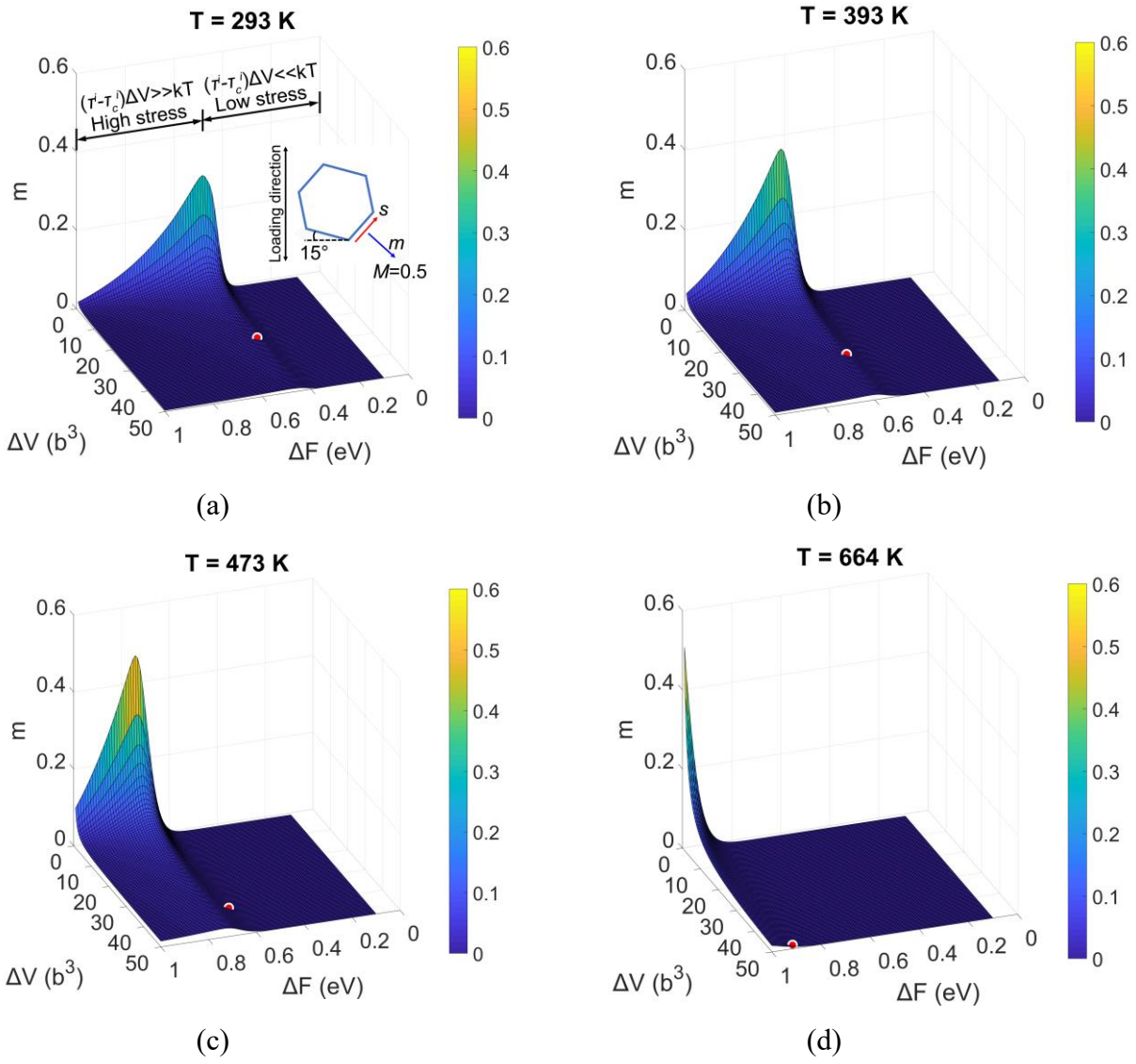

Fig. 6.5 Variation of strain rate sensitivity exponent m resulting from different activation energy ΔF and activation volume ΔV at temperatures of (a) 293 K, (b) 393 K, (c) 473 K, and (d) 664 K. The red circle with white edge indicates the location of the soft grain in Ti-6Al-4V alloy, as shown in Fig. 6.5(a).

In Fig. 6.5(a-d), the peak of the SRS exponent, m, increases from 0.29 to 0.51 with rising temperature, and the corresponding location changes from low activation energies to high. The position

of the SRS peak lies where the $(\tau^i - \tau_c^i)\Delta V$ and kT have competitive values, as shown in Fig. 6.5(a). When $(\tau^i - \tau_c^i)\Delta V \gg kT$ (high stress), the SRS is dominated by $\frac{\tau^i \Delta V}{kT}$. However, when $(\tau^i - \tau_c^i)\Delta V \ll kT$ (low stress), the SRS is governed by $\frac{\tau_c^i}{\tau^i}$ [168]. According to Eq. (3.14), the ratio between $(\tau^i - \tau_c^i)\Delta V$ and kT is $\frac{(\tau^i - \tau_c^i)\Delta V}{kT} = \sinh^{-1}[\frac{\dot{\gamma}}{\rho_m \nu_D \exp(-\frac{\Delta F}{kT})}]$. Thus, the SRS peak slides toward high activation energy as the temperature increases. Within the high-stress region, the SRS exponent maintains the maximum value at the lowest activation volume of $1b^3$ throughout the temperature range. A relatively steep decline of the SRS exponent occurs when the activation volume is approximately below $10b^3$ and the gradient thereafter becomes smoother. Besides, the red circle with a white edge denotes the site for the soft α grain orientated for prismatic slip in Ti-6Al-4V alloy. From Fig. 6.5(a) and (b), it can be observed that the circle is located in the vicinity of the SRS peak for the given activation volume. This results in a rate-sensitive soft grain at low temperatures, which generates a large slip accumulation during the dwell period. However, the SRS peak shifts faster than the increasing rate of activation energy with temperature, and the circle gradually drops into the low-stress region, as shown in Fig. 6.5(c) and (d). As a result, the SRS of the soft grain vanishes at intermediate temperatures.

Based on the above discussion, it is obvious that the evolutions of activation energy and activation volume with temperature have a great impact on the SRS and creep capability of the soft grain. Here, we compared the SRS of the prismatic slip-orientated soft grain with and without consideration of the evolutions of activation energy and activation volume, as plotted in Fig. 6.6. For the condition that activation energy and activation volume are temperature-independent, the values at 293 K are employed according to the assumption made by Zhang et al. [166] that the activation energy and volume vary to a small extent with temperature. As shown by the dash-dotted line in Fig. 6.6, the SRS exponent increases from 293 K and reaches the peak value of 0.024 at 394 K. This result closely correlates with the phenomenon that the largest dwell life debit in Ti-6Al alloy emerges at around 393 K [63]. The disappearance of the dwell life debit at temperatures higher than 503 K can also be linked to the fact that the strain rate sensitivity decreases rapidly to a relatively low degree when the temperature is beyond 500 K. However, the deviation of the SRS peak occurs when the temperature-related property of activation energy and activation volume are considered using Eq. (6.3), as indicated

by the solid line in Fig. 6.6. Compared to the former condition, the SRS peak shifts from 394 K to 416 K and the value decreases from 0.024 to 0.022. Besides, the upper limit of the strain rate sensitive temperature range extends to nearly 600 K. Therefore, the ignorance of the relationship in Eq. (6.3) may result in the misprediction of the location and peak value of the SRS exponent, as well as the underestimation of the strain rate sensitive temperature range.

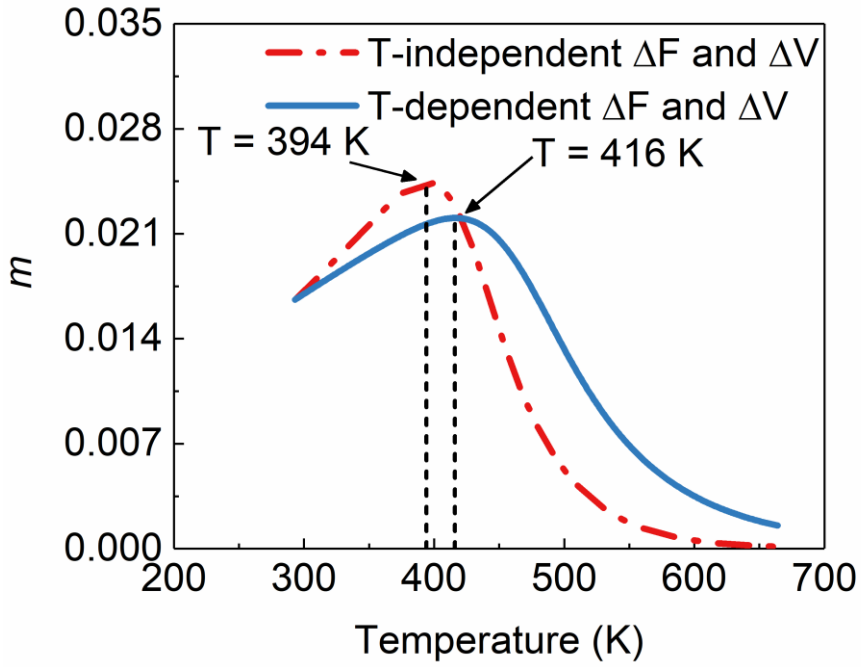

Fig. 6.6 Temperature-dependent strain rate sensitivity of a Ti-6Al-4V soft α grain orientated for prismatic slip, with a strain rate of $1 \times 10^{-3}\ s^{-1}$ and Schmid factor of 0.5.

6.4 Effect of temperature on stress redistribution

The variation of SRS of the prismatic slip-orientated soft grain with temperature alters the time-dependent dislocation pile-ups at hard-soft grain boundaries during dwell fatigue. As a powerful tool, the CPFE method is applied to quantitatively evaluate the magnitude of the pile-up stress and determine the dwell fatigue sensitivity.

A 2D microstructure containing 71 primary α grains is extruded along the z-axis using an ABAQUS plugin Neper2CAE [169] to develop a quasi-3D polycrystalline aggregate model, as shown in Fig. 6.7(a). The average grain size in diameter is 6 μm, as estimated by NASA [156]. The 150 μm × 150 μm × 10 μm model is meshed by 24912 C3D8 elements. The element size is refined

within a hard-soft grain combination in the central area to obtain more precise results. Aiming at depicting the most detrimental condition for dwell facet nucleation, the intergranular β phase is not explicitly modeled for the Ti-6Al-4V alloy with globular microstructure since the redistribution of stress from the soft to hard α grain is inhibited in the presence of the intergranular β lath, as stated in Chapter 5 [170]. The c-axis of the hard grain is parallel to the loading direction. The soft grain with a prismatic Schmid factor of 0.5 is derived from Section 6.3, as shown in Fig. 6.7(b). Line $A-B$ is a path across the hard-soft grain boundary. The crystallographic orientations of the grains surrounding the hard-soft grain combination are randomly generated. The normal displacements of the left, bottom, and back surfaces are fixed to zero. A dwell fatigue cycle is applied on the top surface with the maximum stresses of $0.95\sigma_{0.2}$ (at the strain rate of 1×10^{-3} s^{-1}) for four different temperatures, which are 880 MPa, 748 MPa, 641 MPa, and 555 MPa for 293 K, 416 K (the temperature at which the prismatic slip-orientated soft grain exhibits the highest SRS value), 473 K, and 664 K, respectively. The duration of the dwell period is 120 s.

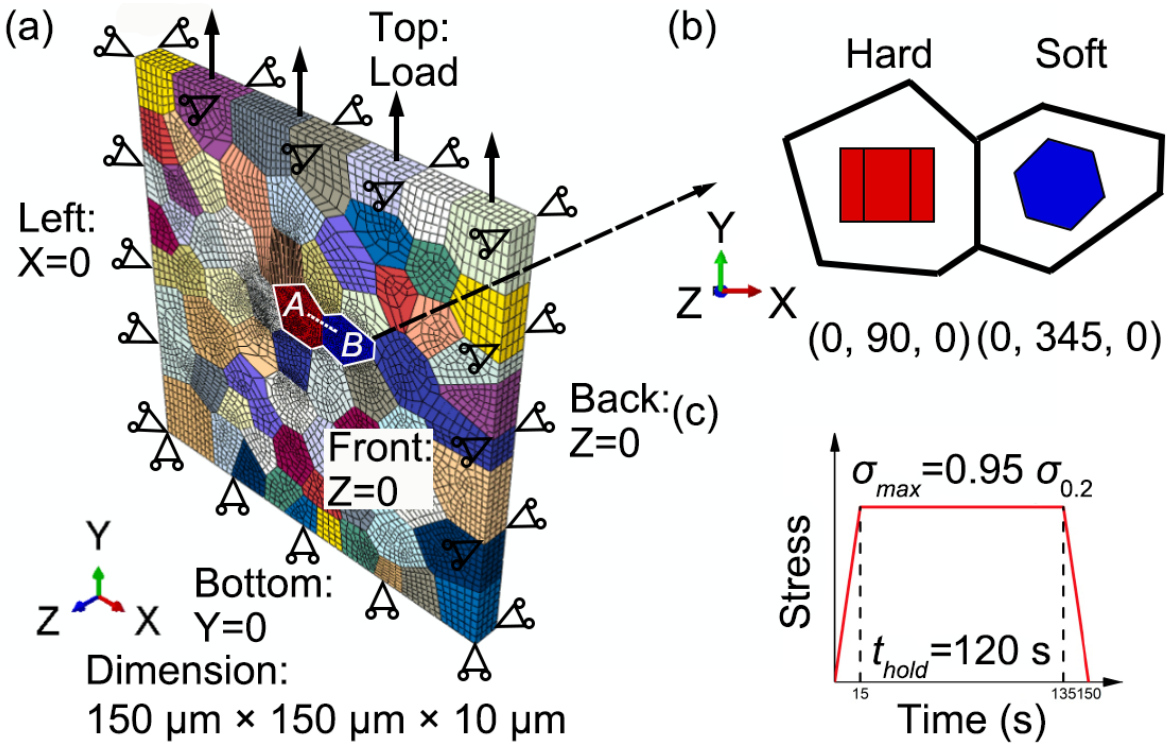

Fig. 6.7 (a) Polycrystalline aggregate model and assigned boundary conditions, (b) hard-soft grain combination at the center area and corresponding Euler angles in Bunge notation (°), and (c) imposed dwell fatigue loading cycle with a maximum stress of $0.95\sigma_{0.2}$ and dwell time of 120 s.

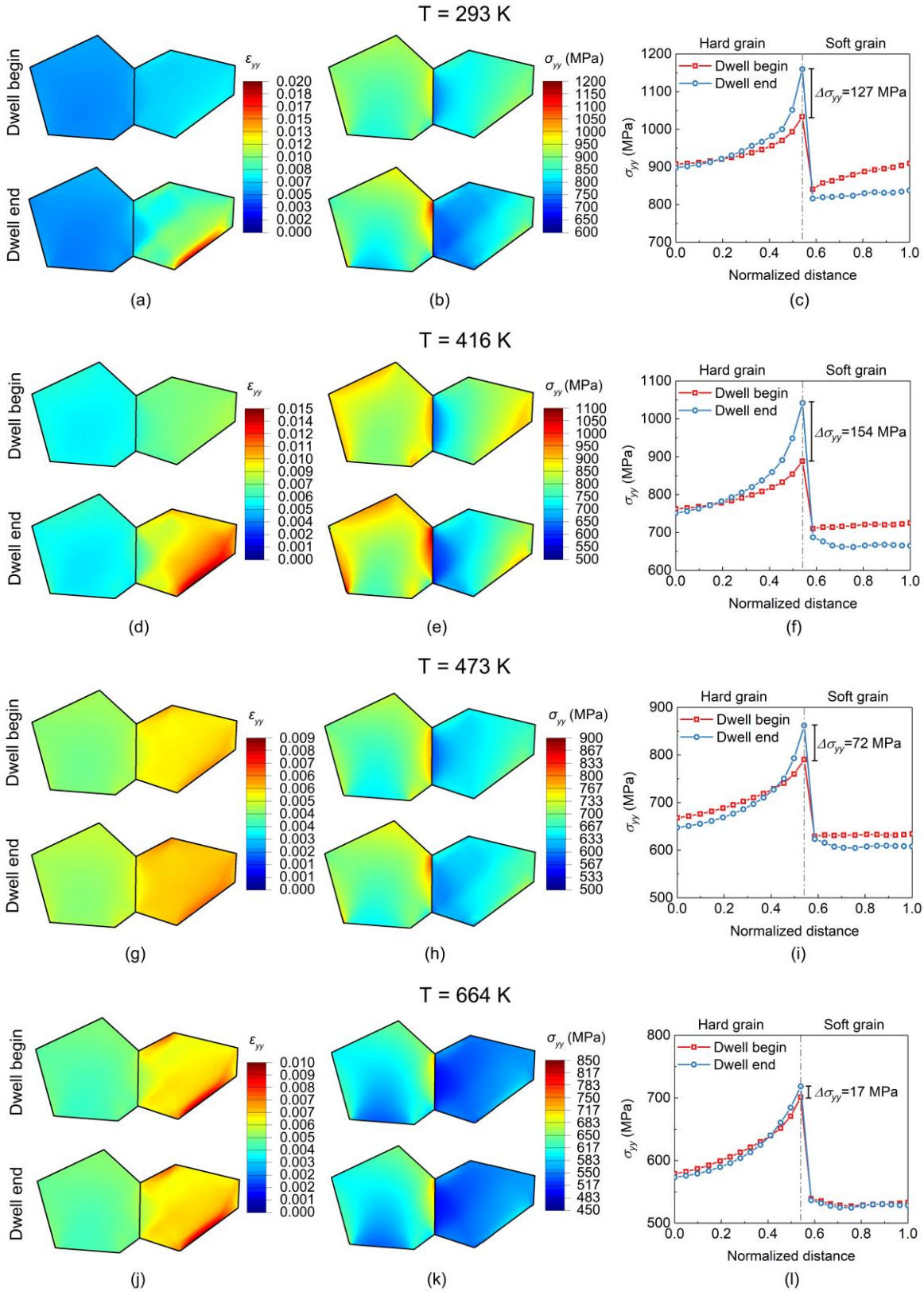

Fig. 6.8 Predicted strain ε_{yy} and stress σ_{yy} contours within the hard-soft grain combination before and after the dwell period, and stress redistribution along the path $A-B$ at (a-c) 293 K, (d-f) 416 K, (g-i) 473 K, and (j-l) 644 K.

The crystal plasticity predictions of the stress and strain distributions within the hard-soft grain combination are summarized in Fig. 6.8. At the beginning of the dwell, the stress difference at the hard-soft grain boundary is predominantly caused by the elastic anisotropy of HCP α-titanium. The larger directional Young's modulus along the *c*-axis generates the stress concentration in the hard grain. As shown in Fig. 6.8(c), (f), (i), and (l), the stress difference across the hard-soft grain boundary varies slightly with the temperature at the start of dwell time since the ratio of Young's modulus along the *c*-axis to that along the *a*-axis is nearly temperature-independent [161].

The stress redistribution process during the dwell period is derived from the plastic anisotropy of α phase. At low temperatures of 293 K and 416 K, the strain accumulation in the soft grain (Fig. 6.8(a) and (d)) aggravates the stress concentration at the hard-soft grain boundary (Fig. 6.8(b) and (e)). A potential explication for the occurrence of stress redistribution at low temperatures is proposed by Zhang et al. [171]. They suppose that the escape of the activated dislocations from pinning points is easier at low temperatures because of the relatively low activation energy and high stress (Fig. 6.5(a) and (b)). Thus, the time-dependent dislocation pile-ups can gradually grow at the hard-soft grain boundary and cause stress redistribution. On path $A-B$, the magnitude of stress redistribution at the hard-soft grain boundary increases from 127 MPa at 293 K to 154 MPa at 416 K (Fig. 6.8(c) and (f)). The increase in stress change can be attributed to the phenomenological relationship that the higher SRS of the soft grain at 416 K causes larger strain accumulation and more serious stress redistribution than at 293 K, as given in Fig. 6.6, while the physical basis is still under active investigation.

At intermediate temperatures of 473 K and 664 K, the creep deformation in the soft grain is less evident at the end of the dwell time (Fig. 6.8(g) and (j)), and the stress redistribution is relieved consequently (Fig. 6.8(h) and (k)). For instance, the maximum redistributed stress at the hard-soft grain boundary descends to 72 MPa at 473 K and 17 MPa at 664 K (Fig. 6.8(i) and (l)). One of the possible mechanistic bases for the dissipation of stress redistribution is that the gliding dislocations confront with fewer obstacles at intermediate temperatures and the dislocation structure attain a steady state rapidly (i.e., quick creep saturation after the stress hold begins), and the magnitude of the redistributed stress falls to a low level [65]. However, this contradicts the descriptions in Section 3 at intermediate temperatures. As shown in Fig. 6.5(c) and (d), the SRS exponent of the prismatic slip-orientated soft grain lies in the low-stress region. In this region, the high activation energy barrier and low effective

resolved shear stress reduce the mobility of dislocations in terms of the gliding velocity at 473 K and 664 K, and hence the strain accumulation during creep is prohibited. Meanwhile, dynamic strain aging (DSA) has also been reported to promote creep resistance in this temperature range since the solute diffusion of interstitial atoms can pin down the mobile dislocations and form a high density of immobile dislocation junctions to further decrease the gliding velocity of free dislocations [172],[173]. It is interesting to note that the decrease in SRS for the soft grain (Fig. 6.6) is correlated to the DSA effect as well even though the fundamental mechanism is still elusive. Additionally, the degeneration of plastic anisotropy for the α-titanium with HCP crystal structure may also contribute to a homogeneous deformation within the hard-soft grain combination at elevated temperatures. Even though the applied stress is insufficient to initiate pyramidal <*c*+*a*> slip activities in the hard grain that carry the plastic deformation along the *c*-axis throughout the considered temperature range, the monotonic declination of the CRSS ratio between pyramidal <*c*+*a*> slip and prismatic <*a*> slip shrinks the stress redistribution to some extent [70]. In summary, the high thermal energy barrier for activating trapped dislocations and modest DSA effect, which are related to the decrease in SRS of the soft grain, along with the reduced plastic anisotropy of α phase, are more sensible for interpreting the negligible amount of accumulated strain in the soft grain and alleviation of stress redistribution at intermediate temperatures for Ti-6Al-4V alloy.

Although there is a strong propensity for dwell life debit to be discovered in the strain rate sensitive temperature range, the strain hardening effect is also presumably involved in this scenario, as mentioned at the beginning of this section [67]. At low temperatures, the plastic deformation is dominated by prismatic slip. As a result, the interaction of dislocations exclusively includes weak self-hardening, which limitedly hampers the glide of dislocation and dwell strain accumulation. In contrast, more slip systems can be activated at intermediate temperatures due to the reduced plastic anisotropy of HCP α-titanium, the increase in probability for dislocations to encounter with forest dislocations retards the average dislocation glide velocity and plastic strain accumulation during the stress-dwell period, thereby hindering the stress redistribution. Nevertheless, the role of the strain hardening mechanism in the dwell fatigue sensitivity of titanium alloys still requires further exploration

The redistribution of stress has a direct relationship with the dislocation pile-ups at the hard-soft grain boundary according to Stroh's model. Although the density of SSDs is not explicitly integrated into the current crystal plasticity model, the effective density of GNDs can partly reflect the dislocation

pile-ups at the hard-soft grain boundary. Therefore, the effective density of GNDs along the path $A-B$ after the dwell period is plotted in Fig. 6.9. It can be seen that the GNDs concentrate in the soft grain, especially in the vicinity of the hard-soft grain boundary, while no GND is produced in the hard grain because the hard grain keeps elastic deformation during the stress dwell. Moreover, the effective density of GNDs at the hard-soft grain boundary is the highest at 416 K, followed by 293 K, 473, and 664 K. From Figs. 6.8 and 6.9, it can be observed that the magnitude of stress redistribution increases as the effective density of GNDs near the hard-soft grain boundary becomes higher.

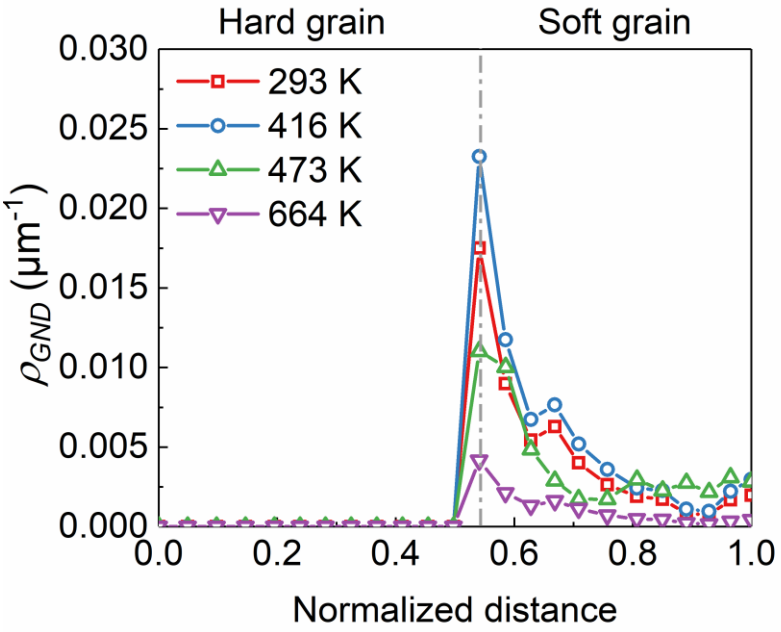

Fig. 6.9 Effective density of GNDs along the path $A-B$ after stress holding at different temperatures.

6.5 Dwell fatigue sensitivity of a fan disc

An in-depth comprehension of the temperature-sensitive SRS and stress redistribution is beneficial to recognize the dwell fatigue failure of titanium alloy aero-engine components in service. Also, the stress level, introduction of stress multiaxiality, and macrozone morphology after manufacturing (e.g., die forging and machining for compressor discs [174], and cross-rolling and machining for blades [27]) affect the dwell facet nucleation. To comprehensively elucidate the effect of these factors, the dwell fatigue sensitivity of a titanium alloy fan disc is studied in this section.

6.5.1 Structural analysis of a three-web fan disc under different operating conditions

A simplified three-web fan disc without the dovetail slots and bolted joint structure [175] is taken as an example for structural analysis at the component level, as shown in Fig. 6.10(a). The material of the fan disc is Ti-6Al-4V alloy with a density of $4.43\ \mathrm{g/cm^3}$ and a thermal expansion coefficient of $8.8 \times 10^{-6}\ \mathrm{K^{-1}}$. The elastic parameters of the material can be calculated using Eq. (6.1). Considering the structural symmetry, a $1/23$ sector model is partitioned from the fan disc to improve the computational efficiency of the finite element simulation, as shown in Fig. 6.10(b). The model is meshed by 16360 C3D8 elements using HyperMesh and exported to ABAQUS. The static structural analysis is carried out at two working phases, which are defined as the takeoff phase (the most crucial phase from the standpoint of performance and safety) and the cruise phase (the majority of a long haul). The fan blades and fan sliders are substituted by a mass point at the equivalent centroid. The mass point is coupled with the nodes on the rim surface of the fan disc through the tie constraint to impose the centrifugal load, while the aerodynamic force on the fan blade, and the pressure on the web, bore, and rim areas are neglected. The axial displacement of two nodes on the back surface of the disc arm is fixed, whereas the deformation along radial and tangential directions is free. The rotational speed of the low-pressure spool (N1) at the takeoff stage is $\mathrm{N1_{takeoff}} = 2800\ \mathrm{rpm}$, while the speed during the cruise stage is designated as $\mathrm{N1_{cruise}} = 0.85\mathrm{N1_{takeoff}}$ [175]. Since the fan disc is deemed a cold disc at the front of the aero-engine, the temperature field within the fan disc is assumed to be homogeneous (i.e., the thermal stress induced by the temperature gradient is ignored) and the working temperatures are set to 357 K and 295 K during the takeoff and cruise phases, respectively [175]. According to the relationship in Fig. 6.6, the soft grains in Ti-6Al-4V alloy demonstrate moderate SRS at these two temperatures, which may lead to stress redistribution between the soft and hard grains during the dwell period.

Fig. 6.11 shows the normalized hoop, radial, and axial stress distributions on the meridian plane of the fan disc. Here, σ_0 is the permissible stress at the corresponding temperature. The hoop and radial stresses at the takeoff phase are higher than those at the cruise phase because of the larger centrifugal load at high rotational speed, while the axial stress is almost the same for the two phases. The hoop stress (σ_H) concentration is located at the bores of the fan disc. The hoop stress level decreases from the first bore to the third bore, and the maximum hoop stress is at the bottom of the first bore, as the

white dots in Fig. 6.11(a) and (b). The radial stress (σ_R) concentrates at the webs of the disc, while the maximum value is smaller than the peak hoop stress, as shown in Fig. 6.11(c) and (d). The overall axial stress (σ_A) is far lower than the radial and hoop stresses, as shown in Fig. 6.11(e) and (f). In agreement with previous numerical and experimental results [26],[27],[176], the hoop stress is generally the principal stress that leads to the dwell fatigue failure and burst of discs. Thus, this study focuses on the position with high hoop stress concentration.

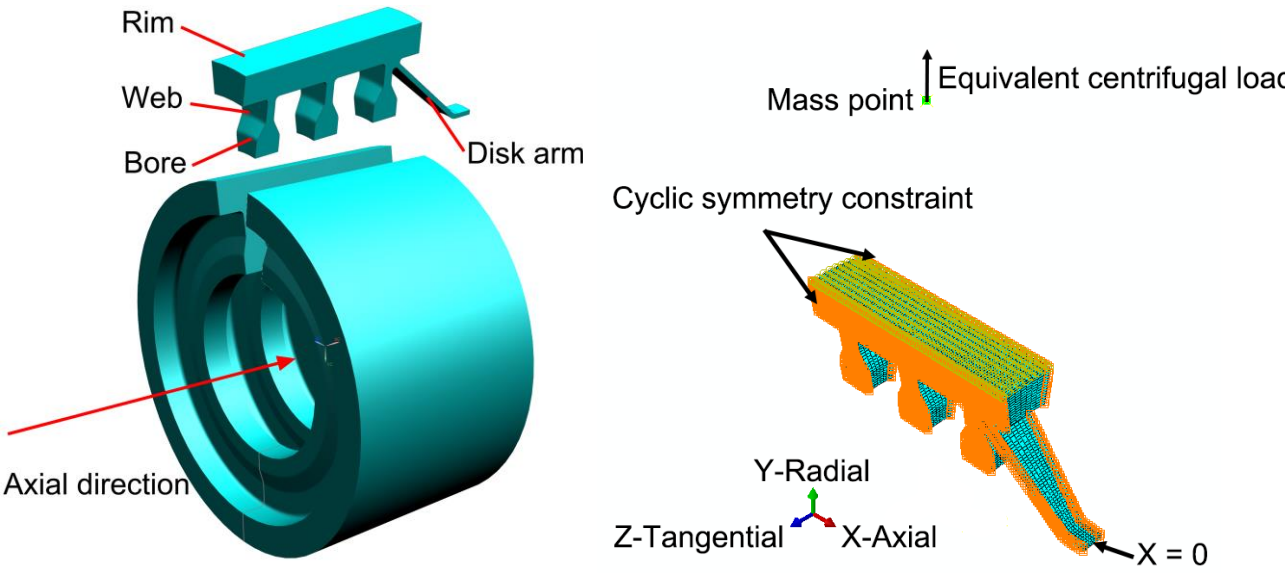

(a) (b)

Fig. 6.10 (a) Simplified model of a three-web fan disc [175], (b) $1/23$ sector finite element model, and relevant boundary conditions for static structural analysis.

Although the webs of the fan disc also exhibit hoop stress, the high radial stress increases the load multiaxiality at this location, which in turn restricts the dwell fatigue sensitivity [78]. The load multiaxiality is evaluated by a stress triaxiality factor, which is defined as [79]

$$TF = \frac{\frac{1}{3}(\sigma_H + \sigma_R + \sigma_A)}{\sigma_{eq}} \tag{6.5}$$

where σ_{eq} is the von Mises stress. The calculation reveals that the TF factor within the web of fan disc ranges from 0.59 to 0.68, whereas the TF factors in the bore region are relatively small and lie between 0.31 and 0.41. In owing to the above discussions, the crystal plasticity submodeling for examining local stress redistribution is performed at the bottom of the first bore with the highest hoop stress and

low stress triaxiality, which is susceptible to dwell facet nucleation.

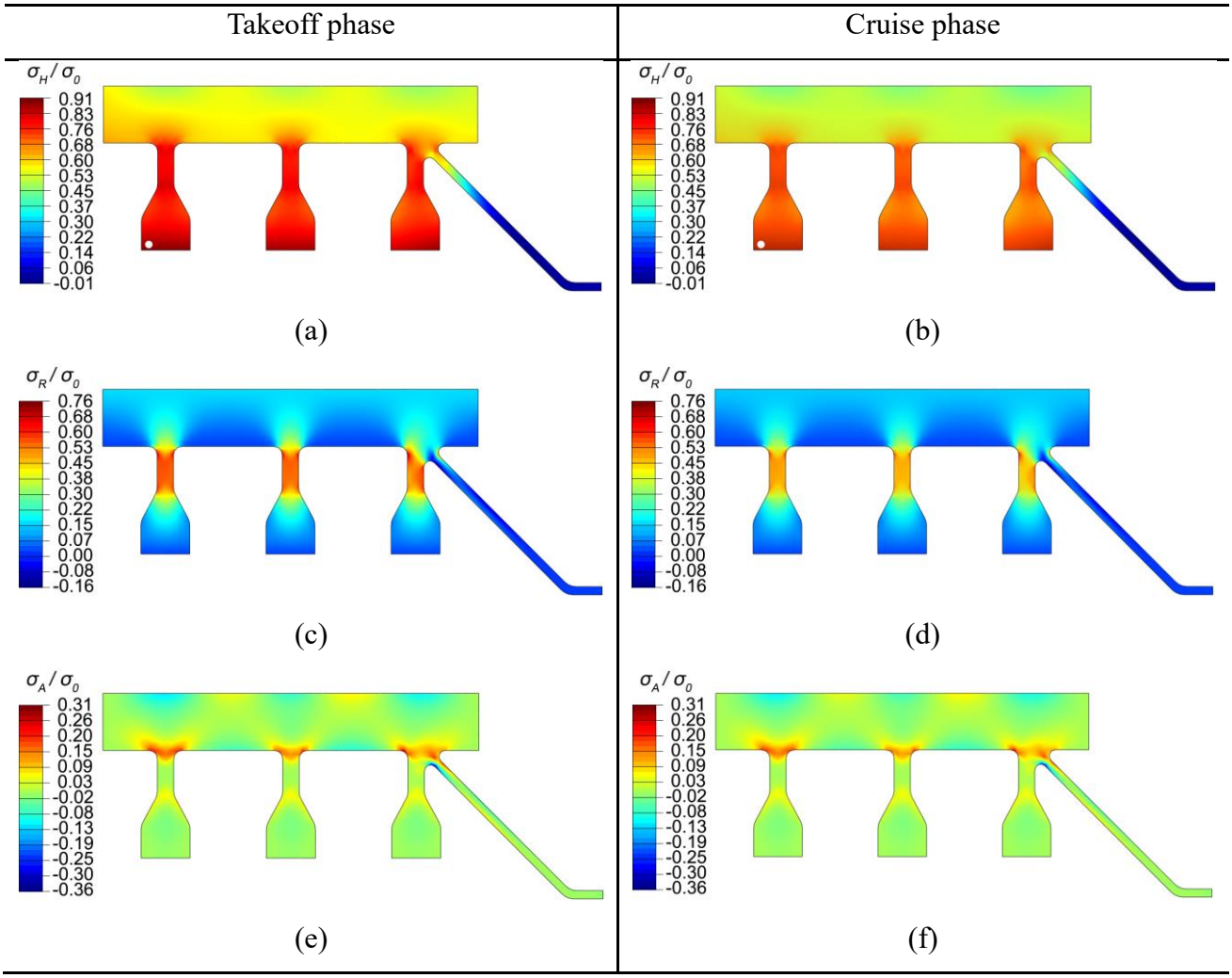

Fig. 6.11 Normalized (a-b) hoop stress, (c-d) radial stress, (e-f) axial stress contours on the meridian plane of the three-web fan disc at takeoff and cruise phases. σ_0 is the permissible stress at corresponding temperatures. The white dot in (a-b) indicates the location with the maximum hoop stress.

6.5.2 Crystal plasticity submodeling of local stress redistribution

The dwell fatigue failure of real parts is associated with α grain colonies with similar orientations, the so-called microtextured regions or macrozones [174], the unit of crystal plasticity submodeling is therefore transformed from the grain to the macrozone based on the concept of effective structural unit proposed by Rugg et al. [12]. As shown in Fig. 6.12(a), the cubic polycrystal model containing 512 macrozones is meshed by 32768 C3D8 elements. The 450 μm size corresponds to the average size of

macrozones in Ti-6Al-4V alloy reported by Pratt & Whitney [27]. The region surrounded by the white line is a hard-soft macrozone combination. Considering that the maximum size of macrozones can be one order of magnitude larger than the average size [27], and the macrozones in Ti-6Al-4V alloy have the morphology of long-range bands [177],[178],[179], the hard-soft macrozone combination is elongated along the y-axis to study the effect of macrozone size on stress redistribution, as shown in Fig. 6.12(b). The aspect ratio, which is defined as $R = \frac{L_n}{L_1}$ [158], is used to assess the length-scale effect. In this model, the aspect ratio R ranges from 1 to 8. Fig. 6.12(c) gives the crystallographic orientations of the hard-soft macrozone combination. The prismatic Schmid factor in the soft macrozones is 0.5. The boundary conditions are the same as the RVE in Fig. 6.1(a). The axial, radial, and hoop stresses are imposed along the x, y, and z directions and held for 120 s. The histories of the individual loads at takeoff and cruise phases are plotted in Fig. 6.12(d). The temperature-dependent crystal plasticity parameters at 295 K and 357 K are calculated using Eqs. (6.2-6.3). The diagonal components in the thermal expansion diagonal tensor $\boldsymbol{\alpha}$ (Eq. (3.2)) are $\alpha_1 = \alpha_2 = 1.1 \times 10^{-5}\ \mathrm{K}^{-1}, \alpha_3 = 1.8 \times 10^{-5}\ \mathrm{K}^{-1}$ [180]. Unlike the near-α titanium alloys used for high-temperature applications, the soft grains in Ti-6Al-4V alloy demonstrate moderate SRS at low temperatures (see Fig. 6.6) and the increase in working temperature at the takeoff phase even promotes the SRS of Ti-6Al-4V alloy, the "thermal alleviation" mechanism that is suggested to reduce the dwell fatigue sensitivity can therefore be neglected for fan discs [171].

The predicted strain and stress contours at the beginning and end of dwell time are shown in Fig. 6.13. For the takeoff phase, the strain accumulation in soft macrozones is not obvious at the end of the stress hold when the aspect ratio is 1 (Fig. 6.13(a)), and the corresponding stress field also barely changes during the dwell period (Fig. 6.13(c)). However, as the aspect ratio increases to 8, marked strain accumulation is observed in the soft macrozones at the end of dwell, as illustrated in Fig. 6.13(b). As a consequence, the stress change at the hard-soft interface occurs (see Fig. 6.13(d)). By comparison, both the accumulated strain in the soft macrozones and the pile-up stress in the hard macrozone with an aspect ratio of 8 are higher than their counterparts when the aspect ratio is 1. As for the cruise phase, the applied stress is far lower than the laboratory load for dwell fatigue tests. Even though the slip initiation in Ti-6Al-4V alloy can be observed at $0.73\sigma_y$ [177], the current load is still insufficient to initiate the prismatic slip in soft macrozones before the stress dwell begins. During the dwell period,

no other force can drive the dislocation to slip, therefore, the strain accumulation (Fig. 6.13(e) and (f)) and the stress redistribution in the vicinity of the hard-soft interface (Fig. 6.13(g) and (h)) vanishes at two aspect ratios.

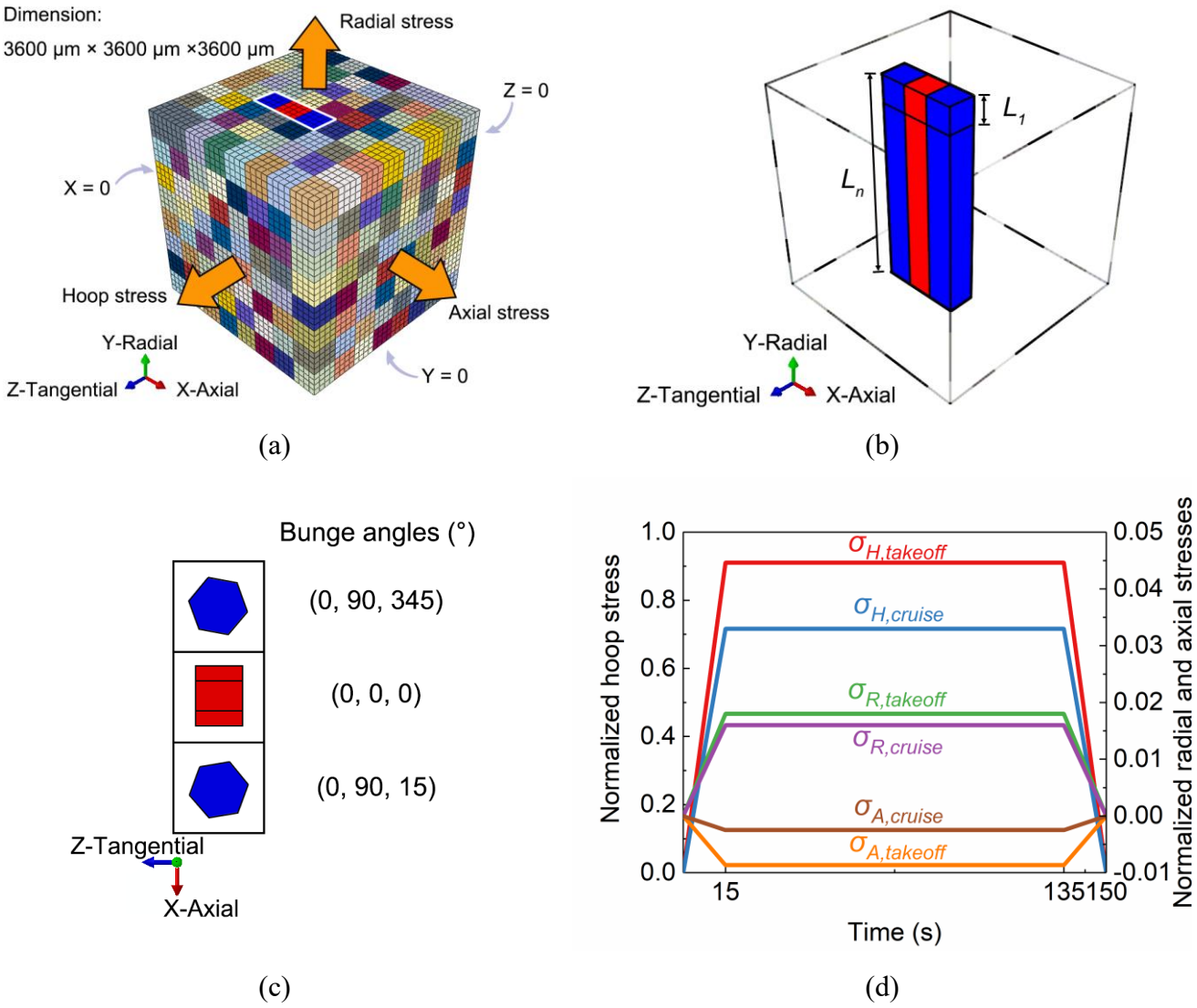

Fig. 6.12 (a) Polycrystalline model with macrozones surrounded by a white line, applied load and boundary conditions, (b) morphology of the macrozones, the aspect ratio of the macrozone is defined as $R = L_n/L_1$, (c) Euler angles of the macrozones in Bunge notation, and (d) loading histories of the hoop, radial, and axial stresses.

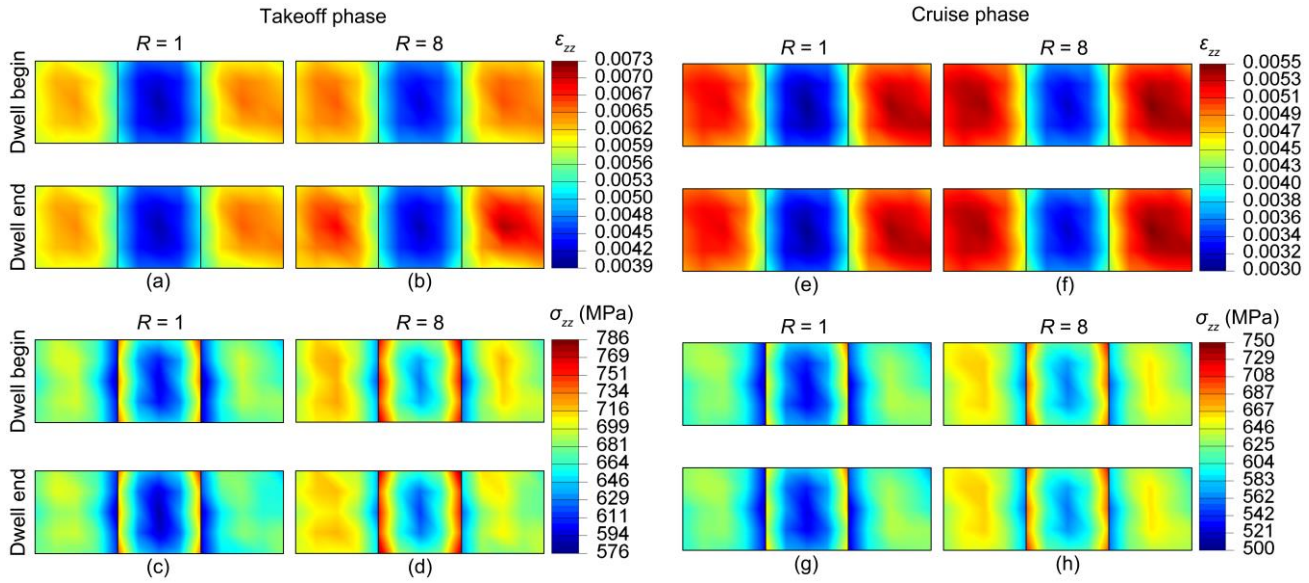

Fig. 6.13 Stress and strain contours within the hard-soft macrozone combination for (a-d) takeoff and (e-h) cruise phases: (a-b) strain and (c-d) stress distributions before and after dwell period for two aspect ratios of 1 and 8 at takeoff stage, (e-f) strain and (g-h) stress distributions before and after dwell period for two aspect ratios of 1 and 8 at cruise stage.

The relationship between the maximum redistributed stress within the hard macrozone and the aspect ratio is plotted in Fig. 6.14. For the takeoff phase, the size of the macrozones significantly affects stress redistribution. The stress change at the hard-soft interface increases from 0.218 MPa to 22.781 MPa as the aspect ratio increases from 1 to 8. The contribution of GND accumulation at the hard-soft interface to the stress enhancement is insignificant because of the large size scale [79]. It is worth noting that the magnitude of stress redistribution is negligible when the aspect ratio is 1 (equiaxed morphology). This is probably the reason why the dwell facets are prone to nucleate in large macrozones [27]. Furthermore, the fact that no stress change in the hard macrozone is observed at the cruise phase may also provide the evidence that dwell fatigue failure is more likely to occur during the takeoff or climbing phase [26],[27]. Therefore, in the absence of the thermal alleviation mechanism, the occurrence of in-service stress redistribution is rather dominated by the applied stress level and size of the macrozones than the high SRS exhibited by the prism slip-orientated soft macrozones at low temperatures.

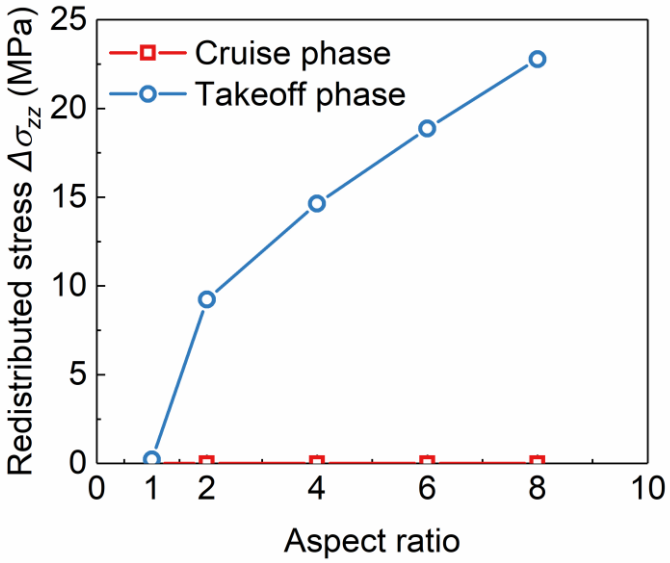

Fig. 6.14 Relationship between the peak redistributed stress $\Delta\sigma_{zz}$ within the hard macrozone and aspect ratio.

6.6 Experimental and industrial considerations

6.6.1 Experimental measurement of stress redistribution

In Section 6.4, the stress redistribution process at ambient and intermediate temperatures is numerically studied by using a crystal plasticity model. To experimentally measure the time-dependent stress redistribution during the dwell fatigue test, time-resolved approaches are required [181]. Since the dislocation pile-ups occur on the order of seconds or minutes, the in-situ SEM-DIC technique is a promising method to understand the temperature-sensitive stress redistribution within hard-soft grain combinations if quick image collection of these regions can be achieved [182]. Nevertheless, high angular resolution electron backscattered diffraction (HR-EBSD) is an ex-situ method to study the temperature-related mechanism as drastic stress redistribution will result in high residual stress at hard-soft grain boundaries [144].

6.6.2 Determination of macrozone properties

As stated in Section 6.5, the local stress redistribution is influenced by the size of the macrozones, which depends on the manufacturing procedure and subsequent thermomechanical processing. The

forging process is more likely to produce smaller macrozones than the cross-rolling process. A greater forging strain can further reduce the occurrence of large macrozones. The size of macrozones can be probed by destructive evaluation such as EBSD analysis and used for dwell fatigue life prediction [183]. To detect the macrozones during manufacturing, a new nondestructive ultrasonic backscatter attenuation method is also developed to determine the size of the macrozones [39]. However, the validity of the measurement at the component level should be verified and due to that no acceptable criterion with respect to the size of macrozones is introduced, experimental work is still under progress for the supplement. Besides, to improve the fuel economy in response to global warming, aero-engine manufacturers tend to increase the bypass ratio to reduce the specific fuel consumption, which will in turn increase the size of fan components. Thus, there is a risk of presence of larger macrozones if the deformation degree is insufficient during the forging process.

6.7 Summary

In this chapter, the effect of temperature on grain-scale strain rate sensitivity and creep behavior in Ti-6Al-4V alloy is investigated to understand the dwell fatigue sensitivity of a fan disc at operating states, with attention focused on the stress redistribution phenomenon occurring at hard-soft grain boundaries. The following results can be summarized:

1. The activation energy (ΔF) and activation volume (ΔV) of α phase in Ti-6Al-4V alloy increase with rising temperature. The higher activation volume at room temperature makes Ti-6Al-4V alloy less dwell sensitive than near-α Ti-6242 alloy, which is supported by the experimental results.
2. Concerning the shifting peak of strain rate sensitivity and the evolutions of activation energy and volume with temperature, the strain rate sensitivity of the prismatic slip-orientated soft grain in Ti-6Al-4V alloy increases from 293 K to 416 K and then declines to a low level at temperatures beyond 600 K. The strain rate sensitive temperature range is different from that of near-α Ti-6242 alloy.
3. The magnitude of stress redistribution is the largest at 416 K, followed by 293 K, 473 K, and 664 K. This trend is consistent with the variation of the strain rate sensitivity of the soft grain and GND accumulation at the hard-soft grain boundary. The diminishment of the strain rate

sensitivity and dwell strain accumulation in the soft grain at intermediate temperatures is suggested to derive from the high energy barrier to activate dislocation slip. Dynamic strain aging, strain hardening effect, and the degeneration of plastic anisotropy in HCP crystal are also accountable for the fading of stress redistribution.

4. Hoop stress is the principal stress leading to the failure and burst of the fan disc. The bore region of the fan disc with high hoop stress concentration and low stress triaxiality is prone to be the dangerous site where dwell facet nucleation occurs.
5. The factors affecting the dwell fatigue sensitivity of disc components vary due to different working temperatures. In default of the thermal alleviation mechanism that can inhibit dwell fatigue sensitivity, the applied stress and size of the macrozones dominate the local stress redistribution at the bore of the fan disc instead of the high strain rate sensitivity of soft macrozones at the working temperatures of the takeoff and cruise phases. The macrozone with high aspect ratios significantly boosts the magnitude of the redistributed stress at the takeoff phase. The low stress level at the cruise phase is insufficient to cause the onset of slip in soft macrozones and no stress redistribution arises. Hence, the phenomenon that dwell facet is prone to nucleate at large macrozones during the takeoff phase is elucidated.

7. Conclusions and future work

7.1 Conclusions

A systematic investigation has been carried out to understand the micromechanics of the cold dwell sensitive fatigue in titanium alloys using experimental and numerical approaches.

Motivated by a thorough review of the factors affecting the time-honored dwell fatigue phenomenon in Chapter 2, three different but interconnected aspects: deformation twinning, microstructural morphology, and temperature sensitivity, were elaborated from the viewpoint of both laboratory and industry.

To this end, a novel dislocation mechanism-based strain gradient crystal plasticity model incorporating deformation twinning and thermal expansion was developed in Chapter 3 to delineate the rate-sensitive, morphologically inhomogeneous, and size-dependent properties of a wide range of titanium alloys.

In Chapter 4, the role of deformation twinning was assessed by comparing the DIC strain measurements after the interrupted dwell fatigue test and crystal plasticity modeling. An essential agreement was found between two parallel predictions. The results indicated that dwell strain localization was dominated by slip activities, i.e., prismatic, basal, and pyramidal <*a*> slip in descending order, rather than deformation twinning, which could be described by a weighted averaged Schmid factor related to the crystallographic orientation. The nucleation of twins in soft grains is difficult at the early stage of dwell fatigue because of the small twin shear. On the other hand, the onset of twins in the hard grain could hinder the local stress enhancement at the hard-soft grain boundary during the dwell period, whilst the pile-up stress in the parent hard grain was almost unaffected. Therefore, the influence of deformation twinning on micromechanical dwell fatigue behavior of titanium alloys is insubstantial.

In Chapter 5, the effect of intergranular β phase on dwell facet initiation was clarified in Ti-Fe-O alloy with globular microstructure and extended to dual-phase titanium alloys. Nanoindentation tests suggested that the β phase was harder than the α phase, which could induce dislocation pile-ups at the α/β interface during the dwell period. This phenomenon was captured by crystal plasticity modeling and predicted to inhibit the stress redistribution within hard-soft grain combinations, particularly when

the α/β interface demonstrated low geometrical compatibility and the β lath presented a large thickness. This conclusion was beneficial to comprehend the "Ti-$624x$" issue. However, the enhanced stress in the β phase was prone to result in the competition of two dwell fatigue failure modes, i.e., the cavity nucleation/coalescence in the β phase and facet formation in the hard α grain.

From an engineering perspective, the effect of temperature on grain-scale strain rate sensitivity and creep mechanisms in Ti-6Al-4V alloy was studied to understand the dwell fatigue sensitivity of an aero-engine fan disc in Chapter 6. The rate-dependent parameters related to slip property were employed to analytically establish the relationship between strain rate sensitivity of a soft α-titanium single crystal and temperature. The variation of strain rate sensitivity with temperature influenced the stress redistribution occurring within the hard-soft grain combination, which in turn affected the dwell fatigue sensitivity. Further, the structural analysis for a Ti-6Al-4V fan disc provided the stress fields at takeoff and cruise phases to examine the in-service stress redistribution. The highly localized hoop stress and presence of large macrozones at the bore of the fan disc, rather than the fair rate sensitivity of soft macrozones at working temperatures, were responsible for triggering basal stress enhancement and dwell facet nucleation in hard macrozones.

7.2 Recommendations for future work

7.2.1 Explicit modeling of SSDs and deformation twinning

In the developed crystal plasticity model, the hardening effect caused by SSDs is based on the strain hardening model, which is merely an empirical attempt. Considering a direct measurement of SSD density is exceptionally demanding at the current time, the hardening mechanism still lacks mechanistic interpretation. Besides, the modeling of deformation twinning is relatively rough. Conventional modeling of twin nucleation depends on the shear strain on the twin plane, however, another physical discipline for twin nucleation is proposed according to the stored energy density related to dislocation interactions [128]. Therefore, the crystal plasticity modeling of deformation twinning necessitates more sophisticated work.

7.2.2 Dwell fatigue microcrack localization

As far as we are concerned, the stress redistribution inducing dwell faceting has been numerically (e.g., crystal plasticity simulation, discrete dislocation plasticity simulation) and analytically (Stroh pile-up model) analyzed, it is challenging to directly measure this process because the dwell fatigue crack initiation sites are generally subsurface. Even though the subsurface fatigue crack can be localized using the ultrasonic method, the resolution is at the millimeter level [184], which cannot cover the dwell facet nucleation and early microcrack propagation stages. Hence, an experimental approach is indispensable to manifest the numerical predictions.

7.2.3 Elastic anisotropy

The elastoplastic anisotropy of HCP crystal leads to the dwell effect in titanium alloys. Till this moment, considerable works have attributed the variation of dwell sensitivity in different titanium alloys to the discrepancy in plastic anisotropy. However, elastic anisotropy is also reported to play an important role [178], as shown in Fig. 1.6, especially when the applied stress level is well below the macroscopic yield strength (notably titanium aero-engine components in working condition). Thus, an investigation into the difference in elastic anisotropy (e.g., the influences of alloying element and temperature on directional Young's modulus of α phase with HCP lattice) is one direction to complement known explanations.

7.2.4 Titanium fan blade

For a high bypass civil turbofan engine, the fan disc is operated below 373 K, whereas the dwell fatigue sensitivity of Ti-6Al-4V alloy is supposed to be the highest at 416 K, as described in Chapter 6. Thus, the working temperatures of this component cannot cover the dwell sensitive temperature range, unlike the near-α titanium alloy discs or bliscs at the first several stages of the high-pressure compressor, which are operated over 573 K (out of the dwell sensitive temperature range) and experience a thermal alleviation during the cruise stage [171]. Since the titanium hollow-core fan blade is also involved in dwell fatigue failure and the maximum operating temperature is higher than the fan disc [27], more studies on fan blades are recommended to contribute to the understanding of the effect

of temperature on dwell fatigue of Ti-6Al-4V aero-engine components.

Appendix A. Effects of metallurgical factors and test condition on dwell fatigue sensitivity of titanium alloys

Table A Effects of microstructure and test condition on dwell fatigue sensitivity

Material	Thermomechanical processing	Microstructure	Volume fraction of α_p	Average grain size of α_p	Maximum stress	Dwell time	Load ratio	Load multiaxiality	Temperature	Dwell debit	Reference
Ti-6242	$\alpha+\beta$ processed	Equiaxed	90%	13.6 µm	$0.95\sigma_{0.2}$	120 s	$R=0$	Uniaxial	RT	7.9	
Ti-6243	$\alpha+\beta$ processed	Equiaxed	85%	11.7 µm	$0.95\sigma_{0.2}$	120 s	$R=0$	Uniaxial	RT	4.0	[52]
Ti-6244	$\alpha+\beta$ processed	Equiaxed	80%	9.6 µm	$0.95\sigma_{0.2}$	120 s	$R=0$	Uniaxial	RT	3.5	
Ti-6246	$\alpha+\beta$ processed	Equiaxed	60%	5.8 µm	$0.95\sigma_{0.2}$	120 s	$R=0$	Uniaxial	RT	2.9	
Ti-600	$\alpha+\beta$ processed	Bimodal	22-24%	14.5 µm 23.3 µm	$0.95\sigma_{0.2}$	120 s	$R=0.1$	Uniaxial	RT	4.2-4.5 2.2-2.4	[185]
Ti-6242	$\alpha+\beta$ processed	Bimodal	64%	8 µm	$0.95\sigma_{0.2}$	120 s	$R=0.05$	Uniaxial	RT	1.54	[167]
Ti-Fe-O	$\alpha+\beta$ processed	Equiaxed	92%	35 µm	$0.85\sigma_{0.2}$ $0.95\sigma_{0.2}$	120 s	$R=0.01$	Uniaxial	RT	13 30	[170]
Ti60	$\alpha+\beta$ processed	Bimidal	20%	63 µm	850 MPa 900 MPa	120 s	$R=0.1$	Uniaxial	RT	2.0-5.2 3.0	[187]
Ti-6242	$\alpha+\beta$ processed	Bimodal	65-70%	10 µm	$0.915\sigma_{0.2}$ $0.955\sigma_{0.2}$	120 s	$R=0$	Uniaxial	RT	15 18	[75]

Material	Thermomechanical processing	Microstructure	Volume fraction of α_p	Average grain size of α_p	Maximum stress	Dwell time	Load ratio	Load multiaxiality	Temperature	Dwell debit	Reference
IMI829	β processed	Basketweave			750 MPa 810 MPa 827 MPa	120 s	$R = 0$	Uniaxial	RT	5.13 11.45 17.79	[51]
Ti-6242	$\alpha + \beta$ processed	Bimodal	5% 33% 60% 69%	10.5 µm 10.9 µm 11.9 µm 11.8 µm	826-950 MPa	120 s	$R = 0$	Uniaxial	RT	3.6-5.1 4.5-10.7 3.7-4.8 8.7-12.6	[47]
Ti-64	$\alpha + \beta$ processed	Equiaxed	>90%	5 µm	750 MPa	30 s 120 s	$R = 0.1$	Uniaxial	RT	96-103 83-193	[186]
IMI685	β processed	Basketweave			750 MPa 700 MPa	300 s	$R = 0.05$	Uniaxial	RT 425 K	16 26	[188]
Ti-6242	$\alpha + \beta$ processed	Bimodal	70%	10 µm	$0.95\sigma_{0.2}$	120 s	$R = 0$	Uniaxial	RT	3.4-15.3	[41]
CP-Ti		Equiaxed	100%		236 MPa	0.2 s 1 s 5 s	$R = 0$	Uniaxial	RT	3.0 4.7 17.0	[30]
Ti-7Al		Equiaxed	100%		709 MPa	120 s	$R = 0$ $R = 0.5$	Uniaxial	RT	74.7 53.3	[39]
IMI834	$\alpha + \beta$ processed	Bimodal		15-30 µm	800 MPa 880 MPa	1 s 15 s 120 s 300 s	$R = 0.1$	Uniaxial	293 K	1.1-1.6 1.9-4.5 6.5-18.3 6.0-25.5	[189]
IMI685	β processed	Basketweave			$0.7 - 0.8\sigma_t$	120 s	$R = 0.1$	Biaxial	RT	1-14	[36]

Material	Thermomechanical processing	Microstructure	Volume fraction of α_p	Average grain size of α_p	Maximum stress	Dwell time	Load ratio	Load multiaxiality	Temperature	Dwell debit	Reference
Ti-64	$\alpha+\beta$ processed	Equiaxed	63%	48 μm	690 MPa 740 MPa 800 MPa 840MPa	80 s	$R=0$	Biaxial	RT	1.1 1.8 2.4 1.7	[78]
Ti-6246	β processed	Acicular			$0.86-0.9\sigma_t$	120 s	$R=0.1$	Uniaxial	293 K 373 K 423 K	1.5-2.2	[62]
Ti-64 ELI	$\alpha+\beta$ processed	Equiaxed	>90%	30 μm	815 MPa	120 s	$R=0$	Uniaxial	RT	8.0	[9]
Ti-6243X	β processed	Basketweave			929 MPa	60 s	$R=-1$	Uniaxial	RT	1.1-2.0	[190]
IMI834	$\alpha+\beta$ processed	Bimodal	15%	60 μm	850-1000 MPa	120 s	$R=0.1$	Uniaxial	RT	1-8	[72]

Appendix B. Slip and twinning systems for HCP crystals

Table B Slip and twinning systems in α phase with HCP structure are presented below.

Slip/twinning systems	Slip plane normal vector			Slip direction vector		
	x	y	z	x	y	z
Basal <*a*> slip	0.000	0.000	1.000	1.000	0.000	0.000
	0.000	0.000	1.000	0.500	-0.866	0.000
	0.000	0.000	1.000	0.500	0.866	0.000
Prismatic <*a*> slip	-0.866	-0.500	0.000	0.500	-0.866	0.000
	0.866	-0.500	0.000	0.500	0.866	0.000
	0.000	-1.000	0.000	1.000	0.000	0.000
Pyramidal <*a*> slip	0.760	-0.439	-0.479	0.500	0.866	0.000
	-0.760	0.439	-0.479	0.500	0.866	0.000
	0.000	0.878	0.479	1.000	0.000	0.000
	0.000	-0.878	0.479	1.000	0.000	0.000
	0.760	0.439	0.479	0.500	-0.866	0.000
	-0.760	-0.439	0.479	0.500	-0.866	0.000
Pyramidal 1st <*c*+*a*> slip	0.760	-0.439	-0.479	0.533	0.000	0.846
	0.760	-0.439	-0.479	0.267	-0.462	0.846
	-0.760	0.439	-0.479	-0.533	0.000	0.846
	-0.760	0.439	-0.479	-0.267	0.462	0.846
	0.000	0.878	0.479	-0.267	-0.462	0.846
	0.000	0.878	0.479	0.267	-0.462	0.846
	0.000	-0.878	0.479	0.267	0.462	0.846
	0.000	-0.878	0.479	-0.267	0.462	0.846
	0.760	0.439	0.479	-0.533	0.000	0.846
	0.760	0.439	0.479	-0.267	-0.462	0.846
	-0.760	-0.439	0.479	0.533	0.000	0.846
	-0.760	-0.439	0.479	0.267	0.462	0.846
Pyramidal 2nd <*c*+*a*> slip $\{11\bar{2}2\}$ Twinning	-0.423	-0.733	0.533	0.267	0.462	0.846
	-0.423	-0.733	-0.533	-0.267	-0.462	0.846
	0.423	-0.733	-0.533	0.267	-0.462	0.846
	0.423	-0.733	0.533	-0.267	0.462	0.846
	0.846	0.000	-0.533	0.533	0.000	0.846
	0.846	0.000	0.533	-0.533	0.000	0.846
$\{10\bar{1}2\}$ Twinning	0.000	-0.676	-0.737	0.000	-0.737	0.676
	-0.585	0.338	0.737	0.639	-0.369	0.676
	-0.585	0.338	-0.737	-0.639	0.369	0.676
	0.000	-0.676	0.737	0.000	0.737	0.676
	0.585	0.338	-0.737	0.639	0.369	0.676
	-0.585	0.338	0.737	0.639	-0.369	0.676

Appendix C. Crystallographic rotations and stiffness matrix transformations

In crystallographic and texture analysis, Euler angles with Bunge notation are commonly used for describing the orientations of each crystal [191]. Thus, the rotation matrix computed by Bunge angles is used to rotate the matrix of a crystal and adhered here:

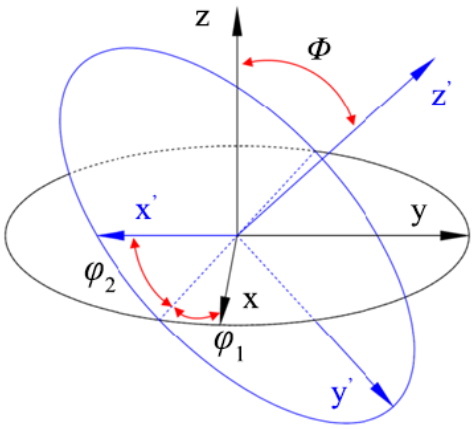

Fig. C Euler angles for Bunge convention.

$$\boldsymbol{R} = \begin{bmatrix} cos\varphi_1 cos\varphi_2 - sin\varphi_1 sin\varphi_2 cos\phi & sin\varphi_1 cos\varphi_2 + cos\varphi_1 sin\varphi_2 cos\phi & sin\varphi_2 sin\phi \\ -cos\varphi_1 sin\varphi_2 - sin\varphi_1 cos\varphi_2 cos\phi & -sin\varphi_1 sin\varphi_2 + cos\varphi_1 cos\varphi_2 cos\phi & cos\varphi_2 sin\phi \\ sin\varphi_1 sin\phi & -cos\varphi_1 sin\phi & cos\phi \end{bmatrix} \quad (C.1)$$

The rotation matrix transforming local elastic matrix to global elastic matrix is given by

$$\boldsymbol{R_{rot}} = \begin{bmatrix} R_{11}^2 & R_{21}^2 & R_{31}^2 & R_{11}R_{21} & R_{21}R_{31} & R_{31}R_{11} \\ R_{12}^2 & R_{22}^2 & R_{32}^2 & R_{12}R_{22} & R_{22}R_{32} & R_{32}R_{12} \\ R_{13}^2 & R_{23}^2 & R_{33}^2 & R_{13}R_{23} & R_{23}R_{33} & R_{33}R_{13} \\ 2R_{11}R_{12} & 2R_{21}R_{22} & 2R_{31}R_{32} & R_{11}R_{22}+R_{12}R_{21} & R_{21}R_{32}+R_{22}R_{31} & R_{31}R_{12}+R_{32}R_{11} \\ 2R_{12}R_{13} & 2R_{22}R_{23} & 2R_{32}R_{33} & R_{23}R_{12}+R_{13}R_{22} & R_{22}R_{33}+R_{23}R_{32} & R_{32}R_{13}+R_{33}R_{12} \\ 2R_{13}R_{11} & 2R_{23}R_{21} & 2R_{33}R_{31} & R_{13}R_{21}+R_{11}R_{23} & R_{23}R_{31}+R_{21}R_{33} & R_{33}R_{11}+R_{31}R_{13} \end{bmatrix} \quad (C.2)$$

Appendix D. Fortran code for calculating shear strain gradient

The following URDFIL code is used for calculating the shear strain gradient in each slip system.

```
      DIMENSION ARRAY(513),JRRAY(NPRECD,513),TIME(2),
     2          TRM3(3), GAUSS1(8), GAUSS2(8), GAUSS3(8), TEMP1(8),
     3          SF(8,8), IITRM(8), DSF(8,24), ACOBI2(3,3), RACOBI2(3,3),
     4          GAUSS11(8), GAUSS22(8), GAUSS33(8), RELACTV(5)
      EQUIVALENCE (ARRAY(1),JRRAY(1,1))

      PARAMETER(NP=1000000,NE=100000,g=0.577350269199626,NUMSYSH=30,NUMSYSC=
     12)

C
C     FIND CURRENT INCREMENT
C      KSTEP: Step number  KINC: Increment number  TIME(1): Value of the step time at the end of
       the increment
C     TIME(2): Value of the total time at the end of the increment
       CALL POSFIL(KSTEP,KINC,ARRAY,JRCD)

C
C---- Initialize the isoparametric coordinates of eight Gauss points
C
      GAUSS1(1)=g
      GAUSS2(1)=-g
      GAUSS3(1)=g

      GAUSS11(1)=g
      GAUSS22(1)=-g
      GAUSS33(1)=g

      GAUSS1(2)=g
      GAUSS2(2)=g
      GAUSS3(2)=g

      GAUSS11(2)=g
      GAUSS22(2)=g
      GAUSS33(2)=g

      GAUSS1(3)=g
      GAUSS2(3)=-g
      GAUSS3(3)=-g
```

GAUSS11(3)=g
GAUSS22(3)=g
GAUSS33(3)=-g

GAUSS1(4)=g
GAUSS2(4)=g
GAUSS3(4)=-g

GAUSS11(4)=g
GAUSS22(4)=-g
GAUSS33(4)=-g

GAUSS1(5)=-g
GAUSS2(5)=-g
GAUSS3(5)=g

GAUSS11(5)=-g
GAUSS22(5)=-g
GAUSS33(5)=g

GAUSS1(6)=-g
GAUSS2(6)=g
GAUSS3(6)=g

GAUSS11(6)=-g
GAUSS22(6)=g
GAUSS33(6)=g

GAUSS1(7)=-g
GAUSS2(7)=-g
GAUSS3(7)=-g

GAUSS11(7)=-g
GAUSS22(7)=g
GAUSS33(7)=-g

GAUSS1(8)=-g
GAUSS2(8)=g
GAUSS3(8)=-g

GAUSS11(8)=-g
GAUSS22(8)=-g
GAUSS33(8)=-g

```
C
C---- Calculate the eight values of shape function at each Gauss point
C
      DO I=1,8
        SF(I,1)=(1+GAUSS1(I))*(1-GAUSS2(I))*(1+GAUSS3(I))*0.125
        SF(I,2)=(1+GAUSS1(I))*(1+GAUSS2(I))*(1+GAUSS3(I))*0.125
        SF(I,3)=(1+GAUSS1(I))*(1+GAUSS2(I))*(1-GAUSS3(I))*0.125
        SF(I,4)=(1+GAUSS1(I))*(1-GAUSS2(I))*(1-GAUSS3(I))*0.125
        SF(I,5)=(1-GAUSS1(I))*(1-GAUSS2(I))*(1+GAUSS3(I))*0.125
        SF(I,6)=(1-GAUSS1(I))*(1+GAUSS2(I))*(1+GAUSS3(I))*0.125
        SF(I,7)=(1-GAUSS1(I))*(1+GAUSS2(I))*(1-GAUSS3(I))*0.125
        SF(I,8)=(1-GAUSS1(I))*(1-GAUSS2(I))*(1-GAUSS3(I))*0.125
      END DO

      DO K1=1,9999999
        CALL DBFILE(0,ARRAY,JRCD)
        IF (JRCD.NE.0) GO TO 110
        KEY=JRRAY(1,2)
C
C----- Obtain the results in .fil
C     1: Index of the element
        IF (KEY.EQ.1) THEN
          IELM=JRRAY(1,3)
          ILEM1=8*IELM
C
C----- Obtain the coordinate of each integration point
C
C     8: Coordinate of the eight integration points for C3D8 element
        ELSE IF (KEY.EQ.8) THEN
          KEL=JRRAY(1,2)
          DO I=3,5
            CDG(NUM2,I-2)=ARRAY(I)
          END DO
C           WRITE (17,130) NUM2,CDG(NUM2,1),CDG(NUM2,2),CDG(NUM2,3)
          NUM2=NUM2+1
C     5: State variables of the eight integration points for C3D8 element
C     3 - NSLPTL+2: current strength in slip systems
C     NSLPTL+3 - 2*NSLPTL+2: shear strain in slip systems
C     2*NSLPTL+3 - 3*NSLPTL+2: resolved shear stress in slip systems
        ELSE IF (KEY.EQ.5) THEN
          KEL=JRRAY(1,2)
          IF (PHASE(NUM1).EQ.0.) THEN
            DO I=NUMSYSH+3,2*NUMSYSH+2
              SSG(NUM1,I-NUMSYSH-2)=ARRAY(I)
```

```
            END DO

110   CONTINUE

C
C----- Calculate the shear strain on slip systems at each node
C
      DO I=1,IELM
        INODE=8*(I-1)
        IF (PHASE(INODE+1).EQ.0.) THEN
          DO J=1,NUMSYSH
            DO K=1,8
              TEMP1(K)=SSG(INODE+K,J)
            END DO

            CALL LUBKSB (SF,8,8,IITRM,TEMP1)
            DO K=1,8
              SSN(INODE+K,J)=TEMP1(K)
            END DO
          END DO
        ELSE
          DO J=1,NUMSYSC
            DO K=1,8
              TEMP1(K)=SSG(INODE+K,J)
            END DO

            CALL LUBKSB (SF,8,8,IITRM,TEMP1)
            DO K=1,8
              SSN(INODE+K,J)=TEMP1(K)
            END DO
          END DO
        END IF
      END DO

C
C----- Correspond Gauss points and nodes with respect to coordinates
C
      DO I=1,IELM
        INODE=8*(I-1)
        DO J=1,8
          IF (J.EQ.3) THEN
            DO K=1,3
              GAUSSNODE(INODE+J,K)=CDG(INODE+J+1,K)
            END DO
```

```
          ELSE IF (J.EQ.4) THEN
            DO K=1,3
              GAUSSNODE(INODE+J,K)=CDG(INODE+J-1,K)
            END DO
          ELSE IF (J.EQ.7) THEN
            DO K=1,3
              GAUSSNODE(INODE+J,K)=CDG(INODE+J+1,K)
            END DO
          ELSE IF (J.EQ.8) THEN
            DO K=1,3
              GAUSSNODE(INODE+J,K)=CDG(INODE+J-1,K)
            END DO
          ELSE
            DO K=1,3
              GAUSSNODE(INODE+J,K)=CDG(INODE+J,K)
            END DO
          END IF
        END DO
      END DO

C
C----- Calculate spatial derivative of isoparametric shape functions at Gauss points
C
      DO I=1,8
        IF (I.EQ.1) THEN
          DO J=1,8
            DSF(J,3*I-2)=0.125*(1-GAUSS22(J))*(1+GAUSS33(J))
            DSF(J,3*I-1)=-0.125*(1+GAUSS11(J))*(1+GAUSS33(J))
            DSF(J,3*I)=0.125*(1+GAUSS11(J))*(1-GAUSS22(J))
          END DO
        ELSE IF (I.EQ.2) THEN
          DO J=1,8
            DSF(J,3*I-2)=0.125*(1+GAUSS22(J))*(1+GAUSS33(J))
            DSF(J,3*I-1)=0.125*(1+GAUSS11(J))*(1+GAUSS33(J))
            DSF(J,3*I)=0.125*(1+GAUSS11(J))*(1+GAUSS22(J))
          END DO
        ELSE IF (I.EQ.3) THEN
          DO J=1,8
            DSF(J,3*I-2)=0.125*(1+GAUSS22(J))*(1-GAUSS33(J))
            DSF(J,3*I-1)=0.125*(1+GAUSS11(J))*(1-GAUSS33(J))
            DSF(J,3*I)=-0.125*(1+GAUSS11(J))*(1+GAUSS22(J))
          END DO
        ELSE IF (I.EQ.4) THEN
          DO J=1,8
```

```
            DSF(J,3*I-2)=0.125*(1-GAUSS22(J))*(1-GAUSS33(J))
            DSF(J,3*I-1)=-0.125*(1+GAUSS11(J))*(1-GAUSS33(J))
            DSF(J,3*I)=-0.125*(1+GAUSS11(J))*(1-GAUSS22(J))
          END DO
        ELSE IF (I.EQ.5) THEN
          DO J=1,8
            DSF(J,3*I-2)=-0.125*(1-GAUSS22(J))*(1+GAUSS33(J))
            DSF(J,3*I-1)=-0.125*(1-GAUSS11(J))*(1+GAUSS33(J))
            DSF(J,3*I)=0.125*(1-GAUSS11(J))*(1-GAUSS22(J))
          END DO
        ELSE IF (I.EQ.6) THEN
          DO J=1,8
            DSF(J,3*I-2)=-0.125*(1+GAUSS22(J))*(1+GAUSS33(J))
            DSF(J,3*I-1)=0.125*(1-GAUSS11(J))*(1+GAUSS33(J))
            DSF(J,3*I)=0.125*(1-GAUSS11(J))*(1+GAUSS22(J))
          END DO
        ELSE IF (I.EQ.7) THEN
          DO J=1,8
            DSF(J,3*I-2)=-0.125*(1+GAUSS22(J))*(1-GAUSS33(J))
            DSF(J,3*I-1)=0.125*(1-GAUSS11(J))*(1-GAUSS33(J))
            DSF(J,3*I)=-0.125*(1-GAUSS11(J))*(1+GAUSS22(J))
          END DO
        ELSE
          DO J=1,8
            DSF(J,3*I-2)=-0.125*(1-GAUSS22(J))*(1-GAUSS33(J))
            DSF(J,3*I-1)=-0.125*(1-GAUSS11(J))*(1-GAUSS33(J))
            DSF(J,3*I)=-0.125*(1-GAUSS11(J))*(1-GAUSS22(J))
          END DO
        END IF
      END DO

C
C----- Calculate the inverse matrix of the Jacobi matrix at the Gauss points (for three coordinates)
C
      DO I=1,NE
        DO J=1,3
          ACOBI1(I,J)=0.
        END DO
      END DO

      DO J=1,IELM
        INODE=3*(J-1)
        IGAUS=8*(J-1)
        DO I=1,8
```

```
      ACOBI1(INODE+1,1)=ACOBI1(INODE+1,1)+GAUSSNODE(IGAUS+I,1)*
2                 DSF(I,3*I-2)
      ACOBI1(INODE+1,2)=ACOBI1(INODE+1,2)+GAUSSNODE(IGAUS+I,1)*
2                 DSF(I,3*I-1)
      ACOBI1(INODE+1,3)=ACOBI1(INODE+1,3)+GAUSSNODE(IGAUS+I,1)*
2                 DSF(I,3*I)
      ACOBI1(INODE+2,1)=ACOBI1(INODE+2,1)+GAUSSNODE(IGAUS+I,2)*
2                 DSF(I,3*I-2)
      ACOBI1(INODE+2,2)=ACOBI1(INODE+2,2)+GAUSSNODE(IGAUS+I,2)*
2                 DSF(I,3*I-1)
      ACOBI1(INODE+2,3)=ACOBI1(INODE+2,3)+GAUSSNODE(IGAUS+I,2)*
2                 DSF(I,3*I)
      ACOBI1(INODE+3,1)=ACOBI1(INODE+3,1)+GAUSSNODE(IGAUS+I,3)*
2                 DSF(I,3*I-2)
      ACOBI1(INODE+3,2)=ACOBI1(INODE+3,2)+GAUSSNODE(IGAUS+I,3)*
2                 DSF(I,3*I-1)
      ACOBI1(INODE+3,3)=ACOBI1(INODE+3,3)+GAUSSNODE(IGAUS+I,3)*
2                 DSF(I,3*I)
    END DO
  END DO

  DO I=1,IELM
    INODE=3*(I-1)
    DO J=1,3
      DO K=1,3
        ACOBI2(J,K)=ACOBI1(INODE+J,K)
      END DO
    END DO

    CALL LUDCMP (ACOBI2, 3, 3, TRM3, DCMP)

    DO J=1,3
      DO K=1,3
        IF (K.EQ.J) THEN
          RACOBI2(K,J)=1.
        ELSE
          RACOBI2(K,J)=0.
        END IF
      END DO
    END DO

    DO J=1,3
      CALL LUBKSB (ACOBI2, 3, 3, TRM3, RACOBI2(1,J))
    END DO
```

```
        DO J=1,3
          DO K=1,3
            RACOBI(INODE+J,K)=RACOBI2(J,K)
          END DO
        END DO
      END DO

C
C----- Calculate the shear strain gradient at eight Gauss points for each slip system
C
      DO I=1,3*NUMSYSH
        DO J=1,NP
          SSGRAD(J,I)=0.
        END DO
      END DO

C----- L: The number of slip systems
C----- M: The number of all integration points
C----- K: The number of all shape functions (For eight nodes)
C----- J: The three value of the strain gradient
      DO N=1,IELM
        M=8*(N-1)
        IELM1=3*(N-1)
        IF (PHASE(M+1).EQ.0.) THEN
          DO L=1,NUMSYSH
            DO I=1,8
              DO K=1,8
                DO J=1,3
                  SSGRAD(M+I,3*L-2)=SSGRAD(M+I,3*L-2)+SSN(M+K,L)*
     2                    DSF(I,3*K+(J-3))*
     3                    RACOBI(IELM1+J,1)
                  SSGRAD(M+I,3*L-1)=SSGRAD(M+I,3*L-1)+SSN(M+K,L)*
     2                    DSF(I,3*K+(J-3))*
     3                    RACOBI(IELM1+J,2)
                  SSGRAD(M+I,3*L)=SSGRAD(M+I,3*L)+SSN(M+K,L)*
     2                  DSF(I,3*K+(J-3))*
     3                    RACOBI(IELM1+J,3)
                END DO
              END DO
            END DO
          END DO
        ELSE
          DO L=1,NUMSYSC
```

```
          DO I=1,8
            DO K=1,8
              DO J=1,3
                SSGRAD(M+I,3*L-2)=SSGRAD(M+I,3*L-2)+SSN(M+K,L)*
     2                    DSF(I,3*K+(J-3))*
     3                    RACOBI(IELM1+J,1)
                SSGRAD(M+I,3*L-1)=SSGRAD(M+I,3*L-1)+SSN(M+K,L)*
     2                    DSF(I,3*K+(J-3))*
     3                    RACOBI(IELM1+J,2)
                SSGRAD(M+I,3*L)=SSGRAD(M+I,3*L)+SSN(M+K,L)*
     2                   DSF(I,3*K+(J-3))*
     3                    RACOBI(IELM1+J,3)
              END DO
            END DO
          END DO
        END DO
      END IF
    END DO
```

Reference

[1]. Lütjering G, Williams JC. Titanium, second edition, Springer, 2007

[2]. Private communication of data, 2018.

[3]. Williams JC, Starke Jr EA. Progress in structural materials for aerospace systems, Acta Mater 2003; 51: 5775-99.

[4]. Boyer RR. An overview on the use of titanium in the aerospace industry, Mater Sci Eng A 1996; 213: 103-14.

[5]. Williams JC, Banerjee D. Perspectives on Titanium Science and Technology, Acta Mater 2013; 61: 844-79.

[6]. Hémery S, Villechaise P, Banerjee D. Microplasticity at room temperature in α/β titanium alloys. Metall Mater Trans A 2020; 51: 4931-69.

[7]. Rugg D, Dixon M, Burrows J. High-temperature application of titanium alloys in gas turbines. Material life cycle opportunities and threats - an industrial perspective, Mater High Temp 2016; 33: 536-41.

[8]. Bache MR. Processing titanium alloys for optimum fatigue performance, Int J Fatigue 1999: 21: S105-S111.

[9]. Sun C, Li Y, Xu B. Effects of intermittent loading time and stress ratio on dwell fatigue behavior of titanium alloy Ti-6Al-4V ELI used in deep-sea submersibles. J Mater Sci Technol 2021; 77:223-36.

[10]. Wang F, Cui W. Experimental investigation on dwell-fatigue property of Ti-6Al-4V ELI used in deep-sea manned cabin. Mater Sci Eng A 2015; 642: 136-41.

[11]. Britton TB, Birosca S, Preuss M, Wilkinson A. Electron backscatter diffraction study of dislocation content of a macrozone in hot-rolled Ti-6Al-4V alloy. Scr Mater 2010; 62: 639-42.

[12]. Rugg D, Dixon M, Dunne FPE. Effective structural unit size in titanium alloys. J Strain Anal Eng 2007; 42(4): 269-79.

[13]. Pilchak AL. A simple model to account for the role of microtexture on fatigue and dwell fatigue lifetimes of titanium alloys. Scr Mater 2014; 74: 68-71.

[14]. Kim JY, Rokhlin SI. Determination of elastic constants of generally anisotropic inclined lamellar structure using line-focus acoustic microscopy. J Acoust Soc Am 2009; 126(6): 2998–3007.

[15]. Kim JY, Yakovlev V, Rokhlin SI. Line-focus acoustic microscopy of Ti-6242 α/β single colony: determination of elastic constants. AIP Conference Proceedings 2002; 615(1): 1118-25.

[16]. Adebisi RA, Sathish S, Pilchak AL, Shade PA. Elastic constants of α Ti-7Al measured using resonant ultrasound spectroscopy. AIP Conference Proceedings 2016; 1706(1): 070005.

[17]. Wielewski E, Boyce DE, Park JS, Miller MP, Dawson PR. A methodology to determine the elastic moduli of crystals by matching experimental and simulated lattice strain pole figures using discrete harmonics. Acta Mater 2017; 126: 469-80.

[18]. Schick A, Fritzen CP, Floer W, Krupp YMHU. Stress concentrations at grain boundaries due to anisotropic elastic material behavior. WIT Trans Eng Sci 2000; 26.

[19]. Raghunathan SL, Stapleton AM, Dashwood RJ, Jackson M, Dye D. Micromechanics of Ti-10V-2Fe-3Al: In situ synchrotron characterization and modeling. Acta Mater 2007; 55(20): 6861-72.

[20]. Williams JC, Baggerly RG, Paton NE. Deformation behavior of HCP Ti-Al alloy single crystals. Metall Mater Trans A 2002; 33: 837-50.

[21]. Zhao Z, Zhang J, Sun Y, Liu Z. Sensor fault diagnosis of aero-engine based on divided flight status. Rev Sci Instrum 2017; 88(11): 115007.

[22]. Cann JL, De Luca A, Dunand DC, Dye D, Miracle DB, Oh HS, Olivetti EA, Pollock TM, Poole WJ, Yang R, Tasan CC. Sustainability through alloy design: Challenges and opportunities. Prog Mater Sci 2021; 117: 100722.

[23]. Bache MR. A review of dwell sensitive fatigue in titanium alloys: the role of microstructure, texture and operating conditions. Int J Fatigue 2003; 25: 1079-87.

[24]. Pugh P. The magic of a name: the Rolls-Royce story, Part 2: the power behind the jets 1945-1987. London, England: Icon Books Ltd.; 2001.

[25]. Aircraft Accident Report AAR9801. Uncontained engine failure Delta Airlines flight 1288 McDonnell Douglas MD-88, N927DA Pensacola, Florida July 6, 1996. National Transportation Safety Board: Washington D.C., USA, 1998.

[26]. Aviation Investigation Report A97F0059. Uncontained engine failure Canadian Airlines International Boeing 767-375ER C-FTCA Beijing, China 06 September 1997. Transportation Safety Board of Canada: Quebec, Canada, 1999.

[27]. BEA2017-0568. Accident to the AIRBUS A380-861 equipped with Engine Alliance GP7270 engines registered F-HPJE operated by Air France on 30 September 2017 in cruise over Greenland (Denmark). Bureau D'enquêtes et D'analyses Pour La Sécurité de L'aviation Civile: Le Bourget, France, 2020.

[28]. Final Report. B777-300ER, Registration 9V-SWB Engine Fire 27 June 2016. Transport Safety Investigation Bureau: Singapore, 2017.

[29]. Glavicic MG, Furrer DU, Shen G. A Rolls Royce Corporation industrial perspective of titanium process modelling and optimization current capabilities and future needs. J Strain Anal Eng 2010; 45(5): 329-36.

[30]. Peng J, Zhou CY, Dai Q, He XH. Dwell fatigue and cycle deformation of CP Ti at ambient temperature. Mater Des 2015; 71: 1-16.

[31]. Eylon D, Hall JA. Fatigue behavior of beta processed titanium alloy IMI 685. Metall Trans A 1977; 8(6): 981-90.

[32]. Davidson DL, Eylon D. Titanium alloy fatigue fracture facet investigation by selected area electron channeling. Metall Trans A 1980; 11(5): 837-43.

[33]. Pilchak AL, Williams JC. Observations of facet formation in near-α titanium and comments on the role of hydrogen. Metall Mater Trans A 2011; 42: 1000-27.

[34]. Sinha V, Mills MJ, Williams JC. Crystallography of fracture facets in a near-alpha titanium alloy. Metall Mater Trans A 2006; 37(6): 2015-26.

[35]. Sinha V, Mills MJ, Williams JC. Determination of crystallographic orientation of dwell-fatigue fracture facets in Ti-6242 alloy. J Mater Sci 2007; 42(19): 8334-41.

[36]. Evans W, Bache MR. Dwell-sensitive fatigue under biaxial loads in the near-alpha titanium alloy IMI685. Int J Fatigue 1994; 16(7): 443-52.

[37]. Stroh AN. The formation of cracks as a result of plastic flow. P Roy Soc Lond.A Mat 1954; 223: 404-14.

[38]. Hasija V, Ghosh S, Mills MJ, Joseph DS. Deformation and creep modeling in polycrystalline Ti–6Al alloys. Acta Mater 2003; 51: 4533-49.

[39]. Mills M, Ghosh S, Rokhlin S, Brandes MC, Pilchak AL, Williams JC. The evaluation of cold dwell fatigue in Ti-6242. Final Report, Federal Aviation Administration, DOT/FAA/AR-06/24; 2018.

[40]. Nelson HG, Williams DP, Stein JE. Environmental hydrogen embrittlement of an $\alpha - \beta$ titanium alloy: Effect of microstructure. Metall Mater Trans B 1972; 3: 473-9.

[41]. Sinha V, Schwarz RB, Mills MJ, Williams JC. Influence of hydrogen on dwell-fatigue response of near-alpha titanium alloys. Acta Mater 2020; 188: 315-27.

[42]. Gerland M, Lefranc P, Doquet V, Sarrazin-Baudoux C. Deformation and damage mechanisms in an α/β 6242 Ti alloy in fatigue, dwell-fatigue and creep at room temperature. Influence of internal hydrogen. Mater Sci Eng A 2009; 507: 132-43.

[43]. Xiong Y, Karamched PS, Nguyen C, Collins DM, Grilli N, Magazzeni CM, Tarleton E, Wilkinson AJ. An in-situ synchrotron in titanium: Effect of temperature and oxygen on cold dwell fatigue. Acta Mater 2021; 213: 116937.

[44]. Venkataramani G, Kirane K, Ghosh S. Microstructural parameters affecting creep induced load shedding in Ti-6242 by a size dependent crystal plasticity FE model. Int J Plast 2007; 24: 428-54.

[45]. Hémery S, Villechaise P. Comparison of slip system activation in Ti-6Al-2Sn-4Zr-2Mo and Ti-6Al-2Sn-4Zr-6Mo under tensile, fatigue and dwell-fatigue loadings. Mater Sci Eng A 2017; 697: 177-83.

[46]. Ashton PJ, Jun TS, Zhang Z, Britton TB, Harte AM, Leen SB, Dunne FPE. The effect of the beta phase on the micromechanical response of dual-phase titanium alloys. Int J Fatigue 2017; 100: 377-87.

[47]. Kassner ME, Kosaka Y, Hall JA. Low-cycle dwell-time fatigue in Ti-6242. Metall Mater Trans A 1999; 30(9): 2383-9.

[48]. Liu J, Yang L, Wang Q, Yang R. Effect of volume fraction of primary α phase on dwell and normal cyclic fatigue behavior of Ti60 alloy. Proceedings of the 13th world conference on titanium. Hoboken, NJ, USA, 2016.

[49]. Zhang Z, Dunne FPE. Phase morphology, variants and crystallography of alloy microstructures in cold dwell fatigue. Int J Fatigue 2018; 113: 324-34.

[50]. Waheed S, Zheng Z, Balint DS, Dunne FPE. Microstructural effects on strain rate and dwell sensitivity in dual-phase titanium alloys. Acta Mater 2019; 162: 136-48.

[51]. Song Z, Hoeppner DW. Size effect on the fatigue behaviour of IMI 829 titanium alloy under dwell conditions. Int J Fatigue 1989; 11(2): 85-90.

[52]. Qiu J, Ma Y, Lei J, Liu Y, Huang A, Rugg D, Yang R. A comparative study on dwell fatigue of

Ti-6Al-2Sn-4Zr-xMo (x= 2 to 6) alloys on a microstructure-normalized basis. Metall Mater Trans A 2014; 45: 6075-87.

[53]. Seal JR, Crimp MA, Bieler TR, Boehlert CJ. Analysis of slip transfer and deformation behavior across the α/β interface in Ti–5Al–2.5 Sn (wt.%) with an equiaxed microstructure. Mater Sci Eng A 2012; 552: 61-8.

[54]. Zhou Y, Wang K, Yan Z, Xin R, Wei S, Wang X, Liu Q. Ex-situ study on mechanical properties and deformation mechanism of three typical microstructures in TA19 titanium alloy. Mater Charact 2020; 167: 110521.

[55]. Seto H, Takebe H, Takahashi K, Fujii H, Mori K. Effects of oxygen concentration and grain size on twinning deformation behavior in commercially pure titanium. Proceedings of the 13th world conference on titanium. Hoboken, NJ, USA, 2016.

[56]. Kang D, Lee K, Kwon E, Tsuchiyama T, Takaki S. Variation of work hardening rate by oxygen contents in pure titanium alloy. Mater Sci Eng A 2015; 632: 120-6.

[57]. Lavogiez C, Hémery S, Villechaise P. Analysis of deformation mechanism operating under fatigue and dwell-fatigue loading in an $\alpha+\beta$ titanium alloy. Int J Fatigue 2020; 131: 105341.

[58]. Britton TB, Dunne FPE, Wilkinson AJ. On the mechanistic basis of deformation at the microscale in hexagonal close-packed metals. Proc R Soc A 2014: 471(2178): 20140881.

[59]. Oberson PG, Ankem S. The effect of time-dependent twinning on low temperature (<0.25Tm) creep of an alpha-titanium alloy. Int J Plast 2009; 25(5): 881-900.

[60]. Luan Q, Britton TB, Jun JS. Strain rate sensitivity in commercial pure titanium: The competition between slip and deformation twinning. Mater Sci Eng A 2018; 734: 385-97.

[61]. Kasemer M, Dawson P. A finite element methodology to incorporate kinematic activation of discrete deformation twins in a crystal plasticity framework. Comput Method Appl M 2020; 358: 112653.

[62]. Spence S, Evans W, Cope M. Dwell fatigue on Ti-6246 at near ambient temperatures. ICF 9-Sydney, Australia-1997.

[63]. Zhang Z, Cuddihy MA, Dunne FPE. On rate-dependent polycrystal deformation: the temperature sensitivity of cold dwell fatigue. Proc R Soc A 2015; 471: 20150214.

[64]. Whittaker MT, Harrison W, Hurley PJ, Williams S. Modelling the behaviour of titanium alloys at high temperature for gas turbine applications. Mater Sci Eng A 2010; 527: 4365-72.

[65]. Zheng Z, Balint DS, Dunne FPE. Mechanistic basis of temperature-dependent dwell fatigue in titanium alloys, J Mech Phys Solid 2017; 107: 185-203.

[66]. Ready AJ, Haynes PD, Grabowski B, Rugg D, Sutton AP. The role of molybdenum in suppressing cold dwell fatigue in titanium alloys. Proc R Soc A 2017; 473: 20170189.

[67]. Yazar KU, Mishra S, Karmakar A, Bhattacharjee A, Suwas S. On the temperature sensitivity of dwell fatigue of a near alpha titanium alloy: Role of strain hardening and strain rate sensitivity. Metall Mater Trans A 2020; 51: 5036-42.

[68]. Peng J, Zhou CY, Dai Q, He XH. The temperature and stress dependent primary creep of CP-Ti at low and intermediate temperature. Mater Sci Eng A 2014; 611: 123-35.

[69]. Harr ME, Daly S, Pilchak AL. The effect of temperature on slip in microtextured Ti-6Al-2Sn-4Zr-2Mo under dwell fatigue. Int J Fatigue 2021; 147: 106173.

[70]. Zhang Z. Microscale crystal slip and macroscopic cold creep transition in dwell fatigue. Int J Fatigue 2021; 142: 105967.

[71]. Ozturk D, Shahba A, Ghosh S. Crystal plasticity FE study of the effect of thermomechanical loading on fatigue crack nucleation in titanium alloys. Fatigue Fract Eng Mater Struct 2016; 39: 752-69.

[72]. Bache MR, Cope M, Davies HM, Evans WJ, Harrison G. Dwell sensitive fatigue in a near alpha titanium alloy at ambient temperature. Int J Fatigue 1997; 19(1): S83-S88.

[73]. Lefranc P, Sarrazin-Baudoux C, Doquet V, Petit J. Investigation of the dwell period's influence on the fatigue crack growth of a titanium alloy. Scripta Mater 2009; 60(5): 281-4.

[74]. Su CY, Zhou CY, Lu L, Li J, Sun PY, He XH. Effect of temperature and dwell time on fatigue crack growth behavior of CP-Ti. Metals 2018; 8(12): 1031.

[75]. Sinha V, Mills MJ, Williams JC. Understanding the contribution of normal fatigue and static loading to the dwell fatigue in a near alpha titanium alloy. Metall Mater Trans A 2004; 35(10): 3141-8.

[76]. Han J, Guo H. An equilibrium multi-objective optimum design for non-circular clearance hole of disc with discrete variables. Chin J Aeronaut 2018; 31: 247-54.

[77]. Yin L, Guo H. Analysis on dimension tolerance design of non-circular hole of labyrinth disc for an aeroengine. Aeroengine 2017; 43: 85-90.

[78]. Doquet V, De Greef V. Dwell-fatigue of a titanium alloy at room temperature under uniaxial or

biaxial tension. Int J Fatigue 2012; 38: 118-29.

[79]. Cuddihy MA, Stapleton A, Williams S. On cold dwell facet fatigue in titanium alloy aero-engine components. Int J Fatigue 2017; 97: 177-89.

[80]. Hommer GM. Mechanism of dwell fatigue crack initiation in Ti-7Al under biaxial tension-tension loads. Ph. D. thesis, CSM; 2018.

[81]. Anahid M, Samal MK, Ghosh S. Dwell fatigue crack nucleation model based on crystal plasticity finite element simulations of polycrystalline titanium alloys. J Mech Phys Solids 2011; 59(10): 2157-76.

[82]. Wilson D, Wan W, Dunne FPE. Microstructurally-sensitive fatigue crack growth in HCP, BCC and FCC polycrystals. J Mech Phys Solids 2019; 124: 206-25.

[83]. Huang Y. A User-Material Subroutine Incroporating Single Crystal Plasticity in the ABAQUS Finite Element Program, Harvard Univ, 1991.

[84]. Asaro RJ. Micromechanics of crystals and polycrystals. Adv Appl Mech 1983; 23: 1-115.

[85]. Hill R, Rice JR. Constitutive analysis of elastic-plastic crystals at arbitrary strain. J Mech Phys Solids 1972; 20(6): 401-13.

[86]. Lee BJ, Vecchio KS, Ahzi S, Schoenfeld S. Modeling the mechanical behavior of tantalum. Metall Mater Trans A 1997; 28(1): 113-22.

[87]. Granato AV, Lücke K, Schlipf J. Entropy factors for thermally activated unpinning of dislcoations. J Appl Phys 1964; 35(9): 2732-45.

[88]. Dunne FPE, Rugg D, Walker A. Lengthscale-dependent, elastically anisotropic, physically-based hcp crystal plasticity Application to cold-dwell fatigue in Ti alloys. Int J Plast 2007; 23: 1061-83.

[89]. Graff S, Brocks W, Steglich D. Yielding of magnesium: From single crystal to polycrystalline aggregates. Int J Plast 2007; 23: 1957-78.

[90]. Han C, Gao H, Huang Y, Nix WD. Mechanism-based strain gradient crystal plasticity—I. Theory. J Mech Phys Solid 2005; 53(5): 1188-203.

[91]. Han C, Gao H, Huang Y, Nix WD. Mechanism-based strain gradient crystal plasticity—II. Analysis. J Mech Phys Solid 2005; 53(5): 1204-22.

[92]. Lee WB, Chen YP. Simulation of micro-indentation hardness of FCC single crystals by mechanism-based strain gradient crystal plasticity. Int J Plast 2010; 26: 1527-40.

[93]. Taylor GI. The mechanism of plastic deformation of crystals. Part I.—Theoretical. Proc R Soc

Lond A 1934; 145: 362-87.

[94]. Busso EP, Meissonnier FT, O'dowd NP. Gradient deformation of two-phase single crystal. J Mech Phys Solid 2000; 48: 2333-61.

[95]. Tomé CN, Lebensohn RA, Kocks UF. A model for texture development dominated by deformation twinning: Application to zirconium alloy. Acta Metall Mater 1991; 39(11): 2667-80.

[96]. ABAQUS Manual Version 6.13-1. Dassault Systémes Simulia Corp., Providence, RI 2013.

[97]. Liang H, Dunne FPE. GND accumulation in bi-crystal deformation: Crystal plasticity analysis and comparison with experiments. Int J Mech Sci 2009; 51(4): 326-33.

[98]. Hama T, Kobuki A, Takuda H. Crystal-plasticity finite-element analysis of anisotropic deformation behavior in a commercially pure titanium Grade 1 sheet. Int J Plast 2017; 91: 77-108.

[99]. Bachmann F, Hielscher R, Schaeben H. Texture analysis with MTEX – free and open source software toolbox. Solid State Phenom 2010; 160: 63-8.

[100]. Bandyopadhyay R, Mello AW, Kapoor K, Reinhold MP, Broderick TF, Sangid MD. On the crack initiation and heterogeneous deformation of Ti-6Al-4V during high cycle fatigue at high R ratios. J Mech Phys Solid 2019; 129: 61-82.

[101]. Blaber J, Adair B, Antoniou A. Ncorr: Open-source 2D digital Image correlation Matlab software. Exp Mech 2015; 55: 1105-22.

[102]. Littlewood PD, Wilkinson AJ. Local deformation patterns in Ti-6Al-4V under tensile, fatigue and dwell fatigue loading. Int J Fatigue 2012; 43: 111-9.

[103]. Barkia B, Doquet V, Couzinié JP, Guillot I, Héripré E. In situ monitoring of the deformation mechanisms in titanium with different oxygen contents. Mater Sci Eng A 2015; 636: 91-102.

[104]. Won JW, Park CH, Hong SG, Lee CS. Deformation anisotropy and associated mechanisms in rolling textured high purity titanium. J Alloy Comp 2015; 651: 245-54.

[105]. Baudoin P, Hama T, Takuda H. Influence of critical resolved shear stress ratios on the response of a commercially pure titanium oligocrystal: crystal plasticity simulations and experiment. Int J Plast 2019; 115: 111-31.

[106]. Zhang Z, Lunt D, Abdolvand H, Wilkinson AJ, Preuss M, Dunne FPE. Quantitative investigation of micro slip and localization in polycrystalline materials under uniaxial tension. Int J Plast 2018: 108: 88-106.

[107]. Xiong Y, Karamched, Nguyen CT, Collins DM, Magazzeni CM, Tarleton E, Wilkinson AJ. Cold

creep of titanium: Analysis of stress relaxation using synchrotron diffraction and crystal plasticity simulations. Acta Mater 2020; 199: 561-77.

[108]. Jun TS, Zhang Z, Sernicola G, Dunne FPE, Britton TB. Local strain rate sensitivity of single α phase within a dual-phase Ti alloy. Acta Mater 2016; 107: 298-309.

[109]. Wang L, Zheng Z, Phukan H, Kenesei P, Park JS, Lind J, Suter RM, Bieler TR. Direct measurement of critical resolved shear stress of prismatic and basal slip in polycrystalline Ti using high energy X-ray diffraction microscopy. Acta Mater 2017; 132: 598-610.

[110]. Morita M, Suzuki S, Kato Y, Li W, Umezawa O. Tensile deformation of texture-controlled titanium with high oxygen content at room temperature. Mater Sci Eng A 2020; 793: 139660.

[111]. Yu Q, Qi L, Tsuru T, Traylor R, Rugg D, Morris JW, Mark A, Chrzan DC, Minor AM. Origin of dramatic oxygen solute strengthening effect in titanium. Science 2015; 347(6222): 635-9.

[112]. Gong J, Wilkinson AJ. Anisotropy in the plastic flow properties of single-crystal α titanium determined from micro-cantilever beams. Acta Mater 2009; 57(19): 5693-705.

[113]. Salem AA, Kalidindi SR, Semiatin SL. Strain hardening due to deformation twinning in α-titanium: Constitutive relations and crystal-plasticity modeling. Acta Mater 2005; 53(12): 3495-502.

[114]. Ren W, Xin R, Liu D. Modeling the strongly localized deformation behavior in a magnesium alloy with complicated texture distribution. Mater Sci Eng A 2019; 762: 138103.

[115]. Knezevic M, Lebensohn RA, Cazacu O, Revil-Baudard B, Proust G, Vogel SC, Nixon ME. Modeling bending of α-titanium with embedded polycrystal plasticity in implicit finite elements. Mater Sci Eng A 2013; 564: 116-26.

[116]. Wu X, Kalidindi SR, Necker C, Salem AA. Prediction of crystallographic texture evolution and anisotropic stress-strain curves during large plastic strains in high purity α-titanium using a Taylor-type crystal plasticity model. Acta Mater 2007; 55(2): 423-32.

[117]. Li YL, Kohar CP, Mishra RK, Inal K. A new crystal plasticity constitutive model for simulating precipitation-hardenable aluminum alloys. Int J Plast 2020; 132: 102759.

[118]. Chen Y, Clausen AH, Hopperstad OS, Langseth M. Stress-strain behaviour of aluminium alloys at a wide range of strain rates. Inter J Solid Struct 2009; 46(21): 3825-35.

[119]. Mikami Y, Oda K, Mochizuki M. Effect of crystal plasticity parameters on microscopic stress distribution in polycrystalline aggregate model. J Multiscale Modell 2013; 5(1): 1350003.

[120]. Yoo MH. Slip, twinning, and fracture in hexagonal close-packed metals. Metall Trans A 1981; 12: 409-18.

[121]. Cuddihy MA. Cold dwell facet nucleation in titanium alloy aero-engine components. Ph.D. thesis, Imperial College London; 2017.

[122]. Ren JQ, Wang Q, Lu XF, Liu WF, Zhang PL, Zhang XB. Effect of oxygen content on active deformation systems in pure titanium polycrystals. Mater Sci Eng A 2018; 731: 530-8.

[123]. Lavogiez C, Hémery S, Villechaise P. Analysis of deformation mechanism operating under fatigue and dwell-fatigue loading in an $\alpha + \beta$ titanium alloy. Int J Fatigue 2020; 131: 105341.

[124]. Zhao J, Lv L, Liu G, Wang K. Analysis of deformation inhomogeneity and slip mode of TA15 titanium alloy sheets during the hot tensile process based on crystal plasticity model. Mater Sci Eng A 2015; 707: 30-9.

[125]. Dunne FPE, Rugg D. On the mechanisms of fatigue facet nucleation in titanium alloys. Fatigue Fract Eng Mater Struct 2008; 31(11): 949-58.

[126]. Zheng Z, Balint DS, Dunne FPE. Discrete dislocation and crystal plasticity analyses of load shedding in polycrystalline titanium alloys. Int J Plast 2016; 87: 15-31.

[127]. Livescu V, Beyerlein IJ, Bronkhorst CA, Dippo OF, Ndefru BG, Capolungo L, Mourad HM. Microstructure insensitive twinning: A statistical analysis of incipient twins in high-purity titanium. Materialia 2019; 6: 100303.

[128]. Paramatmuni C, Zheng Z, Rainforth WM, Dunne FPE. Twin nucleation and variant selection in Mg alloys: An integrated crystal plasticity modelling and experimental approach. Int J Plast 2020; 135: 102778.

[129]. Oliver WC, Pharr GM. An improved technique for determining hardness and elastic modulus using load and displacement sensing indentation experiments. J Mater Res 1992; 7: 1564-83.

[130]. Oliver WC, Pharr GM. Measurement of hardness and elastic modulus by instrumented indentation: Advances in understanding and refinements to methodology. J Mater Res 2004; 19(1): 3-20.

[131]. Fujii H, Maeda T. Titanium alloys developed by Nippon steel & Sumitomo metal corporation. Nippon Steel & Sumitomo Metal Tech Rep 2014; 106: 16-21.

[132]. Min XH, Zhang L, Sekido K, Ohmura T, Emura S, Tsuchiya K, Tsuzaki K. Strength evaluation of α and β phases by nanoindentation in Ti–15Mo alloys with Fe and Al addition. Mater Sci Tech 2012; 28(3): 342-7.

[133]. Jun TS, Armstrong DEJ, Britton TB. A nanoindentation investigation of local strain rate sensitivity in dual-phase Ti alloys. J Alloy Comp 2016; 672: 282-91.

[134]. Zhang Z, Jun TS, Britton TB, Dunne FPE. Determination of Ti-6242 α and β slip properties using micro-pillar test and computational crystal plasticity. J Mech Phys Solid 2016; 95: 393-410.

[135]. Lucas BN, Oliver WC. Indentation power-law creep of high-purity indium. Metall Mater Trans A 1999; 30: 601-10.

[136]. Kami T, Yamada H, Ogasawa N, Chen X. Strain rate behavior of pure aluminum in conical indentation with different indenter control methods. Int J Comp Meth Exp Meas 2018; 6(3): 515-26.

[137]. Groeber MA, Jackson MA. DREAM.3D: A Digital Representation Environment for the Analysis of Microstructure in 3D. Integr Mater Manuf I 2014; 3: 56-72.

[138]. Zhang M, Li J, Tang B, Kou H, Fan J. Mechanical characterization and strain-rate sensitivity measurement of Ti-7333 alloy based on nanoindentation and crystal plasticity modeling. Prog Nat Sci 2018; 28(6): 718-23.

[139]. Zhang Z. Microscale crystal slip and macroscopic cold creep transition in dwell fatigue. Int J Fatigue 2021; 142: 105967.

[140]. Yokoyama H, Umezawa O, Nagai K, Suzuki T, Kokubo K. Cyclic deformation, dislocation structure, and internal fatigue crack generation in a Ti-Fe-O alloy at liquid nitrogen temperature. Metall Mater Trans A 2000; 31: 2793-805.

[141]. Stráský J, Harcuba P, Václavová K, Horváth K, Landa M, Srba O, Janeček M. Increasing strength of a biomedical Ti-Nb-Ta-Zr alloy by alloying with Fe, Si and O. J Mech Behav Biomed Mater 2017; 71: 329-36.

[142]. Louzguine-Luzgin DV. High-strength Ti-based alloys containing Fe as one of the main alloying elements. Mater Trans 2018; 59: 1537-44.

[143]. Demiral M, Roy A, Silberschmidt VV. Indentation studies in b.c.c. crystals with enhanced model of strain-gradient crystal plasticity. Comput Mater Sci 2013;79: 896-902.

[144]. Xu Y, Joseph S, Karamched P, Fox K, Rugg D, Dunne FPE, Dye D. Predicting dwell fatigue life in titanium alloys using modelling and experiment. Nat Commun 2020; 11(1): 1-13.

[145]. Han F, Tang B, Kou H, Li J, Feng Y. Experiments and crystal plasticity finite element simulations of nanoindentation on Ti-6Al-4V alloy. Mater Sci Eng A 2015; 625: 28-35.

[146]. Kapoor K, Ravi P, Noraas R, Park JS, Venkatesh V, Sangid MD. Modeling Ti-6Al-4V using crystal plasticity, calibrated with multi-scale experiments, to understand the effect of the orientation and morphology of the α and β phases on time dependent cyclic loading. J Mech Phys Solid 2021; 146: 104192.

[147]. Umezawa O, Yuasa T, Li W. Fractographical analyses of crack initiation site in high-cycle fatigue for Ti–Fe–O alloy at low temperature. ISIJ Int 2018; 58: 1332-40.

[148]. Luster J, Morris MA. Compatibility of deformation in two-phase Ti-Al alloys: Dependence on microstructure and orientation relationships. Metall Mater Trans A 1995; 26: 1745-56.

[149]. Hémery S, Nizou P, Villechaise P. In situ SEM investigation of slip transfer in Ti-6Al-4V: effect of applied stress. Mater Sci Eng A 2018; 709: 277-84.

[150]. He D, Zhu J, Zaefferer S, Raabe D. Effect of retained beta layer on slip transmission in Ti–6Al–2Zr–1Mo–1V near alpha titanium alloy during tensile deformation at room temperature. Mater Des 2014; 56: 937-42.

[151]. Hamid M, Lyu H, Schuessler BC, Wo PC, Zbib HM. Modeling and characterization of grain boundaries and slip transmission in dislocation density-based crystal plasticity. Crystals 2017; 7(6): 152.

[152]. Yin L, Umezawa O. Heterogeneous deformation in a commercially pure titanium sheet under dwell fatigue loading: Crystal plasticity modeling and experiment. ISIJ Int 2021; 61(6): 1990-2001.

[153]. Lefranc P, Doquet V, Gerland M, Sarrazin-Baudoux C. Nucleation of cracks from shear-induced cavities in an alpha/beta titanium alloy in fatigue, room-temperature creep and dwell-fatigue. Acta Mater 2008; 56: 4450-57.

[154]. Li W, Umezawa O, Koga N. Analysis of Subsurface Fatigue Crack Generation in Ti-Fe-O Alloy at Low Temperature. ISIJ Int 2018; 58(2): 359-63.

[155]. Kirane K, Ghosh S. A cold dwell fatigue crack nucleation criterion for polycrystalline Ti-6242 using grain-level crystal plasticity FE model. Int J Fatigue 2008; 30: 2127-39.

[156]. Lerch BA, Arnold SM. Viscoelastic response of the titanium alloy Ti-6-4: experimental identification of time and rate-dependent reversible and irreversible deformation regions. NASA Report. Cleveland, Ohio; 2014.

[157]. Lerch BA, Arnold SM. Viscoplastic characterization of Ti-6-4: experiments. NASA Report.

Cleveland, Ohio; 2016.

[158]. Liu Y, Dunne FPE. The mechanistic link between macrozones and dwell fatigue in titanium alloys. Int J Fatigue 2021; 142: 105971.

[159]. Quey R, Dawson PR, Barbe F. Large-scale 3D random polycrystals for the finite element method: Generation, meshing and remeshing. Comput Methods Appl Mech Eng 2011; 200: 1729-45.

[160]. Hu P, Liu Y, Zhu Y, Ying L. Crystal plasticity extended models based on thermal mechanism and damage functions: application to multiscale modeling of aluminum alloy tensile behavior. Int J Plast 2016; 86: 1-25.

[161]. Ogi H, Kai S, Ledbetter H, Tarumi R, Hirao M, Takashima K. Titanium's high-temperature elastic constants through the hcp–bcc phase transformation. Acta Mater 2004: 52: 2075-80.

[162]. Nemat-Nasser S, Guo W, Cheng J. Mechanical properties and deformation mechanisms of a commercially pure titanium. Acta Mater 1999; 47: 3705-20.

[163]. Bridier F, McDowell DL, Villechaise P, Mendez J. Crystal plasticity modeling of slip Activity in Ti–6Al–4V under high cycle fatigue loading. Int J Plast 2009;25(6): 1066–82.

[164]. Conrad H. Thermally activated deformation of a titanium below 0.4 T_M. Can J Phys 1967; 45(2): 581-90.

[165]. Chen G, Ren C, Qin X, Li J. Temperature dependent work hardening in Ti–6Al–4V alloy over large temperature and strain rate ranges: experiments and constitutive modeling. Mater Des 2015; 83: 598-610.

[166]. Zhang Z, Dunne FPE. Microstructural heterogeneity in rate-dependent plasticity of multiphase titanium alloys. J Mech Phys Solids 2017; 103: 199–220.

[167]. Joseph S, Joseph K, Lindley TC, Dye D. The role of dwell hold on the dislocation mechanisms of fatigue in a near alpha titanium alloy. Int J Plast 2020; 131: 102743.

[168]. Zhang Z. Micromechanistic study of textured multiphase polycrystals for resisting cold dwell fatigue. Acta Mater 2018; 156: 254-65.

[169]. Grilli N, Tarleton E, Cocks ACF. Neper2CAE and PyCiGen: scripts to generate polycrystals and interface elements in Abaqus. SoftwareX 2021; 13: 100651.

[170]. Yin L, Umezawa O. Influence of dispersed β phase on local deformation pattern in mill-annealed Ti-Fe-O alloy under dwell fatigue loading. Int J Fatigue 2021; 152: 106447.

[171]. Zheng Z, Stapleton A, Fox K, Dunne FPE. Understanding thermal alleviation in cold dwell fatigue

in titanium alloys. Int J Plast 2018; 111: 234-52.

[172]. Lin YH, Hu KH, Kao FH, Wang SH, Yang JR, Lin CK. Dynamic strain aging in low cycle fatigue of duplex titanium alloys. Mater Sci Eng, A 2011; 528(13–14): 4381-9.

[173]. Singh N, Singh V. Effect of temperature on tensile properties of near-α alloy Timetal 834. Mater Sci Eng A 2008; 485(12): 130-9.

[174]. Suarez Fernandez D, Wynne B, Crawforth P, Fox K, Jackson M. The effect of forging texture and machining parameters on the fatigue performance of titanium alloy disc components. Int J Fatigue 2021; 142: 105949.

[175]. Yang W. Research on structural optimization design of four web fan disk of aero-engine. MA thesis, Huaqiao Univ; 2019.

[176]. Huang X, Chen C, Xuan H. Experimental and analytical investigation for fatigue crack growth characteristics of an aero-engine fan disc. Int J Fatigue 2021; 148: 106252.

[177]. Kasemer M, Echlin MP, Stinville JC, Pollock TM, Dawson P. On slip initiation in equiaxed α/β Ti-6Al-4V. Acta Mater 2017; 136: 288-302.

[178]. Hémery S, Naït-Ali A, Gueguen M, Wendorf J, Polonsky AT, Echlin MP, Stinville JC, Pollock TM, Villechaise P. A 3D analysis of the onset of slip activity in relation to the degree of micro-texture in Ti–6Al–4V. Acta Mater 2019; 181: 36-48.

[179]. Cappola J, Stinville J, Charpagne M, Callahan PG, Echlin MP, Pollock TM, Pilchak AL, Kasemer M. On the localization of plastic strain in microtextured regions of Ti-6Al-4V. Acta Mater 2021; 204: 116492.

[180]. Kotha S, Ozturk D, Ghosh S. Parametrically homogenized constitutive models (PHCMs) from micromechanical crystal plasticity FE simulation, part I: Sensitivity analysis and parameter identification for Titanium alloys. Int J Plast 2019; 120: 296-319.

[181]. Wang Q, Ri S, Maenosono A, Tanaka Y, Koyama M. 1-second-resolved strain mapping in Ti-6Al-4V alloys during dwell fatigue in SEM by video sampling moiré. Mech Mater 2019; 133: 63-70.

[182]. Stinville JC, Francis T, Polonsky AT, Torbet CJ, Charpagne MA, Chen Z, Balbus GH, Bourdin F, Valle V, Callahan PG, Echlin MP, Pollock TM. Time-Resolved Digital Image Correlation in the Scanning Electron Microscope for Analysis of Time-Dependent Mechanisms. Exp Mech 2021; 61(2): 331-48.

[183]. Venkatesh V, Noraas R, Pilchak AL, Tamirisa S, Calvert K, Salem A, Broderick T, Glavicic MG,

Dempster I, Saraf V. Data driven tools and methods for microtexture classification and dwell fatigue life prediction in dual phase titanium alloys. MATEC Web Conf 2020; 321: 11091.

[184]. Roklin SI, Kim JY, Xie B, Zoofan B. Nondestructive sizing and localization of internal microcracks in fatigue samples. NDT$E Int 2007; 40(6): 462-70.

[185]. Chandravanshi V, Prasad K, Singh V, Bhattacharjee A, Kumar V. Effects of $\alpha + \beta$ phase deformation on microstructure, fatigue and dwell fatigue behavior of a near alpha titanium alloy. Int J Fatigue 2016; 91: 100-9.

[186]. Everaerts J, Gontcharov D, Verlinden B, Wevers M. The influence of load holds on the fatigue behaviour of drawn Ti-6Al-4V wires. Int J Fatigue 2017; 98: 203-11.

[187]. Yang L, Liu J, Tan J, Chen Z, Wang Q, Yang R. Dwell and normal cyclic fatigue behaviours of Ti60 alloy. J Mater Sci Technol 2014; 30(7): 706-9.

[188]. Evans WJ, Gostelow CR. The effect of hold time on the fatigue properties of a β-processed titanium alloy. Metall Trans A 1979; 10(12): 1837-46.

[189]. Evans WJ. Time dependent effects in fatigue of titanium and nickel alloys. Fatigue Fract Eng Mater Struct 2004; 27(7): 543-57.

[190]. Song Q, Li Y, Wang L, Huang R, Sun C. Effect of rise and fall time on dwell fatigue behavior of a high strength titanium alloy. Metals 2019; 9(8): 914.

[191]. Bunge HJ. Texture analysis in materials science: mathematical methods. Elsevier, 2013.